

Sergey Lukashov · Alexander Petrov
Anatoly Pravilov

The Iodine Molecule

Insights into Intra- and Intermolecular
Perturbation in Diatomic Molecules



Springer

The Iodine Molecule

Sergey Lukashov • Alexander Petrov
Anatoly Pravilov

The Iodine Molecule

Insights into Intra- and Intermolecular
Perturbation in Diatomic Molecules

 Springer

Sergey Lukashov
Department of Physics
Saint Petersburg State University
Saint Petersburg, Russia

Alexander Petrov
Department of Physics
Saint Petersburg State University
Saint Petersburg, Russia

Anatoly Pravilov
Department of Physics
Saint Petersburg State University
Saint Petersburg, Russia

National Research Centre “Kurchatov
Institute”, B.P. Konstantinov Petersburg,
Nuclear Physics Institute
Gatchina, Leningrad district, Russia

ISBN 978-3-319-70071-7 ISBN 978-3-319-70072-4 (eBook)
<https://doi.org/10.1007/978-3-319-70072-4>

Library of Congress Control Number: 2017960170

© Springer International Publishing AG 2018

This work is subject to copyright. All rights are reserved by the Publisher, whether the whole or part of the material is concerned, specifically the rights of translation, reprinting, reuse of illustrations, recitation, broadcasting, reproduction on microfilms or in any other physical way, and transmission or information storage and retrieval, electronic adaptation, computer software, or by similar or dissimilar methodology now known or hereafter developed.

The use of general descriptive names, registered names, trademarks, service marks, etc. in this publication does not imply, even in the absence of a specific statement, that such names are exempt from the relevant protective laws and regulations and therefore free for general use.

The publisher, the authors and the editors are safe to assume that the advice and information in this book are believed to be true and accurate at the date of publication. Neither the publisher nor the authors or the editors give a warranty, express or implied, with respect to the material contained herein or for any errors or omissions that may have been made. The publisher remains neutral with regard to jurisdictional claims in published maps and institutional affiliations.

Printed on acid-free paper

This Springer imprint is published by Springer Nature
The registered company is Springer International Publishing AG
The registered company address is: Gewerbestrasse 11, 6330 Cham, Switzerland

Preface

Methods of theoretical and experimental studies of spectroscopic characteristics of the iodine molecule valence, ion-pair (IP) and Rydberg states, spectroscopic characteristics themselves, nonadiabatic perturbations of these states, and RgI_2 van der Waals (vdW) complexes as well as collision-induced processes are reviewed in the book. The emphasis of the book is focused on nonadiabatic perturbation in a free molecule, and intermolecular nonadiabatic perturbation occurred in collision-induced nonadiabatic transitions and RgI_2 vdW complexes. Spectroscopic characteristics as well as population and decay of the RgI_2 excited states are analyzed. The principal features of intermolecular perturbations which manifest in excited states of vdW complexes formed in collisions and optically are discussed.

Nonadiabatic interactions between excited bound states in diatomic molecules are one of fundamental problems of modern chemical physics and molecular spectroscopy. The iodine molecule is a unique system for understanding of the intramolecular and intermolecular nonadiabatic perturbations in diatomic molecules.

Saint Petersburg, Russia

Sergey Lukashov
Alexander Petrov
Anatoly Pravilov

Acknowledgments

The authors are very grateful to Springer-Verlag GmbH for its suggestion to publish this book.

A considerable part of the data described in the book was obtained in studies which were carried out by the authors with the assistance of colleagues. The authors very much appreciate their help and collaboration. S. Lukashov and A. Privilov are especially grateful to Prof. Mikhail Akopyan, Dr. Vera Baturo, and Dr. Sergey Poretsky.

Contents

1	Introduction	1
1.1	General	1
1.2	The Iodine Molecule	3
	References	5
2	Overview of Instrumentation and Methods	7
2.1	Absorption Spectroscopy	7
2.2	Emission Spectroscopy	8
2.3	(1 + 1) Two-Step and (1 + 2) Photon Optical-Optical Double Resonance	8
2.4	Three-Step Three-Color Laser Population	11
2.5	Perturbation-Facilitated Two-Step Excitation Scheme	13
2.6	Perturbation-Facilitated Three-Step Excitation Scheme	14
2.7	Resonance Enhanced Multiphoton Ionization (REMPI)	15
2.8	Velocity Map Imaging	16
	References	17
3	Electronic States of Iodine Molecule and Optical Transitions Between Them	21
3.1	Theoretical Background	21
3.2	Valence States and Valence-Valence Transitions	25
3.2.1	Transitions from the <i>X</i> State	27
3.2.2	Transitions from the <i>B</i> State	29
3.3	Ion-Pair States and Valence-Ion-Pair Transitions	31
3.3.1	General	31
3.3.2	First Tier IP States	33
3.3.3	Second and Third Tier IP States	34
3.3.4	High-Lying Vibrational Levels of IP States	35
3.3.5	Ion-Pair – Valence State Transition	37

3.4	Rydberg States	42
3.4.1	General	42
3.4.2	The $[^2\Pi]_c$ <i>ns</i> Series	43
3.4.3	The $[^2\Pi]_c$ <i>np</i> Series	45
3.4.4	The $[^2\Pi]_c$ <i>nd</i> Series	47
3.4.5	The $[^2\Pi]_c$ <i>nf</i> Series	48
3.4.6	Other Rydberg States	49
	References	50
4	Intramolecular Perturbations in the Electronically Excited States	57
4.1	Theoretical Background	57
4.2	Spontaneous Predissociation	63
4.2.1	Valence States	63
4.2.2	Rydberg States	65
4.3	Perturbation Between Bound States	67
4.3.1	Valence States	67
4.3.2	Ion-Pair States	72
4.3.3	Rydberg-IP State Interaction	82
	References	87
5	Collision-Induced Processes in Iodine Molecule	91
5.1	Background	91
5.2	Rotational, Vibrational and Rovibrational Energy Transfer in Iodine Molecule	94
5.3	Collision-Induced Nonadiabatic Processes in Iodine Molecule	95
5.3.1	Collision-Induced Predissociation of the $I_2(B0_u^+)$ State	95
5.3.2	Collision-Induced Nonadiabatic Transitions between the Ion-Pair States	96
	References	134
6	Van der Waals Complexes of Iodine Molecules	139
6.1	General	139
6.2	Overview of Experimental Methods. State-of-the-Art	141
6.2.1	Design and Characteristics of the Set-Up Utilized in the Author's Group	142
6.3	Theoretical Models	148
6.4	The RgI_2 vdW Complexes	153
6.4.1	The HeI_2 vdW Complexes	153
6.4.2	The NeI_2 vdW Complexes	163
6.4.3	The ArI_2 vdW Complexes	168
6.4.4	The KrI_2 vdW Complexes	178
6.4.5	The XeI_2 vdW Complexes	180

6.5 The Principal Features of Decay of the Electronically-Excited RgI ₂ vdW Complexes Populated in Collisions and Optically	181
References	183
Conclusions	189
Appendix	191
References	194
Index	197

Abbreviations

<i>aa</i>	$I(^2P_{3/2}) + I(^2P_{3/2})$ dissociation limit
<i>ab</i>	$I(^2P_{3/2}) + I(^2P_{1/2})$ dissociation limit
<i>bb</i>	$I(^2P_{1/2}) + I(^2P_{1/2})$ dissociation limit
CC	Coupled cluster
CC	Close coupled
CCSD	Coupled-cluster method with single and double excitations
CCSD(T)	Coupled-cluster method with single and double and triple excitations
CI	Configuration interaction
CINAT	Collision-induced nonadiabatic transition
DIM	Diatomic-in-molecules
EDW	Exponential distorted wave
EDW-IOS	Exponential distorted wave infinite-order sudden
<i>EP</i>	Electronic predissociation
EVCC-IOS	Infinite-order sudden approximation keeping close coupling of electronic and vibrational degrees of freedom
<i>FCD</i>	Franck-Condon density
<i>FCF</i>	Franck-Condon factor
FWHM	Full width half maximum
<i>HFI</i>	Hyperfine interaction
<i>HFP</i>	Hyperfine predissociation
IDIM	Intermolecular diatomics-in-molecule
IDIM PT1	The first-order intermolecular diatomics-in-molecule perturbation theory
IOS	Infinite-order sudden
IP	Ion pair
IP-V	Ion-pair valence
IR	Infrared
KER	Kinetic energy release
LIF	Laser-induced fluorescence
LR	Long range

<i>MD</i>	Magnetic dipole
<i>MO</i>	<i>Molecular orbital</i>
MR-CI	Multi-reference configuration interaction
MR-CISD	Multi-reference configuration interaction with single and double excitation
<i>MQ</i>	Electric quadrupole
NDE	Near-dissociation expansion
OODR	Optical-optical double resonance
<i>PEC</i>	Potential energy curve
<i>PES</i>	Potential energy surface
PFOODR	Perturbation-facilitated optical-optical double resonance
PMT	Photomultiplier tube
RCC	Restricted Hartree-Fock coupled-cluster (CC) methods
RCCSD(T)	Restricted coupled-cluster method with single, double, and triple excitations
REMPI	Resonance enhanced multiphoton ionization
<i>RKR</i>	Rydberg-Klein-Rees
$R \leftrightarrow T$	Rotational-translational energy transfer process
<i>RS</i>	Repulsive state
TPE	Threshold photoelectron
$T \leftrightarrow T$	Translational-translational energy transfer process
UHFCC	Unrestricted Hartree-Fock coupled-cluster (CC) methods
UCCSD(T)	Unrestricted coupled-cluster method with single, double, and triple excitations
VMI	Velocity map imaging
<i>VP</i>	Vibrational predissociation
vdW	Van der Waals
<i>VD</i>	Vibrational distribution
UV	Ultraviolet
$V \leftrightarrow T$	Vibrational-translational energy transfer process
VUV	Vacuum ultraviolet
X ₂	Homonuclear halogen molecule
XY	Heteronuclear halogen molecule
ZEKE-PFI	Zero kinetic energy pulsed field ionization

List of Symbols

Latin

B_e	Rotational constant for a $v = 0$ vibrational level
B_v	Rotational constant for a $v \neq 0$ vibrational level
C	Mixing coefficient
D	Debye
D_e	Potential well depth
D_0	Binding energy (vdW complex)
D_0	Dissociation energy for the $v = 0$ vibrational level
e	Electron (elementary) charge
E	Energy
E	Irradiance
$E_{h\nu}$	Photon irradiance
eV	Electron-volt
g	Gerade
h	Planck's constant
\hbar	Planck's constant
\hat{H}	Hamiltonian
IE	Ionization energy
J	Rotational quantum number
j	Electronic angular momentum
$k(\nu)$	Absorption coefficient
k	Rate constant
$k^M(i, v_i \rightarrow f)$	Partial rate constant of the $i, v_i \xrightarrow{M} f$ CINAT process
M	Molecule
M	Reduced mass of a molecule
n	Principal quantum number
n	Vibrational quantum number of vdW mode

n^*	Effective principal quantum number
P	Probability
$P(v)$	Vibrational distribution
$P_i(j)$	Term of a $RgI_2(E, v_E, n_E \leftarrow B, v_B, n_B)$ progression
r	I-I internuclear distance in RgI_2 vdW complexes
R	I-I internuclear distance
R	Distance between Rg atoms and I_2 center of mass in RgI_2 vdW complexes
Rg	Rare gas atom
Ry	Rydberg constant
T_e	Electronic energy
v	Vibrational quantum number
u	Ungerade
V	Perturbation matrix element
V	interaction potential operator
$ v\rangle$	Vibrational wavefunction

Greek

δ_l	quantum defect, depending on orbital quantum number l of outer electron
Λ	Projection of the orbital electronic angular momentum on the molecular axis
σ	Absorption cross-section
σ	Collision cross-section
τ	Lifetime
λ	Wavelength
μ	Reduced mass of the Rg + I_2 system
μ	Dipole moment
$\mu_e(R)$	Dipole moment function
ν	Wavenumber
θ	Angle between \mathbf{R} and \mathbf{r} vectors in RgI_2 vdW complexes
Θ	electric quadrupole moment
Φ	Photon flux
Ψ	Molecular wavefunction
ω_e	Vibrational constant
$\omega_e x_e$	Anharmonicity
Ω	Projection of the total electronic angular momentum on the molecular axis

Chapter 1

Introduction

1.1 General

Nonadiabatic interactions between excited bound states in diatomic molecules are one of fundamental problems of modern chemical physics and molecular spectroscopy. Perturbations of the states occur both in free (isolated) molecules (*intramolecular* perturbation) and in weakly-bound complexes of molecules and collisions of a molecule with a partner (*intermolecular* perturbations).

An understanding of mechanism of intramolecular perturbation in diatomic molecules is very useful for description of nonadiabatic processes in more complex systems. Besides, a study of perturbations in free molecules stimulates developments of the theory and accurate definition of molecule spectroscopic characteristics.

Exact data on characteristics and dynamics of diatomic molecules become urgent due to elaboration of the methods of preparations of the molecular Bose-Einstein condensate using photoassociation of ultracold atoms, as well as new methods of control of molecular systems.

The basic source of the information on internal constitution of a free molecule is the energetic structure of its rovibronic states which can be distorted due to nonadiabatic perturbations. The latter can affect radiative, magnetic and other molecular characteristics. Therefore, the exact experimental and theoretical descriptions of the intramolecular perturbations are critically important in the context of the fundamental and applied sciences.

Intermolecular or noncovalent interactions occur in gas phase, liquids, solids and polymers. These interactions are of great importance in energy transfer processes in gas phase, organization of structures and properties of biomolecules. Noncovalent bonds are the base of supramolecular chemistry. Understanding of nature of the intermolecular interactions is one of fundamental problems of modern chemical physics and molecular spectroscopy, and van der Waals (vdW) complexes

of excited state diatomic molecules are ideal model systems to predict the properties and dynamic behavior of more complex system. The partners building the complex retain their identity, and energy transfers are thus easily identified due to the weakness of the intermolecular bond. Their decay represents the half of a collision with a limited range of impact parameters, which allows one to make fruitful comparisons with processes occurring in collisions. Finally, studying the dependence of the energy redistribution and fragmentation processes on the size of the cluster may help to bridge the gap with condensed-phase dynamics [1].

Long-range forces between atoms which interact in traps, photoassociation of ultracold molecules, many-body interactions in ultracold systems become more and more urgent. These fields require the appropriate theoretical description of the noncovalent interaction. The simplest vdW complexes along rare gas dimers, Rg_2 , are complexes of rare gases and diatomic halogens. The latter are ideal subject for study the effects of weak non-covalent forces on molecule characteristics.

Collision-induced non-adiabatic transitions (CINATs) in the gas phase, in which vdW complexes are formed in collisions and then decay, play a fundamental role in the kinetics and dynamics of highly excited molecular electronic states. They are responsible for radiative emission and energy transfer in the atmosphere, energy pooling and conversion in laser media, relaxation phenomena in chemiluminescence processes, plasma formation, and in many other situations where electronically-excited states are involved. Description of vdW complex formation and decay is very important for understanding of mechanisms of non-adiabatic transitions in weakly-bound complexes of any molecules and clusters. An understanding of these processes is also essential for interpretation and modeling of various photoinitiated processes in clusters, liquids, and solids, where the role of intermolecular interaction is greatly magnified through the formation of solvation shell(s) and multiple collisions between a molecule and a solvent.

Mechanism and dynamics of vdW complex formation and decay are governed by multidimensional potential energy surface (*PES*) of intermolecular interaction. Data on *PESs* are necessary for finding effect of weak intermolecular interaction in a photoinduced process. These data facilitate understanding of mechanism of interactions between specific reagents as well as functions of intermolecular interactions in chemical processes. Determination of propensity rules for vdW complex decay is necessary for development of description of dynamics in weakly-bound complexes.

Weakly bound complexes can be employed for reagent preparations: it is possible to populate the weakly bound complex of the reagent with a molecular partner to the selected rovibronic level and to align the complex (see [2, 3] and refs). Such preparations make possible to study in detail processes of energy transfer in collisions, chemical reactions, as well as the influence of translational, vibrational and rotational excitation energy, mutual orientation of the reagents on their dynamics and reaction behavior *etc.*

Photochemical and photophysical investigations of weakly bound complexes are necessary for the understanding, how the weak intermolecular interaction of partners, in excited electronic states in particular, acts on the excitation energy transfer

process. In spite of the weak binding of partner molecules in the vdW complex, there are several examples in literature in which vdW complex demonstrate new chemical channels which are closed in the isolated molecule.

Both, intra- and intermolecular interactions have nonadiabatic character. Therefore, the authors have decided to discuss them jointly in this book.

1.2 The Iodine Molecule

Iodine molecule has 23 valence states, that are grouped by correlation with three dissociation limits: $I(^2P_{3/2}) + I(^2P_{3/2})$ (*aa*), $I(^2P_{3/2}) + I(^2P_{1/2})$ (*ab*) and $I(^2P_{1/2}) + I(^2P_{1/2})$ (*bb*), 20 so-called ion-pair (IP) states nestled in four tiers and correlating with the $I^-(^1S_0) + I^+(^3P_2, ^3P_{0,1}, ^1D_2 \text{ and } ^1S_0)$, as well as multitude of Rydberg states (Fig. 1.1).

All the IP states have different angular momenta, parities and very dense rovibronic levels. The potential energy curve of each states are embedded each other. Therefore, many states of free iodine molecule may be perturbed. Besides, collisions of the $I_2(\text{IP})$ with atomic or molecular partners have to lead to CINATs. The similar feature occurs in valence states correlating with the *bb* dissociation limit (see Figs. 1.1 and 1.2).

The bulk of accidental resonances between rovibronic levels make these systems interesting model objects for studies intramolecular perturbations and CINATs between *bound* states, as well as dynamics of decay of optically populated vdW complex state to other bound states. Spectroscopic characteristics of majority of the valence and IP state are well known. There are some perfect methods of optical populations of iodine excited states rovibronic levels and studies of mixing of valence, IP and Rydberg states as well as vdW complex decay and CINATs.

This makes I_2 a unique system for spectroscopic studies of intramolecular and intermolecular perturbations in diatomic molecules.

The book is organized as follows:

An overview of instrumentation and methods utilized for studies of I_2 spectroscopic characteristics are presented in Chap. 2. Classical, the absorption and emission spectroscopy, methods are considered briefly, whereas contemporary,

- (1 + 1) two-step and (1 + 2)-photon optical-optical double resonance,
- three-step three-color laser population scheme,
- perturbation-facilitated two- and three-step excitation scheme
- resonance enhanced multiphoton ionization, and
- velocity imaging

methods are discussed more substantially.

Chapter 3 is devoted to description of the spectroscopic characteristics of the valence, ion-pair and Rydberg states of the iodine molecules, as well as optical

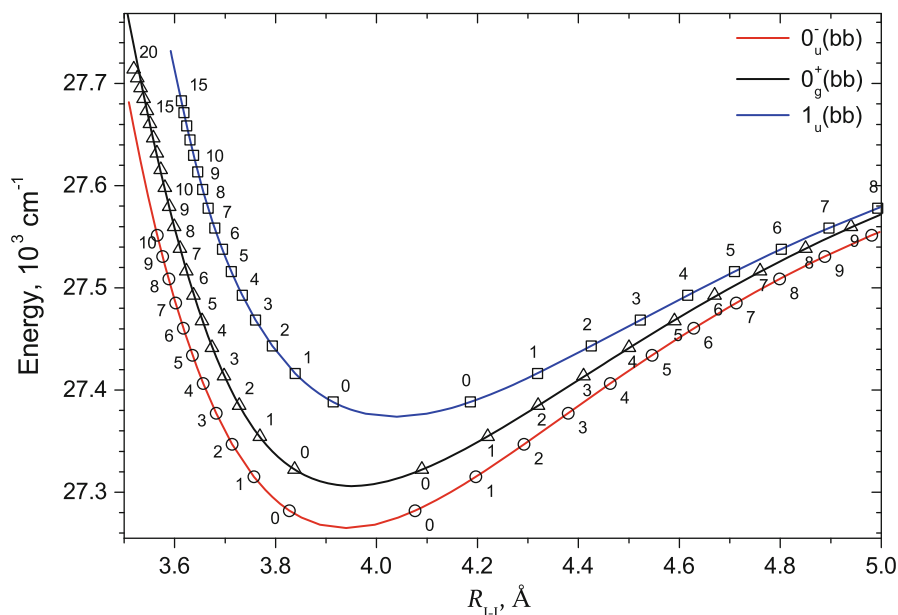


Fig. 1.2 Potential energy curves of the states correlating with the bb dissociation limit [4–6]

Chapter 6 is devoted to optically populated $\text{RgI}_2(\text{XO}_g^+, \text{BO}_u^+ \text{ and IP})$ vdW complexes. Overview of experimental methods used as well as detailed description of design and characteristics of the set-up utilized supersonic molecular beam technique created in the author's group are carried out. Survey of experimental and theoretical works devoted to studies of vdW complexes of different geometry are performed. The particular attention has been given to $\text{RgI}_2(\text{IP})$ vdW complexes.

In Conclusions, the principal features of the intra- and intermolecular nonadiabatic perturbations are summarized.

In Appendix a survey of spectroscopic characteristics of the iodine molecule valence and IP state are given.

References

1. Buchachenko, A.A., Halberstadt, N., Lepetit, B., Roncero, O.: $\text{Ar}\cdots\text{I}_2$: A model system for complex dynamics. *Int. Rev. Phys. Chem.* **22**, 153–202 (2003)
2. Casavecchia, P.: Chemical reaction dynamics with molecular beams. *Rep. Prog. Phys.* **63**, 355–414 (2000)
3. Bernstein, E.R.: *Chemical Reactions in Clusters*. Oxford University Press, Oxford/New York (1996)

4. Akopyan, M.E., Baturo, V.V., Lukashov, S.S., Poretsky, S.A., Pravilov, A.M.: Spectroscopic constants and potential energy curves of the iodine weakly bound 1_u state correlating with the $I(^2P_{1/2}) + I(^2P_{1/2})$ dissociation limit. *Phys. B: At. Mol. Opt. Phys.* **48**, 025101–025107 (2015)
5. Akopyan, M.E., Baturo, V.V., Lukashov, S.S., Poretsky, S.A., Pravilov, A.M.: Spectroscopic constants and potential energy curves of the iodine weakly bound 0_g^+ state correlating with the $I(^2P_{1/2}) + I(^2P_{1/2})$ dissociation limit. *Phys. B: At. Mol. Opt. Phys.* **46**, 055101–055109 (2013)
6. Baturo, V.V., Cherepanov, I.N., Lukashov, S.S., Poretsky, S.A., Pravilov, A.M., Zhironkin, A. I.: Heterogeneous and hyperfine interactions between valence states of molecular iodine correlated with the $I(^2P_{1/2}) + I(^2P_{1/2})$ dissociation limit. *J. Chem. Phys.* **144**, 184310–184318 (2016)

Chapter 2

Overview of Instrumentation and Methods

2.1 Absorption Spectroscopy

Cross-section of the dipole electric allowed transition to the lowest state (bound-free perpendicular $I_2(A1_u \leftarrow X0_g^+)$ transition, $\lambda \approx 550\text{--}850$ nm) is negligible, maximal cross-section, $\sigma_{A-X} \leq 1.5 \cdot 10^{-19}$ cm², *appr.* 15 time less than that of bound-free $B0_u^+ \leftarrow X0_g^+$, $\lambda \approx 410\text{--}498.9$ nm, one. Besides, bound-free perpendicular $I_2(C(B'')1_u \leftarrow X0_g^+)$ transition, $\lambda \approx 410\text{--}630$ nm occurs in the visible spectral range (see [4] and references therein).

Very weak ($\sigma_{max} < 7 \cdot 10^{-20}$ cm²) absorption bands corresponding to bound-free perpendicular transitions has been observed in the $\lambda \approx 205\text{--}420$ nm spectral range (see [5, 6] and references). In shorter wavelength region, strong transitions to very high vibronic levels of the ion-pair (IP) states (see [2] and references) and then to Rydberg states (see [3] and references) occur.

Cross-sections of the bound-free transitions have been determined with moderate (0.1 nm) or low (~ 1 nm) resolution utilizing commercial spectrophotometers. The $B \leftarrow X$ bound-bound transition superimposes with bound-free $A \leftarrow X$ and $C \leftarrow X$ transitions. The former remained unresolved at the spectral resolutions used, and simulation of the spectra was needed (see [4, 7] and references therein).

Fourier-transform spectroscopy method was successfully utilized to determine positions of numerous lines of the bound-bound $A, v_A, J_A \leftarrow X, v_X, J_X$ and $B, v_B, J_B \leftarrow X, v_X, J_X$ transitions up to the $v_A = 35$ vibronic levels and up to the B state dissociation limit, $\lambda \approx 498\text{--}1350$ nm, with very low uncertainties ($\sim \pm 0.005$ cm⁻¹) (see [1, 8] and references). As to cross-sections of the $A, v_A, J_A \leftarrow X, v_X, J_X$ and $B, v_B, J_B \leftarrow X, v_X, J_X$ absorption lines, they cannot be measured with low uncertainties since their full width half maxima (FWHM) are much less than spectral resolution of spectrometers used for measurements of absorption spectra. Besides, absorption

follows Beer-Lambert-Bouguer law (Beer law) [8, 9] only in the limit of zero absorption [7]. Besides, absorption lines are strongly overlapped.

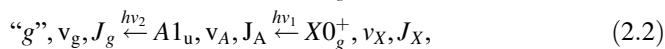
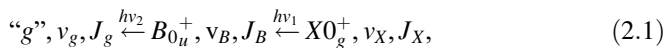
To measure I_2 absorption spectra corresponding to transitions to the IP and Rydberg states, $\lambda < 205$ nm, vacuum monochromators equipped by double-beam attachments, usually, were utilized. Intensities of reference and passed through the sample containing I_2 vapor beams were recorded by sodium salicylate/photomultiplier tube systems (see [2, 10], e.g.). The FWHMs were much less than spectral resolutions of monochromators used, and absorption did not follow Beer law in these measurements, so measured absorption cross-sections had to be regarded as lower limits.

2.2 Emission Spectroscopy

To measure excitation spectra of I_2 luminescence in absolute units, one has to measure the latter at each excitation wavelengths and determine total intensity of luminescence. Otherwise, one can obtain information on the position of excitation lines, only, using an excitation spectrum. To measure luminescence spectrum, one has to calibrate recording system just at the same layout that is used for the measurement [11]. To the best of our knowledge, nobody carried out calibration of experimental setups used for emission spectroscopy in such manner. Therefore, one should consider data on luminescence spectra of IP and Rydberg states as well as their luminescence quantum yields (see [2] as an example) as rough estimations. Einstein coefficients of the $I_2(\text{IP} \rightarrow \text{valence state})$ ($\text{IP} \rightarrow \text{V}$) transitions are large (see Appendix). Therefore, the $I_2(\text{IP} \rightarrow \text{V})$ luminescence is easily detectable.

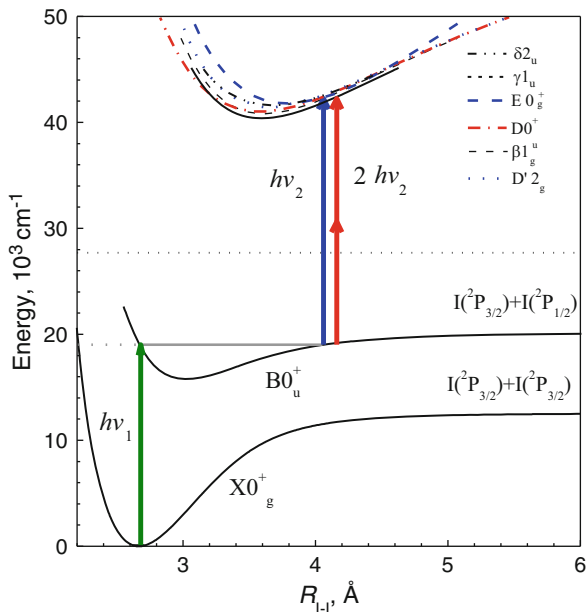
2.3 (1 + 1) Two-Step and (1 + 2) Photon Optical-Optical Double Resonance

The (1 + 1) two-step method successfully uses for laser population of selected rovibronic levels of the IP states in the cases of intermediate and final states can be populated in electric dipole allowed transitions (see [12–14] and references) (Fig. 2.1):



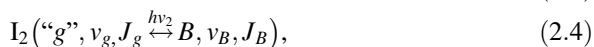
Here, “g” designates 0_g^+ and 1_g IP states of the 1-st, 2-nd and 3-rd tiers (see Fig. 1.1).

Fig. 2.1 The (1 + 1) two-step and (1 + 2)-photon coherent population of selected rovibronic level of *gerade/ungerade* IP state via intermediate BO_u^+, ν_B, J_B rovibronic state



The $u \leftrightarrow g$, $\Delta J = \pm 1$ (parallel, $\Delta\Omega = 0$, transitions), $\Delta J = 0, \pm 1$ (perpendicular, $\Delta\Omega = \pm 1$, transitions) and $+\leftrightarrow +$, $-\leftrightarrow -$ are valid for one-photon electric dipole allowed transitions [15].

One can estimate a population of the I_2 (“g”, ν_g, J_g) states if photon irradiance $E_{h\nu}$ (photon/(s·cm²)) and cross-sections of the optical transitions are large enough to achieve saturation of them, for example:



so concentrations of the states involved in transitions are equal:

$$[B, \nu_B, J_B] = [X, \nu_X, J_X], [\text{“g”}, \nu_g, J_g] = [B, \nu_B, J_B] \quad (2.5)$$

One should note that International Commission on Illumination has recommended the *photon irradiance* term, $E_{h\nu}$ (photon/(s·cm²)), in 1970 [11, 16, 17]. Nevertheless, the term *photon flux* Φ (photon/(s·cm²)) is often used instead of photon irradiance, $E_{h\nu}$, in spectroscopic literature (according to [16, 17], photon flux Φ_p (photon/s) (or $\Phi_{h\nu}$ [11]) is “number of photon, emitted, transferred or received in an element of time”). Below, we will use quantities and units recommended in [16] (see Sect. 1.2 in [11] for details).

For typical conditions of many experiments, namely:

- $p_{12} \approx 0.3$ Torr,
- energies, temporal profile, and diameters of laser pulses ~ 3 mJ/pulse, FWHM $\approx 10^{-8}$ s, and $d \approx 2$ mm, respectively,
- laser spectral width, FWHM ≈ 0.07 cm $^{-1}$, $\lambda \approx 600$ nm,
- transitions start from the $X, \nu_X = 0, J_X \approx 50$ rovibronic level,

the saturation in the transition (2.3) can be easily achieved. In this case, irradiance is $E_e \approx 10^7$ W/cm 2 , photon irradiance is $E_{hv} \approx 3 \cdot 10^{25}$ photon/(s·cm 2). Cross-section of transitions (2.3) at the maxima of Doppler contour of the rovibronic line is $\sigma_{2.3} \approx 10^{-14}$ cm 2 , and the spectral width is ~ 0.03 cm $^{-1}$ if one takes into account its hyperfine structure (see [18, 19] and references). Therefore, *appr.* a half of photon irradiance is used for pumping, and pumping rate, $\sigma_{2.3} \cdot E_{hv} \approx 3 \cdot 10^{11}$ photon/s, is much larger than the rate of B, ν_B, J_B radiative decay and predissociation, $\sim 10^6$ s $^{-1}$ (see [20] and references). One has also to take into account bound-free $0_g^+, 1_g(aa, ab) \xleftarrow{hv_1} B$ transitions, $\sigma \approx 10^{-18}$ cm 2 [19], but the rate of these processes, $\sim 3 \cdot 10^7$ s $^{-1}$, is much less than that of pumping. Consequently, saturation occurs in process (2.3), and a half of the $I_2(X, 0, J_X \approx 50)$ molecules ($\sim 0.01 \cdot 10^{16}$ cm $^{-3}$ at $p_{12} \approx 0.3$ Torr (see [21]), or $\sim 3 \cdot 10^{12}$ molecules in 2×10 mm 2 volume, e.g.), are found in the B state.

Cross-sections of IP – V transitions are much larger than that of $I_2(B-X)$ (see [2, 7], e.g.), so $1/4$ of the $I_2(X, 0, J_X \approx 50)$ molecules or $\sim 1.5 \cdot 10^{12}$ molecules in the same volume, e.g.), are found in a *gerade* IP state, if one use (1 + 1) two-step population scheme.

To populate an *ungerade* “ u ” IP state from intermediate $B0_u^+$ and $A1_u$ states (1 + 2)-photon optical-optical double resonance methods were utilized (see [12, 22, 23], e.g.).

Two-photon absorption (2PA) per unit length in the case shown in Fig. 2.1 (transition via *virtual* state), for example, (dE/dx) is:

$$dE_{hv}/dx = -\sigma^{(2)} \cdot [B, \nu_B, J_B] \cdot E_{hv}^2. \quad (2.6)$$

Here, $\sigma^{(2)} \cdot (\text{cm}^4 \cdot \text{s}/\text{photon})$ is 2PA cross-section, 1–10 GM, typically (1 GM = 10^{-50} cm $^4 \cdot \text{s}/\text{photon}$) The $u \leftrightarrow u, g \leftrightarrow g$ and $\Delta J = 0, \pm 2$ selection rules are valid for the 2PA (see [24, 25] and references).

For typical conditions of experiments mentioned above, pumping rate of an *ungerade* states population via the $[B, \nu_B, J_B]$ one (2.3, 2.7)

$$\text{“}u\text{”}, \nu_u, J_u \xleftarrow{2hv_2} B0_u^+, \nu_B, J_B, \quad (2.7)$$

is $\sim (1-10) \cdot 10^{-50} \cdot 10^{51}$ s $^{-1} \approx (10^2-10^3)$ s $^{-1}$, more than 10^8 less, than that of (1 + 1) two-step pumping. Therefore, one should use a focused laser beam for pumping. Nevertheless, if diameter of the laser pulse beam waist is $d \approx 0.1$ mm as it has been in [23], pumping rate increases ~ 400 times up to $(0.4-4) \cdot 10^5$ s $^{-1}$, and remains much less than rate of the bound-free $0_g^+, 1_g(aa, bb) \xleftarrow{hv_1} B$ transitions, $\sim 10^{10}$ s $^{-1}$.

One sees that a $(1 + 2)$ -photon optical-optical-double resonance is a very inefficient way of *ungerade* IP state population. The methods, described in Sects. 2.1.4 and 2.1.5 are more preferable.

2.4 Three-Step Three-Color Laser Population

This method has been described in [26] for the first time. To populate selected rovibronic levels of the $I_2(D)$ state, authors employed three-step three-color, $h\nu_1 + h\nu_f^i + h\nu_2$, excitation scheme using $B0_u^+$ and $0_g^+(bb)$ intermediate states (Fig. 2.2).

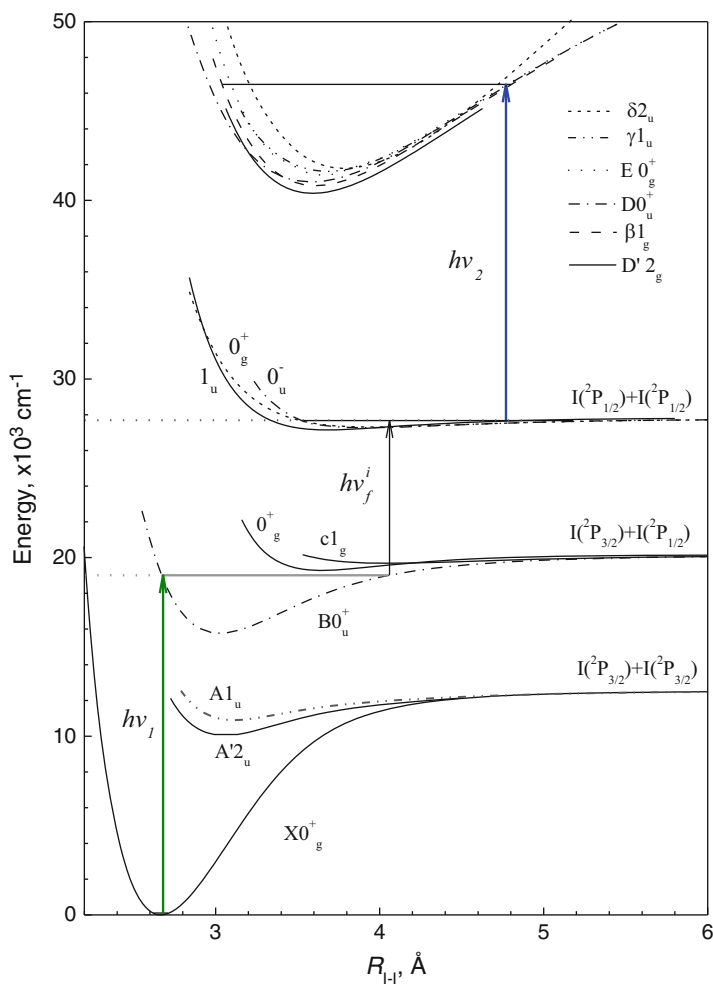


Fig. 2.2 The three-step three-color excitation scheme of population of the I_2 (IP) states

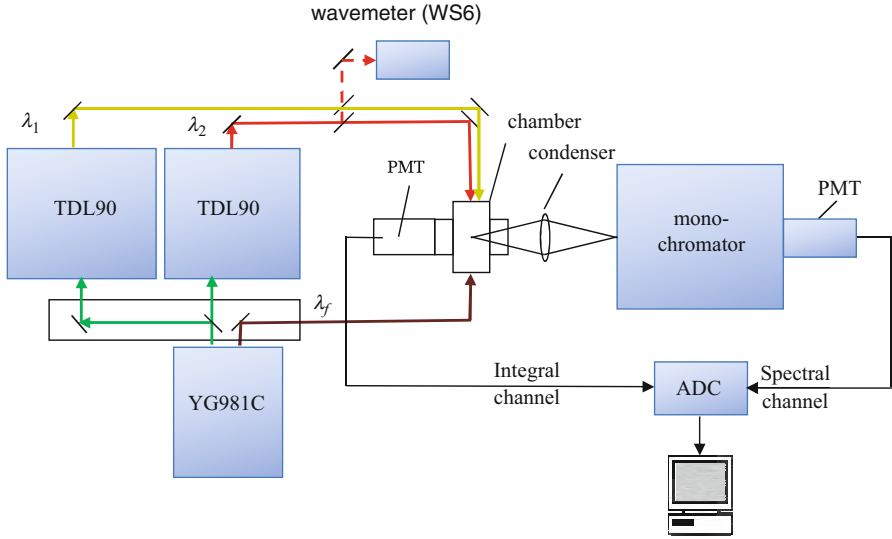


Fig. 2.3 Schematic diagram of the experimental setup utilized to realize three-step three color and perturbation facilitated excitation schemes

Schematic diagram of the experimental setup utilized to realize these excitation schemes is given in Fig. 2.3.

The λ_1 pump wavelength was tuned to the selected $B, \nu_B, J_B \xleftarrow{h\nu_1} X, \nu_X = 0, J_X$ transition. Then the $0_g^+, \nu_0, J_0 \xleftarrow{h\nu_f^i} B0_u^+, \nu_B, J_B$ and $D0_u^+, \nu_D, J_D \xleftarrow{h\nu_2} 0_g^+, \nu_0, J_0$ transitions occur

$$D0_u^+, \nu_D, J_D \xleftarrow{h\nu_2} 0_g^+(bb), \nu_0, J_0 \xleftarrow{h\nu_f^i} B0_u^+, \nu_B, J_B \xleftarrow{h\nu_1} X0_g^+, \nu_X, J_X \quad (2.8)$$

All the transitions involved in excitation Scheme (2.8) are electric dipole allowed.

A Nd:YAG laser which pumped two dye lasers system was used in the experiments. The laser beams were spatially and temporally overlapped. To populate the $0_g^+(bb), \nu_0, J_0$ rovibronic states, the fundamental Nd:YAG laser harmonic was utilized. It consisted of 3 spectral components: $\nu_f^1 = 9395.12 \pm 0.02 \text{ cm}^{-1}$, $\nu_f^2 = 9393.53 \pm 0.07 \text{ cm}^{-1}$ and $\nu_f^3 = 9396.67 \pm 0.10 \text{ cm}^{-1}$ with relative intensities of about 1: 0.3: 0.05, and a very weak line with the frequency of $\nu_f^4 = 9392.04 \text{ cm}^{-1}$. The $0_g^+(bb), \nu_0, J_0 \xleftarrow{h\nu_f^i} B0_u^+, \nu_B, J_B$ transitions can be realized due to accidental resonances (see [27–30] and references). Transitions to several rovibronic levels, $0_g^+(bb), \nu_0, J_0$, since their density is high. A number of these transitions has to occur largely if on use tunable dye laser instead of a fundamental

Nd:YAG laser harmonic in the $\lambda \geq 1120$ nm spectral range and double fundamental Nd:YAG laser harmonic for pumping (see [31] and references):



The



transition dipole moment is *ca.* 10 times less than that of $B \rightarrow X$ [7, 19], but pumping rate of these transitions $\sigma_{2,9} \cdot E_{hv} \approx 10^{10}$ photon/s, is much larger than the rate of $I_2(0_g^+(bb))$ radiative decay, $\sim 10^6$ s⁻¹ [19, 26]. Therefore, a saturation in the transition (2.9) can be easily achieved. Numerous experiments of the authors show that the



transitions are also saturated at hv_2 laser pulse energy ~ 3 mJ/pulse (see [32], *e.g.*).

So, 1/8 of the $I_2(X, 0, J_X \approx 50)$ molecules or $\sim 7 \cdot 10^{11}$ molecules in 2×10 mm² volume, *e.g.*, are found in a *ungerade* IP state, if one use three-step three-color excitation Scheme.

2.5 Perturbation-Facilitated Two-Step Excitation Scheme

The (1 + 1) two-step excitation scheme can be utilized for a population of IP states of different symmetry if intermediate rovibronic levels are perturbed by nearest levels of the states of suitable symmetry. It was successfully carried out for population of the $\gamma 1_u$, $F0_u^+$, $H1_u$, $\delta 2_u$ [33, 34], $1_u(^1D)$, $2_u(^1D)$ [35] states via mixed $B0_u^+ \sim c1_g$ states, the $h0_u^-$ and $H1_u$ states via mixed $B0_u^+ \sim {}^3\Pi(0_g^-)(ab)$ states [36], $D'2_g$ [37] and $2_g(^1D)$ [38] states via mixed $B0_u^+ \sim b'2_u$ states, and $g0_u^-$ state via mixed $B0_u^+ \sim (3)0_u^-$ state [39]. As a result, spectroscopic characteristics of the upper states were determined.

The $B0_u^+ \sim c1_g$ hyperfine mixing resulting in the $\gamma 1_u$, $F0_u^+$, $H1_u$, $\delta 2_u$, $1_u(^1D)$, $2_u(^1D)$ state electric dipole allowed population has been studied in [33–35]. It has been shown that fourteen $B0_u^+ \sim c1_g$ mixed rovibronic states are available for the population of rovibronic levels of the IP *ungerade* states under discussion. Matrix elements of the hyperfine interaction (*HFI*) is low, ~ 0.01 cm⁻¹ [33], so the electronic matrix elements [40–43] is ~ 0.1 cm⁻¹ (Franck-Condon factors, *FCFs*, of the vibronic states mixed is ~ 0.1). Fortunately, *FCFs* of the transitions from the $c1_g$ state to the IP states under study are high, so authors of [33–35] have successfully determined spectroscopic characteristics of the latter.

The $B0_u^+ \sim b'2_u$ state *HFI* has been found to allow to populate eleven rovibronic levels of the $B0_u^+, v_B = 76 - 79 \sim b'2_u, v_b = 22-25$ vibronic states. The *HFI* electronic matrix elements, $\sim 0.027 \text{ cm}^{-1}$ is higher than that for the $B0_u^+ \sim c1_g$ mixing, but *FCFs* is less, $\sqrt{FCF} \approx (1.0 - 3.8) \cdot 10^{-2}$, so the *HFI* matrix elements is $(0.3-1.0) \cdot 10^{-3}$ [37].

Nine rovibronic levels of the $B0_u^+, v_B = 76 - 80 \sim (3)0_u^-, v_0$ states was found to be mixed by the *HFI*. Matrix elements of the interaction have been unknown [39].

2.6 Perturbation-Facilitated Three-Step Excitation Scheme

This scheme was successfully realized in [26] for the first time for a population of the $I_2(D'2_g)$ state using the $B0_u^+$ and $0_g^+ \sim 1_u(bb)$ intermediate states. The mechanism of the optical transitions involved in the scheme was unknown at that moment. It has been found later [29, 30], that all three $0_g^+, 0_u^-, 1_u(bb)$ states are mixed due to *HFI*. Therefore, *all the $I_2(IP)$ states except the $\delta 2_u$ and $2_u(^1D)$* (see Fig. 1.1) can be populated utilizing the excitation schemes described in this section and Sect. 2.1.4.

$$IP, v_{IP}, J_{IP} \xleftarrow{h\nu_2} 0_g^+ \sim 0_u^- \sim 1_u(bb) \xleftarrow{h\nu_f^i} B, v_B, J_B \xleftarrow{h\nu_1} X, v_X, J_X \quad (2.11)$$

To determine vibrational and rotational quantum numbers of the intermediate B and $0_g^+ \sim 0_u^- \sim 1_u(bb)$ as well as IP states one has to measure so-called *action* and *excitation* spectra of the $B \rightarrow X$ and IP $\rightarrow V$ luminescence as well as IP $\rightarrow V$ luminescence spectra themselves. Measurements of the:

- $B \rightarrow X$ luminescence excitation spectra allow determining quantum numbers of the B state,
- IP $\rightarrow V$ action spectra (scanning of the λ_1 wavelength at fixed λ_2 value) allow determining the quantum numbers of the intermediate states and final IP state,
- IP $\rightarrow V$ excitation spectra (scanning of the λ_2 wavelength at fixed λ_1 value) allow determining the energies of the final IP state rovibronic levels

(see [28], *e.g.*, for details).

This excitation scheme was utilized to study:

- collision-induced non-adiabatic transitions (CINATs) between iodine molecule first tier IP states, $E0_g^+, D0_u^+, \beta 1_g, D'2_g$ [44] (see Sect. 5.3.2),
- mechanism of interactions between $I_2(0_g^+, 0_u^-, 1_u(bb))$ states [28, 30],
- spectroscopic parameters of iodine molecule weakly-bound states and dipole moment transition between them and IP states [45–47],
- mechanism of mixing of the $I_2(D0_u^+$ and $\delta 2_u)$ states [32].

2.7 Resonance Enhanced Multiphoton Ionization (REMPI)

The (2 + 1) resonance enhanced multiphoton ionization, (2 + 1) REMPI, method has been used for assignments of I_2 (*gerade* Rydberg state $\leftarrow X$) transition bands, as well as perturbation of the *gerade* Rydberg and IP states (see [48–50] and references). Vibronic levels of a Rydberg state is populated due to 2PA of $h\nu$ photons (see Sect. 2.1.3), and then this molecule is ionized by the photon of the same energy (Fig. 2.4). Since Rydberg states rapidly predissociate, quantum yield α their luminescence is small, and REMPI method is more preferable.

A laser beam has to be focused. The best results can be achieved if one uses supersonic beams to study rotationally and vibrationally cooled iodine molecules and time-of-flight mass spectrometer to detect I_2^+ and I^+ ions (see comparison in [3]). This method has been used for studies of Rydberg state $\leftarrow X$ transitions, $[3/2]_c5pd; 1_g \leftarrow X, 0$ one, if one takes into account vibrationally cooled I_2 ($2h\nu \geq 59,700 \text{ cm}^{-1}$ [49]). - Two-photon transitions to the D'_2g and 1_g IP states as well as coupling of the Rydberg and IP states have been observed, also [50] (see Sects. 3.4 and 4.3.3).

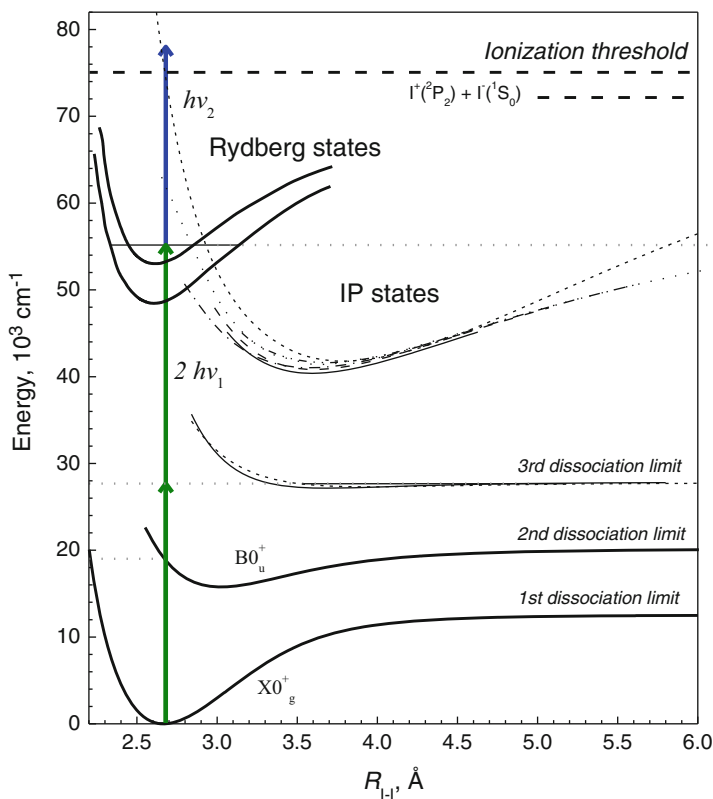


Fig. 2.4 The (2 + 1) REMPI excitation scheme

2.8 Velocity Map Imaging

The velocity map imaging (VMI) method provides getting detailed information on channels of predissociation of high-lying *gerade* Rydberg states [3] (see Sect. 4.2.2 for details). The VMI experimental apparatus used in [3] is similar to that of described in [51] (see Fig. 2.5).

Supersonic (helium carrier gas/molecules under study) molecular beam is produced by pulsed supersonic jet expansion generated by a pulse valve (*PV*) into a source chamber evacuated with high pumping speed. A central part of the gas jet passes through a skimmer into electrostatic lens chamber where it crosses with a focused pulse laser beam. An energy of the laser pulse has to be enough to excite ground state molecule to Rydberg state and then ionize it in the $(2 + 1)$ schemes. Ions produced at the laser beam spot are extracted by three-electrode electrostatic lens to time-of-flight (TOF) tube. After passing it, ions hit an imaging detector consisting of a microchannel plate (MCP) and phosphor screen (PS). A 2D image of the phosphor screen is recorded by a charge coupled device (CCD) (see [51] for details).

The ring structures in the VMI images reflect the distribution of the ions as a function of kinetic energy. The sum of the kinetic energies of the fragment ions formed in the dissociation or predissociation processes is termed as Kinetic Energy Release (KER). Analysis of the KER spectra allows to assign the channels of Rydberg state predissociation. Methods of interpretation of velocity map images are described in [3].

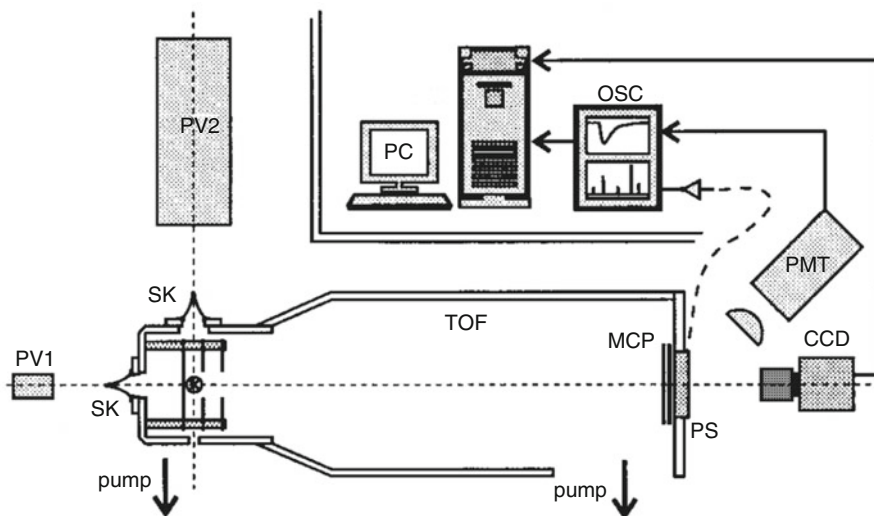


Fig. 2.5 VMI apparatus [51]

References

1. Gerstenkorn, S., Luc, P., Vergès, J.: Atlas du Spectre d'Absorption de la Molecule d'Iode, Vol. O. 7220–11,200 cm^{-1} Laboratoire Aimé Cotton, CNRS II, Orsay (1993)
2. Hiraya, A., Shotabake, K., Donovan, R.J., Hopkirk, A.: Vacuum ultraviolet fluorescence excitation spectrum of I_2 . *J Chem Phys.* **88**, 52–57 (1988)
3. Bogomolov, S.A., Grüner, B., Kochubei, S.A., Mudrich, M., Baklanov, A.V.: Predissociation of high-lying Rydberg states of molecular iodine via ion-pair states. *J Chem Phys.* **140**, 124311–124319 (2014)
4. Tellinghuisen, J.: Least-squares analysis of overlapped bound-free absorption spectra and predissociation data in diatomics: The $\text{C}(1_u)$ state of I_2 . *J Chem Phys.* **135**, 054301–054311 (2011)
5. Tamres, M., Walter, K., Duerksenn, W.K., Goodenow, J.M.: Vapor-phase charge-transfer complexes. II. The $2\text{I}_2 \leftrightarrow \text{I}_4$ System. *J Phys Chem.* **72**, 966–970 (1968)
6. Privilov A.M.: Photoprocesses in molecular gases. Energoatomizdat, Moscow (1992) (in Russian)
7. Tellinghuisen, J.: Intensity analysis of overlapped discrete and continuous absorption by spectral simulation: The electronic transition moment for the B–X system in I_2 . *J Chem Phys.* **134**, 084301–084308 (2011)
8. Salami H, and Ross A.J.J.: A Molecular Iodine Atlas in ASCII Format. *Mol. Spectrosc.*, 233, 157–159 (2005) (see also http://library.osu.edu/sites/msa/suppmat/v233.i1.pp157-159//Supplementary_material.txt)
9. Okabe, H.: Photochemistry of Small Molecules. Wiley, New York (1978)
10. Myer, J.A., Samson, J.A.R.: Absorption cross section and photoionization yield of I_2 between 1050 and 2200 Å. *J Chem Phys.* **52**, 716–718 (1970)
11. Privilov A.M.: Radiometry in Modern Scientific Experiments. Springer, Wien/New York (2011)
12. Brand, J.C.D., Hoy, A.R.: Multiphoton spectra and states of halogens. *Appl Spectrosc Rev.* **23**, 285–328 (1987)
13. Ishiwata, T., Takekawa, H., Obi, K.: Optical-optical double-resonance of the I_2 $1_g(^1\text{D})$ ion-pair state. *J. Mol. Spectrosc.* **159**, 443–457 (1993)
14. Kagi, E., Yamamoto, N., Fukushima, H., Ishiwata, T.: Optical-optical double resonance spectroscopy of the $1_g(^3\text{P}_1) - \text{A}^3\Pi(1_u) - \text{X}^1\Sigma_g^+$ transition of I_2 . *J. Mol. Spectrosc.* **216**, 48–51 (2002)
15. Herzberg, G.: Molecular Spectra and Molecular Structure, Vol.1, Spectra of Diatomic Molecules. Van Nostrand, New York (1950)
16. International Lighting Vocabulary: CIE publ. CIE No. 17 (E-1.1). Paris (1970)
17. Grum, G., Becherer, R.J.: Radiometry. In: Grum, F. (ed.) Optical Radiation Measurements, a Treatise, vol. 4. Academic, New York (1979)
18. Lukashov, S.S., Novikova, I.Y., Poretsky, S.A., Privilov, A.M., Torgashkova, A.S.: Optical population of free iodine molecule ion-pair states and their $\text{RgI}_2(\text{IP})$ complexes via RgI_2 vdW complexes of valence states correlating with the third dissociation limit. *Chem Phys.* **336**, 109–120 (2007)
19. Akopyan, M.E., Baturo, V.V., Lukashov, S.S., Poretsky, S.A., Privilov, A.M., Teschmit, N.: Cross-sections of bound-free $0_g^+, 1_g(aa, bb) \xrightarrow{h\nu_f} B0_u^+, v_B = 18 - 21$ and bound-bound $0_g^+, 1_u(bb) \xrightarrow{h\nu_f} B0_u^+, v_B = 18 - 21, J_B$ transitions at fundamental harmonic of Nd:YAG laser. *J. Phys. B: At. Mol. Opt. Phys.* **47**, 055101. (9pp) (2014)
20. Broyer, M., Vique, J., Lehmann, J.C.: Hyperfine predissociation of molecular iodine. *J Chem Phys.* **64**, 4793–4794 (1976)
21. Ubachs, W., Aben, I., Milan, J.B., Somsen, G.J., Stuiver, A.G., Hogervorst, W.: Radiative and collisional relaxation of a single rovibrational quantum state of I_2 : $\text{E}(0_g^+), v = 8, J = 56$. *Chem. Phys.* **174**, 285–295 (1993)

22. Ishiwata, T., Kusayanagi, T., Hara, T., Tanaka, I.: An analysis of the $F(0_u^+)$ ion-pair state of I_2 by optical-optical double resonance. *J. Mol. Spectrosc.* **119**, 337–351 (1986)
23. Akopyan, M.E., Khadikova, E.I., Lukashov, S.S., Poretsky, S.A., Pravilov, A.M., Buchachenko, A.A., Suleimanov, Y.V.: Dynamics and mechanism of non-adiabatic transitions from the ungerade $I_2(D0_u^+)$ state induced by collisions with iodine ground state molecules and rare gas atoms. *J. Chem. Phys.* **133**, 244304–244310 (2010)
24. Rumi, M., Perry, J.W.: Two-photon absorption: an overview of measurements and principles. *Adv. Opt. Photon.* **2**, 405–518 (2010)
25. Letokhov, V.: *Laser Photoionization Spectroscopy*. Academic Press, New York (1987)
26. Akopyan M.E., Batur V.V., Lukashov S.S., Poretsky S.A., Pravilov A.M.: Dipole moment functions of the iodine $D'2_g-A'2_u$, $D0_u^+ - a'0_g^+$, $D0_u^+ - X0_g^+$ and $E0_g^+ - B0_u^+$ transitions. *J. Phys. B: At. Mol. Opt. Phys.* **44**, 205101 (9pp) (2011)
27. Akopyan, M.E., Batur V.V., Lukashov, S.S., Poretsky, S.A., Pravilov, A.M.: Non-adiabatic transitions from $I_2(E0_g^+ \text{ and } D0_u^+)$ states induced by collisions with $M = I_2(X0_g^+)$ and H_2O . *J. Chem. Phys.* **136**, 234302–234311 (2012)
28. Akopyan, M.E., Batur V.V., Lukashov, S.S., Poretsky, S.A., Pravilov, A.M.: Spectroscopic constants and potential energy curve of iodine weakly bound 0_g^+ state correlating with $I(^2P_{1/2}) + I(^2P_{1/2})$ dissociation limit. *J. Phys. B. At. Mol. Opt. Phys.* **46**, 055101. (9pp) (2013)
29. Akopyan, M.E., Batur V.V., Lukashov, S.S., Mikheev, L.D., Poretsky, S.A., Pravilov, A.M., Vasyutinskii, O.S.: Hyperfine interaction in molecular iodine between the 0_g^+ , 1_u and 0_u^+ states correlating with the $I(^2P_{1/2}) + I(^2P_{1/2})$ dissociation limit. *J. Phys. B. At. Mol. Opt. Phys.* **48**, 025102. (14pp) (2015)
30. Batur V.V., Cherepanov, I.N., Lukashov, S.S., Poretsky, S.A., Pravilov, A.M., Zhironkin, A. I.: Heterogeneous and hyperfine interactions between valence states of molecular iodine correlating with the $I(^2P_{1/2}) + I(^2P_{1/2})$ dissociation limit. *J Chem Phys.* **144**, 184310–184318 (2016)
31. http://www.quantel-laser.com/en/products/item/q-scan_200_nm-4.5_%C2%B5m.html
32. Batur V.V., Lukashov, S.S., Poretsky, S.A., Pravilov, A.M., Vasyutinskii, O.S.: Mixing of the $D0_u^+$ and $\delta 2_u$ ion-pair states of iodine molecule. *Chem. Phys. Lett.* **638**, 244–248 (2015)
33. Jewsbury, P.J., Ridley, T., Lawley, K.P., Donovan, R.J.: Parity mixing in the valence states of I_2 probed by optical-optical double-resonance excitation of ion-pair states. Characterization of a new ion-pair state $H1_u(^3P_1)$ and a valence state $c1_g$. *J. Mol. Spectrosc.* **157**, 33–49 (1993)
34. Ishiwata, T., Yotsumoto, T., Motohiro, S.: Optical-optical double resonance spectroscopy of I_2 through the parity mixed valence states. *Bull Chem Soc Jpn.* **74**, 1605–1610 (2001)
35. Motohiro, S., Umakoshi, A., Ishiwata, T.: Perturbation-facilitated optical-optical double resonance spectroscopy of the $1_u(^1D)$ and $2_u(^1D)$ ion-pair states of I_2 through parity mixing intermediate state. *J. Mol. Spectrosc.* **208**, 213–218 (2001)
36. Motohiro, S., Nakajima, S., Ishiwata, T.: Perturbation-facilitated optical-optical double resonance spectroscopy of the $h0_u(^3P_1)$ and $H1_u(^3P_1)$ ion-pair states of I_2 . *J Chem Phys.* **117**, 187–196 (2002)
37. Motohiro, S., Nakajima, S., Ishiwata, T.: Absolute position of the $D'2_g(^3P_2)$ ion-pair state of I_2 determined by perturbation-facilitated optical-optical double-resonance. *J. Mol. Spectrosc.* **212**, 194–202 (2002)
38. Nakano, Y., Ukeguchi, H., Ishiwata, T.: Observation and analysis of the $2_g(^1D)$ ion-pair state of I_2 : The g/u mixing between $1_u(^1D)$ and $2_g(^1D)$ states. *J Chem Phys.* **121**, 1397–1404 (2004)
39. Motohiro, S., Nakajima, S., Aoyama, K., Kagi, E., Fujiwara, H., Fukushima, M., Ishiwata, T.: Analysis of the $0_g^-(^3P_1) - B^3\Pi(0_u^-)$ system of I_2 by perturbation-facilitated optical-optical double-resonance. *J Chem Phys.* **117**, 9777–9784 (2002)
40. Vigué, J., Broyer, M., Lehmann, J.C.: Natural hyperfine and magnetic predissociation of the I_2B state. I. – theory. *J. Phys. France.* **42**, 937–947 (1981)

41. Vigué, J., Broyer, M., Lehmann, J.C.: Natural hyperfine and magnetic predissociation of the I_2B state. II. – Experiments on natural and hyperfine predissociation. *J. Phys. France*. **42**, 949–959 (1981)
42. Pique, J.P., Hartmann, F., Churassy, S., Bacis, R.: Hyperfine interactions in homonuclear diatomic molecules and u - g perturbations. I. Theory. *J. Phys. France*. **47**, 1909–1916 (1986)
43. Pique, J.P., Hartmann, F., Churassy, S., Bacis, R.: Hyperfine interactions in homonuclear diatomic molecules and u - g perturbations. II. Experiment on I_2 . *J. Phys. France*. **47**, 1917–1929 (1986)
44. Akopyan, M.E., Baturo, V.V., Lukashov, S.S., Poretsky, S.A., Pravilov, A.M.: Population of the iodine first tier ion-pair states following optical population of rovibronic levels of the $I_2(E0_g^+, D0_u^+, \beta 1_g$ and $D^1 2_g)$ states in presence of argon. *Chem. Phys.* **462**, 3–11 (2015)
45. Akopyan, M.E., Baturo, V.V., Lukashov, S.S., Poretsky, S.A., Pravilov, A.M.: Spectroscopic constants and the potential energy curve of the iodine weakly-bound 1_u state correlating with the $I(^2P_{1/2}) + I(^2P_{1/2})$ dissociation limit. *J. Phys. B. At. Mol. Opt. Phys.* **48**, 025101. (7pp) (2014)
46. Baturo, V.V., Cherepanov, I.N., Lukashov, S.S., Poretsky, S.A., Pravilov, A.M.: Spectroscopic constants and potential energy curve of some iodine ungerade weakly-bound states. *J. Phys. B: At. Mol. Opt. Phys.* **48**, 055101. (8pp) (2015)
47. Baturo, V.V., Cherepanov, I.N., Lukashov, S.S., Poretsky, S.A., Pravilov, A.M.: Molecular parameters for weakly-bound $2_g(aa, ab)$ and $0_u^-(ab)$ states of molecular iodine and dipole moment functions of transitions to these states. *J. Phys. B: At. Mol. Opt. Phys.* **49**, 125101. (8pp) (2016)
48. Donovan, R.J., Flood, R.W., Lawley, K.P., Yench, A.J., Ridley, T.: The resonance enhanced (2 + 1) multiphoton ionization spectrum of I_2 . *Chem Phys.* **164**, 439–450 (1992)
49. Kvaran, Á., Wang, H., Jóhannesson, G.H., Yench, A.J.: REMPI spectra of I_2 . The $[^2\Pi_{3/2}]_c 5d; 1_g$ Rydberg state and interactions with ion-pair states. *Chem Phys.* **222**, 436–442 (1994)
50. Lawley, K.P., Ridley, T., Min, Z., Wilson, P.J., Al-Kahali, M.S.N., Donovan, R.J.: Vibronic coupling between Rydberg and ion-pair states of I_2 investigated by (2 + 1) resonance enhanced multiphoton ionization spectroscopy. *Chem. Phys.* **197**, 37–50 (1995)
51. Eppink, A.T.J.B., Parker, D.H.: Velocity map imaging of ions and electrons using electrostatic lenses: application in photoelectron and photofragment ion imaging of molecular oxygen. *Rev. Sci. Instrum.* **68**, 3477–3484 (1997)

Chapter 3

Electronic States of Iodine Molecule and Optical Transitions Between Them

3.1 Theoretical Background

In the iodine molecule, electronic levels mostly obey the intermediate between the Hund's case (c) and Hund's case (a) coupling Scheme [1]. Accordingly, the notation $(i)\Omega_{\omega}^{\sigma}(^{2S+1}\Lambda \omega^{\sigma}mpqn)$ will be used below for their classification. Here:

- i numerates states with the same symmetry by their excitation energy,
- Ω_{ω}^{σ} , $\Omega(\Lambda)$ is the projection of the total (orbital) electronic angular momentum on the molecular axis,
- $\sigma = \pm$ (used only for $\Omega(\Lambda) = 0$ terms) is the reflection through a plane containing the molecular axis parity,
- $\omega = u$ (ungerade) or g (gerade) specifies the symmetry with respect to inversion of electronic coordinates,
- S is the spin angular momentum,
- $^{2S+1}\Lambda_{\omega}^{\sigma}$ is the main (Hund's case (a)) non-relativistic term,
- $mpqn$ specify the main electronic configuration (see below).

Valence electronic states of the iodine molecule go on dissociation to neutral atoms in their ground state configuration $[\text{Kr}]4d^{10}5s^25p^5$, where $[\text{Kr}]$ means the electronic configuration of krypton. 23 valence states are grouped by correlation with three dissociation limits separated by the spin-orbit interaction in the iodine atom. Ten states, $(1)0_{\text{g}}^{+}(X^1\Sigma \text{g}^+ 2440)$, $(2)0_{\text{g}}^{+}(a'^3\Pi \text{g}2341 \rightarrow ^3\Sigma \text{g}^-2422)$, $(1)0_{\text{u}}^{-}(B'^3\Pi_{\text{u}}2431)$, $(2)0_{\text{u}}^{-}(^3\Sigma \text{u}^+1441)$, $(2)0_{\text{u}}^{-}(^3\Sigma \text{u}^+1441)$, $(1)1_{\text{g}}(a^3\Pi \text{g} 2341)$, $(1)1_{\text{u}}(A^3\Pi \text{u} 2431)$, $(2)1_{\text{u}}(C(B'')^1\Pi \text{u} 2431)$, $(1)2_{\text{g}}(^3\Pi \text{g} 2341)$, $(1)2_{\text{u}}(A'^3\Pi \text{u} 2431)$, $(1)3_{\text{u}}(^3\Delta \text{u} 2332)$ correlate with the first, $I(^2P_{3/2}) + I(^2P_{3/2})$ (aa), limit. Ten states $(3)0_{\text{g}}^{+}(^3\Sigma_{\text{g}}^-2422 \rightarrow ^3\Pi_{\text{g}}234)$, $(1)0_{\text{g}}^{-}(^3\Pi_{\text{g}}2341)$, $(1)0_{\text{u}}^{+}(B^3\Pi \text{u} 2431)$, $(3)0_{\text{u}}^{-}(^1\Sigma \text{u}^- 2332)$, $(2)1_{\text{g}}(^1\Pi \text{g} 2341)$, $(3)1_{\text{g}}(^3\Sigma \text{g}^- 2422)$, $(3)1_{\text{u}}(^3\Sigma \text{u}^+ 1441)$, $(4)1_{\text{u}}(^3\Sigma \text{u}^+ 2332)$, $(1)2_{\text{g}}(^1\Delta \text{g} 2422)$, $(2)2_{\text{u}}(b'^3\Delta_{\text{u}} 2332)$ correlate with the second, $I(^2P_{3/2}) + I(^2P_{1/2})$ (ab), limit. Three states $(4)0_{\text{g}}^{+}(^1\Sigma \text{g}^+ 2422 + ^1\Sigma \text{g}^+ 2242)$,

(4) 0_u^- (${}^3\Sigma u^+2332$), (5) 1_u (${}^3\Delta u2332$) correlate with the third, $I(^2P_{3/2}) + I(^2P_{1/2})$ (bb), limit. The principal non-relativistic terms and electronic configurations are taken from [2]. The (2) 0_g^+ ($a^3\Pi g2341 \rightarrow {}^3\Sigma g^-2422$) and (3) 0_g^+ (${}^3\Sigma g^-2422 \rightarrow {}^3\Pi g2341$) states have avoided crossing at the ground state equilibrium internuclear distance R_e where they interchange character.

In the framework of the *molecular orbital (MO) theory*, electron configurations of valence states are [1] $\sigma_g^m \pi_u^p \pi_g^q \sigma_u^n$ with $m+n+p+q=10$. In the simplest approximation, the MO are linear combinations of atomic 5p orbitals

$$\sigma = 5p_z(a) \pm 5p_z(b), \quad (3.1)$$

$$\pi = 5p_{x(y)}(a) \pm 5p_{x(y)}(b), \quad (3.2)$$

where indexes a, b distinguish iodine centers, the upper sign is for *ungerade* (u) and the lower sign is for *gerade* (g) states. Following Mulliken, we use the notation $mpqn$ to designate the electronic configurations. The σ_g and π_u are *bonding* molecular orbitals with energies lower than that of the 5p in separate atoms. Similarly, the π_g and σ_u are *anti-bonding* molecular orbitals with energies higher than that of the separate atoms. The overlap of 5p_z orbitals forming the σ MO is more long range than that of for the 5p_{x(y)} forming the π MO. Therefore, the σ_g (σ_u) MO has larger bonding (anti-bonding) power than the π_u (π_g). The fall or rise of potential curves as R decreases as well as excitation energy is related to the numbers and types of bonding and antibonding electrons in its electron configuration. Due to the two electrons on the σ_g bonding MO and absence of electrons on σ_u anti-bonding MO the 2440(${}^1\Sigma_g^+$) $X0_g^+$ ground state has attractive potential with the largest dissociation energy among the valence states. The 2431 group consisted of

$$A'^3\Pi_{2u}(2_u), A^3\Pi_{1u}(1_u), B'^3\Pi_{0_u^-}(0_u^-), B^3\Pi_{0_u^+}(0_u^+), C(B)''^1\Pi_u(1_u) \quad (3.3)$$

states is the next in vertical energy. The energy levels of the 2431 configuration can be well explained by accounting for exchange and spin-orbit interactions [1]. The exchange interaction splits levels with different multiplicity, ${}^3\Pi$ and ${}^1\Pi$. The spin-orbit interaction further divides the ${}^3\Pi$ state into multiplet components ${}^3\Pi_2$, ${}^3\Pi_1$, ${}^3\Pi_0$ and mixes the ${}^3\Pi_1$ and ${}^1\Pi_1$ states. For molecular orbitals (3.1), (3.2), the spin-orbit interactions is

$$H^{SO} = a\Sigma(I_{5p} \cdot s_{5p}), \quad (3.4)$$

where I_{5p} and s_{5p} are the orbital and spin momenta of the 5p atomic orbital. The constant a determining the strength of the interaction is known from the spin-orbit splitting of the iodine atom:

$$a = 2/3(E(^2P_{1/2}) - E(^2P_{3/2})) = 5069 \text{ cm}^{-1}.$$

Then the energies of the states (3.3) are [1]

$$\begin{aligned}
A'^3\Pi2u(2_u) : E = E_0 - X/2 - a/2, A^3\Pi1u(1_u) : E \\
= E_0 - 1/2\sqrt{X^2 + a^2}, B'^3\Pi0^-_u(0^-_u) : E = E_0 - X/2 + a/2, \\
B^3\Pi0^+_u(0^+_u) : E = E_0 - X/2 + a/2, \\
C^1\Pi_u(1_u) : E = E_0 + 1/2\sqrt{X^2 + a^2}
\end{aligned} \quad (3.5)$$

where E_0 is the vertical energy of the 2431 configuration relative to the ground one, X is the value of the exchange interaction. Eq. (3.5) takes into account only the intra-configuration spin-orbit interaction. For heavy atom molecule, such as iodine, the spin-orbit interaction between states belonging to different configurations (inter-configuration interactions) and coming to the same dissociation limit $I(^2P) + I(^2P)$ can be comparable in magnitude to intra-configuration interactions. Following Mulliken, such interactions are called separate-atom case- c effect. Since almost all configurations (except of 2440) lies higher than 2431, these case- c interactions must cause energy depressions of all the 2431 states except for $^3\Pi0^+u$. At this level of the theory, energies of the $^3\Pi0^-_u(0^-_u)$ and $^3\Pi0^+_u(0^+_u)$ become different and case- a coupling scheme is violated. Using experimental energies for vertical transitions $X \rightarrow A$ and $X \rightarrow C$ Mulliken found that $E_0 = 18,880 \text{ cm}^{-1}$ and $X = 4320 \text{ cm}^{-1}$. With estimated case- c energy depressions (at the ground state R_e) the energies of the states (3.3) become [1]

$$\begin{aligned}
A'^3\Pi2u(2_u) : E = E_0 - X/2 - a/2 - 420 \text{ cm}^{-1} \\
= 13765 (13631) \text{ cm}^{-1}, A^3\Pi1u(1_u) : E \\
= E_0 - 1/2\sqrt{X^2 + a^2} - 550 \text{ cm}^{-1} \\
= 15000 (14840) \text{ cm}^{-1}, B'^3\Pi0^-_u(0^-_u) : E \\
= E_0 - X/2 + a/2 - 1980 \text{ cm}^{-1} \\
= 17270 (17179) \text{ cm}^{-1}, B^3\Pi0^+_u(0^+_u) : E = E_0 - X/2 + a/2 \\
= 19000 (19115) \text{ cm}^{-1}, C^1\Pi_u(1_u) : E \\
= E_0 + 1/2\sqrt{X^2 + a^2} - 1910 \text{ cm}^{-1} = 20300 (20083) \text{ cm}^{-1}, \quad (3.6)
\end{aligned}$$

where in the brackets are experimental values [3–5].

One can see that the agreement with experiment is better than 300 cm^{-1} . The depth of the potentials of the states A' , A , B' , C correlates with their excitation energies (3.6). The exclusion is the B state which correlates with the second dissociation limit that increases the depth of its potential. The potential curves of other valence states with configurations 2341, 1441, 2422, 2332 have larger excitation energy and only shallow minima due to long range dispersion forces. Only states X , B , A' and A have deep minima greater than 0.2 eV.

Rydberg states correlate with atoms, in which the higher orbitals with general quantum number $n > 5$ are occupied. However, there is a group of states in the iodine molecule placed between valence and Rydberg states. These, *ion-pair (IP) states* will be discussed in Sect. 3.3. The IP states correlate asymptotically to

ionic limits $I^+(^1D_2, ^3P_{2,1,0}, ^1S) + I^-(^1S_0)$. In addition to the considered above MO theory, applied to describe the IP states [1, 6], there is an alternative approach, the “pure precession” or “atoms-in-molecule” model [7]. In this model, wavefunction of the molecule AB is a linear combination the antisymmetric products of atomic functions:

$$|n\Omega\omega\sigma\rangle = \hat{A} \sum_{j_A j_B m_A m_B} C_{j_A j_B m_A m_B}^{n\Omega\omega\sigma}(R) |j_A^e m_A\rangle |j_B^e m_B\rangle, \quad (3.7)$$

Where \hat{A} is the antisymmetrization operator, $|n\Omega\omega\sigma\rangle$ is the Dirac notation for the molecular electronic wave-function ($n\Omega\omega\sigma$), $|j_A^e m_A\rangle$ is atomic wavefunction with total electronic momentum j_A^e and its projection on the internuclear axis m_A , R is the internuclear distance. At the limit of separated atoms coefficients, $C_{j_A j_B m_A m_B}^{n\Omega\omega\sigma}(R \rightarrow \infty)$ can be determined from the symmetry consideration [8]. For the two lowest tiers with limits $I^+(^3P_j) + I^-(^1S)$ one can obtain

$$|n\Omega\omega\sigma, j^e\rangle = \frac{1}{\sqrt{2}} (|j^e m\rangle_a |00\rangle_b + p |00\rangle_a |j^e m\rangle_b), \quad (3.8)$$

where antisymmetrization operator is omitted for simplicity, indexes a , b distinguish iodine centers, $\Omega = m$, $p = 1(-1)$ for g (u) terms, $\sigma = (-1)^j$ (for $\Omega = 0$ states). Corresponding wave functions are presented in Table 3.1. In the *asymptotic model*, it is assumed that wave functions of the IP states are given by Eq. (3.8) for all internuclear distances. This approximation looks reasonable up to equilibrium distances of IP states [9]. Note, that j^e is a good quantum number in this approximation. Asymptotic model is the basis for the construction of the intermolecular diatomics-in-molecule (IDIM) model (see Sect. 5.3.2.3) for diabatic

Table 3.1 Wave functions of the two lowest tiers of I_2 in the asymptotic model

State	Wave function
First tier	
D^2_g	$(2 \pm 2\rangle_a 00\rangle_b + 00\rangle_a 2 \pm 2\rangle_b) / \sqrt{2}$
$\delta 2_u$	$(2 \pm 2\rangle_a 00\rangle_b - 00\rangle_a 2 \pm 2\rangle_b) / \sqrt{2}$
$\beta 1_g$	$(2 \pm 1\rangle_a 00\rangle_b + 00\rangle_a 2 \pm 1\rangle_b) / \sqrt{2}$
$\gamma 1_u$	$(2 \pm 1\rangle_a 00\rangle_b - 00\rangle_a 2 \pm 1\rangle_b) / \sqrt{2}$
$E 0_g^+$	$(20\rangle_a 00\rangle_b + 00\rangle_a 20\rangle_b) / \sqrt{2}$
$D 0_u^+$	$(20\rangle_a 00\rangle_b - 00\rangle_a 20\rangle_b) / \sqrt{2}$
Second tier	
$G 1_g$	$(1 \pm 1\rangle_a 00\rangle_b + 00\rangle_a 1 \pm 1\rangle_b) / \sqrt{2}$
$H 1_u$	$(1 \pm 1\rangle_a 00\rangle_b - 00\rangle_a 1 \pm 1\rangle_b) / \sqrt{2}$
$g 0_g^-$	$(10\rangle_a 00\rangle_b + 00\rangle_a 10\rangle_b) / \sqrt{2}$
$h 0_u^-$	$(10\rangle_a 00\rangle_b - 00\rangle_a 10\rangle_b) / \sqrt{2}$
$f 0_g^+$	$(00\rangle_a 00\rangle_b + 00\rangle_a 00\rangle_b) / \sqrt{2}$
$F 0_u^+$	$(00\rangle_a 00\rangle_b - 00\rangle_a 00\rangle_b) / \sqrt{2}$

potential curves and coupling between them for the Rg + I₂ system, where Rg is a rare gas atom.

Rydberg states. One of the useful features of the Rydberg states is a relative simplicity of their describing. Outer (Rydberg) electron is placed far from the ionic core, so these states can be described by a couple of ionic core and remaining electron, weakly interacting with it.

The energy of the Rydberg series can be well approximated as

$$E_{nli} = IE_i - \frac{Ry}{(n - \delta_l)^2}, \quad n = n_i, n_i + 1, \dots \infty, \quad (3.9)$$

where Ry is a Rydberg constant ($Ry \approx 109737.311 \text{ cm}^{-1}$), IE_i is an ionization energy of the i -th state, δ_l – quantum defect, depending on orbital quantum number l of the outer electron. For lowest Rydberg states of the iodine molecule, the spin-orbit coupling in the ionic core is comparable with the exchange energy between the core and outer electron. The interaction between outer electron and ion core rapidly decreases with the principal quantum number as n^{-3} . For high lying Rydberg states a spin-orbit coupling in the ionic core dominates. Therefore, a large amount of Rydberg states can be classified by ion core state and outer electron orbital quantum value. The lowest energy state of the I₂⁺ ion is an X²Π_g, and corresponds to removing of the π_u or π_g electrons, which are only mildly bonding or antibonding. Therefore molecular parameters (equilibrium internuclear distance) of the ionic and corresponding Rydberg states are not significantly different from those of the ground state.

The last known value of the first ionization potential is $IE_1 = 75069.25 \text{ cm}^{-1}$ measured by the zero kinetic energy pulsed field ionization (ZEKE-PFI) spectroscopy [10]. Large spin-orbit interaction split this state to the two components: ²Π_{3/2g} and ²Π_{1/2g}, which will be denoted below as X[3/2]_c and X[1/2]_c for simplicity. The energy gap between the X[1/2]_c and X[3/2]_c ionic states was determined in the same work as about 5197 cm^{-1} [10]. Two lowest excited ion states are A[²Π_{3/2, u}] and a[⁴Σ_u⁻]. They lie about $11,000 \text{ cm}^{-1}$ above the X²Π_g state and can form additional series of Rydberg states.

The major configuration of all the Rydberg states based on the ground core X state is [2430; ²Π_ω]_cnl. Spin-orbit coupling in the core results in minor configuration [2331; ²Δ_{3/2}]_cnl for the X[3/2]_c states or [2331; ³Σ 1/2⁻]_cnl for the X [1/2]_c ones.

3.2 Valence States and Valence-Valence Transitions

Iodine molecule has 23 valence states, that are grouped by correlation with three dissociation limits: I(²P_{3/2}) + I(²P_{3/2}) (*aa*), I(²P_{3/2}) + I(²P_{1/2}) (*ab*) and I(²P_{1/2}) + I(²P_{1/2}) (*bb*) (see Sect. 3.1 and Fig. 3.1).

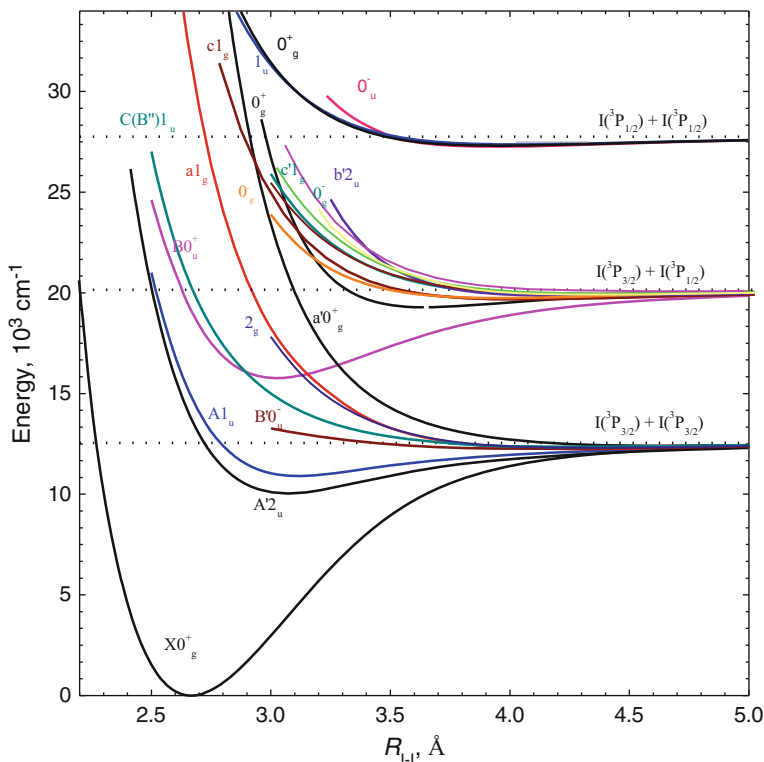


Fig. 3.1 Potential energy curves of the valence iodine molecule states. Any spectroscopic parameters of the 3_u , $(2)0_u^-$ (aa) states are unknown at present

Ten states, $X0_g^+$, $A'2_u$, $A1_u$, $B'0_u^-$, $a1_g$, $C(B'')1_u$, $a'0_g^+$, 2_g , as well as 3_u , $(2)0_u^-$, which unstudied at the present, correlate with the (aa) limit. Ten states $B0_u^+$, 0_g^+ , $c1_g$, $c'1_g$, 0_g^- , 2_u , $(3,4)1_u$, correlate with the (ab) limit and three, 0_g^+ , 1_u and 0_u^- with the (bb) limit.

Spectroscopic constants and potential energy curves ($PECs$) of four deeply bound (dissociation energy exceeds 1000 cm^{-1}) states, namely, $X0_g^+$ (aa), $A'2_u$ (aa), $A1_u$ (aa) and $B0_u^+$ (ab), have been determined with high precision. Remaining 19 states are weakly bound. They, with the exception of the 3_u , 0_g^- (aa) states, are characterized more or less precisely (see Appendix).

Electric dipole allowed, $\Delta\Omega = 0, \pm 1$, $g \leftrightarrow u$, optical transition between the valence states (absorption and emission) have been observed and studied. One should note that parallel transitions, $\Delta\Omega = 0$, are more intense than the perpendicular, $\Delta\Omega = \pm 1$ [1]. Transitions from the ground $X0_g^+$ (aa) state are the

most important and studied among valence-valence transitions. These and other transitions will be discussed in the following Sects.

3.2.1 Transitions from the X State

Bound-bound transition between the X and the lowest excited A state, $A, v_A, J_A \leftarrow X, v_X = 0, J_X$, lies in the near infrared (IR) region, $\lambda \approx 917\text{--}803.8\text{ nm}$ ($10905\text{--}12,440\text{ cm}^{-1}$) spectral range, if one takes into consideration the X,0 vibronic level only, though absorption up to 7220 cm^{-1} has been detected at high temperature [11–13]. Positions of numerous lines of the $A, v_A, J_A \leftarrow X, v_X, J_X$ transitions up to the $v_A = 35$ vibronic levels were determined with very low uncertainties ($\sim \pm 0.005\text{ cm}^{-1}$) using Fourier-transform spectroscopy method. The lines have been assigned. Cross-sections of the absorption lines are unknown. The A state radiative lifetime, $\sim 450\text{ }\mu\text{s}$ [14, 15], has been only estimated.

The $A \leftarrow X, v_X = 0, J_X$ bound-free transition, only, has to be observed in the $\lambda \approx 803.8\text{--}634\text{ nm}$ spectral range (Fig. 3.2), if one take into account transition from the X,0 vibronic level ($\lambda \approx 634\text{ nm}$ corresponds to the $B, 0, J_B \leftarrow X, v_X = 0, J_X$ transition [3]). At the shorter wavelengths, the $A \leftarrow X, v_X, J_X$, bound-bound $B, v_B, J_B \leftarrow X, v_X, J_X$ ($\lambda \approx 500\text{--}634\text{ nm}$), bound-free $B \leftarrow X, v_X, J_X$ ($\lambda \approx 410\text{--}500\text{ nm}$) and bound-free $C(B'') \leftarrow X, v_X, J_X$ ($\lambda \approx 410\text{--}600\text{ nm}$) transition spectra are overlapped (see Fig. 3.2).

J. Tellinghuisen believes [17] that the $I_2(B, v_B, J_B \leftarrow X, v_X, J_X)$ is possibly the most extensively studied transition in diatomic molecules: more than 10^5 lines have been

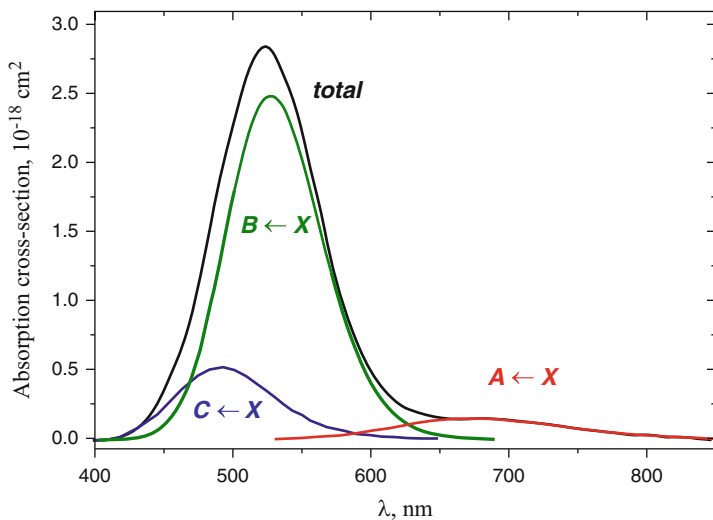


Fig. 3.2 Total and partial absorption cross-sections of gaseous I_2 near room temperature [16]. For the $B \leftarrow X$ transition, only bound-free cross-section, $\lambda \approx 410\text{--}500\text{ nm}$, may be used

assigned, and their wavenumbers have been measured with uncertainties $\sim 10^{-3} \text{ cm}^{-1}$ in energy range within 2 cm^{-1} the B state dissociation limit [18–20]. This spectrum has provided spectral calibration in high-resolution spectroscopic studies. Besides, it can be calculated with $\sim 0.002 \text{ cm}^{-1}$ uncertainties using spectroscopic parameters of the X and B states (see Appendix) and [21–23], e.g.). In the author's opinion, for many practical applications (calibration of luminescence excitation spectra and so on), it is more convenient to use absorption spectrum of iodine in a single ASCII file, covering the $14,250\text{--}20,000 \text{ cm}^{-1}$, presented in [20].

Cross-sections of the $B, \nu_B, J_B \leftarrow X, \nu_X, J_X$ absorption lines cannot be measured with low uncertainties since their full width half maxima (FWHM) are much less than spectral resolution of spectrometers used for measurements of absorption spectra, even if one take into consideration hyperfine structure of the lines, $\sim 0.03\text{--}0.04 \text{ cm}^{-1}$ [24]. Absorption follows Beer-Lambert-Bouguer law (Beer's law) [25, 26] only in the limit of zero absorption [17]. Besides, absorption lines are strongly overlapped. Therefore, one may use the absorption cross-sections $\sigma(\nu)$ (cm^2), absorption coefficients $\alpha(\nu)$, $k(\nu)$ ($\text{cm}^{-1}\cdot\text{atm}^{-1}$) or molar absorptivities $\epsilon(\nu)$ ($\text{l/mol}\cdot\text{cm}$) for spectral resolution and temperature used in the experiments in which absorbance has been measured and at low absorbance (see [17] for details).

The $I_2(B \leftarrow X)$ bound-bound transition presents some features of interest up to date. For example, the $B, \nu_B = 16\text{--}18, J_B \leftarrow X, 1, J_X$ transitions at $\lambda = 578 \text{ nm}$, that are near the $^1S_0 - ^3P_0$ clock transition of atomic ytterbium (Yb) were studied [27]. Therefore, the hyperfine lines of $B\text{-}X$ transition can be frequency references for Yb atom research.

If one needs to calculate absorption at a single rovibronic line, method and the transition dipole moment function $\mu_e(R)$ (Fig. 3.3) given in [17], as well as

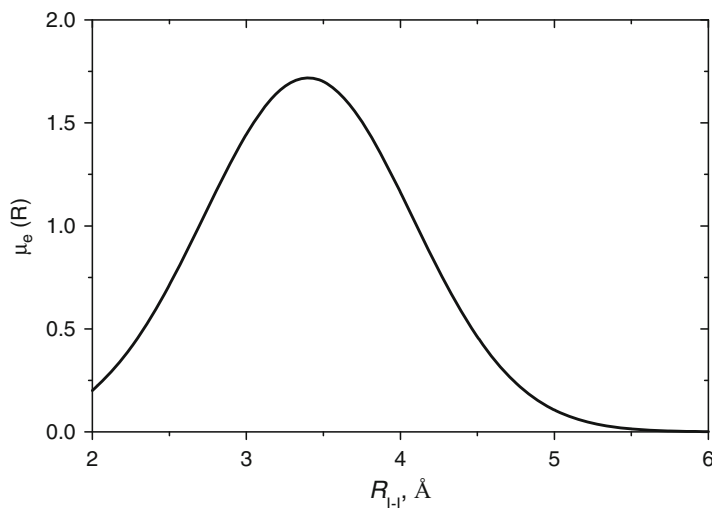


Fig. 3.3 The $I_2(B - X)$ transition dipole moment function [17]

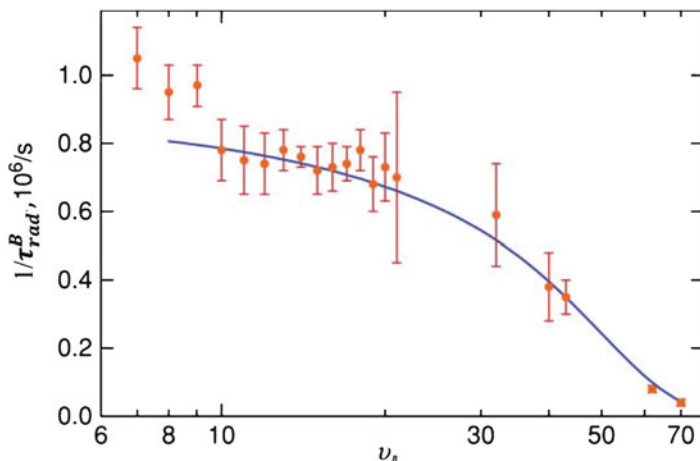


Fig. 3.4 The $1/\tau_{rad}^B = f(\nu_B)$ functions from [28] and calculated using dipole moment function recommended in [17]

wavenumbers and Franck-Condon factors (*FCFs*) of the transitions calculated using data from [21–23] can be utilized. The most reliable data on radiative lifetimes $1/\tau_{rad}^B(\nu_B)$ is given in Fig. 3.4.

Transitions to 1_u states correlating with the *aa*, *ab* and *bb* dissociation limits can occur in the $\lambda \approx 410\text{--}210$ nm ($\lambda \approx 210$ nm corresponds to the red limit of the $D0_u^+, \nu_D, J_D \leftarrow X, \nu_X, J_X$ bound-bound transition spectrum. The only 0_u^+ valence state is the $B0_u^+$. Transitions to both $A1_u$, $C1_u$ states have to be eliminated from consideration since they occur from near infrared (IR) to visible spectral range. According to [1, 2, 29–31], this band is ascribed as the $1441(^3\Sigma_u^+)1_u(ab) - 2440(^1\Sigma_g^+)X0_g^+$ transition. The $2332(^3\Delta_u)1_u(ab) - 2440(^1\Sigma_g^+)X0_g^+$ transition is two-electron, and, therefore, has to be very weak. Nevertheless, intensities of luminescence in the $\beta 1_g \rightarrow (3,4)1_u$, as well as $G1_g \rightarrow (3,4)1_u$ transitions are similar, so electronic configurations of the $(3,4)1_u$ states differ from mentioned above [32] (see Sect. 3.3.5).

To the best of our knowledge, absorption spectrum in the $\lambda \approx 410\text{--}210$ nm spectral range has been measured in [29], only (Fig. 3.5).

3.2.2 Transitions from the B State

Emission [33, 34] as well as absorption [35, 36] from the *B* state, have been observed and studied. The authors of [33] measured the $B,43,J_B \rightarrow a1_g,\nu_a,J_a$ and $B,43,J_B \rightarrow a'0_g^+,\nu_a',J_a'$ luminescence spectra excited by the 514.5 nm line of a multimode Ar^+ laser using Fourier transform spectrometer in the

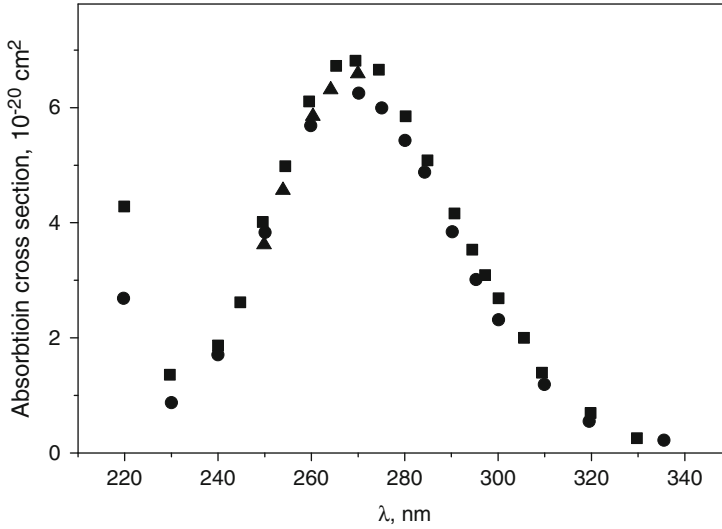


Fig. 3.5 Iodine molecule absorption spectrum in the $\lambda = 335\text{--}220$ nm spectral range [29]

$\lambda = 1370\text{--}1430$ nm spectral range and determined Dunham parameters for the a and a' states, $v_a = 0\text{--}14$ and $v_{a'} = 0\text{--}9$, respectively. The Rydberg-Klein-Rees (*RKR*) curves for the $v_a = 0\text{--}14$ and $v_{a'} = 0\text{--}4$ were determined, also. Transitions to the $a, 23, J_a$ and $a', v_{a'} \leq 9$ vibronic levels were observed in [34]; the *RKR* curves for the $v_{a'} = 0\text{--}9$ were also determined.

To the best of our knowledge, dipole moment functions of the transitions are unknown at the present.

Bound-free electric dipole allowed $a1_g, a'0_g^+(aa), 0_g^+, c1_g, c'1_g(ab) \xleftarrow{h\nu_f^i} B0_u^+$ and bound-bound electric dipole allowed $0_g^+(bb) \xleftarrow{h\nu_f^i} B0_u^+$ and electric dipole forbidden $0_u^-, 1_u(bb) \xleftarrow{h\nu_f^i} B0_u^+$ transitions at fundamental harmonic of the Nd:YAG laser, $h\nu_f^i$, have been observed and studied in [35, 36]. The electric dipole forbidden transitions occur due to *HFI* between $0_g^+, 0_u^-, 1_u(bb)$ states resulting in mixing of the 0_g^+ state to the $0_u^-, 1_u$ states. Excitation spectra of the $I_2(B, v_B, J_B \rightarrow X, v_X = 1, J_X)$ luminescence and temporal behaviors of the luminescence intensities were measured with switched on and switched off $h\nu_f^i$ generation. These data allow the authors of [36] to determine or estimate cross-sections of the transitions and determine dipole moment of the $0_g^+(bb), 5 \xleftarrow{h\nu_f^i} B, v_B = 18\text{--}21$ transition, $\mu = 0.09$ D, ~ 10 times less than maximum value of that of $B - X$ (see Fig. 3.3).

3.3 Ion-Pair States and Valence-Ion-Pair Transitions

3.3.1 General

Ion-pair states are traditionally called states in highly polar diatomic molecules, because of correlation with two ions at dissociation limit. For example, NaCl ground state has an IP features, where the Na and Cl atoms carry large opposite partial charges. As a consequence, binding potential can be well approximated by the Coulomb interaction potential, $U(r) \sim -e^2/r$. *PECs* of such states has a great depth (~ 4 eV) and relatively large interatomic distance. However, IP states exist for all diatomics, including homonuclear ones, such the iodine molecule. In the Hal_2 dimers dissociation limit $\text{Hal}^+ + \text{Hal}^-$ of IP states lies higher than the $\text{Hal} + \text{Hal}^*$ (e.g. $5p^4 6s$ for I_2), with which Rydberg states correlate, but due to the large depth of IP *PECs*, they are placed between valence and Rydberg states.

The ion-pair character of these states was proved experimentally by their photodissociation when the result of dissociation was both the positive and negative atomic ions:



The possibility of this process was firstly suggested by Mulliken [37], and experimentally observed [38–40]. Akopyan et al. [40] observed the simultaneous formation of the positive I^+ and negative I^- ions, and both ion current spectra were identical in the range of the first photoionization band.

Iodine molecule has 20 IP states, that can be classified by correlation with dissociation limit $\text{I}^+(^1\text{D}_2, ^3\text{P}_{2,1,0}, ^1\text{S}) + \text{I}^-(^1\text{S}_0)$. All the IP states are well approximated by Coulomb interaction potential and have similar depth of their *PECs*. The difference of T_e values is due to the difference in energy of the positive ion I^+ only, to which correlates each IP state. Strong spin-orbit interaction split J -sublevels of $\text{I}^+(^3\text{P})$ state, and as a result iodine molecule has a series of dissociation limits. The energy gap between almost degenerate $^3\text{P}_0$, $^3\text{P}_1$ and $^3\text{P}_2$ states of I^+ is about 6000 cm^{-1} (72169.3 cm^{-1} and 78617.2 cm^{-1} , respectively). The $\text{I}^+(^1\text{D}_2)$ dissociation limit lies at $E = 82258 \text{ cm}^{-1}$.

Therefore, there are 4 groups (or tiers) of IP states that correlate with 4 different dissociation limits. Each state in the tier has similar dissociation energy ($\sim 30000 \text{ cm}^{-1}$), equilibrium internuclear distance ($\sim 3.6\text{--}3.8 \text{ \AA}$), vibrational frequency ($\sim 100 \text{ cm}^{-1}$) and other molecular parameters (Fig. 3.6).

Six states $0_g^+(E^3\Pi_g 1432)$, $0_u^+(D^1\Sigma_u^+ 1441)$, $1_g(\beta^3\Sigma_g^- 2242)$, $1_u(\gamma^3\Delta_u 2332)$, $2_g(D'^3\Pi_g 1432)$, $2_u(\delta^3\Delta_u 2332)$ which form the first tier correlate with the lowest IP limit, $\text{I}^+(^3\text{P}_2) + \text{I}^-(^1\text{S})$. Six states form the second tier. Four states $0_g^-(g^3\Pi_g 1432)$, $0_u^-(h^3\Pi_u 1342)$, $1_g(G^3\Pi_g 1432)$, $1_u(H^3\Pi_u 1342)$ correlate with the $\text{I}^+(^3\text{P}_1) + \text{I}^-(^1\text{S})$ limit, and two states $0_g^+(f^3\Pi_g 1432)$, $0_u^+(F^1\Sigma_u^- 1441)$ with the $\text{I}^+(^3\text{P}_0) + \text{I}^-(^1\text{S})$ one. The dominant non-relativistic terms and electronic configurations are taken from [1, 6].

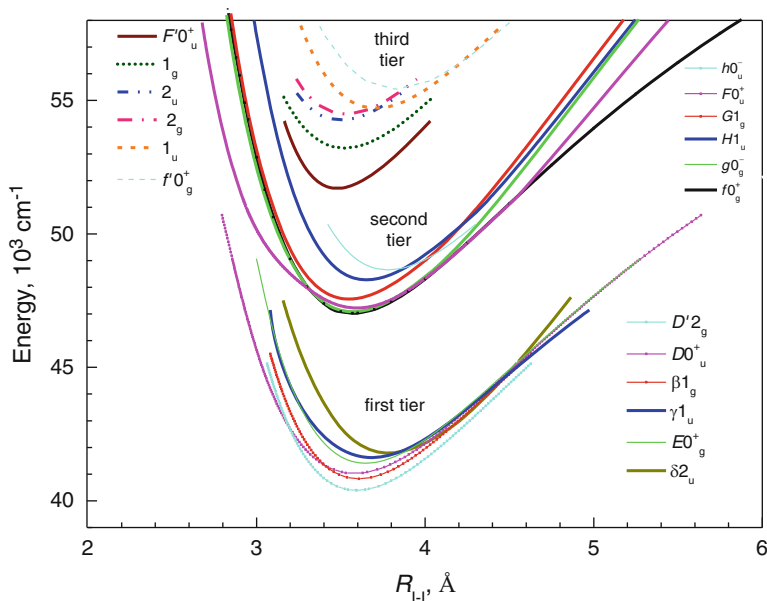


Fig. 3.6 Potential energy curves of IP states

Wave functions of the first and second tier IP states determined on the separated cation and anion basis set (asymptotic model), described in Sect. 3.1, are presented in Table 3.1.

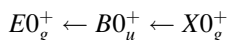
These states were studied for over 20 years because of some reasons of interest.

- Such featured tiers of IP states are very convenient systems for detailed studies of a collisional energy transfer. Highly mixed and irregular vibrational and rotational structure of different electronic states within each tier results in occurrence of many accidental resonances. An efficiency of the collisional energy transfer is inversely depended on energy gap. Therefore one can study collisional energy transfer dependence on various energy gaps and symmetry of coupled states. Short lifetimes of the IP states (3–30 ns [41]) (see Appendix) allow to study collisional processes in the “single collisions” conditions without molecular beam apparatus needed. Experimental and theoretical aspects of collision-induced processes are presented in Chap. 5.
- Optical transitions between the IP and valence states of halogens have charge-transfer character and are interesting examples of the strong influence of electronic configurations of the states and momentum coupling on their radiative characteristics and dipole moments of transitions.

3.3.2 First Tier IP States

Only two, DO_u^+ and $\gamma 1_u$ of the first tier states are accessible in the direct one-photon absorption from the ground XO_g^+ state due to selection rules. Because of large changes of IP state equilibrium distances, only high lying vibrational levels can be populated from the ground state. No experiments of the $\gamma 1_u$ direct optical population are known. Direct excitation of the D state is limited by $h\nu \approx 44300 \text{ cm}^{-1}$ and $v_D \geq 37$ and is responsible for the strongest absorption in the vacuum ultraviolet (VUV) spectral range, Cordes band system. The high-lying D state vibrational levels were analyzed in the fluorescence excitation spectra for $v_D = 113\text{--}201$ [42] and for $v_D = 140\text{--}342$ [43]. Lower vibrational levels in $v_D = 0\text{--}124$ range were characterized using three color optical-optical double resonance (OODR) excitation scheme [44, 45], or stimulated emission pumping method, where the D state was populated from excited vibrational levels of the X state [46]. Currently known spectroscopic constants and RKR potential curve were determined by J. Tellinghuisen after comprehensive reanalysis of the all previous data [47]. New parameters allowed to describe rovibrational levels up to $v_D = 290$ with a standard error that is $<0.05 \text{ cm}^{-1}$ throughout the region.

The most detailed studied state both experimentally and theoretically is the EO_g^+ state [1, 48–51]. It was excited by convenient and efficient OODR method that allows population a wide range of rovibrational levels:



Spectroscopic parameters and improved RKR potential were determined from analysis of the 1050 rovibrational transitions [52]. At present day, the Dunham expansion is applicable up to $v_E = 422$ with the correct reproducing of experimental data [49]. The most modern *ab initio* calculations were performed for the EO_g^+ IP state by using multireference variational methods with relativistic effective core potentials and large basis set [48]. However, the calculated potential curve is not consistent with the existing empirical potential curve [49] in the range of vibrational levels observed.

Another, $\beta 1_g$ IP state was studied by the same way in the LIF experiments [53, 54]. In that experiments, continuous wave laser pumped different B, v_B vibrational levels, and probe pulsed laser excited the E or β states. The rovibrational structure of the β state was determined in the $v_\beta = 0\text{--}52$ and $J_\beta = 8\text{--}148$ range from analysis of the $\beta \leftarrow B$ perpendicular transition. It was observed that the heterogeneous interaction of the β state results in anomalous intensities of the rotational branches and Ω -splitting effect [55]. From analysis of anomalous in rotational structure of excitation spectra, the authors determined the ratio of transition dipole moments $\mu_{E \leftarrow B} / \mu_{\beta \leftarrow B}$ and estimated the dipole moment of the $\beta \leftarrow B$ transition as $\mu_{\beta \leftarrow B} = (6.6 - 11.6) 10^{-2} \text{ D}$ for $R = 3.35\text{--}3.40 \text{ \AA}$ [55]. The $A1_u$ valence state was also used as the intermediate gate

for the $\beta 1_g$ (1 + 1 scheme) [56] and $\gamma 1_u$ (1 + 2 scheme) [57] state population. The $\beta \leftarrow A$ transition was analyzed in the group of M.C. Heaven in the jet-experiments, which allowed to extend the β state structure up to the $v_\beta = 68$ [56].

The $\gamma 1_u$ state is characterized in the $v_\gamma = 0-11$ and $J_\gamma = 5-119$ ranges [57-59]. In the two-photon $\gamma 1_u \leftarrow A 1_u$ transition [57], some extra lines in the excitation spectra were found and assigned to the $\delta 2_u$ state population. The $\delta 2_u \leftarrow A 1_u$ transition is forbidden according to the symmetry selection rule and the $\delta 2_u$ state can be excited due to mixing of the wave functions with the $\gamma 1_u$ state by heterogeneous interaction. Two sets of similar progressions relate to the $\gamma 1_u$ and $\delta 2_u$ perturbed states. A solution of the 4-state problem (for e and f sublevels of both IP states) allowed the authors to determine molecular constants and calculate *RKR PECs* of the both $\gamma 1_u$ and $\delta 2_u$ state. Later, spectroscopic parameters of the both states were improved for the $v_\gamma = 0-11$ and $v_\delta = 0-7$, $J_\delta = 9-103$ ranges in the analysis of the PFOODR spectra via the $B 0_u^+ \sim c 1_g$ perturbed intermediate state [60].

Fluorescence from the $D' 2_g$ IP state, $D' \rightarrow A'$ at 340 nm is the most intense emission band at high pressures in discharge [61]. After the $D' \rightarrow A'$ transition in halogen dimers was proposed for laser generation, many works appeared to study this IP state [61, 62].

3.3.3 Second and Third Tier IP States

The IP states of higher tiers have similar *PECs* that their first tier partner. Therefore, many states were populated and studied by the same methods. The $F 0_u^+$ and $F' 0_u^+$ states are ascribed in the $v_F = 0-220$ and $v_{F'} = 0-38$ respectively [63-65].

The OODR technique allows to avoid Frank-Condon limitations in direct excitation from the ground state. Low- v levels of the F [63, 64] and F' [65] states were populated by three-photon excitation scheme via the intermediate B state. Strongly allowed $F, F' \rightarrow X$ transitions, which are dominating radiation decay channels result in short lifetimes (4.5 ns and 3.2 ns, respectively) for the IP states.

The *gerade* $f 0_g^+ (^3P_0)$ and $f' 0_g^+ (^1D_2)$ states were excited with the two-photon OODR scheme via the same B intermediate state [66, 67] or by the (1 + 1 + 1) resonance enhanced multiphoton ionization (REMPI) method [49]. Dunham expansion and *RKR* potential curves for f and f' states are known in the $v_f = 0-228$ and $v_{f'} = 0-166$ ranges, respectively, using the step-wise ionization method [49]. The $G 1_g$ and $1_g (^1D_2)$ states can be efficiently populated via $A 1_u$ [68, 69] or $1_u(bb)$ [70] valence states using the OODR scheme.

Because of symmetry selection rules, direct population of another IP states from the ground $X 0_g^+$ states or OODR schemes via the intermediate $B 0_u^+$ or $A 1_u$ states are not effective or impossible. Perturbation facilitated optical-optical double

resonance (PFOODR) methods via the B intermediate state, mixed with some of the weakly-bound states are more preferable.

The *ungerade* $H1_u(^3P_1)$, $1_u(^1D)$, $2_u(^1D)$, $h0_u^-(^3P_1)$ and *gerade* $g0_g^-(^3P_1)$, $2_g(^1D)$ IP states were studied by means of such PFOODR schemes. Excitation via the $B0_u^+ \sim c1_g$ mixed state were utilized for the $H1_u$ [71], $1_u(^1D)$ and $2_u(^1D)$ [72] state analysis.

The $h0_u^-(^3P_1)$ IP state position was firstly estimated indirectly by analysis of the structure of the $H1_u$ rovibrational terms [73]. The heterogeneous interaction between $h0_u^-$ and $H1_u$ states results in Ω -doubling of the double-degenerated rovibronic levels of the latter. Calculations of the interaction matrix elements allowed to estimate T_e of the $h0_u^-$ state. Later, this state was excited via the $B0_u^+ \sim (3)0_g^-$ hyperfine coupled state in the same group [71], which obtained its spectroscopic constants and confirmed previous estimations.

The $B0_u^+ \sim (3)0_u^-$ coupling cluster allowed to describe the $g0_g^-(^3P_1)$ IP state [74]. Finally, the $B0_u^- \sim b'2_u$ hyperfine mixed states were used for $2_g(^1D_2)$ IP state analysis [75].

A three-step perturbation-facilitated excitation scheme via the $B0_u^+$ and $0_g^+ \sim 1_u \sim 0_u^-(bb)$ states was performed to populate IP states of the both *gerade* $G1_g(^3P_0)$ and $g0_g^-(^3P_1)$ and *ungerade* $F0_u^+(^3P_0)$, $F'0_u^+(^1D_2)$ states [70]. The cluster of coupled (bb) states will be described in Sect. 4.3.1.2 in detail.

3.3.4 High-Lying Vibrational Levels of IP States

High-lying vibrational levels of IP states are overlapped with Rydberg states (Fig. 3.7). Avoiding crossing, intensity borrowing in the excitation spectra or extra lines appearance complicate the assignments and analysis of rovibrational structure for both IP and Rydberg states. High-lying vibrational levels of the *gerade* IP $E0_g^+, f0_g^+(^3P_0)$ and $f'0_g^+(^1D_2)$ [49], $\beta1_g$ and $D'2_g$ states [76] were studied by different schemes of REMPI method. Two-photon absorption of the ground state populates high-lying vibrational levels accessible in the vertical transition, and probe laser ionized excited molecules subsequently.

Near the dissociation limit, the near-dissociation expansion (NDE) approximation cannot be applied for description of the high lying vibrational levels of IP states because of the Coulomb interaction at the long-range interatomic distance. However, another, “heavy Rydberg”, model can be applied for description of the high lying vibrational levels behavior in the IP states of dihalogen molecules [77] (see Chap. 4 for details). This model allows to make more revealing fit to the vibrational structure in the high excitation region with fewer coefficients. The authors of [77] showed that the method allows to check assignments and numbering of the vibrational levels. Avoiding crossing in PECs of IP and

Rydberg states on the inner wall results in significant changes in the fitting parameters. No major interactions were found for the E and D' states. However, the avoided crossing in the inner branch of the $D0_u^+$ state was found. Experimental studies showed perturbations in the vibrational progressions of the D state near 58600 cm^{-1} and 59350 cm^{-1} [43, 78], which attributed to interaction with the $X[3/2]_c 6p1_u$ and 0_u^+ Rydberg states, respectively.

Vibrational levels of the E state were assigned up to $\nu_E = 422$ (61700 cm^{-1}) [49]. Later, some levels previously attributed to the β state were re-assigned and added to the E state with $\nu_E = 518\text{--}592$ [76]. At the energy ranges close to 55000 cm^{-1} and 60000 cm^{-1} , it was observed irregular behavior of rovibrational structure caused by crossing with 0_g^+ Rydberg states. The lowest Rydberg state of the 0_g^+ symmetry is the $X[1/2]_c 6s0_g^+$ whose $\nu_{Ry} \sim 14$ level lies near 56200 cm^{-1} and can be responsible for the interaction. The f' IP state crosses this Rydberg state at $\sim 60000\text{ cm}^{-1}$, and perturbations of the several vibrational levels were found at this energy region. The next 0_g^+ Rydberg states belong to the $X[1/2]_c 5d$ cluster [67] and extensively interacts with the E and f IP states at 60000 cm^{-1} region (Fig. 3.7).

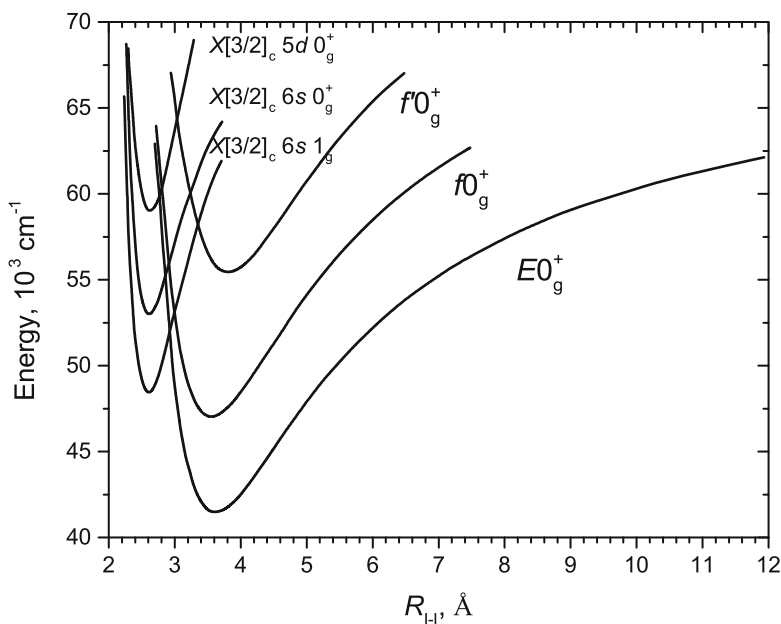


Fig. 3.7 The potential energy curves of some IP and Rydberg states. [49]

3.3.5 Ion-Pair – Valence State Transition

Parallel ion-pair – valence state (IP – V) transitions at equilibrium R_e has large transitions dipole moments, $\mu = 0.7\text{--}3.7$ D, much stronger than those of perpendicular transitions with almost unchanged $\mu = 0.2\text{--}0.3$ D. At long I-I distances, the asymptotic model is well-suited, whereas at short R electronic wave functions can be ascribed often by single MO term (see Sect. 3.1). Outer branch of the IP states is determined by Coulomb interaction and inner branch has an electronic antibonding character. It strongly affects the dependence of configuration interaction on interatomic distance.

Dipole allowed transitions from the ground state allow to populate *ungerade* 0_u^+ IP states, but only one, the $D \leftarrow X, v_X = 0, 1$ transition has the large absorption cross-section (Fig. 3.13). The MO configuration theory ascribes $D \leftarrow X$ transition as one-electron transition between dominant configurations $1441 \leftarrow 2440$ (see Sect. 3.1). This is a well-known example of the applicability of the MO configuration approach. However, the lifetime of the second F and third F' IP state are very short (see Appendix) and their luminescence back to the X state is very strong. Variations in contributions of different configurations with R can explain these features. An alternative model of separated atoms or ions can be also applied for IP–V transitions description.

It is clear that separation fragments description can be resolved into a linear combination of MO configurations. And *vice versa*, the electronic configuration of the state can be considered as a result of mixing of different cation $|j^e_{AmA}\rangle$ states due to the intramolecular field. The IP–V transitions in the halogens, their transition dipole moment functions present an interesting example of evolution such two approaches, changes in the electronic structure of states involved in the transition as a function of R_{I-I} . Here we consider some examples of such effects.

Dominate channel of fluorescence from 0_u^+ IP states is a $IP \rightarrow X$ transition, but another transitions were also observed [41]. For example, relative contribution of the $D \rightarrow X$ transition is equal to 0.89 for $v_D = 0$ and 0.78 for $v_D = 18$, but the $D \rightarrow a'0_g^+$ and $D \rightarrow (3)0_g^+$ systems are also seen (Fig. 3.8). Configurations of these lower valence states are $^3\Pi_g 2341$ and $^3\Sigma_g^- 2422$, respectively, and one-electron transitions to them are forbidden from the D 1441 configuration. The dipole moment function of the $D \rightarrow X$ transition has a maximum at $R \approx R_e^D$, whereas that of the $D \rightarrow a'$ transition slowly decreases with R (Fig. 3.9). Dipole moment functions are good indicators of electronic structure evolution of the states involved in the transition.

As is shown in [41], the asymptotic model (*jj* coupling) adequately describes the electronic structure of IP states in the $R > R_e$ range. From this point of view the IP – V transitions are charge-transfer transitions, dipole functions of which decrease to zero at $R_{I-I} \rightarrow \infty$ due to decreasing overlap of Γ^+ and Γ^- atomic orbitals. With R decreasing, different states of cation become mixed by the intramolecular field, and relative contribution of different basis wavefunctions changes. Finally, exchange terms prevail the interaction energy, and the single MO configuration emerges. Within the *jj* coupling

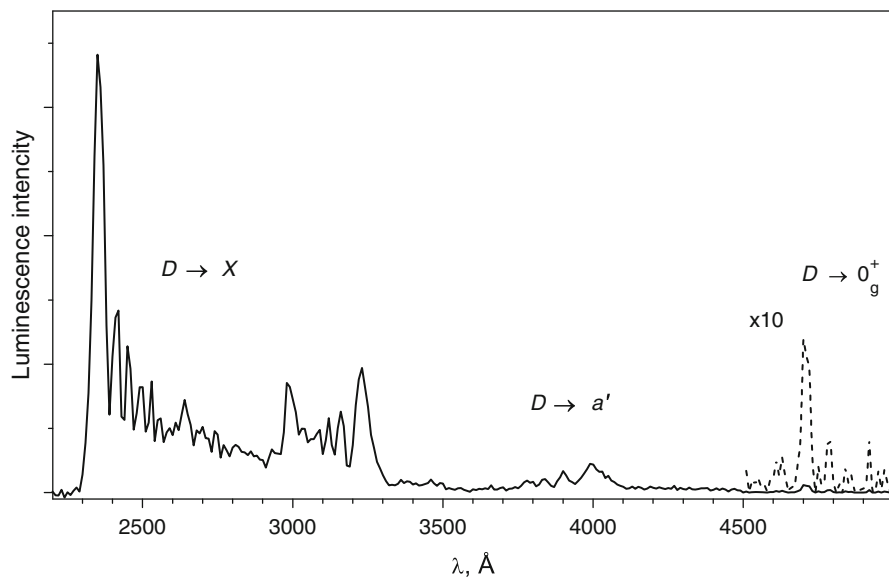


Fig. 3.8 Luminescence spectra of the transitions from the D , $v_D = 54$, $J_D = 62$ state [80]

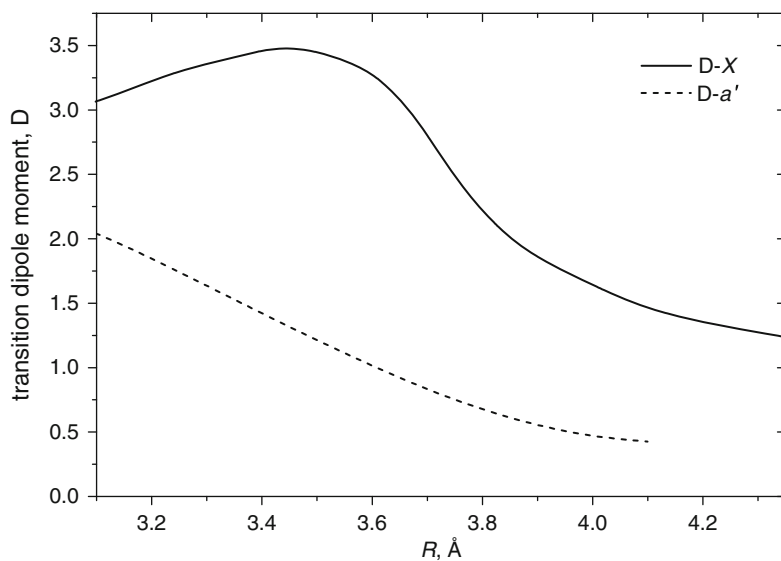


Fig. 3.9 Transition dipole moment functions of the $D \rightarrow X$ and $D \rightarrow a'$ transitions [45]

scheme, cation wavefunctions are represented as a linear combinations of spin-orbital Slater determinants, including 4 outer p -electrons (p^4 configurations) [7, 41]. Thus, the $^3P_{2,2}(122)$ state ascribed by a single configuration $\|1^+1^-0^+-1^+\|$ (short notation $\|p_\pi^3 p_\sigma^1\|$), where 1 or 0 corresponds to m_l and sign \pm is a spin orientation $m_s = \pm 1/2$. There are three possible p^4 configurations: $\|p_\pi^2 p_\sigma^2\|$, $\|p_\pi^3 p_\sigma^1\|$ and $\|p_\pi^4\|$.

The authors of [7, 41] used this pure precession model in analysis of IP–V transition dipole momenta and obtained that the $p_\pi - p_\pi$ and $p_\sigma - p_\sigma$ electron transfers only are involved to the parallel dipole transition, and the latter has about 3–4 times more contribution to the parallel transition. The $p_\sigma - p_\sigma$ electron transfer contributes if only p_σ -vacancy is accessible in the transition.

The D state wavefunction on the separated ionic basis set includes the $\Gamma^+(^3P_2)$ $\|p_\pi^2 p_\sigma^2\|$ and $\|p_\pi^3 p_\sigma^1\|$ determinants. The possible $p_\sigma - p_\sigma$ electron transfer – $\|p_\pi^3 p_\sigma^1\| \cdot \|p_\pi^4 p_\sigma^2\| \leftrightarrow \|p_\pi^3 p_\sigma^2\| \cdot \|p_\pi^4 p_\sigma^1\|$ corresponds to the $D \rightarrow X$ transition. Another $D \rightarrow a'$ transition is allowed only by $p_\pi - p_\pi$ electron transfer $\|p_\pi^2 p_\sigma^2\| \cdot \|p_\pi^4 p_\sigma^2\| \rightarrow \|p_\pi^3 p_\sigma^2\| \cdot \|p_\pi^3 p_\sigma^2\|$, that 3–4 times less than the $p_\sigma - p_\sigma$ one. Consideration of spin-orbit and interionic interactions gives no contribution. So, the $D - a'$ transition dipole moment has less value, and its character is only caused by exponential decreasing of cation and anion atomic orbitals overlap with R [45].

All *gerade* 0_g^+ IP states (E, f, f') are accessible in the OODR experiments via the intermediate $B0_u^+$ state [45, 80, 81]. Fluorescence from these states was found also with domination (~97%) of IP $\rightarrow B$ transition. In framework of the Mulliken MO configuration theory, only $f^3\Pi_g 1432 \leftarrow B^3\Pi_u 2431$ transition is allowed, but this state has longest lifetime (142(6) ns) [49], that is not supported by the single MO description. The $E \rightarrow B$ and $f \rightarrow B$ transition dipole function $\mu_e(R)$ are shown in Fig. 3.10. Both functions have the maximum around R_e of the appropriate IP state and decrease rapidly at smaller distances. According to the relativistic *ab initio* calculation, dominate contribution at R_e to the E and f states gives the $^3\Pi_g 1432$ configuration (~60%), one-electron transition from the $B^3\Pi_u 2431$ state is allowed. At shorter distances contribution of the $^3\Sigma_g^+ 2242$ configuration increases and the $E, f \rightarrow B$ transitions become one-electron forbidden [81].

It is of interest to compare the two *gerade*, $\Omega = 1$ IP states: $\beta 1_g$ and $G 1_g$. Transitions from both states are more spread over the valence states compared to the 0_u^+ IP ones. The dominant $\beta, G \rightarrow A 1_u$ transition has contribution about 81% and 87% for β and G states, respectively. From the MO theory, both $G^3\Pi_{1g} 1432 \rightarrow A^3\Pi_{1u} 2431$ and $G^3\Pi_{1g} 1432 \rightarrow B''^1\Pi_{1u} 2431$ are allowed as a one-electron transitions, both transitions from the $\beta^3\Sigma_g^- 2242$ state require two-electron transfer and are forbidden. Minor contribution of the $1432 \ ^3\Pi_{1g}$ configuration at the more long separations explains the observation of the $\beta \rightarrow A$ transition.

Similar differences are observed in transitions to the two closed states of the second dissociation limit, $(3,4)1_u$. Moderate contribution to the total luminescence from the β state has the $\beta \rightarrow (3,4)1_u(ab)$ transition, whereas the $G \rightarrow (3,4)1_u(ab)$ transition has contribution ~2%. Transition dipole moment functions of the $\beta, G \rightarrow (3,4)$

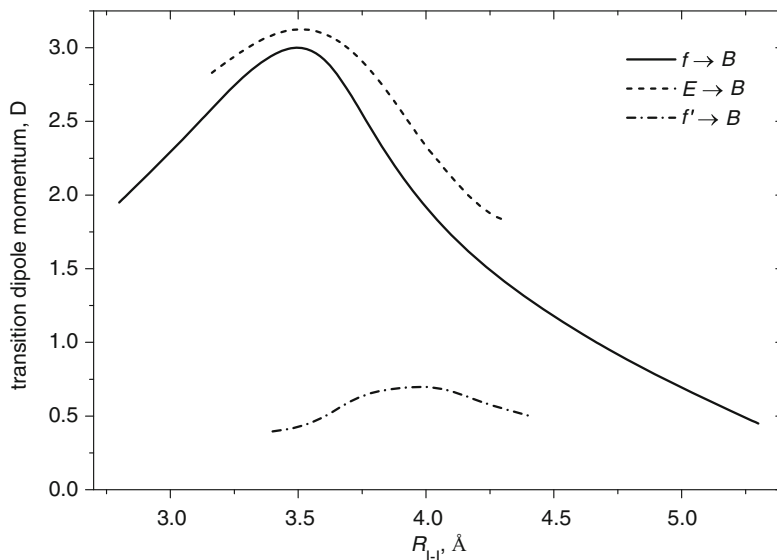


Fig. 3.10 Transition dipole moments as a function of I-I distance $\mu_e(R)$ for $E \rightarrow B$ [45], $f \rightarrow B$ [81] and $f' \rightarrow B$ [49] transitions

$1_u(ab)$ transitions are shown in Fig. 3.11. In the “atoms-in-molecule” model, exponential decreasing of overlap integrals of cation and anion orbitals with R is the reason of dipole moment functions fall-off. The only, $\beta \rightarrow (3)1_u$ transition dipole function has a maximum at long separation [32].

The $(3)1_u$ and $(4)1_u$ states have the 1441 and 2332 dominant configurations at small atomic separations, respectively [2]. So, the $\beta \rightarrow (4)1_u(ab)$ transition is one-electron and parallel, $\pi_u \rightarrow \pi_g$, while the second $\beta \rightarrow (3)1_u(ab)$ transition has two-electron character and is forbidden at short atomic separations. The alternative atom-in-molecule model predicts both strong $\beta 1g \rightarrow (3,4)1_u$ transitions, which involve $p_\sigma \rightarrow p_\sigma$ electron transfer. Competition between forbidden multi-electron transfer at small atom separations in the $\beta \rightarrow (3)1_u$ transition and allowed $p_\sigma \rightarrow p_\sigma$ electron transfer at large R results in the maximum of dipole moment function (Fig. 3.11).

In case of transitions from the $G1_g$ state, both $G1_g \rightarrow (3,4)1_u(ab)$ transitions are one-electron and perpendicular ($1432 \rightarrow 2332$, $\pi_u \rightarrow \sigma_g$ and $1432 \rightarrow 1441$, $\pi_g \rightarrow \sigma_u$, respectively), thus both transitions could have similar small contributions to the luminescence as observed in the experiment [32].

As it was shown, in spite of the intramolecular field of heavy iodine atoms, strong spin-orbit interaction, representation of IP states wavefunctions in the basis of separated ions is a good approximation up to the equilibrium separations. So, both the MO configuration model and the separated atoms (ions) representation

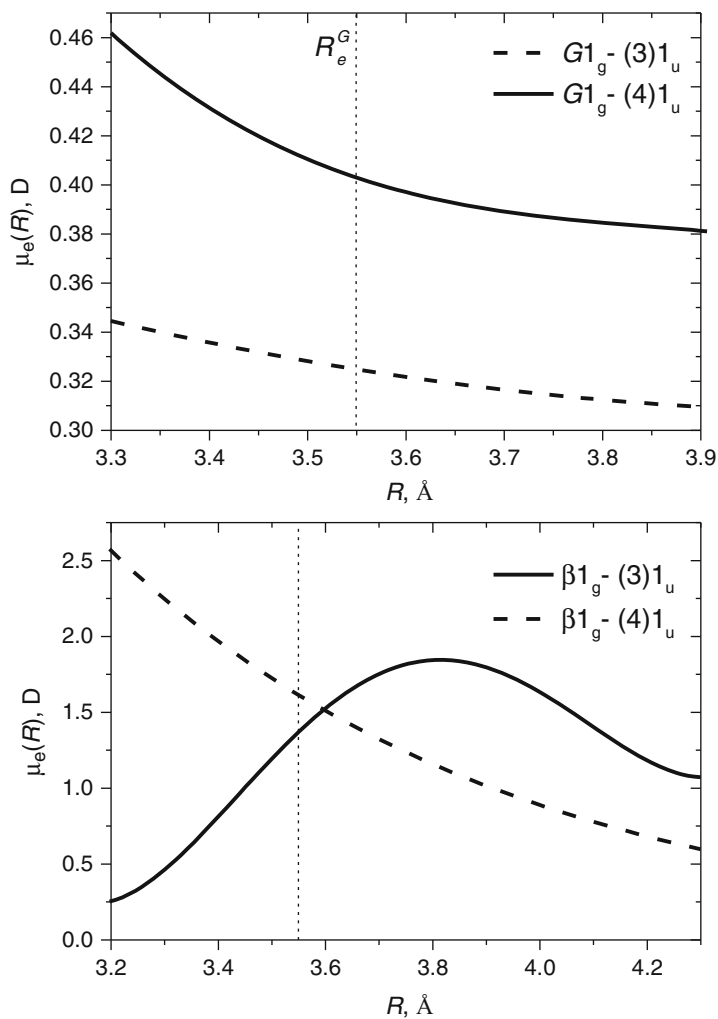


Fig. 3.11 The $\beta, G \rightarrow (3,4)1_u$ transition dipole moment functions [32]

(atom-in-molecule model) can be successfully applied for description of the valence and IP states, their electronic structure and optical transitions between them. Moreover, these models are quite suitable for analysis and interpretation of both intramolecular and intermolecular perturbations.

3.4 Rydberg States

3.4.1 General

Symmetry of Rydberg states is determined by an ion core state, ${}^2\Pi_{3/2g}$ and ${}^2\Pi_{1/2g}$, and outer electron. The outer electron with different electronic orbitals can be taken into consideration by using the Ω - ω coupling scheme [37]. The projection of total angular momentum on the molecular axis, Ω , is well defined by

$$\Omega = \Omega_c + \omega,$$

where Ω_c and $\omega = \lambda + m_\lambda$ are projections of the ion-core and outer electron total angular momenta on the molecular axis, respectively. λ and m_λ are orbital and spin projections of Rydberg electron.

For example, the $X[3/2]_c np\sigma_u$ configuration gives Π_{1u} and Π_{2u} states, the $X[3/2]_c np\pi_u$ one gives 4 states: ${}^3\Delta(3_u)$, ${}^3\Delta(2_u)$, ${}^3\Delta(1_u)$, ${}^1\Sigma^+(0^+_u)$ and ${}^1\Sigma^-(0^-_u)$, and so on. Selection rules for optical transitions from the iodine $X0^+_g$ ground state can exclude from consideration a lot of them. The Franck-Condon principle together with the selection rules defines optically accessible states which can be observed. Collisions with a partner can result in different electronic states population, but an analysis of such spectra are difficult.

Vibrational structure, “hot” transitions from vibrationally excited ground state make assignment procedure difficult to realize. Vibrational frequencies of the most Rydberg states are similar within 190–284 cm^{-1} range [83] that allows to separate them from other states.

According to [83], the energy of Rydberg state weakly depends on ω quantum number of Rydberg electron. A splitting of states with couplings of ω to different cores (for example, $X[3/2]_c 6s 1_g$ and $X[1/2]_c 6s 1_g$ states) is much larger than those to identical cores (for example, $X[3/2]_c 6s 1_g$ and $X[3/2]_c 6s 0_g$ states). So, all the states of the same core/electron configuration are aggregated into clusters (see Fig. 3.12, for example).

The information that can be deduced directly from experimental data is the effective principal quantum number, $n^* = n - \delta_l$. One of the main problems of such assignments is the uncertainty in the quantum defect δ_l definition. It is very tentatively to vary δ_l in order to describe all the experimental results. For example, the choice between a $7s$ state with $\delta = 3.95$ and a $5d$ state with $\delta = 1.95$ for $n^* = 3.05$ cannot be made unambiguously [84]. Actually, selection of the quantum defect is not so ambiguous. Experiments and theoretical calculations showed that quantum defects remain approximately constant. The s series of states have markedly non-zero values 0.9–1.2 and the p series have $\delta = 0.3$ –0.5. The non-penetrating with the core orbitals, d and f have small values, $\delta < 0.1$.

Additionally, the assignment of the absorption band depends on using correct ionization energy I_i and the ion core state. At high n numbers, the density of the states increases, and an uncertainty of the ionization energy affect the assignment

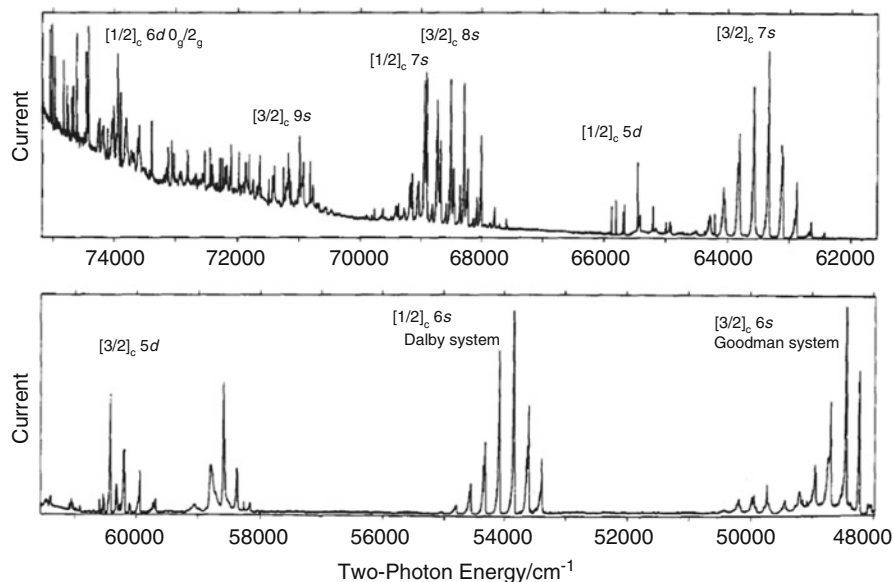


Fig. 3.12 The (2 + 1) REMPI spectrum of I_2 recorded with linear polarized light for $\lambda_{ex} = 266\text{--}417$ nm [67]

result. Rydberg states are arranged starting from 48000 cm^{-1} and overlaps with IP states of the second and third tier. At the energy $E > 58000\text{ cm}^{-1}$ PECs of Rydberg states are crossed with those of the IP states, and avoiding crossing leads to strong perturbations of the vibrational and rotational structures (see Chap. 4). Along with it, due to the homogeneous coupling of the Rydberg and IP states, emission from them can be detected in the visible or near ultraviolet region [78].

3.4.2 The $[^2\Pi]_c$ ns Series

The lowest Rydberg states are placed in the $48000\text{--}56000\text{ cm}^{-1}$ energy range and belong to the first members of the $[^2\Pi]_c$ ns series ($n = 6$). Coupling of the σ_g electron with the $X[1/2]_c$ and $X[3/2]_c$ cores includes 1_g and 0_g states and 2_g , 1_g , 1_g and 0_g ones, respectively. Parity selection rules do not allow direct population of these states in the VUV spectral range from the ground state, so indirect excitation schemes are available via perturbative states or multiphoton absorption (see Sects. 2.1.7 and 2.1.8).

Analysis of emission spectra in the UV and visible ranges showed the existence of two states near 51258 cm^{-1} and 56000 cm^{-1} [84]. Appropriate bands in absorption spectra were not observed, and the authors of [84] assumed that this bands can be assigned to population of the $X[3/2]_c 6s \sigma_g 1_g$ and $X[1/2]_c 6s \sigma_g 0_g^+$ gerade Rydberg states with $\omega_{Rb} = 215\text{ cm}^{-1}$ and 360 cm^{-1} respectively. Rydberg states are highly overlapped with IP ones in this energy range, but latter have

sufficiently different vibrational frequencies ω_{IP} due to high equilibrium distances (see Sect. 3.3) and can be excluded easily.

Two band systems, “Dalby system” [85, 86] (band origin 53563 cm^{-1}) and “Goodman system” [87] (band origin $48426(8) \text{ cm}^{-1}$) were studied by the (2 + 1) REMPI method. Analysis of rotational envelope of this system, circular (CP)/linear (LP) polarization photoionization ratio, $I_{\text{CP}}/I_{\text{LP}}$, and selection rules restrictions of optical transitions allowed to assign these band systems as $X[1/2]_c 6s 1_g$ and $X[3/2]_c 6s; 2_g$ states, respectively. A polarization ratio $I_{\text{CP}}/I_{\text{LP}} \sim 1.5$ for all branches with $|\Delta\Omega| \leq 2$ with the exception of the Q branch in the $\Delta\Omega = 0$ case in two-photon transitions in diatomic molecules [88]. In the $\Delta\Omega = 0$ two-photon transitions $I_{\text{CP}}/I_{\text{LP}}$ depends on rotational quantum number and can range from 0 to 0.25. Therefore, an analysis of the two-photon transitions from the ground $\Omega = 0$ states allows to determine the symmetry of the Rydberg state.

Unknown weak bands in this spectral range were found using multiphoton ionization mass spectroscopy in the supersonic beam experiments [89]. One of the band with the origin at 53006 cm^{-1} was tentatively assigned to the $X[1/2]_c 6s; 0_g$ Rydberg state. However, these band systems were not observed in the experiments hereafter.

Higher lying $[^2\Pi]_c ns$ states with $n = 7-11$ were found in the $67500-75000 \text{ cm}^{-1}$ energy range [67]. Donovan *et al.* compared REMPI spectra, also, using the radiation with LP and CP polarization and found sufficiently large differences in band relative intensities [67]. Some sub-system of vibrational progressions have higher intensity with CP, while those of other 1_g bands decrease. Wu *et al.* recorded similar REMPI spectra of both $[I^+]$, $[I_2^+]$ (molecular jet) and total ion signal (static cell) [90]. Their $[I_2^+]$ spectra resemble those obtained later in the CP [67]. Such variation of band intensities in different experiment conditions (ion fragment collection or laser polarization) were explained by perturbations in Rydberg 1_g states being crossed with repulsive states [67]. This Rydberg \sim repulsive state coupling results in I atom formation and subsequent ionization. Therefore the 1_g Rydberg states were observed primarily in $[I^+]$ REMPI spectra. In addition, non-resonant ionization cross-sections of atoms is dramatically smaller in circularly than in linear polarized radiation [92], and the 1_g Rydberg states were observed predominantly in LP conditions. This phenomenon allowed in particular to reassign some bands corresponding to the $[^2\Pi_{3/2}]_c 7s 2_g$ and $[^2\Pi_{3/2}]_c 7s 1_g$ states instead of nd ones previously obtained [90].

It is clear that interactions of Rydberg states with other states result in perturbations both in vibrational and rotational structure. The “Dalby” and “Goodman” band systems which do not have perturbations (Fig. 3.12) and hence are convenient objects for spectroscopic analysis were extensively studied [67, 92, 93]. Dalby *et al.* compared relative band intensities with calculated Franck-Condon factors and made an estimation of the internuclear distance of the excited $X[1/2]_c 6s; 1_g$ states as $R_e = 2.568(2) \text{ \AA}$. Rotational constant B were derived from it as $B_e = 0.04028(6) \text{ cm}^{-1}$. Accurate analysis of the rotational structure allowed to refine spectroscopic characteristics of some Rydberg states hereafter.

Such rotational branch behavior was observed for the Goodman system ($X[3/2]_c$ $6s\ 1_g$ (0,0) band) [67], Dalby system: (0,1) band [94] and other. Extensive spectroscopic analysis of $X[1/2]_c$ $6s\ 1_g$ bands performed to derive rotational as well as vibrational spectroscopic constants [93].

3.4.3 The $[^2\Pi]_c$ np Series

Coupling of the np Rydberg electron with the $X[3/2]_c$ ion core forms 6 *ungerade* electronic sub-states. Because of selection rules ($\Omega \leq 1$), only 3 ungerade states are available in direct transition from the ground state. As well, the 5 Rydberg states of the 6 ones derived from the $X[1/2]_c$ np configuration can be excited.

The first systematic investigation of the *ungerade* Rydberg states of the iodine molecule was made by P. Venkateswarlu [82]. He analyzed high resolved absorption spectra in the VUV spectral region (125–195 nm, 80000–51300 cm^{-1}). Another research groups [39, 78] extended the range of absorption spectra up to 60 nm (167000 cm^{-1}).

P. Venkateswarlu found three band series associated with $X[3/2]_c$ np configurations (*c*, *d* and *e* series) with the common ionization limit 75815 cm^{-1} [83]. Based on the analysis of band intensities in the absorption spectra, the author assigned two strong bands with the $X[3/2]_c$ $np\ \sigma_u 1_u$ (*c* series) and $X[3/2]_c$ $np\ \pi_u 0^+_u$ (*e* series) states, and one weak band corresponding to the perpendicular transition to the $X[3/2]_c$ $np\ \pi_u 1_u$ state with a wide range of n up to $n = 36$. Determined value of the common limit as an ionization energy of vibrationally unexcited $v_{\bar{X}} = 0$ ground state differ significantly from the last known value 75069.25 cm^{-1} measured by ZEKE-PFI spectroscopy [10]. Additionally, some series were assigned to $X[1/2]_c$ ion core with the ionization limit of $80895 \pm 50\ \text{cm}^{-1}$, while the best last known value is 80266 cm^{-1} [10]. It is not surprising that later substantial part of the bands was re-assigned, although the assignments at the lower energy range remained qualitatively.

First member of the series, $X[3/2]_c$ $6p$ cluster lie in the 56000–67000 cm^{-1} energy range (Fig. 3.13). With the exception of the origin ($v_{1_u} = 0$), the vibrational bands of transitions to the $6p\ \sigma_u 1_u$, $v_{1_u} = 1, 2, \dots, 5$ states are diffuse. Additionally, vibrational bands has separations of 200 cm^{-1} , less that about 240 cm^{-1} for regular $X[3/2]_c$ Rydberg states. From the fluorescence excitation spectra (Fig. 3.14) it was proposed, that this state is predissociated due to a crossing with a repulsive state [78] (see details in Sect. 4.2.2).

The spin-orbit partner, $X[1/2]_c$ $6p$ states, cluster lies $\sim 5000\ \text{cm}^{-1}$ above in the 61000–67000 cm^{-1} region. Spectroscopic analysis in this region is more difficult due to strong interactions between electronic states. It is believed that all five of the allowed $X[1/2]_c$ $6p$ states were identified. Highly irregular exhibition of the vibrational band systems, different behavior in the fluorescence excitation spectra, energy shifts of the bands indicates a different type of interactions [83]. Venkateswarlu [82] assigned some series of bands to the $X[1/2]_c$ $6p$ ion core

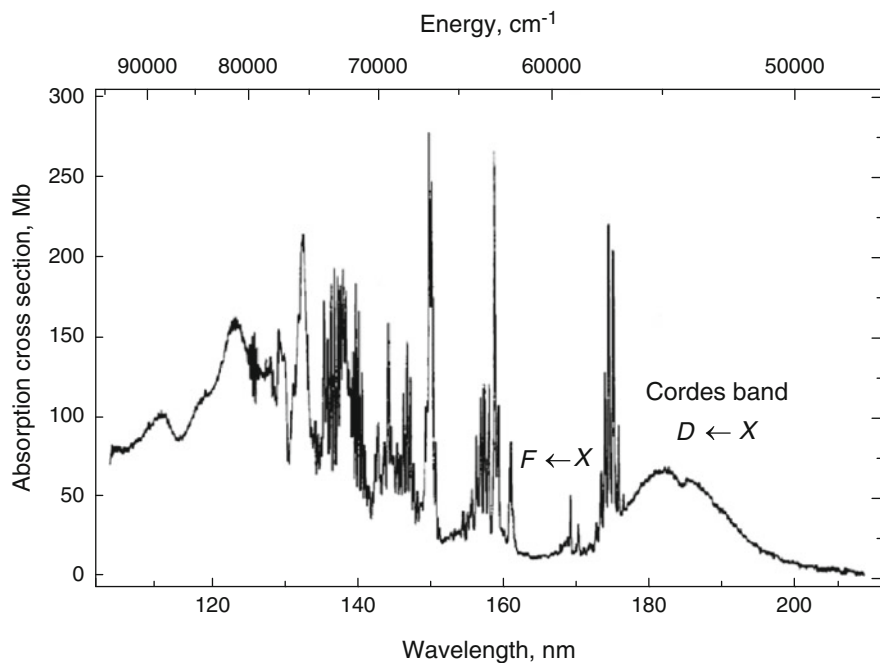


Fig. 3.13 Vacuum-ultraviolet absorption spectrum (0.2 nm resolution) [78]

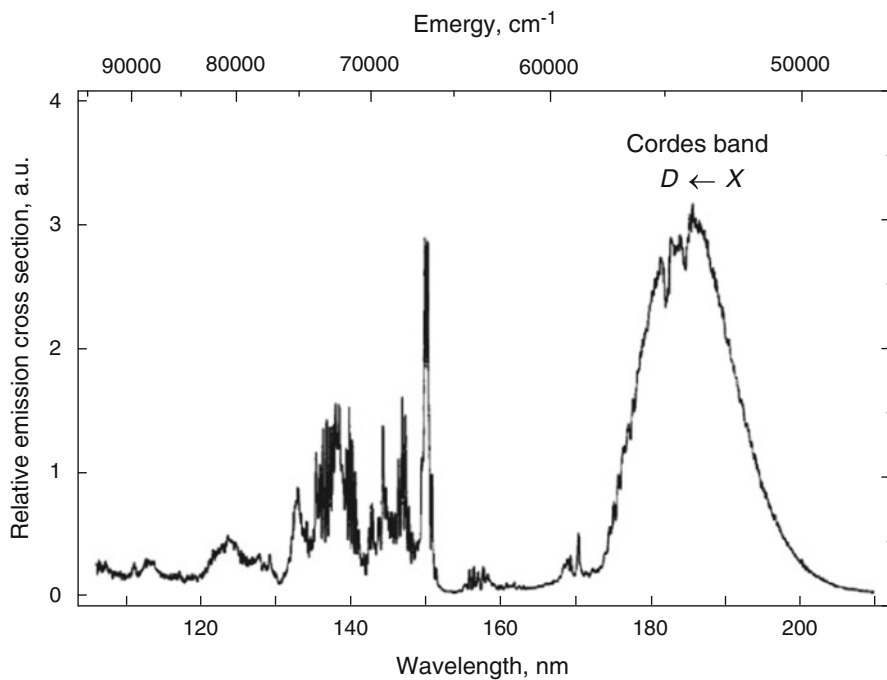


Fig. 3.14 Fluorescence (185–650 nm) excitation spectrum (0.2 nm resolution) [78]

(*f6, h6, i6, j6* series). The lowest $X[1/2]_c 6p\sigma_u 0_u^+$ state was determined with origin at 62700 cm^{-1} , however Ridley et al. reordered the bands of this $X[1/2]_c 6p$ cluster. The lowest state progressions were assigned to the two $X[1/2]_c 6p 1_u$ states from a comparison with the equivalent Br_2 spectrum with the origin at 61956 cm^{-1} and 61972 cm^{-1} .

In the same region, population of the ungerade 0_u^+ Rydberg state, $R0_u^+$, was observed with the origin at 61769 cm^{-1} in the two-step three-photon ($1 + 2$) experiments via the intermediate $B0_u^+$ state [94, 95]. It was suggested that this state can be attributed probably to the $X[1/2]_c 6p\sigma_u$ configuration [95]. Along with it, these bands were not observed in one-photon absorption experiments [82]. However, rotational analysis gave equilibrium distance of the $R0_u^+$ state $R_e = 2.63\text{ \AA}$, significantly larger than that of the $X[1/2] 6s 1_g$, and vertical one-photon transition from the ground state should occur. Observed data were explained by the homogeneous interaction with the $F0_u^+$ IP state in the range of vibrational levels of about $\nu_F = 200\text{--}250$ [96] (see Sect. 4.3.3 also).

The next $X[3/2]_c 7p$ cluster lies in the $66000\text{--}67000\text{ cm}^{-1}$ region. All the band progressions have been found being diffuse in the absorption spectra and very strong in the fluorescence excitation spectra [78, 83]. Additionally, the $X[3/2]_c 7p 0_g$ state has a smaller vibrational constant compared to typical for Rydberg states. It was believed that the strong interaction of the $X[3/2]_c 7p$ states with ion-pair states is responsible for these band behaviors. In this case, the $7p$ state is a doorway for the ion-pair states population with subsequent fluorescence in the $185\text{--}650\text{ nm}$ wavelength range [78].

Other $X[3/2]_c np$ ($n = 8\text{--}10$) and $X[1/2]_c np$ ($n = 7\text{--}8$) states have been found in the $69770\text{--}75500\text{ cm}^{-1}$ range. Frank-Condon analysis of the excitation spectra for both I^+ and I^- products formation was performed for $X[3/2]_c np$ states ($n = 9\text{--}11$) and an estimation of the $R_e = 2.60\text{ \AA}$ ($n = 9$), 2.58 \AA ($n = 10$) and 2.58 \AA ($n = 11$) was made [96].

3.4.4 The $[^2\Pi]_c$ nd Series

Gerade Rydberg states based on the $[^2\Pi]_c$ ion core and the *nd* outer electron were studied by the $(2 + 1)$ REMPI method [67, 90, 97, 98]. Only three of the I_2 Rydberg states with $\Omega = 2, 1$ and 0^+ in each $X[3/2]_c nd$ or $X[1/2]_c nd$ cluster are accessible by two-photon excitation, without spin-flip. Population of all the states with $5d$ configuration was found at band origins: 58580 cm^{-1} , 59695 , 60316 cm^{-1} for the $X[3/2]_c$ ion core and 64096 , 64708 and 65409 cm^{-1} for the $X[1/2]_c$ one [67]. Comparison of REMPI spectra recorded using LP and CP radiation was not shown any differences in relative band intensities unlike $7s$ and $9s$ states (see Sect. 3.4.1 and Fig. 3.15). Therefore it was impossible to determine Ω quantum number unambiguously. However, analysis of the rotational structure of one of the $5d$ states with origin at 59695 cm^{-1} (Fig. 3.15) allows describing the appropriate Rydberg state as 1_g . Two other $X[3/2]_c 5d$ states have 2_g or 0_g^+ symmetry.

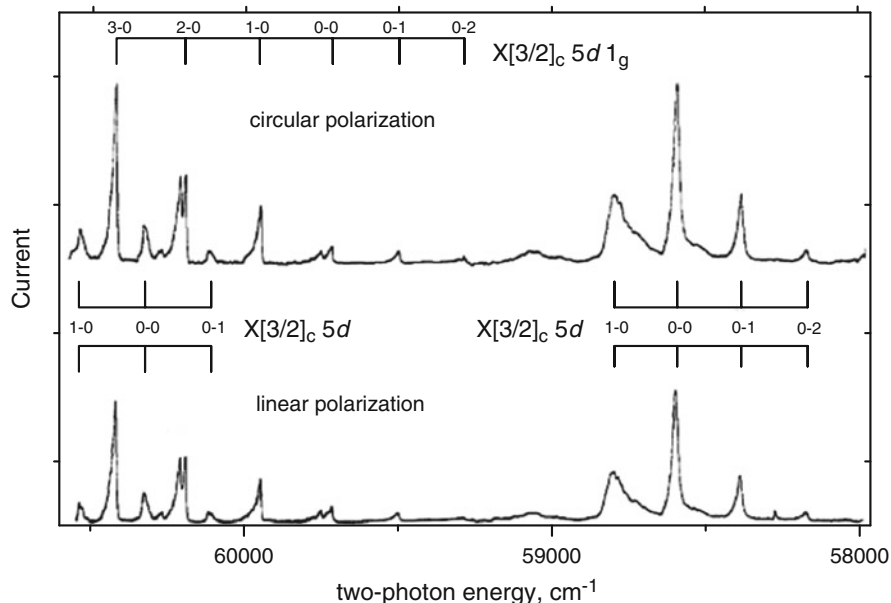


Fig. 3.15 The $(2 + 1)$ REMPI spectrum followed by linear (lower) and circular (upper) polarization light. $\lambda_{\text{ex}} = 330\text{--}345$ nm. Spectrum normalized to the square of the laser power [67]

Another difference from the ns states is a diffuse character of vibrational bands in the REMPI spectra (Fig. 3.15), that indicates strong interaction with repulsive or IP states. A number of $X[3/2]_c 5d$ states rotational structures were found to show weak perturbations, that is explained of the homogeneous interaction between Rydberg states or Rydberg-IP interaction [67, 98].

As it was mentioned above, the REMPI spectra have many vibrational overlapped progressions along with atomic lines in the $E > 70000$ cm^{-1} . Therefore, no high-lying nd states with $n > 5$ were assigned in the REMPI spectra [67]. However, the $X[1/2]_c 8s 0_g$ and 1_g states were reassigned as the $X[1/2]_c 6d 2_g$ and 0_g^+ ones respectively from comparison of similar REMPI spectra in Cl_2 , Br_2 and I_2 [83].

3.4.5 The $[^2\Pi]_c nf$ Series

Three band series (g , k and l) in the VUV absorption spectra were observed and assigned as $X[3/2]_c nf$ series with $n = 4\text{--}14$ range and similar quantum defect values $\delta \approx 0.8\text{--}1.0$ [79, 82]. However, f orbitals do not penetrate the core and quantum defect $\delta \approx 0$. They were re-assigned by using accurate IE values from [10] and quantum defect $\delta = 0.1\text{--}0.2$ [83]. It was found all the accessible four sub-states in the $X[3/2]_c nf$ cluster for $n = 4\text{--}7$.

Four vibrational progressions of the first nf series member $X[3/2]_c 4f$ assigned in the 67000–69000 range with $\omega_e \approx 220\text{--}270\text{ cm}^{-1}$. The vibrational progressions are essential unperturbed, that means no strong interactions with other electronic states. The $X[1/2]_c 4f$ (72647–74367 cm^{-1}) and $X[3/2]_c 5f$ (70300–71600 cm^{-1}) manifolds were observed also with wide unperturbed progressions. Assignments of higher Rydberg states are difficult due to high density of bands in the spectra, and only some bands of other Rydberg states at $E_b > 71955\text{ cm}^{-1}$ were showed.

3.4.6 Other Rydberg States

Two lowest excited ion states, $A[{}^2\Pi_{3/2, u}]$ and $a[{}^4\Sigma_u^-]$, have estimations of the energy as not exceeding $86367 \pm 2\text{ cm}^{-1}$ and $86022 \pm 2\text{ cm}^{-1}$ respectively [10]. Absolute vibrational numbering was not determined due to Franck-Condon restrictions for the low vibrational levels of these I_2^+ states.

Rydberg states based on these ion cores lie below and above the first ionization potential, and in the latter case, exhibited in the autoionization processes only. From the comparison with equivalent states in Br_2 made in [67] the $A[3/2]_c 6s$ ungerade states should be placed in the energy region around 58000 cm^{-1} . In spite of this fact, no bands in the one-photon absorption and REMPI spectra were found in this region [83]. Some bands were assigned to the the $A[3/2]_c 8s$ in the one-photon ionization spectra at 79365 cm^{-1} , near the I_2^+ (${}^2\Pi_{1/2}$) ionization threshold (80266 cm^{-1}) [96].

P. Venkateswarlu assigned some bands of the VUV absorption spectrum as transitions to such states [82], but his assignments were based on sufficiently different ionization energy. Some anomalies in the structure of threshold photoelectron spectra recorded with a synchrotron radiation photoionization [99] were also explained as an influence of Rydberg states converging to the $A[3/2]$ or higher ion I_2^+ states. Interaction of the high- n Rydberg states with the ion ground state at energy region below the $A[3/2]$ ionization threshold can result in autoionization. This additional channel of the electron formation gives perturbations in the vibrational structure of the spectra. It should be noted that the equilibrium interatomic distances of the excited ion states are estimated to be large (3.0–3.5 Å). Due to weak interaction between ion core and outer electron, Rydberg states should have similar R_e values that are large compared to 2.66 Å for $I_2(X)$, and they lie outside the Frank-Condon range. Direct transitions to these states from the ground I_2 state should be very weak.

Ion-pair states have equilibrium distances close to those of these Rydberg states and can be used as intermediate states for excited ion core Rydberg state population. Three-color optical triple resonance excitation scheme was performed for ungerade Rydberg states population [100, 101]. The $a[{}^4\Sigma_{u,1/2}^-] 6s 0_u^+$ Rydberg state was found to be deeply bound ($D_e \sim 7000\text{ cm}^{-1}$) [100]. A wide vibrational progression of this state were identified in the $v = 0\text{--}63$ range (Fig. 3.16). Another $[{}^4\Sigma_{u,1/2}^+] 6s 0_u^+$

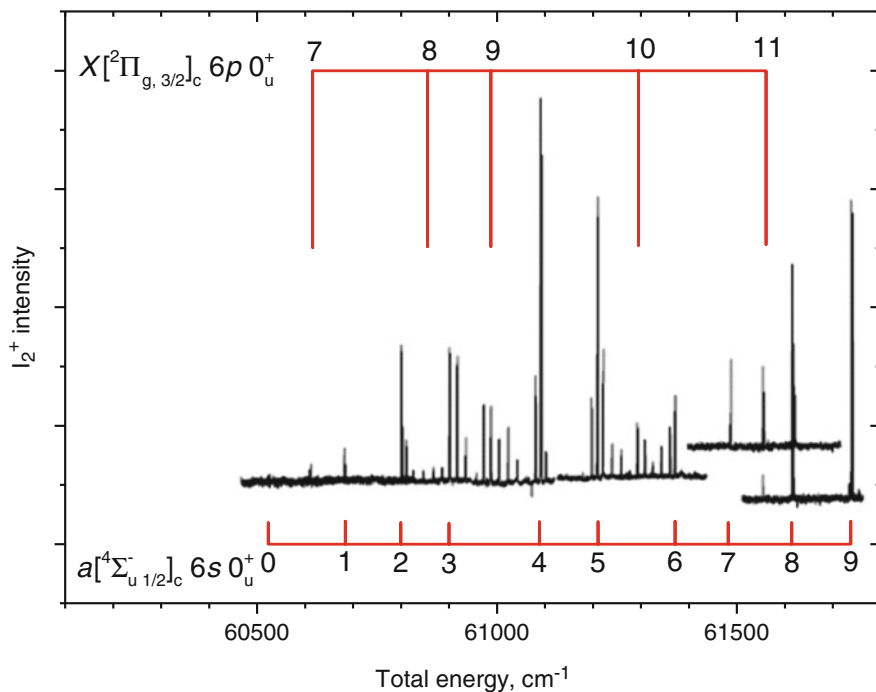


Fig. 3.16 The Optical Triple Resonance together with resonance ionization spectrum of I_2 at the excitation pathway via the $E, \nu_E = 41, J = 25$ IP state [101]

state are shallow-bound and has longer equilibrium distance $R = 4.500(2) \text{ \AA}$ [101]. Three-photon excitation of Rydberg states based on the $A[3/2]_c$ ion core were unobserved.

References

1. Mulliken, R.S.: Iodine revisited. *J. Chem. Phys.* **55**, 288–309 (1971). <https://doi.org/10.1063/1.1675521>
2. de Jong, W.A., Visscher, L., Nieuwpoort, W.C.: Relativistic and correlated calculations on the ground, excited, and ionized states of iodine. *J. Chem. Phys.* **107**, 9046–9058 (1997). <https://doi.org/10.1063/1.475194>
3. Huber, K.P., Herzberg, G.: *Molecular Spectra and Molecular Structure*. Springer, Boston (1979)
4. Tellinghuisen, J.: Resolution of the visible-infrared absorption spectrum of I_2 into three contributing transitions. *J. Chem. Phys.* **58**, 2821–2834 (1973). <https://doi.org/10.1063/1.1679584>

5. Tellinghuisen, J.: Transition strengths in the visible–infrared absorption spectrum of I_2 . *J. Chem. Phys.* **76**, 4736–4744 (1982). <https://doi.org/10.1063/1.442791>
6. Li, J., Balasubramanian, K.: Spectroscopic properties and potential energy curves of I_2 and I_2^+ . *J. Mol. Spectrosc.* **138**, 162–180 (1989). [https://doi.org/10.1016/0022-2852\(89\)90108-2](https://doi.org/10.1016/0022-2852(89)90108-2)
7. Jewsbury, P., Lawley, K.P.: A model for the relative intensities among ion pair \rightarrow valence transitions in the heavier halogens and rare gas halides. *Chem. Phys.* **141**, 225–239 (1990). [https://doi.org/10.1016/0301-0104\(90\)87058-J](https://doi.org/10.1016/0301-0104(90)87058-J)
8. Landau, L.D., Lifshitz, E.M.: *Quantum Mechanics* (3rd Edn, Revised and Enlarged). Pergamon, Oxford (1977)
9. Lawley, K.P.: Dispersion and polarization forces associated with the ion-pair states of diatomic molecules. *Chem. Phys.* **127**, 363–371 (1988). [https://doi.org/10.1016/0301-0104\(88\)87134-9](https://doi.org/10.1016/0301-0104(88)87134-9)
10. Cockett, M.C.R., Donovan, R.J., Lawley, K.P.: Zero kinetic energy pulsed field ionization (ZEKE-PFI) spectroscopy of electronically and vibrationally excited states of I_2^+ : The $A^2\Pi_{3/2,u}$ state and a new electronic state, the $a^4\Sigma^-_u$ state. *J. Chem. Phys.* **105**, 3347–3360 (1996). <https://doi.org/10.1063/1.472535>
11. Gerstenkorn, S., Luc, P., Vergès, J.: Atlas du spectre d'absorption de la molécule d'iode, Vol. O. 7220–11,200 cm^{-1} . Laboratoire Aime' Cotton, CNRS II, Orsay (1993)
12. Gerstenkorn, S., Vergès, J., Chevillard, J.: Atlas du spectre d'absorption de la molécule d'iode (11000–14,000 cm^{-1}). Edition CNRS II, Orsay (1982)
13. Appadoo, D.R.T., Le Roy, R.J., Bernath, P.F., Gerstenkorn, S., Luc, P., Vergès, J., Sinzelle, J., Chevillard, J., D'Aignaux, Y., Vergès, J., Sinzelle, J., Chevillard, J., D'Aignaux, Y.: Comprehensive analysis of the A–X spectrum of I_2 : an application of near-dissociation theory. *J. Chem. Phys.* **104**, 903–913 (1996). <https://doi.org/10.1063/1.470814>
14. Beeken, P.B., Hanson, E.A., Flynn, G.W.: Photochemical and photophysical dynamics of I_2 isolated in a rare gas cage. *J. Chem. Phys.* **78**, 5892–5899 (1983). <https://doi.org/10.1063/1.444609>
15. Tellinghuisen, J., Phillips, L.F.: Kinetics of iodine following photolysis at 1930 Å: temperature dependence of A-state quenching. *J. Phys. Chem.* **90**, 5108–5120 (1986). <https://doi.org/10.1021/j100412a046>
16. Tellinghuisen, J.: Least-squares analysis of overlapped bound-free absorption spectra and predissociation data in diatomics: The $C(^1\Pi_u)$ state of I_2 . *J. Chem. Phys.* **135**(54), 301–311 (2011). <https://doi.org/10.1063/1.3616039>
17. Tellinghuisen, J.: Intensity analysis of overlapped discrete and continuous absorption by spectral simulation: The electronic transition moment for the B–X system in I_2 . *J. Chem. Phys.* **134**(84), 301–308 (2011). <https://doi.org/10.1063/1.3555623>
18. Gerstenkorn, S., Luc, P.: Atlas du spectre d'absorption de la molécule d'iode (15600–20,000 cm^{-1}). Editions CNRS, Paris (1977)
19. Gerstenkorn, S., Luc, P.: Atlas du spectre d'absorption de la molécule d'iode (14000–15,600 cm^{-1}). CNRS II, Orsay (1980)
20. Salami, H., Ross, A.J.: A molecular iodine atlas in ascii format. *J. Mol. Spectrosc.* **233**, 157–159 (2005). <https://doi.org/10.1016/j.jms.2005.06.002>
21. Gerstenkorn, S., Luc, P.: Description of the absorption spectrum of iodine recorded by means of Fourier Transform Spectroscopy: the (B–X) system. *J. Phys.* **46**, 867–881 (1985). <https://doi.org/10.1051/jphys:01985004606086700>
22. Martin, F., Bacis, R., Churassy, S., Vergès, J.: Laser-induced-fluorescence Fourier transform spectrometry of the $X0_g^+$ state of I_2 : extensive analysis of the $B0_u^+ \rightarrow X0_g^+$ fluorescence spectrum of $^{127}I_2$. *J. Mol. Spectrosc.* **116**, 71–100 (1986). [https://doi.org/10.1016/0022-2852\(86\)90254-7](https://doi.org/10.1016/0022-2852(86)90254-7)
23. Barrow, R.F., Yee, K.K.: $B0_u^+ - X0_g^+$ system of $^{127}I_2$: rotational analysis and long-range potential in the $B0_u^+$ state. *J. Chem. Soc. Faraday Trans.* **2**(69), 684–700 (1973). <https://doi.org/10.1039/F29736900684>

24. Levenson, M.D.M., Schawlow, A.L.: Hyperfine interactions in molecular iodine. *Phys. Rev. A*, **6**, 10–20 (1972). <https://doi.org/10.1103/PhysRevA.6.10>
25. Okabe, H.: *Photochemistry of Small Molecules*. Wiley, New York (1978)
26. Privilov, A.M.: *Radiometry in Modern Scientific Experiments*. Springer, Vienna/New York (2011)
27. Kobayashi, T., Akamatsu, D., Hosaka, K., Inaba, H., Okubo, S., Tanabe, T., Yasuda, M., Onae, A., Hong, F.-L.: Absolute frequency measurements and hyperfine structures of the molecular iodine transitions at 578 nm. *J. Opt. Soc. Am. B*, **33**, 725–734 (2016). <https://doi.org/10.1364/JOSAB.33.000725>
28. Vigué, J., Broyer, M., Lehmann, J.C.: Natural hyperfine and magnetic predissociation of the I₂ B state III. — Experiments on magnetic predissociation. *J. Phys.* **42**, 961–978 (1981). <https://doi.org/10.1051/jphys:01981004207096100>
29. Tamres, M., Duerksen, W.K., Goodenow, J.M.: Vapor-phase charge-transfer complexes. II. 2I₂ ↔ I₄ system. *J. Phys. Chem.* **72**, 966–970 (1968). <https://doi.org/10.1021/j100849a030>
30. Clear, R.D., Wilson, K.R.: Assignment of continuous spectra by photofragment spectroscopy: C state of I₂. *J. Mol. Spectrosc.* **47**, 39–44 (1973). [https://doi.org/10.1016/0022-2852\(73\)90074-X](https://doi.org/10.1016/0022-2852(73)90074-X)
31. Teichteil, C., Pelissier, M., et al.: *Chem. Phys.* **180**, 1–18 (1994). [https://doi.org/10.1016/0301-0104\(93\)E0395-C](https://doi.org/10.1016/0301-0104(93)E0395-C)
32. Baturo, V.V., Cherepanov, I.N., Lukashov, S.S., Poretsky, S.A., Privilov, A.M.: Spectroscopic constants and potential energy curves of some iodine valence ungerade weakly bound states. *J. Phys. B At. Mol. Opt. Phys.* **48**, 055101. (8 pp) (2015). <https://doi.org/10.1088/0953-4075/48/5/055101>
33. Churassy, S., Martin, F., Bacis, R., Vergès, J., Field, R.W.: Rotation–vibration analysis of the B_{0_u⁺} → a1_g and B_{0_u⁺} → a'0_g⁺ electronic systems of I₂ by laser-induced-fluorescence Fourier-transform spectroscopy. *J. Chem. Phys.* **75**, 4863–4868 (1981). <https://doi.org/10.1063/1.441923>
34. Martin, F., Churassy, S., Bacis, R., Field, R.W., Vergès, J., Vergès, J.: Long range behavior of the gerade states near the ²P_{3/2} + ²P_{3/2} iodine dissociation limit by laser-induced-fluorescence Fourier-transform spectroscopy. *J. Chem. Phys.* **79**, 3725–3737 (1983). <https://doi.org/10.1063/1.446293>
35. Akopyan, M.E., Baturo, V.V., Lukashov, S.S., Mikheev, L.D., Poretsky, S.A., Privilov, A.M., Vasyutinskii, O.S.: Hyperfine interaction in molecular iodine between the 0_g⁺, 1_u and – states correlating with the I(²P_{1/2}) + I(²P_{1/2}) dissociation limit. *J. Phys. B At. Mol. Opt. Phys.* **48**, 25102. (14 pp) (2015). <https://doi.org/10.1088/0953-4075/48/2/025102>
36. Akopyan, M.E., Baturo, V.V., Lukashov, S.S., Poretsky, S.A., Privilov, A.M., Teschmit, N.: Cross-sections of bound-free (0_g⁺, 1_g (aa, ab) $\xleftarrow{h\nu_f}$ B_{0_u⁺}, v_B = 18–21) and bound-bound I₂(0_g⁺, 1_u(bb) $\xleftarrow{h\nu_f}$ B_{0_u⁺}, v_B = 21, J_B). *J. Phys. B At. Mol. Opt. Phys.* **47**, 055101. (9 pp) (2014). <https://doi.org/10.1088/0953-4075/47/5/055101>
37. Mulliken, R.S.: The halogen molecules and their spectra. J–J-like coupling. Molecular ionization potentials. *Phys. Rev.* **46**, 549–571 (1934). <https://doi.org/10.1103/PhysRev.46.549>
38. Watanabe, K.: Ionization potentials of some molecules. *J. Chem. Phys.* **26**, 542–547 (1957). <https://doi.org/10.1063/1.1743340>
39. Myer, J.A., Samson, J.A.R.: Absorption cross section and photoionization yield of I₂ between 1050 and 2200 Å. *J. Chem. Phys.* **52**, 716–718 (1970). <https://doi.org/10.1063/1.1673044>
40. Akopyan, M.E., Vilesov, F.I., Sergeev, Y.L.: Photoionization of molecular iodine. *Opt. Spectrosc.* (USSR, Eng.transl.) **35**, 472–477 (1973)
41. Road, W.M., Lawley, K., Jewsbury, P., Ridley, T., Langridge-Smith, P., Donovan, R.: Einstein A-coefficients and transition dipole moments for some ion-pair to valence transitions in I₂. *Mol. Phys.* **75**, 811–828 (1992). <https://doi.org/10.1080/00268979200100621>

42. Bartels, M., Donovan, R.J., Holmes, A.J., Langridge-Smith, P.R.R., MacDonald, M.A., Ridley, T.: Tunable vacuum ultraviolet laser spectroscopy of the $D0_u^+$ ion-pair state of jet-cooled I_2 . *J. Chem. Phys.* **91**, 7355–7360 (1989). <https://doi.org/10.1063/1.457258>
43. Hoy, A.R., Lipson, R.H.: Reinvestigation of the Cordes band system of I_2 using a vacuum ultraviolet laser. *Chem. Phys.* **140**, 187–193 (1990)
44. Ishiwata, T., Tanaka, I.: A Spectroscopic study of the $D0_u^+$ ion-pair state of I_2 by optical-optical double resonance. *Laser Chem.* **7**, 79–93 (1987). <https://doi.org/10.1155/LC.7.79>
45. Akopyan, M.E., Baturo, V.V., Lukashov, S.S., Poretsky, S.A., Pravilov, A.M.: Dipole moment functions of the iodine $D'2_g-A'2_u$, $D0_u^+ - a'0_g^+$, $D0_u^+ - X0_g^+$ and $E0_g^+ - B0_u^+$ transitions. *J. Phys. B At. Mol. Opt. Phys.* **44**, 205101. (9 pp) (2011). <https://doi.org/10.1088/0953-4075/44/20/205101>
46. Nowlin, M.L., Heaven, M.C.: Improved spectroscopic constants for $I_2 D^1\Sigma_u^+$. *Chem. Phys. Lett.* **239**, 1–5 (1995)
47. Tellinghuisen, J.: The D state of I_2 : A case study of statistical error propagation in the computation of RKR potential curves, spectroscopic constants, and Frank-Condon factors. *J. Mol. Spectrosc.* **217**, 212–221 (2003). [https://doi.org/10.1016/S0022-2852\(02\)00055-3](https://doi.org/10.1016/S0022-2852(02)00055-3)
48. Kalemou, A., Valdes, A., Prosimiti, R.: An ab Initio Study of the $E^3\Pi_g$ State of the Iodine Molecule. *J. Phys. Chem. A.* **116**, 2366–2370 (2012). <https://doi.org/10.1021/jp3000202>
49. Wilson, P.J., Ridley, T., Lawley, K.P., Donovan, R.J.: Double resonance ionisation nozzle cooled spectroscopy (DRINCS) of the $E(^3P_2)$, $f(^3P_0)$ and $f(^1D_2)0_g^+$ ion-pair states of I_2 . *Chem. Phys.* **182**, 325–339 (1994). [https://doi.org/10.1016/0301-0104\(94\)00047-6](https://doi.org/10.1016/0301-0104(94)00047-6)
50. Inard, D., Cerny, D., Nota, M., Bacis, R., Churassy, S., Skorokhodov, V.: $E0_g^+ \rightarrow A1_u$ and $E0_g^+ \rightarrow B'1_u$ laser-induced fluorescence in molecular iodine recorded by Fourier-transform spectroscopy. *Chem. Phys.* **243**, 305–321 (1999). [https://doi.org/10.1016/S0301-0104\(99\)00077-4](https://doi.org/10.1016/S0301-0104(99)00077-4)
51. Brand, J.C.D., Hoy, A.R.: Multiphoton Spectra and States of Halogens. *Appl. Spectrosc. Rev.* **23**, 285–328 (1987). <https://doi.org/10.1080/05704928708060449>
52. Brand, J.C.D., Hoy, A.R., Kalkar, A.K., Yamashita, A.B.: The E-B band system of diatomic iodine. *J. Mol. Spectrosc.* **95**, 350–358 (1982). [https://doi.org/10.1016/0022-2852\(82\)90134-5](https://doi.org/10.1016/0022-2852(82)90134-5)
53. Perrot, J.P., Broyer, M., Chevalyere, J., Femelat, B.: Extensive study of the $1_g(^3P_2)$ ion pair state of I_2 . *J. Mol. Spectrosc.* **98**, 161–167 (1983). [https://doi.org/10.1016/0022-2852\(83\)90211-4](https://doi.org/10.1016/0022-2852(83)90211-4)
54. Perrot, J.P.P., Femelat, B., Broyer, M., Chevalyere, J.: Ω -doubling in 1_g state and electronic transition moments for $B0_u^+$ towards 0_g^+ and $1_g(^3P_2)$ states of iodine. *Mol. Phys.* **61**, 97–108 (1987). <https://doi.org/10.1080/00268978700101011>
55. Perrot, J.P., Femelat, B., Subtil, J.L., Broyer, M., Chevalyere, J.: Electronic transitions moments from both fluorescence intensities and lifetime measurements for transitions involving the I_2 ionic states. *Mol. Phys.* **61**, 85–95 (1987). <https://doi.org/10.1080/00268978700101001>
56. Zheng, X., Fei, S., Heaven, M.C., Tellinghuisen, J.: Observation and analysis of the $\beta \leftarrow A$ transition of I_2 in a free-jet expansion. *J. Mol. Spectrosc.* **149**, 399–411 (1991). [https://doi.org/10.1016/0022-2852\(91\)90295-L](https://doi.org/10.1016/0022-2852(91)90295-L)
57. Ishiwata, T., Motohiro, S., Kagi, E., Fujiwara, H., Fukushima, M.: Optical-optical double-resonance spectroscopy of the $1_u(^3P_2)$ and $2_u(^3P_2)$ states of I_2 through the $A^3\Pi(1_u)$ state. *Bull. Chem. Soc. Jpn.* **73**, 2255–2261 (2000). <https://doi.org/10.1246/bcsj.73.2255>
58. King, G.W., Littlewood, I.M., Robins, J.R.: Two-photon sequential absorption spectroscopy of iodine-127 and 129 in the 5 eV region. *Chem. Phys.* **56**, 145–156 (1981)
59. Jewsbury, P.J., Ridley, T., Lawley, K.P., Donovan, R.J.: Parity mixing in the valence states of I_2 probed by optical-optical double-resonance excitation of ion-pair. *J. Mol. Spectrosc.* **157**, 33–49 (1993). <https://doi.org/10.1006/jmsp.1993.1003>

60. Ishiwata, T., Yotsumoto, T., Motohiro, S.: Optical–optical double resonance spectroscopy of I_2 through the parity mixed valence states. *Bull. Chem. Soc. Jpn.* **74**, 1605–1610 (2001). <https://doi.org/10.1246/bcsj.74.1605>
61. Tellinghuisen, J.: The $D' \rightarrow A'$ transition in I_2 . *J. Mol. Spectrosc.* **94**, 231–252 (1982). [https://doi.org/10.1016/0022-2852\(82\)90002-9](https://doi.org/10.1016/0022-2852(82)90002-9)
62. Zheng, X., Fei, S., Heaven, M.C., Tellinghuisen, J.: Spectroscopy of metastable species in a free-jet expansion: The $D' \leftarrow A'$ transition of I_2 . *J. Chem. Phys.* **96**, 4877–4883 (1992). <https://doi.org/10.1063/1.462895>
63. Hoy, A.R., Brand, J.C.D.: The $F0_u^+$ state of diatomic iodine: effects of configuration interaction. *Chem. Phys.* **109**, 109–115 (1986). [https://doi.org/10.1016/0301-0104\(86\)80189-6](https://doi.org/10.1016/0301-0104(86)80189-6)
64. Ishiwata, T., Kusayanagi, T., Hara, T., Tanaka, I.: An analysis of the $F(0_u^+)$ ion-pair state of I_2 by optical-optical double resonance. *J. Mol. Spectrosc.* **119**, 337–351 (1986). [https://doi.org/10.1016/0022-2852\(86\)90029-9](https://doi.org/10.1016/0022-2852(86)90029-9)
65. Ishiwata, T., Tokunaga, A., Shinzawa, T., Tanaka, I.: An analysis of the $F'0_u^+$ ion-pair state of I_2 by optical-optical double resonance. *J. Mol. Spectrosc.* **117**, 89–101 (1986). [https://doi.org/10.1016/0022-2852\(86\)90094-9](https://doi.org/10.1016/0022-2852(86)90094-9)
66. Ishiwata, T., Yamada, J., Obi, K.: Optical-optical double-resonance spectroscopy of the $I_20_g^+(\ ^1D)$ ion-pair state. *J. Mol. Spectrosc.* **158**, 237–245 (1993). <https://doi.org/10.1006/jmsp.1993.1068>
67. Donovan, R.J., Flood, R.V., Lawley, K.P., Yench, A.J., Ridley, T.: The resonance enhanced $(2 + 1)$ multiphoton ionization spectrum of I_2 . *Chem. Phys.* **164**, 439–450 (1992)
68. Kagi, E., Yamamoto, N., Fujiwara, H., Fukushima, M., Ishiwata, T.: Optical–Optical Double Resonance Spectroscopy of the $I_g(^3P_1)$ - $A^3\Pi(1_u)$ - $X^1\Sigma_g^+$ Transition of I_2 . *J. Mol. Spectrosc.* **216**, 48–51 (2002). <https://doi.org/10.1006/jmsp.2002.8676>
69. Ishiwata, T., Takekawa, H., Obi, K.: Optical-optical double-resonance spectroscopy of the $I_2 I_g(^1D)$ ion-pair state. *J. Mol. Spectrosc.* **159**, 443–457 (1993). <https://doi.org/10.1006/jmsp.1993.1141>
70. Baturo, V.V., Cherepanov, I.N., Lukashov, S.S., Poretsky, S.A., Pravilov, A.M., Zhironkin, A.I.: Heterogeneous and hyperfine interactions between valence states of molecular iodine correlating with the $I(^2P_{1/2}) + I(^2P_{1/2})$ dissociation limit. *J. Chem. Phys.* **144**(184), 309–308 (2016). <https://doi.org/10.1063/1.4948630>
71. Motohiro, S., Nakajima, S., Ishiwata, T.: Perturbation-facilitated optical-optical double resonance spectroscopy of the $h0_u^- (^3P_1)$ and $H1_u(^3P_1)$ ion-pair states of I_2 . *J. Chem. Phys.* **117**, 187–196 (2002). <https://doi.org/10.1063/1.1481391>
72. Motohiro, S., Umakoshi, A., Ishiwata, T.: Perturbation-facilitated optical–optical double-resonance spectroscopy of the $1_u(^1D)$ and $2_u(^1D)$ ion-pair states of I_2 through the parity mixing intermediate state. *J. Mol. Spectrosc.* **208**, 213–218 (2001). <https://doi.org/10.1006/jmsp.2001.8379>
73. Motohiro, S., Ishiwata, T.: Optical–optical double resonance spectroscopy of the $H1_u(^3P_1)$ - $A^3\Pi_u-X^1\Sigma_g^+$ Transition of I_2 . *J. Mol. Spectrosc.* **204**, 286–290 (2000). <https://doi.org/10.1006/jmsp.2000.8229>
74. Motohiro, S., Nakajima, S., Aoyama, K., Kagi, E., Fujiwara, H., Fukushima, M., Ishiwata, T.: Analysis of the $0_g^- (^3P_1) - B'^3 \prod (0_u^-)$ system of I_2 by perturbation-facilitated optical–optical double resonance. *J. Chem. Phys.* **117**, 9777–9784 (2002). <https://doi.org/10.1063/1.1516790>
75. Nakano, Y., Ukeguchi, H., Ishiwata, T.: Observation and analysis of the $2_g(^1D)$ ion-pair state of I_2 : The g/u mixing between the $1_u(^1D)$ and $2_g(^1D)$ states. *J. Chem. Phys.* **121**, 1397–1404 (2004). <https://doi.org/10.1063/1.1756134>
76. Lawley, K.P., Ridley, T., Min, Z., Wilson, P.J., AlKahali, M.S.N., Donovan, R.J.: Vibronic coupling between Rydberg and ion-pair states of I_2 investigated by $(2 + 1)$ resonance enhanced multiphoton ionization spectroscopy. *Chem. Phys.* **197**, 37–50 (1995)

77. Donovan, R.J., Lawley, K.P., Ridley, T.: Heavy Rydberg behaviour in high vibrational levels of some ion-pair states of the halogens and inter-halogens. *J. Chem. Phys.* **142**, 1–10 (2015). <https://doi.org/10.1063/1.4921560>
78. Hiraya, A., Shobatake, K., Donovan, R.J., Hopkirk, A.: Vacuum ultraviolet fluorescence excitation spectrum of I₂. *J. Chem. Phys.* **88**, 52 (1988). <https://doi.org/10.1063/1.454485>
79. Lukashov, S.S., Poretsky, S.A., Pravilov, A.M., Khadikova, E.I., Shevchenko, E.V.: Optical population of iodine molecule ion-pair states via MI₂ vdW complexes, M = I₂, Xe, of valence states correlating with the third, I(²P_{1/2}) + I(²P_{1/2}) dissociation limit. *Opt. Spectrosc. (English Transl. Opt. i Spektrosk.)* **109**, 493–501 (2010). <https://doi.org/10.1134/S0030400X10100036>
80. Holmes, A.J., Lawley, K.P., Ridley, T., Donovan, R.J., Patrick, R.R.: Optical-Optical Double Resonance (OODR) studies of the Halogen ion-pair states. *J. Chem. Soc. Faraday Trans.* **87**, 15–18 (1991). <https://doi.org/10.1039/FT9918700015>
81. Akopyan, M.E., Bibinov, N.K., Kokh, D.B., Pravilov, A.M., Stepanov, M.B.: The iodine E 0_g⁺ – B0_u⁺ and D0_u⁺ – X0_g⁺ transition dipole moment functions. *Chem. Phys.* **242**, 253–261 (1999). [https://doi.org/10.1016/S0301-0104\(99\)00002-6](https://doi.org/10.1016/S0301-0104(99)00002-6)
82. Venkateswarlu, P.: Vacuum ultraviolet spectrum of the iodine molecule. *Can. J. Phys.* **48**, 1055–1080 (1970)
83. Ridley, T., Beattie, D.a., Cockett, M.C.R., Lawley, K.P., Donovan, R.J.: A re-analysis of the vacuum ultraviolet absorption spectrum of I₂, Br₂, and ICl using ionization energies determined from their ZEKE-PFI photoelectron spectra. *Phys. Chem. Chem. Phys.* **4**, 1398–1411 (2002). <https://doi.org/10.1039/b109555m>
84. Venkateswarlu, P.: Emission bands of halogens. *Proc. Indian Acad. Sci.* **25**, 119–132 (1947)
85. Petty, G., Tai, C., Dalby, F.W.: Nonlinear resonant photoionization in molecular iodine. *Phys. Rev. Lett.* **34**, 1207–1209 (1975). <https://doi.org/10.1103/PhysRevLett.34.1207>
86. Dalby, F.W., Petty-Sil, G., Pryce, M.H.L., Tai, C.: Nonlinear resonant photoionization spectra of molecular iodine. *Can. J. Phys.* **55**, 1033–1046 (1977). <https://doi.org/10.1139/p77-139>
87. Lehmann, K.K., Smolarek, J., Goodman, L.: Multiphoton resonance ionization bands in I₂. *J. Chem. Phys.* **69**, 1569 (1978). <https://doi.org/10.1063/1.436729>
88. Bray, R.G., Hochstrasser, R.M.: Two-photon absorption by rotating diatomic molecules. *Mol. Phys.* **31**, 1199–1211 (1976). <https://doi.org/10.1080/00268977600100931>
89. Miller, J.C.: Multiphoton ionization of jet-cooled iodine. *J. Phys. Chem.* **91**, 2589–2592 (1987). <https://doi.org/10.1021/j100294a028>
90. Wu, M., Johnson, P.M.: High lying gerade Rydberg states of molecular iodine. *J. Chem. Phys.* **90**, 74–80 (1989). <https://doi.org/10.1063/1.456469>
91. Bucksbaum, P.H., Bashkansky, M., Freeman, R.R., McIlrath, T.J., DiMauro, L.F.: Suppression of multiphoton ionization with circularly polarized coherent light. *Phys. Rev. Lett.* **56**, 2590–2593 (1986). <https://doi.org/10.1103/PhysRevLett.56.2590>
92. Huasheng, W., Ásgeirsson, J., Kvaran, Á., Donovan, R.J., Flood, R.V., Lawley, K.P., Ridley, T., Yencha, A.J.: Rotationally resolved (2 + 1) REMPI spectra of gerade Rydberg state of molecular iodine: The (v' = 0, v'' = 1) band of the Dalby system. *J. Mol. Struct.* **293**, 217–221 (1993). [https://doi.org/10.1016/0022-2860\(93\)80053-X](https://doi.org/10.1016/0022-2860(93)80053-X)
93. Kvaran, Á., Wang, H., Ásgeirsson, J.: The Dalby system of iodine revisited: rotationally resolved (2 + 1) REMPI spectra of the rydberg state [2P_{1/2}]c6s; 1 g of I₂. *J. Mol. Spectrosc.* **163**, 541–558 (1994). <https://doi.org/10.1006/jmsp.1994.1046>
94. Williamson, A.D., Compton, R.N.: Sequentzal multiphoton ionizatxon spectroscopy: extension of a useful spectroscopic tool. *Chem. Phys. Lett.* **62**, 295–299 (1979). [https://doi.org/10.1016/0009-2614\(79\)80181-5](https://doi.org/10.1016/0009-2614(79)80181-5)
95. Hoy, A.R., Jaywant, S.M., Brand, J.C.D.: A rotationally-resolved Rydberg transition of I₂. *Mol. Phys.* **60**, 749–759 (1987). <https://doi.org/10.1080/00268978700100511>

96. Kvaran, A., Yench, A.J., Kela, D.K., Donovan, R.J., Hopkirk, A.: Vibrationally resolved excitation functions for direct ion-pair ($I^+ + I^-$) formation from photodissociation of I_2 . *Chem. Phys. Lett.* **179**, 263–267 (1991). [https://doi.org/10.1016/0009-2614\(91\)87035-A](https://doi.org/10.1016/0009-2614(91)87035-A)
97. Kvaran, Á., Wang, H., Jóhannesson, G.H., Yench, A.J.: REMPI spectra of I_2 . The [$^2\Pi_{3/2}$],5d; I_g Rydberg state and interactions with ion pair states. *Chem. Phys. Lett.* **222**, 436–442 (1994). [https://doi.org/10.1016/0009-2614\(94\)00387-4](https://doi.org/10.1016/0009-2614(94)00387-4)
98. Kvaran, Á., Jóhannesson, G.H., Wang, H.: Rotational perturbations in the (2 + 1) REMPI spectrum of the Rydberg state. *Chem. Phys.* **204**, 65–75 (1996). [https://doi.org/10.1016/0301-0104\(95\)00389-4](https://doi.org/10.1016/0301-0104(95)00389-4)
99. Yench, A.J., Cockett, M.C.R., Goode, J.G., Donovan, R.J., Hopkirk, A., King, G.C.: Threshold photoelectron spectroscopy of I_2 . *Chem. Phys. Lett.* **229**, 347–352 (1994). [https://doi.org/10.1016/0009-2614\(94\)01060-9](https://doi.org/10.1016/0009-2614(94)01060-9)
100. Sjödin, A.M., Ridley, T., Lawley, K.P., Donovan, R.J.: Observation of a substantially-bound excited-core Rydberg state in I_2 by optical triple resonance. *Chem. Phys. Lett.* **416**, 64–69 (2005). <https://doi.org/10.1016/j.cplett.2005.09.029>
101. Sjödin, A.M., Ridley, T., Lawley, K.P., Donovan, R.J.: Observation of a new high-energy, shallow-bound Rydberg state in I_2 by optical triple resonance. *Chem. Phys. Lett.* **412**, 110–115 (2005). <https://doi.org/10.1016/j.cplett.2005.06.095>

Chapter 4

Intramolecular Perturbations in the Electronically Excited States

4.1 Theoretical Background

There are two types of intramolecular perturbations, hyperfine interaction and nonadiabatic heterogeneous (Coriolis) interaction which can couple electronic states of different symmetries. They are considered below in this section.

Symmetry of Homonuclear Diatomic Molecule Wavefunction Let us consider symmetry properties of the wavefunction of a diatomic molecule at the space inversion operation. Let X, Y, Z be a laboratory frame and x, y, z be a molecular body frame. The Euler angles α and β are defined so that the z axis coincides with the molecular axis and the third angle $\gamma = 0$. In the adiabatic approximation, the molecular wavefunction is the product of electronic $\psi_{n\Omega}^{\omega\sigma}$, vibrational χ_ν rotational $\Theta_{M,\Omega}^J$ and nuclear $U_{M_I}^I$ wavefunctions:

$$\Psi_{n\Omega\omega\sigma\nu JMIM_I} = \psi_{n\Omega}^{\omega\sigma}(\dots x_j, y_j, z_j, \tilde{\sigma}_j \dots) \chi_\nu(R) \Theta_{M,\Omega}^J(\alpha, \beta) U_{M_I}^I(\sigma_a^n, \sigma_b^n), \quad (4.1)$$

where $\sigma = \pm 1$ (used only for $\Omega = 0$ terms) is the reflection through a plane containing the molecular axis parity, $\omega = -1$ (ungerade) or $+1$ (gerade) specifies the symmetry with respect to inversion of electronic coordinates, R is internuclear distance, $\Theta_{M,\Omega}^J(\alpha, \beta) = \sqrt{\frac{2J+1}{4\pi}} D_{M,\Omega}^J(\alpha, \beta, \gamma = 0)$, $D_{M,\Omega}^J$ is the Wigner function, M (Ω) is the projection of the total *electronic* plus *rotational* angular momentum, \mathbf{J} , on the $Z(z)$ axis, subscript j enumerates electrons, $\tilde{\sigma}_j = \pm 1$ is the electronic spin variable which corresponds to the projection of the electron spin of the j -th electron on the z axis, ν is the vibrational quantum number, I and M_I are the total nuclear spin and its projection on the Z axis, $\sigma_{a(b)}^n$ is the nuclear spin variable which corresponds to the projection of the nuclear spin on the Z axis, indexes a, b distinguish iodine centers.

In the laboratory frame, the inversion operator \hat{P} is

$$\begin{aligned}\hat{P}X &= -X, \\ \hat{P}Y &= -Y, \\ \hat{P}Z &= -Z, \\ \hat{P}R &= R, \\ \hat{P}\alpha &= \alpha + \pi, \\ \hat{P}\beta &= \pi - \beta, \\ \hat{P}\sigma_j &= \sigma_j, \\ \hat{P}\sigma_{a(b)}^n &= \sigma_{a(b)}^n,\end{aligned}$$

where $\sigma_j = \pm 1$ is the electronic spin variable which corresponds to the projection of the electron spin of the j -th electron on the Z axis. The inversion operator in the molecular body frame coordinate system is

$$\hat{P} = (\hat{U}\hat{P}\hat{U}^+)_{X,Y,Z,\sigma_j \rightarrow x,y,z,\tilde{\sigma}_j}, \quad (4.2)$$

where $\hat{U} = e^{i\beta J_Y^e} e^{i\alpha J_Z^e}$ is the unitary transformation operator from laboratory to body frame, J^e is the total *electronic* angular momentum operator. Then Eq. (4.2) gives [1]

$$\begin{aligned}\hat{P}\Psi_{n\Omega}^{\omega\sigma}(\dots x_j, y_j, z_j, \tilde{\sigma}_j \dots) \chi_\nu(R) \Theta_{M,\Omega}^J(\alpha, \beta) U_{M_l}^I(\sigma_a^n, \sigma_b^n) = \\ \Psi_{n\Omega}^{\omega\sigma}(\dots x_j, -y_j, z_j, -\tilde{\sigma}_j \dots) \chi_\nu(R) \Theta_{M,\Omega}^J(\alpha + \pi, \pi - \beta) U_{M_l}^I(\sigma_a^n, \sigma_b^n).\end{aligned} \quad (4.3)$$

It follows from Eq. (4.3) that transformation of the electronic wavefunction corresponds to the reflection in the xz plane which changes the sign of Ω if $\Omega \neq 0$ and gives phase factor σ for $\Omega = 0$:

$$\Psi_{n\Omega}^{\omega}(\dots x_j, -y_j, z_j, -\tilde{\sigma}_j \dots) = \Psi_{n-\Omega}^{\omega}(\dots x_j, y_j, z_j, \tilde{\sigma}_j \dots), \quad (4.4)$$

$$\Psi_{n\Omega=0}^{\omega\sigma}(\dots x_j, -y_j, z_j, -\tilde{\sigma}_j \dots) = \sigma \Psi_{n\Omega=0}^{\omega\sigma}(\dots x_j, y_j, z_j, \tilde{\sigma}_j \dots). \quad (4.5)$$

For rotational wavefunction we have [2]

$$\Theta_{M,\Omega}^J(\alpha + \pi, \pi - \beta) = (-1)^J \Theta_{M,-\Omega}^J(\alpha, \pi). \quad (4.6)$$

Thus, using Eqs. (4.3, 4.4, 4.5 and 4.6), one can construct basis wavefunctions of definite parity (P or *sign* quantum number)

$$\Psi_{n\Omega \neq 0 \omega \nu J M I}^P = \frac{1}{\sqrt{2}} \left(\Psi_{n\Omega \omega \nu J M I} + P(-1)^J \Psi_{n-\Omega \omega \nu J M I} \right), \quad (4.7)$$

$$\Psi_{n\Omega=0 \omega \sigma \nu J M I}^P = \Psi_{n\Omega=0 \omega \sigma \nu J M I}, \quad (4.8)$$

where $P = \sigma(-1)^J$ in Eq. (4.8).

Due to Pauli Exclusion Principle for two identical nuclei, the sign of a molecular term is related to the parity of the total nuclear spin I . Indeed, let us represent the interchange of nuclear coordinates as

$$\hat{P}_{ab} = \hat{P}_{ab}^r \hat{P}_{ab}^s, \quad (4.9)$$

where \hat{P}_{ab}^r and \hat{P}_{ab}^s interchange nuclear spatial and spin coordinates, respectively. Interchange of nuclear spatial coordinates can be presented as the inversion of the spatial coordinates of all the nuclei and electrons, \hat{P} , through the molecular center of mass followed by the inversion \hat{i} of spatial coordinates of electrons only [3]:

$$\hat{P}_{ab}^r = \hat{i}\hat{P}. \quad (4.10)$$

Hence,

$$\hat{P}_{ab}^r \Psi_{n\Omega\omega\sigma\nu JMIM_I}^P = \hat{i}\hat{P} \Psi_{n\Omega\omega\sigma\nu JMIM_I}^P = P\omega \Psi_{n\Omega\omega\sigma\nu JMIM_I}^P. \quad (4.11)$$

Using the angular momentum algebra [2], it can be shown that

$$\hat{P}_{ab}^s U_{M_I}^I(\sigma_a^n, \sigma_b^n) = U_{M_I}^I(\sigma_b^n, \sigma_a^n) = (-1)^{I+2I_a} U_{M_I}^I(\sigma_a^n, \sigma_b^n), \quad (4.12)$$

where $I_\alpha = 2.5$ is spin of ^{127}I nucleus. Equations (4.9, 4.11 and 4.12) give

$$\hat{P}_{ab} \Psi_{n\Omega\omega\sigma\nu JMIM_I}^P = (-1)^{I+2I_a} P\omega \Psi_{n\Omega\omega\sigma\nu JMIM_I}^P. \quad (4.13)$$

On the other hand, according to Pauli Exclusion Principle we must have

$$\hat{P}_{ab} \Psi_{n\Omega\omega\sigma\nu JMIM_I}^P = (-1)^{2I_a} \Psi_{n\Omega\omega\sigma\nu JMIM_I}^P. \quad (4.14)$$

So, finally we get from Eqs. (4.13 and 4.14)

$$(-1)^I = P\omega. \quad (4.15)$$

Equation (4.15) means that for the u negative ($\omega = -1$, $P = -1$) and g positive ($\omega = +1$, $P = +1$) terms, the total nuclear spin I is even. For the u positive ($\omega = -1$, $P = +1$) and g negative ($\omega = +1$, $P = -1$) terms I is odd.

Hyperfine Interaction The leading terms in hyperfine interaction Hamiltonian of iodine molecule are

$$\hat{H}_{HFS} = \sum_{k=1}^2 \hat{H}_{HFS}^k = \sum_{k=1}^2 \sum_{q=-k}^k \sum_{\alpha=a,b} (-1)^q Q_q^k(\mathbf{I}_\alpha) V_{-q}^k(x_\alpha^e), \quad (4.16)$$

where, $Q_q^k(\mathbf{I}_\alpha)$ and $V_q^k(x_\alpha^e)$ are the tensorial operators of rank k which acts only on the nuclear spin of the nucleus α and electrons correspondingly, \hat{H}_{HFS}^1 ($k = 1$) corresponds to the nuclear magnetic-dipole interaction with the electrons, \hat{H}_{HFS}^2 ($k = 2$) corresponds to the nuclear electric-quadrupole interaction with the electrons. Spherical components of $Q_q^k(\mathbf{I}_\alpha)$ and $V_q^k(x_\alpha^e)$ are given by

$$\mathcal{Q}_q^k(\mathbf{I}_\alpha) = I_{\alpha z}, \quad (4.17)$$

$$\mathcal{Q}_{\pm 1}^1(\mathbf{I}_\alpha) = \mp \frac{I_{\alpha x} \pm i I_{\alpha y}}{\sqrt{2}}, \quad (4.18)$$

where $I_{\alpha x}$, $I_{\alpha y}$ and $I_{\alpha z}$ are cartesian components of nuclear momentum operator \mathbf{I}_α ,

$$V_0^1(x_\alpha^e) = \frac{\mu_I}{I_\alpha} \sum_j \left(\frac{\boldsymbol{\alpha}_j \times \mathbf{r}_j}{r_j^3} \right)_z \quad (4.19)$$

$$V_{\pm 1}^1(x_\alpha^e) = \mp \frac{1}{\sqrt{2}} \frac{\mu_I}{I_\alpha} \sum_j \left(\frac{\boldsymbol{\alpha}_j \times \mathbf{r}_j}{r_j^3} \right)_x \pm i \left(\frac{\boldsymbol{\alpha}_j \times \mathbf{r}_j}{r_j^3} \right)_y \quad (4.20)$$

$\mu_I = 2.81$ and $I_\alpha = 2.5$ are the magnetic moment and spin of ^{127}I nucleus, $\boldsymbol{\alpha}_j$ are the Dirac matrices for the j -th electron, \mathbf{r}_j is its radius vector in the coordinate system centered on iodine atom α ,

$$\mathcal{Q}_q^2(\mathbf{I}_\alpha) = \frac{\sqrt{6}}{2I_\alpha(2I_\alpha - 1)} \sum_{nm} C_{1n1m}^{2q} \mathcal{Q}_n^1(\mathbf{I}_\alpha) \mathcal{Q}_m^1(\mathbf{I}_\alpha), \quad (4.21)$$

C_{1n1m}^{2q} are Clebsch-Gordan coefficients,

$$V_q^k(x_\alpha^e) = -e^2 Q \sqrt{\frac{4\pi}{3}} \sum_{jj'} \frac{1}{r_j r_{j'}} Y_{kq}(\theta_j, \varphi_j), \quad (4.22)$$

e is the charge of the electron, $Q = 0.689 b$ is a quadrupole moment of ^{127}I nucleus, r_j, θ_j, φ_j are spherical coordinates of \mathbf{r}_j , Y_{kq} is a spherical function. In Eq. (4.16), we neglect much smaller contributions of $k > 2$ tensorial operators, as well as nuclear spin-rotational and nuclear spin-spin interactions.

\hat{H}_{HFS}^1 and \hat{H}_{HFS}^2 are scalar products of nuclear and electronic tensorial operators of ranks 1 and 2, respectively. Accordingly, selection rules for matrix elements of hyperfine interaction of wavefunctions (4.7, 4.8) are $\Delta\Omega = 0, \pm 1$; $\Delta J = 0, \pm 1$; $\Delta I = 0, \pm 1$ for the nuclear magnetic-dipole interaction with the electrons and $\Delta\Omega = 0, \pm 1, \pm 2$; $\Delta J = 0, \pm 1, \pm 2$; $\Delta I = 0, \pm 1, \pm 2$ for the nuclear electric-quadrupole interaction with the electrons. The hyperfine Hamiltonian is of even parity and therefore conserves sign (P) but not electronic parity ω . Since P is conserving and taking into account Eq. (4.15), one sees that any $u\sim g$ hyperfine coupling implies an odd ΔI , whereas $u\sim u$ and $g\sim g$ hyperfine coupling implies an even ΔI . There is no precise selection rule for vibrational quantum number v . For a good approximation, propensity rule is defined by the Franck-Condon factors (FCFs). The evaluation of matrix elements of hyperfine interaction Hamiltonian (4.16) for wavefunctions (4.7 and 4.8) is rather tedious. Their explicit form can be found in [3]. Limiting by one electronic state, a simple effective Hamiltonian can be obtained after averaging on electronic and vibrational variables:

$$\hat{H}_{HFS}^{\text{eff}} = A_{\parallel} [(\mathbf{J} \cdot \hat{z})(\mathbf{I}_a \cdot \hat{z}) + (\mathbf{J} \cdot \hat{z})(\mathbf{I}_b \cdot \hat{z})] + \frac{eQq_0}{2} \sum_q (-1)^q \left(Q_q^2(\mathbf{I}_a) C_{2-q}(\alpha, \beta) + Q_q^2(\mathbf{I}_b) C_{2-q}(\alpha, \beta) \right), \quad (4.23)$$

where \hat{z} is a unit vector along z axis, $C_{lm}(\alpha, \beta) = \sqrt{\frac{4\pi}{2l+1}} Y_{lm}(\alpha, \beta)$,

$$A_{\parallel} = \frac{1}{\Omega} \langle \chi_{\nu} | \langle \Psi_{n\Omega}^{\omega\sigma} | V_0^1(x_a^e) | \Psi_{n\Omega}^{\omega\sigma} | \chi_{\nu} \rangle, \quad (4.24)$$

$$eQq_0 = 2 \langle \chi_{\nu} | \langle \Psi_{n\Omega}^{\omega\sigma} | V_0^2(x_a^e) | \Psi_{n\Omega}^{\omega\sigma} | \chi_{\nu} \rangle. \quad (4.25)$$

Heterogeneous Perturbation The nonadiabatic heterogeneous perturbation (see Sect. 5.3.2.3 for details) is given by:

$$\hat{H}_C = \frac{-\hbar^2}{2MR^2} (J_-^e J_+ + J_+^e J_-), \quad (4.26)$$

where $J_{\pm} = J_x \pm iJ_y$, $J_{\pm}^e = J_x^e \pm iJ_y^e$. The selection rules for \hat{H}_C are $\Delta\Omega = \pm 1$, $\Delta J = 0$; $\Delta I = 0$ and both sign (P) and electronic parity ω are conserved. The matrix elements for wavefunctions (4.1) are

$$\begin{aligned} & \langle \Psi_{n\Omega\omega\sigma\nu JMIM_I} | \hat{H}_C | \Psi_{n'\Omega\pm 1\omega'\sigma'\nu' J'M'I'M_I'} \rangle = \\ & \delta_{\omega\omega'} \delta_{JJ'} \delta_{MM'} \delta_{I'I'} \delta_{M_I M_I'} \sqrt{(J \pm \Omega + 1)(J \mp \Omega)} \left\langle \chi_{\nu} | \left\langle \Psi_{n\Omega}^{\omega\sigma} \left| \frac{-\hbar^2 J_{\mp}^e}{2MR^2} \right| \Psi_{n'\Omega\pm 1}^{\omega\sigma} \right\rangle | \chi_{\nu'} \right\rangle \approx \\ & \delta_{\omega\omega'} \delta_{JJ'} \delta_{MM'} \delta_{I'I'} \delta_{M_I M_I'} \sqrt{(J \pm \Omega + 1)(J \mp \Omega)} \langle \chi_{\nu} | \chi_{\nu'} \rangle \left\langle \Psi_{n\Omega}^{\omega\sigma} \left| \frac{-\hbar^2 J_{\mp}^e}{2MR^2} \right| \Psi_{n'\Omega\pm 1}^{\omega\sigma} \right\rangle, \end{aligned} \quad (4.27)$$

where $\langle \chi_{\nu} | \chi_{\nu'} \rangle^2$ is Franck-Condon factor.

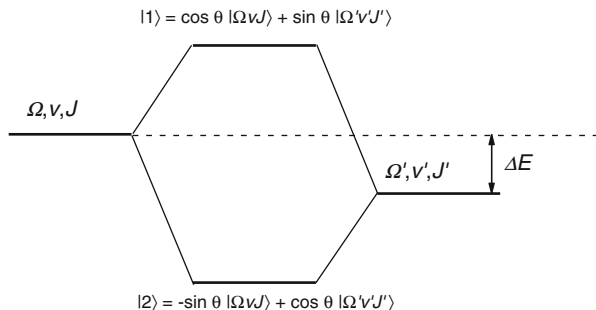
Two-State Perturbation Model In practice, it is convenient often to use a simple two-level model to describe the coupling between close-lying rovibrational states. Let consider two close lying rovibrational states $\Psi = |\Omega\nu Jn\rangle$ and $\Psi' = |\Omega\nu' J'n'\rangle$ coupled by interaction, where the notation is described earlier. According to the two-state perturbation model [4, 5], the mixed $|1\rangle$ and $|2\rangle$ states are the following:

$$\begin{aligned} |1\rangle &= \cos\theta |\Omega\nu Jn\rangle + \sin\theta |\Omega\nu' J'n'\rangle \\ |2\rangle &= -\sin\theta |\Omega\nu Jn\rangle + \cos\theta |\Omega\nu' J'n'\rangle, \end{aligned} \quad (4.28)$$

where the mixing angle is given as

$$\tan 2\theta = \frac{2H}{\Delta E} \quad (4.29)$$

Fig. 4.1 The coupling scheme of two rovibrational states



$$H = \sqrt{FCF} \langle \Omega \nu J n \hat{H} | \Omega' \nu' J' n' \rangle \quad (4.30)$$

Here \hat{H} is the operator of the interaction between the Ψ and Ψ' states, ΔE is an energy gap between unperturbed rovibrational states (see Fig. 4.1).

Well-known local effects of perturbation, such as intensity borrowing or appearing of some extra lines, lifetime variations or anomalies of the rotational structure can be described in the two-level model. Excitation of perturbed levels leads to the luminescence from the both Ψ and Ψ' zero-order states. Assuming the absence of saturation in excitation processes, the population ratio of the $|1\rangle$ and $|2\rangle$ states is equal to $\cos^2\theta/\sin^2\theta$. Intensities of luminescence from the Ψ and Ψ' components are functions of the mixing angle θ also. The intensity of the $\Psi \rightarrow i$ and $\Psi' \rightarrow k$ luminescence can be written therefore as:

$$I_{|1\rangle}(\Psi \rightarrow i) \sim (\nu_{|1\rangle}^3 \cos^4\theta) \langle \Psi | \hat{M}_{\Psi \rightarrow i} | i \rangle^2 \quad (4.31)$$

$$I_{|2\rangle}(\Psi \rightarrow i) \sim (\nu_{|2\rangle}^3 \sin^4\theta) \langle \Psi | \hat{M}_{\Psi \rightarrow i} | i \rangle^2 \quad (4.32)$$

$$I_{|1\rangle}(\Psi' \rightarrow k) \sim (\nu_{|1\rangle}^3 \cos^2\theta \sin^2\theta) \langle \Psi' | \hat{M}_{\Psi' \rightarrow k} | k \rangle^2 \quad (4.33)$$

$$I_{|2\rangle}(\Psi' \rightarrow k) \sim (\nu_{|2\rangle}^3 \cos^2\theta \sin^2\theta) \langle \Psi' | \hat{M}_{\Psi' \rightarrow k} | k \rangle^2 \quad (4.34)$$

In Eqs. 4.31, 4.32, 4.33 and 4.34, \hat{M} are dipole moment operators of the considered transitions, $\nu_{|1\rangle}$, $\nu_{|2\rangle}$ are transition frequencies.

The Eqs. (4.31) – (4.34) are applicable for a weak interaction. If the transition to the Ψ state is allowed, an admixture of the Ψ' state results in extra lines corresponding to the $|2\rangle$ excitation, which borrows the intensity from the $|1\rangle$ transition. Some examples of the local two-level perturbation will be ascribed below.

4.2 Spontaneous Predissociation

4.2.1 Valence States

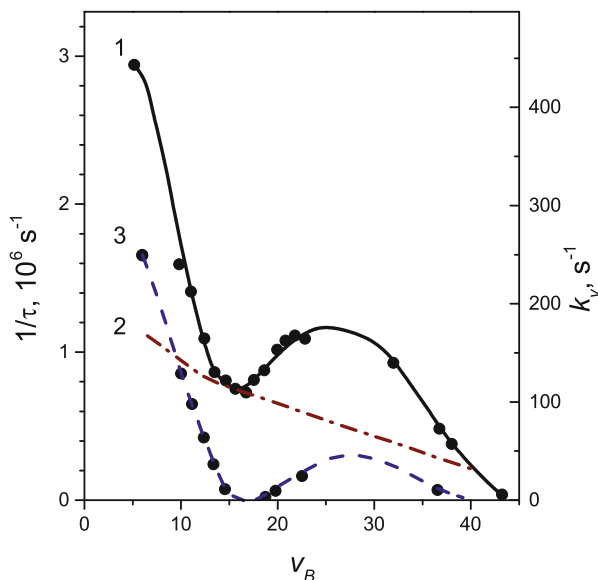
Ten states, $X0_g^+$, $A'2_u$, $A1_u$, $B'0_u^-$, $a1_g$, $C(B'')1_u$, $a'0_g^+$, 2_g , as well as 3_u , $(2)0_u^-$, which unstudied at the present, correlate with the (aa) limit (see Sect. 3.2). The X , A' and A states are deeply-bound, and their $PECs$ do not cross that of the $B0_u^+$.

According to the selection rules [6], two types of spontaneous predissociation of the $B0_u^+$ state are possible, namely, gyroscopic (heterogeneous) one via $C(B'')1_u$ state and hyperfine predissociation via this and other states with the exception of the 3_u . It is known from experimental data, that $PECs$ of the *ungerade* $C1_u$, $B'0_u^-$ and *gerade* $a1_g$, $a'0_g^+$, 2_g cross that of B state, really (see [7] and references), but, as it follows from theoretical data, $PECs$ of all other weakly bound states cross that of the B state, also [8, 9].

4.2.1.1 Gyroscopic Predissociation

High rovibrational levels of the B state are populated in the $B \leftarrow X$ transitions, and rate of gyroscopic predissociation, $1/\tau_g = k_v \cdot J_B(J_B + 1)$ (k_v is gyroscopic predissociation constant) [10, 11] could be large due to low rotational constants of the X state ($B_e = 0.037 \text{ cm}^{-1}$ [12]). The $k_v \leq 250 \text{ s}^{-1}$, (Fig. 4.2), and $1/\tau_g < 1.3 \cdot 10^5 \text{ s}^{-1}$ is much less than the radiative decay rate.

Fig. 4.2 The rate of spontaneous decay of the $I_2(B, v_B)$ vibronic levels, total for $J_B = 0$ (1), radiative (2) as well as gyroscopic predissociation constant k_v (3) [13]



4.2.1.2 Hyperfine Predissociation

A coupling of the nuclear and electronic angular momenta (the hyperfine magnetic-dipole (MD) and electric-quadrupole (EQ) interaction, selection rules are $\Delta\Omega = \pm 1$ and ± 2 , respectively) is the only non-Born-Oppenheimer term of molecular Hamiltonian that breaks g/u symmetry of electronic states of a homonuclear diatomic molecule and mixes near-degenerate rovibrational levels of the states of opposite electronic parity [3, 6, 10, 13–15].

In principle, the B state hyperfine predissociation (HFP) could be due to its perturbation by the all (aa) states with the exception of the 3_u . It was proved however that it is due to the $B\sim C$ coupling since predissociation rate follows ν -dependences of B/C Franck-Condon density (FCD) (Fig. 4.3) just as those of B state gyroscopic predissociation [7, 11, 15] (see Fig. 3.2, also).

The B/C FCD has a strong maximum at $\nu_B = 5$ and another one at $\nu_B \approx 24$ and then decreases smoothly (Fig. 4.3). The B/a' and B/a FCD s are highly oscillating functions of ν_B [7].

The rate of $B\sim C$ gyroscopic and hyperfine predissociation is

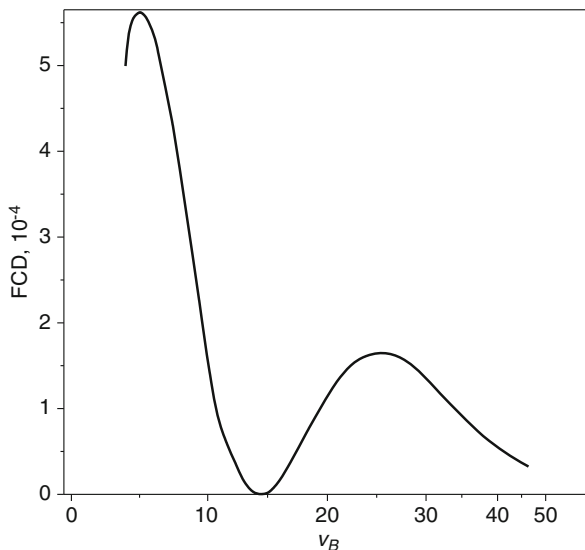
$${}'it\Gamma_{pred}(\nu, J, \varepsilon, F) = \sum_I |\alpha(I\varepsilon JF)|^2 \Gamma_{IJF}. \quad (4.35)$$

Here

ε – is a label,

$$\Gamma_{IJF} = C_v^2 J(J+1) + \frac{\alpha_v^2}{3} \left(I^2 + \frac{3(\mathbf{I}\cdot\mathbf{J})^2 + \frac{3}{2}\mathbf{I}\cdot\mathbf{J} - I^2 J^2}{(2J-1)(2J+3)} \right) - \alpha_v C_v \sqrt{2} \mathbf{I}\cdot\mathbf{J}, \quad (4.36)$$

Fig. 4.3 The $I_2(B/C)$ Franck-Condon density as a function of ν_B [10]



$$I \cdot J = (F(F+1) - J(J+1) - I(I+2))/2, \quad (4.37)$$

F is the total angular momentum [6, 10].

$\Gamma_{hfp} \approx (0.4-1.7) \cdot 10^6 \text{ cm}^{-1}$ in the $v_B = 5-40$ range, slightly different for the *ortho*- and *para*-states. The hyperfine (α_v^2) and gyroscopic (C_v^2) predissociation parameters follow the *B/C FCD*, and their ratio is independent of v_B [10, 11].

According to Fermi Golden rule, *hfp* rate is equal to

$$\Gamma_{hfp} = \frac{4\pi^2}{h} \langle \Psi_B | V_{HFI} | \Psi_C \rangle^2. \quad (4.38)$$

Therefore, the *HFP* matrix element is

$$\langle \Psi_B | V_{HFI} | \Psi_C \rangle = \sqrt{\frac{\Gamma_{hfp} \cdot h}{4\pi^2}} \approx (0.1 - 0.5) \cdot 10^{-2} \text{ cm}^{-1}. \quad (4.39)$$

4.2.2 Rydberg States

Low-lying Rydberg states cross with the repulsive branches of different valence states, leading to fast predissociation with the formation of atoms in one of the spin-orbital sub-states, $^2P_{3/2}$ and $^2P_{1/2}$.

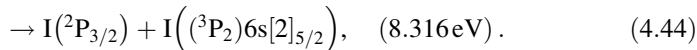
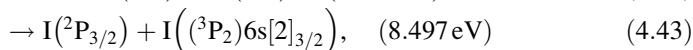
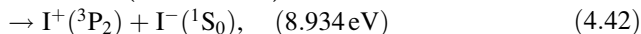
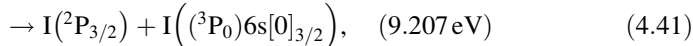
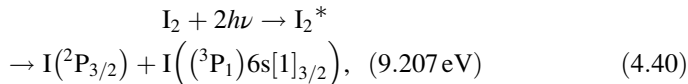
Additionally, ion-pair states lie in the same energy region (see Sect. 4.3.3) and homogeneous coupling of the Rydberg and IP states results in the anomalies of predissociation rates [16].

The radiative rate is much smaller than predissociation rate. Therefore, luminescence of Rydberg states was not always observed. A more effective method is resonance enhanced multiphoton ionization (REMPI) technique [16, 17]. In REMPI spectra, both I_2^+ and I^+ signals are observed. The former is a result of direct ionization of populated Rydberg state. The I^+ ions are formed by atomic fragments ionization after predissociation. Therefore, the I^+ REMPI spectra reflect direct predissociation of excited molecule mostly.

In the energy range above the first IP dissociation limit ($E = 72169.3 \text{ cm}^{-1}$) additional channel leading to formation of ion pair $I^+ + I^-$ becomes available. This process was first suggested by Mulliken [18] and experimentally observed in [19, 20]. The threshold for ion-pair formation lies below the molecular ionization energy, unlike Cl_2 molecule, and only two competing predissociation channels, leading to the formation of ion pair or free atoms are possible.

High-lying Rydberg states can predissociate producing atoms $I(5s^25p^46s^1)$ in Rydberg states. Emission from such Rydberg atoms formed in the predissociation process was observed [21]. Some studies of predissociation of the high-lying Rydberg states were performed in one-photon or multiphoton excitation schemes [17, 22–26]. It was shown that IP states play a great role in predissociation of

Rydberg states, but detail mechanism of this process remained unclear. In the recent works [27, 28], several predissociation channels were suggested for $X[1/2]_c6d\ 2_g$ and $X[1/2]_c6d\ 0_g^+$ Rydberg states, which are shown here in order of threshold energy.



Here, threshold excitation energies are shown in parentheses, the term $I(^3P_J)6s$ denotes a Rydberg atom in the $I^+(^3P_J)$ core state and $6s$ Rydberg electron.

The pump-probe technique with velocity-map imaging (VMI) of photofragments (I^+) was utilized to determine the role of IP states in the predissociation of the high-lying Rydberg states [27, 28]. In the channel (4.42), the ion I^+ appears directly. In other channels, it appears due to photoionization by the same laser pulse. Identification of dissociation channels was based on measuring the photofragments distribution as a function of kinetic energy release (KER). In the femtosecond time scale, it is possible to determine the internuclear distance at the ionization moment by varying the pump-probe time delay with analysis of the kinetic energy of fragment ions [28]. Moreover, knowledge of potential curves allows controlling the time evolution of the internuclear distance.

The KER signals as a function of pump-probe time delay show that some channels (4.40, 4.41, 4.42, 4.43 and 4.44) appear at non-zero delays except (4.42). The Rydberg I atoms are formed in all channels except (4.42) with a characteristic time of their appearance of about 7–8 ps. The optically populated Rydberg state does not cross at short internuclear distance any suitable states, which dissociate with the formation of the Rydberg atoms. Direct predissociation of the Rydberg state via all these channels is impossible. It was assumed a stepwise character of the predissociation via the IP states [27]. The IP states cross both the $X[1/2]_c6d\ 2_g$ and $X[1/2]_c6d\ 0_g^+$ states at larger internuclear distances (Fig. 4.4).

The appearance time τ can be simply evaluated from the classical trajectory approach as a half of the vibrational period of the IP state (a propagation time from the inner to the outer turning point). This estimation gives shorter time than that of observed experimentally for all channels, which yield the Rydberg atoms [28]. Modifications of the outer branch of IP states caused by avoiding crossing with Rydberg states allowed to explain observed results. Contributions of all first, second and third tier IP states as an intermediate states were observed.

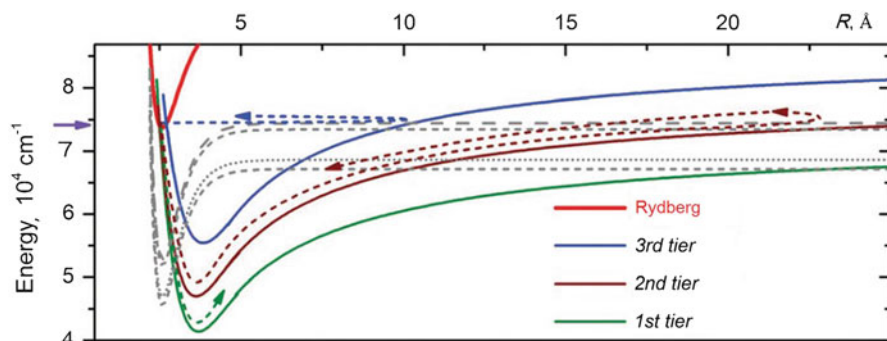


Fig. 4.4 Crossings of IP and Rydberg states [28]

So, IP states play a significant role in the predissociation of Rydberg states as intermediate states facilitating the formation of the Rydberg atoms $[R(^3P_J)]$ and ion pairs.

4.3 Perturbation Between Bound States

4.3.1 Valence States

4.3.1.1 The $B \sim$ Valence States Interaction

Among the 10 valence states corresponding to the second (*ab*) dissociation limit, the only B state is deeply bound. Interactions between different electronic states can be observed in the near-dissociation region, where multiple accidental resonances occur. Low-lying rovibrational levels of the B state have a hyperfine structure, which was perfectly described in the framework of the second-order perturbation theory. Higher lying rovibrational levels with $E > 20000 \text{ cm}^{-1}$ energy can interact directly with the rovibrational levels of other electronic states, which can be described within the first-order perturbation theory. Selection rules for the heterogeneous and hyperfine interaction define the possible coupling between the B and 9 other states with $\Omega = 0, \pm 1$ and ± 2 quantum numbers [3, 15]. Additionally, there is also superhyperfine structure at low- J rotational levels, where the energy gap between levels are lower than hyperfine interaction (*HFI*) matrix elements, and several rotational levels are coupled. These effects result in a complicated rovibrational structure of the B state.

Extensive analysis of the $B - X$ transition (more than 10000 hyperfine lines) was performed in the range from dissociation limit down to 30 cm^{-1} below ($v_B = 71-82$) [3, 15]. It was shown that the perturbations caused by the $\Omega = 2$ states are negligible, and several states have significant contribution to the *HFI*.

The *HFI* coupling is effective between near-lying rovibrational levels, which have sufficiently large *FCFs*. Due to differences of potential curves of the deeply bound *B* and other shallow states, effective overlapping of their vibrational wavefunctions is localized at the outer branch of the *B* state. Calculation of the *FCFs* using accurate long-range ($R > 7 \text{ \AA}$) *PECs* [29] shows strong $BO_u^+ \sim c1_g$ and moderate $BO_u^+ \sim (3)1_u$ mixing, that agrees with experiments. So, the $B \sim c$ interaction is the most effective and was found near at $\nu_B = 77$ and 78 [15] vibrational levels. Analysis of the experimental data showed that the $B \sim c$ interaction has essentially *MD* character.

Simultaneous population of the FO_u^+ , $H1_u$ and EO_g^+ IP states via the perturbative intermediate $B,59 \sim c,14$ state was observed also [4]. Within the two-state model (see Sect. 4.1), this mixing state can be considered as a linear combination of zero-order wavefunctions. Admixture of the $c1_g$ state allows the population of *ungerade* IP states. Because of the $u \sim g$ character of coupling, any crossed transitions can be excluded, i.e. *ungerade* IP states are populated from the $c1_g$, only, and *gerade* ones can be excited from the BO_u^+ state, only. Therefore, ratio of luminescence intensities of the IP states reflects relative contributions of the $(BO_u^+,59,J_B)$ and $(c1_g,14,J_C)$ zero-order wavefunctions to the perturbed state.

Let us consider the population of the k state, which can occur in the $k \leftarrow \Psi'$ allowed transition (see Sect. 4.1). Due to admixture of the Ψ' zero-order wavefunction to both $|1\rangle$ and $|2\rangle$ perturbed states in the two-level system, the upper state k can be populated from both states. Any crossed transitions are excluded, and the transition $k \leftarrow \Psi$ is forbidden. Modification of the Eqs. (4.31) – (4.34) gives the same result. If the resolution of excitation spectra is insufficient to resolve $|1\rangle$ and $|2\rangle$ perturbed states, transitions from both mixed states occur within the laser bandwidth, and the Eqs. (4.31) – (4.34) should be considered jointly. By neglecting saturation effects, the luminescence intensity of the upper state k can be written:

$$I_k \sim 2\cos^2\theta \sin^2\theta \langle k | \hat{M}_{\Psi' \rightarrow k} | \Psi' \rangle^2 \quad (4.45)$$

Taking into account Eq. (4.29) and considering luminescence intensity I_k as a function of the energy gap ΔE between coupling states one can estimate interaction matrix element H :

$$I_k \sim \frac{4H^2}{4H^2 + \Delta E^2}$$

P. Jewsbury *et al.* analyzed luminescence intensity from the $H1_u$ IP state in the range $J_B = 6\text{--}29$ with a strong maximum at $J = 22$ and weak maximum at $J = 8$ [4]. Electronic matrix element for the $BO_u^+,59,J_B \sim c1_g,14,J_C$ coupling was estimated of about 0.1 cm^{-1} , similar that obtained by Pique *et al.* (0.206 cm^{-1}) [15]. Later, several additional resonance rotational levels with $\nu_B = 57\text{--}59, 63, 69, 71, 74$ and 76 were found and used as intermediate states for population of the $\gamma1_u$ and $H1_u$ IP states [30, 31].

The interaction between the $B0_u^+$ and $(3)0_u^-$ (B') states was also found for a number of rovibrational levels [32]. In the perturbation-facilitated optical-optical double resonance (PFOODR) method, the $E0_g^+$ and $g0_g^-$ IP states were populated simultaneously via the $B \sim B'$ coupled intermediate state, like in the cases discussed above. The coupling matrix elements were not estimated.

4.3.1.2 Interactions Between States of the Third Dissociation Limit

Three weakly bound 0_g^+ , 1_u and 0_u^- states correlating with the third (bb) dissociation limit have very similar potential curves and dense rovibrational structures (see Fig. 1.2). The bulk of accidental resonances between rovibrational levels makes this system an interesting model object for studies of different perturbations. Indeed, as it was shown in the series of works [33–35], this system can be considered as a strongly coupled cluster of three electronic states.

Luminescence from the $1_u(bb)$, probably, was found in iodine atom recombination studies [36] for the first time. The $IP \rightarrow (bb)$ luminescence near 750 nm appeared under the 193 nm ArF laser excitation of the $D0_u^+$ IP state [37]. Ridley et al. [38] described the 0_g^+ and $1_u(bb)$ states in analysis of the vibrationally resolved $IP \rightarrow (bb)$ luminescence spectra. Finally, rovibrational analysis of the $IP \leftarrow (bb)$ excitation spectra recorded in perturbation facilitated optical scheme allowed to describe these states [33, 39, 40].

Luminescence from these states is very weak because of their large lifetimes (estimated in μs). It is more convenient to observe them in optical transitions to higher-lying IP states. This system is similar to $B \sim$ valence state coupled cluster, which is a convenient intermediate state for PFOODR methods. Moreover, equilibrium distances of IP states ($\sim 3.6 \text{ \AA}$) similar to that of the (bb) states ($\sim 3.9 \text{ \AA}$) compared with the $B0_u^+$ state (3.02 \AA). It makes this excitation scheme very effective for IP states population. All the IP states of the first and second tiers with the exception of the $\delta 2_u$ and $2_u(^1D_2)$ states can be populated via the (bb) intermediate states.

Direct population of the (bb) states from the ground state is impossible due to Franck-Condon principle. Another, three-step three-color excitation scheme via the $B0_u^+$ and $0_g^+(bb)$ states was successfully realized for investigation of the (bb) coupled states in the series of works [33–35] (see Sect. 2.1.6). In spite of the dense system of the rovibrational levels, a limited number of rovibrational levels of (bb) states could be populated in experiments if accidental resonances in the 0_g^+ , 0_u^- , $1_u(bb) \leftarrow B, \nu_B, J_B$ transitions occur, only because of the fixed wavelength of the second step laser, Nd:YAG fundamental frequency ν_f . Fortunately, the ν_f laser utilized had 4 close frequencies and some resonances were found.

The $0_g^+ \sim 1_u$ and $0_g^+ \sim 0_u^-$ are coupled by HFI , whereas the 0_u^- and 1_u states are coupled by heterogeneous interaction. The second step of the multistep excitation scheme is available due to the $0_g^+ \leftarrow B0_u^+$ transition and results in population of the

ungerade IP states. Two other interacting states, 1_u and 0_u^- , are mixed with 0_g^+ one, and transitions to the *gerade* IP states become available, also. For example, population of the $D0_u^+$ and $\beta 1_g$ IP states in the same excitation scheme allowed to study $0_g^+ \sim 1_u$ coupling [35].

Correct analysis of the intra-molecular interaction requires the solution of the full Hamiltonian and analysis of perturbations in the energy structure of rovibrational levels. The IP $\leftarrow (bb)$ transitions were used to determine absolute positions of rovibrational levels. Spectroscopic constants of the IP states are well known and quite accurate within one state, but a little inconsistent with each other. An accuracy of the energies of (bb) rovibrational levels and resolution of the lasers used was insufficient to perform such analysis.

Another available method involves analysis of the mixing of wavefunctions, which was performed for the $B0_u^+ \sim c1_g$ coupling analysis [4]. The observed coupling of different states allows considering the problem within the first-order perturbation theory, in which a selected zero-order state is mixed by two others. By measuring of relative luminescence intensities of the IP states, it is possible to determine relative contributions of all zero-order (bb) wavefunctions to the perturbed state. For example, Fig. 4.5 shows simultaneous excitation of the F , G and g states from a single rovibrational level. Luminescence spectra of the

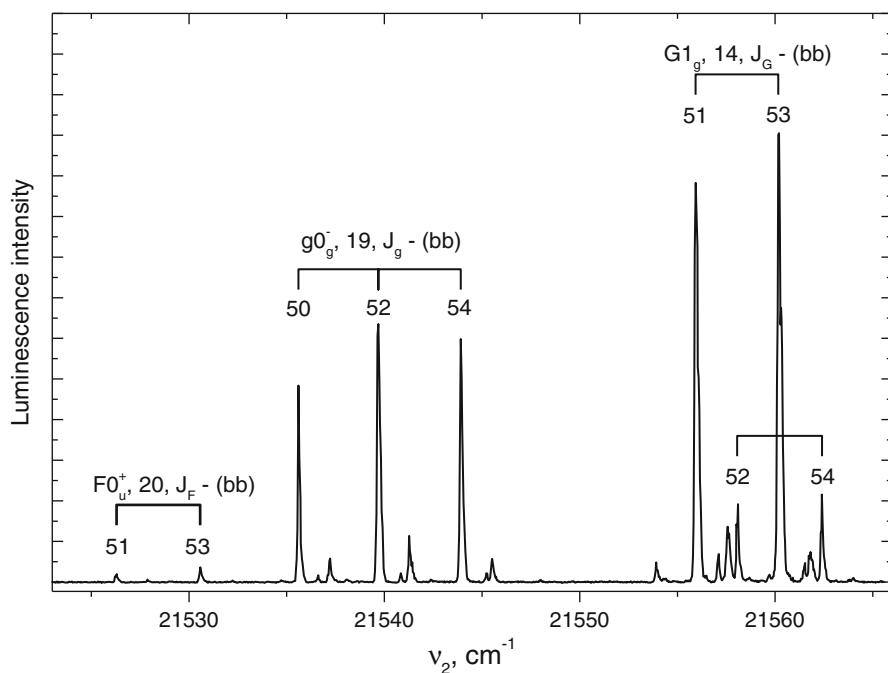


Fig. 4.5 Excitation F , G and $g \leftarrow (bb)$ spectrum corresponding to the excitation pathways via the $B,21,53$ rovibrational state [33]. Luminescence was collected at 285 nm. The weak unassigned lines are due to “satellite” components of ν_2

$F \rightarrow X$, $G \rightarrow A, C$ and $g \rightarrow B'$ transitions which arise from each perturbed (bb) state were measured for such analysis [33].

In the framework of the two-state model, the dipole allowed transitions $i \leftarrow \Psi$ and $k \leftarrow \Psi'$ can be considered from the intermediate perturbed state $|1\rangle$ or $|2\rangle$ (see Sect. 4.1). Modification of the Eqs. 4.31, 4.32, 4.33 and 4.34 gives the same expressions for the i and k states (see Eq. 4.45). Only two transitions $i \leftarrow \Psi$ and $k \leftarrow \Psi'$ are allowed and any crossed transitions are neglected.

The ratio of intensities of observed luminescence from the i and k states can be expressed as:

$$\frac{I_i}{I_k} = ctg^2 \theta \frac{\langle i | \hat{M}_{i \leftarrow \Psi} | \Psi^2 \rangle}{\langle k | \hat{M}_{k \leftarrow \Psi'} | \Psi' \rangle^2}. \quad (4.46)$$

By taking into account the Eq. (4.29), one can determine the mixing angle and the interaction matrix element. In the case where more than two levels interact, the mixed wavefunction should be expanded over the zero-order wavefunctions as:

$$\Psi_{bb} = \sum_n c_n \Psi_n^{(0)}, \quad (4.47)$$

where c_k are expansion coefficients, $\Psi_n^{(0)}$ are zero-order wavefunctions of (bb) states (n denotes coupling levels of the 0_g^+ , 1_u and 0_u^- states), $\sum_n c_n^2 = 1$. Equations 4.31, 4.32, 4.33 and 4.34 can be simply modified.

This analysis allows determining the matrix element averaged over components of the hyperfine structure. Hyperfine electronic matrix elements determined for the $0_g^+ \sim 1_u$ and $0_g^+ \sim 0_u^-$ couplings were estimated as $0.3(1) \text{ cm}^{-1}$ and $0.5(2) \text{ cm}^{-1}$, respectively [33]. These values are close to the theoretical estimation $0.1\text{--}0.4 \text{ cm}^{-1}$ made for the B state [3, 6] (see Sect. 4.3.1.1).

The coupling of the 0_g^+ and 0_u^- (bb) states can occur by another, indirect mechanism via the 1_u intermediate state in the second-order perturbation approach. The 0_u^- state couples with the $1_u, v_1, J_1$ one by the heterogeneous interaction according to the $\Delta J = 0$ selection rule. The $1_u, v_1, J_1$ state is mixed with the $0_g^+, v_0, J_0$ one by HFI with the $|\Delta J| \leq 2$ selection rule. However, the observed $0_g^+, 0.49$ and $0_u^-, 1.48/50$ coupling states lie significantly lower than the $1_u, v_1 = 0$ level ($\Delta E > 90 \text{ cm}^{-1}$), so the 0_g^+ and 0_u^- states are coupled directly.

The effects of heterogeneous interaction between 1_u and 0_u^- states was also observed in [33, 35, 40]. The splitting of the $1_u, 5, 59$ rovibrational level induced by heterogeneous interaction was determined being equal to $0.138(8) \text{ cm}^{-1}$ [35, 40]. According to the parity selection rule, the e (f) sublevels of the double degenerated state with $\Omega = 1$ interact with e (f) sublevels of the $\Omega = 0$ state, only. The interaction of e and f sublevels differs that results in different energy shift of the sublevels, the Ω -splitting or Ω -doubling.

The splitting can be calculated by the second-order perturbation theory as an cumulative effect of interactions between the selected $1_u, \nu_1, J$ rovibrational level and all rovibrational levels of the 0_u^- state:

$$\Delta E(v_1, J) = \sum_{v_0} \frac{|\langle 0_u^-, \chi_{v_0} | \hat{H}_C | 1_u, \chi_{v_1} \rangle|^2}{E_1(v, J) - E_0(v_0, J)}, \quad (4.48)$$

where \hat{H}_C is a Hamiltonian of the heterogeneous interaction (4.26), $E_{0,1}$ are energies of the 0_u^- and 1_u rovibrational levels, respectively. According to Eq. (4.27), electronic and rotational part of the sum in Eq. (4.48) can be extracted:

$$\Delta E(v_1, J) = \left| \left\langle 0_u^- \left| \frac{-\hbar^2 J_{\mp}^e}{2\mu R^2} \right| 1_u \right\rangle \right|^2 J(J+1) \sum_{v_0} \frac{|\langle \chi_{v_0} | \chi_{v_1} \rangle|^2}{E_1(v, J) - E_0(v_0, J)} \quad (4.49)$$

With known vibrational energies of the coupled states, the summation over v_0 can be calculated numerically. To demonstrate the correctness of the description, let us take into account that the all (*bb*) states have similar potential energy curves (see Sect. 3.2), their vibrational structures are almost equidistant, and only a few vibrational levels can be kept in the summation. In this case, the sum in Eq. (4.48) can be simplified to $1/\Delta E_{01}$, where $\Delta E_{01} = 96.28 \text{ cm}^{-1}$ is the energy gap between the 1_u and 0_u^- electronic states. Within the “pure precession” model, electronic matrix element can be estimated, and the Eq. (4.48) gives $\Delta E_1(5,59) = 0.117 \text{ cm}^{-1}$ that is close to the experimental value.

4.3.2 Ion-Pair States

As it was mentioned in Chap. 3, the IP states of molecular iodine form four tiers (manifolds) consisting of the electronic states with different g/u and $+/-$ parities and similar close-lying *PECs*. These features make them very attractive as a model system for study of the intramolecular interactions. The IP-valence states charge-transfer transitions are convenient to observe, and the effects of interactions can be observed in the IP-valence states luminescence spectra.

The hyperfine interaction becomes appreciable when *FCFs* between coupling rovibrational levels are rather large. High *B* state vibrational levels near the dissociation limit are coupled effectively with the weakly-bound states at the outer *PEC* branch. Analysis of this system requires accurate long-range potential curves. Along with that, the system of IP states is a system, where such effects can be observed at shorter interatomic distances and studies are much simplified. From analysis of some IP-valence states (IP-V) luminescence spectra, the “atom-in-molecule” model was shown to be applicable for description wavefunctions of IP states in the range near equilibrium distances (see Sect. 3.3.3). Studies of the

non-adiabatic interactions between IP states allows to check the validity of this approximation.

4.3.2.1 Heterogeneous Interaction

6 first tier IP states correlate with the $\Gamma^-(^1S) + \Gamma^+(^3P_2)$ dissociation limit (see Sect. 3.3). On the basis of separated atoms (asymptotic model), there are four pairs of states, $E0_g^+ \sim \beta1_g$, $D0_u^+ \sim \gamma1_u$, $\beta1_g \sim D'2_g$ and $\gamma1_u \sim \delta2_u$, which can be coupled by heterogeneous interaction according to the $\Delta\Omega = \pm 1$ selection rule. The second tier consists of 6 IP states corresponding to the two dissociation limits: $\Gamma^-(^1S) + \Gamma^+(^3P_1)$ ($G1_g$, $g0_g^-$, $H1_u$, and $h0_u^-$) and $\Gamma^-(^1S) + \Gamma^+(^3P_0)$ ($f0_g^+$ and $F0_u^+$). Therefore, a heterogeneous interaction between the $G1_g \sim g0_g^-$ and $H1_u \sim h0_u^-$ states can only be possible.

J.Perrot *et al.* determined the empirical formula of the $\beta1_g$ *elf* splitting [41] as follows:

$$\Delta E_\beta(v, J) = -[7.11 \cdot 10^{-6} + 1.68 \cdot 10^{-7}(v + 1/2) - 5.35 \cdot 10^{-9}(v + 1/2)^2 J(J + 1) + 2.91 \cdot 10^{-11} J^2(J + 1)^2] \quad (4.50)$$

Assuming that the interaction between $E0_g^+$ and $\beta1_g$ states is responsible for the Ω -splitting of rovibrational levels, the second order of the perturbation theory can be applied. Evaluation of the sum in Eq. (4.49) gives equation as a function of v_β :

$$\Delta E_\beta(v_\beta, J) = -\left[6.8 \cdot 10^{-7} + 3.3 \cdot 10^{-9}\left(v_\beta + \frac{1}{2}\right)\right] J(J + 1)^* \left|\langle E0_g^+ | J_e^\pm | \beta1_g \rangle\right|^2 \quad (4.51)$$

The comparison of Eqs. (4.50) and (4.51) gives the electronic matrix element, that is in good agreement with the predictions made in the framework of pure precession model [41]. A good agreement with the experimental results demonstrates a validity of the pure precession model for description of the IP states. The Ω -splitting of the $\beta1_g$ state was used for estimation of the splitting in the $1_u(bb)$ valence state [40].

Analogous experiments were made by T. Ishiwata's research group. They observed heterogeneous interaction effects in the $\gamma1_u$ [42], $G1_g$ [43], $H1_u$ [31, 44], $1_u(^1D)$ and $2_u(^1D)$ [45] IP states. The Ω -splitting of the $G1_g$ and $H1_u$ states was found for a wide range of rovibrational levels.

As it follows from Eq. (4.50), the Ω -splitting weakly depends on vibrational quantum number v . All the IP states, especially *gerade* states, have similar potential energy curves, and their vibrational structures are almost equidistant. Therefore, the sum in (4.48) can be simplified as for the (*bb*) states (see Sect. 4.3.1.2) to $1/R_e^2 \times 1/\Delta E$, where R_e is equilibrium distance of the $\Omega = 1$ IP state and ΔE is the energy gap between interacting IP states.

In spite of the roughness of this approach, it predicts a relative location of the interacting states rather good. Analysis of the Ω -splitting of the $G1_g$ state rovibrational levels using Eq. (4.48) has predicted that the $g0_g^-$ state lies 512 cm^{-1} below and has electronic term value $T_e = 47046 \pm 51\text{ cm}^{-1}$ [43]. Later, the value $T_e = 47086\text{ cm}^{-1}$, which confirm the theoretical prediction, was determined experimentally in the population of the $g0_g^-$ state in the PFOODR scheme [32]. The same calculations of the location of the $h0_u^-$ ungerade state from analysis of the $H1_u$ state Ω -splitting give $T_e \sim 48640\text{ cm}^{-1}$, whereas direct population of the $h0_u^-$ state gives $T_e = 48646.548\text{ cm}^{-1}$ [31].

Heterogeneous interaction results in coupling of the $\gamma1_u$ state with both $D0_u^+$ and $\delta2_u$ IP states of the same dissociation limit. The Ω -splitting of the $\gamma1_u$ state was observed (Fig 4.6) and proposed due to interaction with the $D0_u^+$ state [42]. Direct coupling of the other, $\delta2_u$ state with the $D0_u^+$ one is forbidden for heterogeneous interaction in the first-order perturbation theory due to $\Delta\Omega = \pm 1$ selection rule, and the Ω -splitting of the $\delta2_u$ state occurs through the $\gamma1_u$ state. This effect is much less than that of the $\gamma1_u$ state and the Ω -splitting of the $\delta2_u$ state was not observed.

However, another effect of interaction, namely, mixing of the $\gamma1_u$ and $\delta2_u$ wavefunctions was observed. Due to admixture of the $\gamma1_u$ rovibrational levels to the $\delta2_u$ ones, the latter can be also populated from the $A1_u$ intermediate state in two-photon transition [42]. The extra lines in the excitation spectra of the $\gamma \rightarrow A$ luminescence were observed due to “intensity borrowing” from the γ state and assigned to transition to the $\delta2_u$ perturbed state. Energy diagram in Fig. 4.7 shows two series of levels corresponding to the γ and δ states. One sees that the heterogeneous interaction leads to avoiding crossing between coupled states. Interaction matrix elements between γ and δ IP states were determined for $v_\gamma = 2\text{--}11$ vibrational levels.

The more complex system, “indirect” $D0_u^+ \sim \delta2_u$ coupling, was observed in [46]. Optical population of the $D0_u^+$ state by three-step laser excitation from the ground state via the valence $B0_u^+$ and $0_g^+(bb)$ intermediate states was performed (see Sect. 4.3.1). Some extra lines were observed in the excitation spectra near the $D0_u^+$, $v_D = 22, J_D$ rotational lines, which assigned to the population of the $\delta2_u, v_\delta = 13$ state by luminescence spectra simulation (Fig. 4.8). The lack of coupling between rovibrational levels with $J_D \neq J_\delta$ excludes possible hyperfine interaction. The Stark effect and CINAT population of the $\delta2_u$ state are excluded also. The only explanation of the $\delta2_u$ population is the heterogeneous coupling of these states occurring through the intermediate $\gamma1_u$ state. The $D0_u^+ \sim \delta2_u$ coupling can be described in the second order of the quantum mechanical perturbation theory including summation over all possible states of the 1_u symmetry. As mentioned above, the $\gamma1_u$ state is the only close-lying state which correlates with the same, $\Gamma^-(^1S) + \Gamma^+(^3P_2)$, dissociation limit as the $D0_u^+$ and $\delta2_u$ ones, and the $\gamma1_u, v_\gamma, J_\gamma, J_\gamma = J_D = J_\delta$ rovibrational states give the major contribution to the interaction.

Within the second-order perturbation theory [25], the wavefunction of the perturbed $\delta2_u$ state can be represented as a sum of the zero-order wavefunction $\Psi_\delta^{(0)}$ and the second-order perturbation wavefunction $\Psi_\delta^{(2)}$:

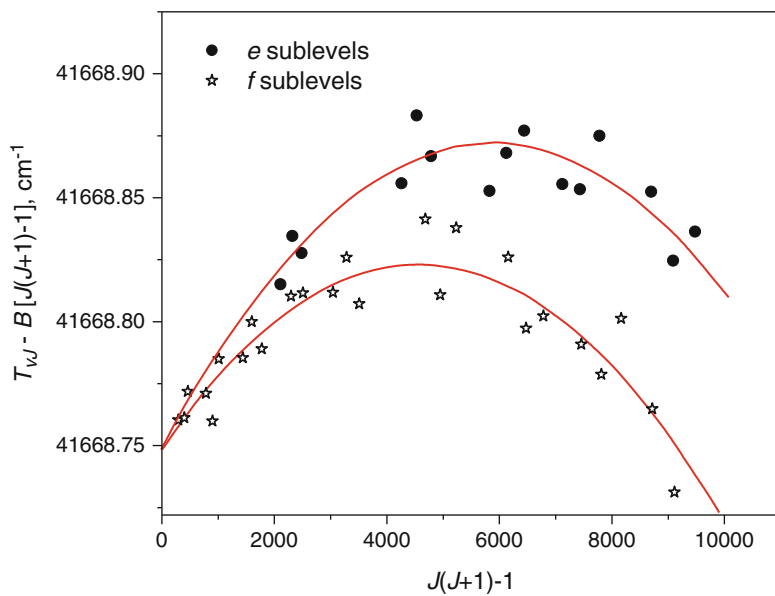


Fig. 4.6 Energy level diagram of the $\gamma 1_u, v = 0$ state [42]

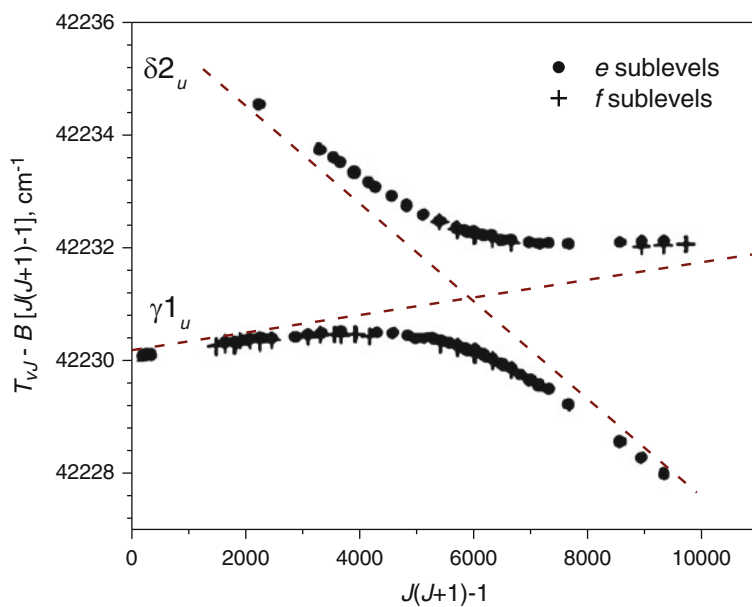


Fig. 4.7 Energy level diagram of the $\gamma 1_u, v = 6$ and $\delta 2_u, v = 4$ states [42]

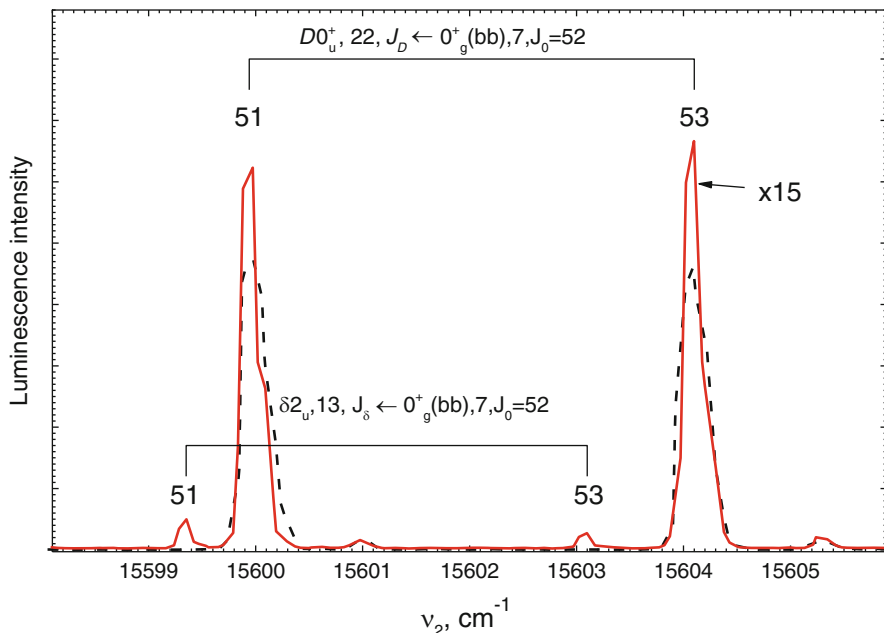


Fig. 4.8 Excitation spectra of the $\delta, 13, J_\delta$ (solid line) and $D, 22, J_D$ (broken line) states luminescence [46]

$$\Psi_\delta = \Psi_\delta^{(0)} + \Psi_\delta^{(2)}, \quad (4.52)$$

where

$$\Psi_\delta^{(2)} = \sum_k \frac{V_{Dk} V_{k\delta}}{\Delta E_{\delta k} \Delta E_{\delta D}} \Psi_D^{(0)} - \frac{V_{\delta\delta} V_{D\delta}}{\Delta E_{\delta D}^2} \Psi_D^{(0)} - \frac{V_{D\delta}^2}{2\Delta E_{\delta D}^2} \Psi_\delta^{(0)}. \quad (4.53)$$

V_{nm} (n, m are D, γ or δ) is matrix element of the operator of the heterogeneous interaction \hat{H}_C (4.27), $\Delta E_{mn} = E_m - E_n$ are energy differences between the corresponding rovibrational states. The $\delta 2_u$ state cannot couple directly with the $D 0_u^+$ state due to selection rules for heterogeneous interaction. The $V_{D\delta}$ matrix elements are equal to zero, and two last terms in Eq. (4.53) vanish. Summation in the remaining term of Eq. (4.53) over all vibrational levels of the 1_u electronic states can be replaced by one dominant term, related to the close-lying vibronic level $\gamma, 16$. So, the wavefunction $\Psi_\delta^{(2)}$ is presented in the form:

$$\Psi_\delta^{(2)} = \frac{\langle D, \nu_D | \hat{H}_C | \gamma, \nu_\gamma \rangle \langle \gamma, \nu_\gamma | \hat{H}_C | \delta, \nu_\delta \rangle}{\Delta E_{\delta\gamma} \Delta E_{\delta D}} \Psi_D^{(0)} \approx A(\Delta E_{\delta D}) \Psi_D^{(0)} \quad (4.54)$$

The large energy gaps between the close-lying $\gamma, 16$ and $\delta, 48$ vibrational levels, $\Delta E_{\delta\gamma}$, weakly depends on the J quantum number and can be replaced by the constant

value, $\sim 33.7 \text{ cm}^{-1}$. Finally, the admixture of the D IP state is a function of the small energy gap $\Delta E_{\delta D}$. Analysis of the energy gap dependence in the range $J_\delta = 46\text{--}56$ gives the estimation of the product of two matrix elements in Eq. (4.54) and is found to be $\sim 0.27 \text{ cm}^{-2}$. Assuming that the matrix elements $V_{D\gamma}$ and $V_{\gamma\delta}$ have approximately the same values, one gets: $|\langle D, v_D | \hat{H}_C | \gamma, v_\gamma \rangle| \approx |\langle \gamma, v_\gamma | \hat{H}_C | \delta, v_\delta \rangle| \approx 0.5 \text{ cm}^{-1}$. The comparison with the matrix elements determined in [42] shows a good agreement between two results.

4.3.2.2 Hyperfine Interaction

Hyperfine structures of the IP rovibrational levels of the first tier $E0_g^+$ [47, 48] and $\beta 1_g$ [47, 49] states have been studied using Doppler-free two-photon excitation spectroscopy. Some hyperfine constants have been derived for several vibrational and rotational levels.

An estimation of the *HFI* constants can be made on the basis of separated ions $\text{I}^+(^3\text{P}_0) + \text{I}^-(^1\text{S}_0)$ (see Table 3.1). However, the difference of the eQq_0 values calculated in this assumption and experimentally determined is significant (for example, $eQq_0 = 659 \text{ MHz}$ calculated and $\sim 490 \text{ MHz}$ observed for the $E0_g^+$ state [47]). Another asymptotic state of I^+ , which has the same total electronic momentum number $J_e = 2$, is the $\text{I}^+(^1\text{D}_2)$ state. By including this state to the separated atoms basis set, the authors of [47] obtained more agreeing results. To improve such estimations, more atomic and ionic states should be included in the basis set.

The same representation of the wavefunctions was used for the *MD* interaction constant, $A_{||}$ (see 4.24). The constant has been determined for the $\beta 1_g$ state [48], $A_{||} = 477 \text{ MHz}$, whereas calculations give twice the value, 967 MHz . So, the description of wavefunctions in the basis set of separated ions is unsuitable for description of the *HFI* structure of IP states.

As mentioned above, the hyperfine as well as Stark interactions can be responsible for coupling of the states with different parity, $u \leftrightarrow g$. All coupling effects induced by the *HFI* are weak and can be observed for a few rovibrational levels of some IP states despite the dense rovibrational structure of the ion-pair manifolds. So, coupling of the $E0_g^+ \sim \gamma 1_u$ [5], $2_g(^1\text{D}) \sim 1_u(^1\text{D})$ [50], and $D0_u^+ \sim \beta 1_g$ were found for some rovibrational levels.

The procedure of the *HFI* matrix element determination is reduced to the solution of the coupled Eqs. (4.31)–(4.34). Hyperfine interaction should be analyzed for each hyperfine component. Such analysis is possible for experiments with high resolution; however, often it is possible to estimate matrix elements averaged over hyperfine components, and coupling of the mentioned above IP states was studied by simpler methods.

The excitation of the coupled $E0_g^+ \sim \gamma 1_u$ complex states was performed by the standard OODR $E \leftarrow B \leftarrow X$ scheme used in [5]. Two pairs of vibrational levels are close enough to find effective hyperfine coupling in the low- v range: $v_E = 3 \sim v_\gamma = 1$

and $v_E = 19 \sim v_\gamma = 18$. Selection rules $\Delta J = 0, \pm 1$ and ± 2 allow to couple different vibrational states at some rotational quantum numbers (Fig. 4.9).

The partly resolved spectrum of the $E,3,41 \sim \gamma,1,41$ mixed state excitation is shown in Fig. 4.10 as an example. The $\gamma \rightarrow c, c'$ luminescence is observed at 474 nm due to admixture of the γ zero-order state to both $|1\rangle$ and $|2\rangle$ states (see Eq. (4.28)).

The coupling of the $D, v_D = 12 \sim \beta, v_\beta = 13$ and $D, v_D = 48 \sim \beta, v_\beta = 47$ rovibrational levels was found in the experiments with population of both D and β states by different excitation schemes. The coupling of the $1_u(^1D), v_1 = 0$ and $2_g(^1D), v_2 = 2$ third tier IP states has been studied in the PFOODR experiments via the perturbed intermediate states: $B \sim c1_g$ and $B \sim b'2_u$ respectively [50].

In all experiments mentioned above, rovibrational levels are coupled according to the $\Delta J = 0, \pm 1$ selection rule (see Sect. 4.1). No electric quadrupole hyperfine interaction ($\Delta J = \pm 2$) was found, and the coupling occurs due to the MD interaction only. As mentioned above, hyperfine coupling of the B valence state with *gerade* states has also essentially MD character [15]. The interaction matrix element of the electric quadrupole interaction between the $B0_u^+$ and $c1_g$ vibrational states was determined as 446 MHz, 5 times less, than that of MD interaction ($A_\perp = -2340$ MHz)

The constant of the hyperfine interaction is very small, and only near-resonant rovibrational levels are mixed sufficiently. The resolution of measured spectra is limited by laser band width and was insufficient to resolve $|1\rangle$ and $|2\rangle$ perturbed states [5, 50]. In this case, transitions to both mixed states occur within the laser bandwidth, and the Eqs. (4.31)–(4.34) should be considered jointly.

Often, luminescence of the Ψ and Ψ' zero-order states can be easily separated spectroscopically. For example, the dominating transition from the E state is the $E \rightarrow B$ transition in the 400–440 nm spectral range, while emission from the coupling partner $\gamma 1_u$ state occurs mainly at ~ 350 nm ($\gamma \rightarrow a$ transition) and 450, 480 nm ($\gamma \rightarrow c, c'$ transitions) (Fig 4.11).

Both $|1\rangle$ and $|2\rangle$ states have admixtures of the Ψ and Ψ' states and give contributions to the luminescence (see Sect. 4.3.1). However, it is possible to extract admixture coefficients and determine interaction matrix elements from the ratio of the total luminescence of the Ψ and Ψ' components.

In the framework of the two-state model, Eqs. (4.31)–(4.34) gives expression for the total luminescence intensity of $\Psi \rightarrow i$ bands from both $|1\rangle$ and $|2\rangle$ states:

$$I_\Psi \sim (\cos^4\theta + \sin^4\theta)\nu^3 \sum_i \langle \Psi | \hat{M}_{\Psi \rightarrow i} | i \rangle^2, \quad (4.55)$$

Luminescence intensity of the $\Psi' \rightarrow k$ band is equal to

$$I_{\Psi'} \sim 2 \cos^2\theta \sin^2\theta \nu^3 \sum_j \langle \Psi' | \hat{M}_{\Psi' \rightarrow k} | k \rangle^2 \quad (4.56)$$

The total emission intensity ratio for the transitions in the case of optical population of the Ψ' state is:

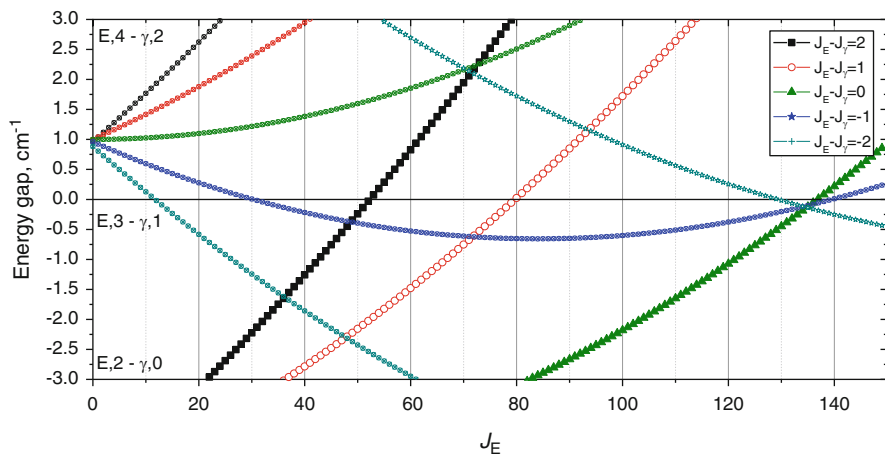


Fig. 4.9 The diagram of the energy gap between E and γ rovibrational levels accessible for coupling by the hyperfine interaction

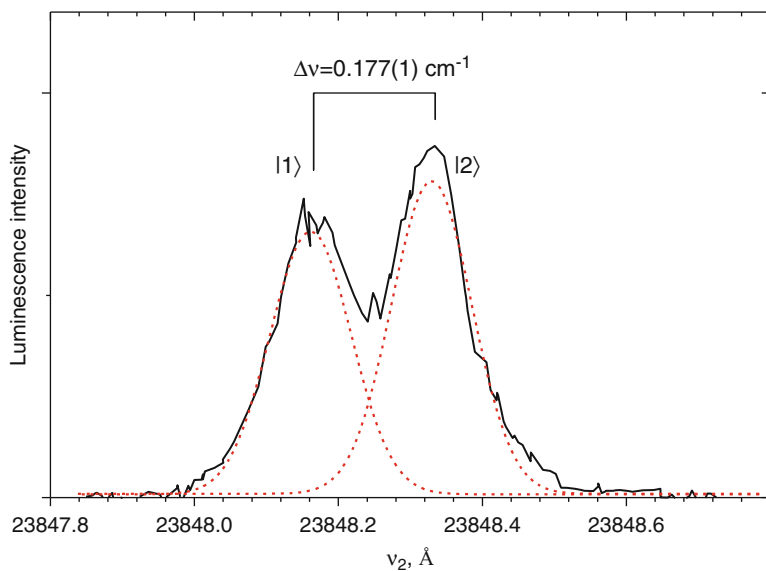


Fig. 4.10 Excitation spectra of the luminescence at 430 and 474 nm. Spectra recorded after population in the $E0_g^+, 3,40 \leftarrow B0_u^+, 19,21 \leftarrow X, 0,20$ transition. Both components are approximated by the Gauss profile

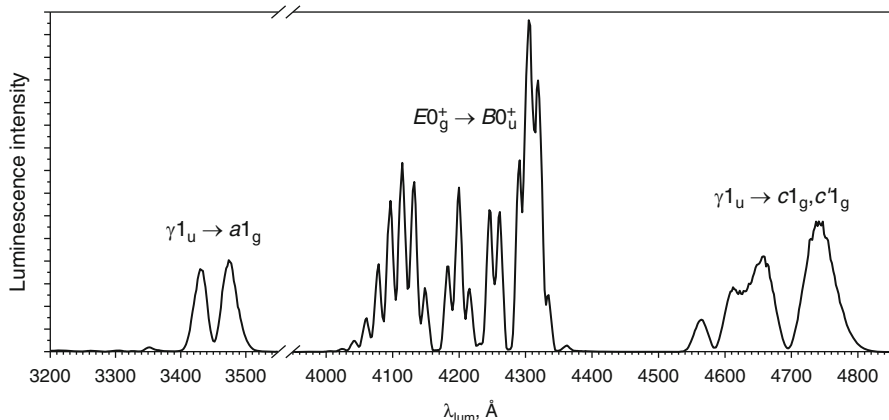


Fig. 4.11 Luminescence spectrum of the coupled $E0_g^+ \rightarrow B0_u^+$ $v_E = 3, J_E = 32 \sim \gamma 1_u, v_\gamma = 1, J_\gamma = 33$ states

$$\frac{I_\Psi}{I_{\Psi'}} \equiv R_{\Psi/\Psi'} = \frac{2 \cos^2 \theta \sin^2 \theta}{\cos^4 \theta + \sin^4 \theta} \frac{\int \nu^3 M_{\Psi \rightarrow i}^2 d\nu}{\int \nu^3 M_{\Psi' \rightarrow j}^2 d\nu} = \frac{2 \tan^2 \theta}{1 + \tan^4 \theta} \frac{\sum_i A_{\Psi \rightarrow i}}{\sum_j A_{\Psi' \rightarrow j}}, \quad (4.57)$$

According to (4.29), it can be written as:

$$R_{\Psi/\Psi'}(J_\Psi) = \frac{1}{1 + \frac{\Delta E^2}{2H_{hf}^2}} \cdot \frac{\tau_{\Psi'}}{\tau_\Psi} \cdot K(J_\Psi) \quad (4.58)$$

Here, an additional factor K , if Ψ and Ψ' states have different electronic parities ω , has to be introduced. Indeed, let us suppose that the u positive or g negative term of Ψ' is populated in the optical transition. For the u positive and g negative terms the $I = 1, 3, 5$ are odd. On the other hand, any $u \sim g$ hyperfine coupling implies an odd ΔI (see Sect. 4.1). Therefore Ψ' is coupled with the $I = 0, 2, 4$ nuclear spin states of Ψ . Total number of the nuclear spin states of Ψ' with odd I and Ψ with even I is $g_{\Psi'} = 21$ and $g_\Psi = 15$, respectively. One can construct 15 *bright* states from 21 spin states of Ψ' which interact with 15 spin states of Ψ and 6 *dark* states which do not interact with Ψ . The population of the dark states of Ψ' does not lead to the $\Psi \rightarrow i$ optical transition resulting in $K = \frac{g_\Psi}{g_{\Psi'}} = \frac{15}{21}$. In the opposite case, if the u negative or g positive term of Ψ' is populated in an optical transition, the number of nuclear spin states of Ψ' is less than number of nuclear spin states of Ψ . In this case, each spin state of Ψ' interacts with Ψ , and therefore, population of every Ψ' hyperfine level leads to optical transition from Ψ , which result in $K = 1$.

Normalized ratio of luminescence intensities

$$R'_{\Psi/\Psi'} = R_{\Psi/\Psi'} / K \quad (4.59)$$

can be approximated by a simple Lorentz function. If the Ψ' state is populated optically, the ratio of luminescence intensities $R_{\Psi'/\Psi}$ should be used:

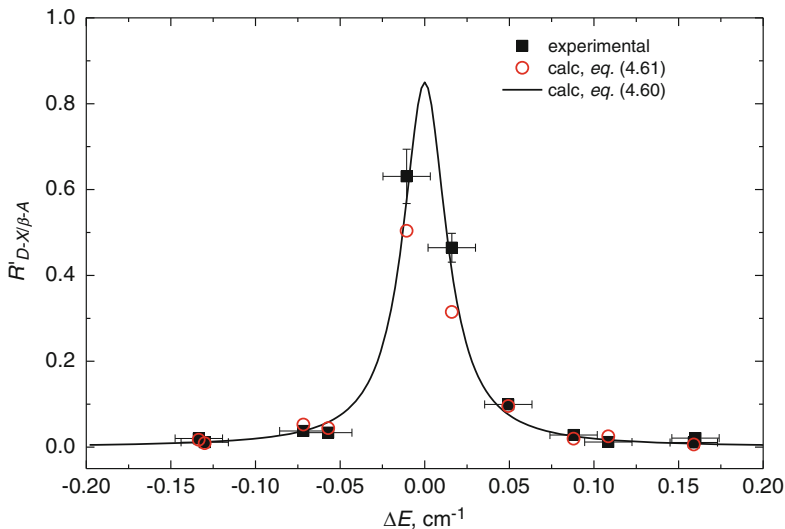


Fig. 4.12 The $R_{D-X/\beta-A}$ normalized ratio determined at the coupled $\beta, 13, J_\beta \sim D, 12, J_D$ rovibrational states, plotted as a function of the energy gaps between zero-order states. Squares are the experimental data, circles are data calculated by Eq. (4.61). Curves are data obtained by Eq. (4.60)

$$R_{\Psi'/\Psi}(J_\Psi) = \frac{1}{1 + \frac{\Delta E^2}{2H_{hf}^2}} \cdot \frac{\tau_\Psi}{\tau_{\Psi'}} \cdot K(J_\Psi) \quad (4.60)$$

Such normalized ratio of luminescence intensities from near resonant rovibrational levels of the $D, 12$ and $\beta, 13$ states as a function of energy gap ΔE is shown in Fig. 4.12. Fitting of the experimental data by Eq. (4.58) gives values of the electronic interaction matrix element $H_{hf}^{el} = 0.049(3) \text{ cm}^{-1}$. The mixing of the close-lying rovibrational levels of the $\beta, \nu_\beta = 47$ and $D, \nu_D = 48$ states have been observed by population of the β state. The matrix element value is equal $H_{hf}^{el} = 0.063(7) \text{ cm}^{-1}$ and increases slightly with vibrational quantum number of the states.

The matrix element of interaction between the $E, 3, J$ and $\gamma, 1, J$ vibrational states has similar value $H_{hf}^{el} = 0.084 \text{ cm}^{-1}$ in analogous experiments. Resolution of utilized lasers was insufficient to estimate the matrix element by Eqs. (4.58) and (4.59) for the $E, 19, J$ and $\gamma, 18, J$ coupled states [5]. The near-resonant rovibrational levels $J_E = 81$ and $J_\gamma = 80$ have a dominate contribution to the averaged coupling, and the electronic interaction matrix element can be estimated of about 0.02 cm^{-1} , significantly less than that of the $E, 3 \sim \gamma, 1$ interaction.

Beyond the two-state perturbation model, summation over all hyperfine components should be performed for the total emission intensities calculation. The ratio of luminescence intensities (4.58) for the $D \sim \beta$ coupling is given by

$$R_{D-X/\beta-A} = \frac{\sum_{i,j=1}^3 \sum_{n=1}^2 \sum |\langle X|d_i|n\rangle \langle n|d_j|B\rangle|^2}{\sum_{i,j=1}^3 \sum_{n=1}^2 \sum |\langle A|d_i|n\rangle \langle n|d_j|B\rangle|^2} \cdot \frac{\omega_{D \rightarrow X}^3}{\omega_{\beta \rightarrow A}^3}, \quad (4.61)$$

and similarly for $R_{\beta-A/D-X}$. Here \sum means summation over all hyperfine components of initial, intermediate and final states. Fitting the experimentally observed $R_{D-X/\beta \rightarrow A}$ and $R_{\beta-A/D-X}$ ratios, the values $A_{\perp} = 980$ and 1150 MHz for the $D, 12\sim\beta, 13$ and $D, 48\sim\beta, 47$ couplings were obtained, respectively. Figure 4.12 shows good agreement of observed and calculated ratios. This constants are two times larger than the $A_{\parallel} = 477$ MHz for the $\beta 1_g$ states derived from hyperfine structure analysis [47]. Assuming that the D and β wavefunctions are described adequately in the separated ions approach, these constants should be equal, $A_{\perp} = A_{\parallel}$, that is not observed.

In the case of the $2_g(^1D) \sim 1_u(^1D)$ coupling, interaction matrix elements were determined by solving the equations in the two-state model. Laser band width was also insufficient to resolve the splitting of the near resonant rovibrational levels of the $2_g(^1D)$ and $1_u(^1D)$ IP states [50]. Hence, the authors employed another method. The line shapes were deconvoluted by two lines with the Lorentzian form to derive their transition frequencies for determining the energies of coupled rovibrational levels. The electronic interaction matrix element was determined as $H_{hf}^{el} = 0.0482$ (59) cm^{-1} similar with that for $D \sim \beta$ and $E \sim \gamma$.

Due to mixing of the zero-order states, which have different luminescence lifetimes (τ and τ' for states Ψ and Ψ' , respectively), the luminescence lifetimes for the perturbed $|1\rangle$ and $|2\rangle$ states are determined as follows:

$$\tau_1^{-1} = \tau^{-1} \cdot \cos^2 \theta + \tau'^{-1} \cdot \sin^2 \theta \quad (4.62)$$

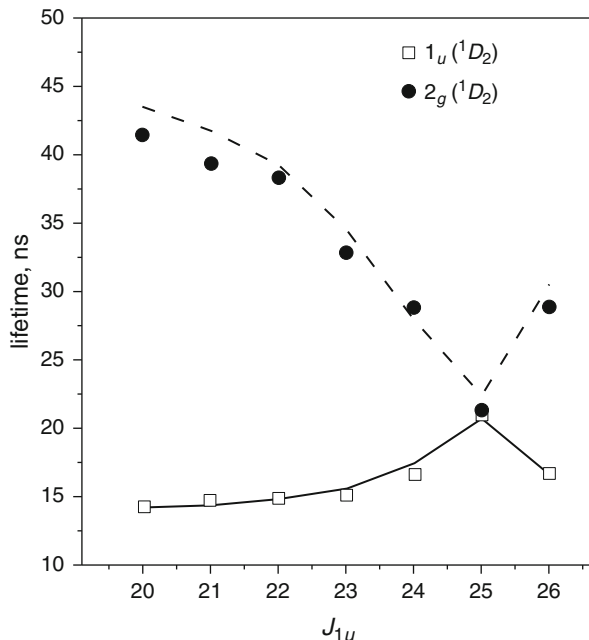
$$\tau_2^{-1} = \tau^{-1} \cdot \sin^2 \theta + \tau'^{-1} \cdot \cos^2 \theta \quad (4.63)$$

Direct measurements of the radiation lifetimes allow to estimate the mixing angle which is determined in Eq. (4.29) and hence matrix elements of the hyperfine interaction. Figure 4.13 demonstrates the reasonability of this method. Luminescence lifetimes observed for the $1_u(^1D)$ and $2_g(^1D)$ mixing states strongly depends on the rotational quantum number near the avoiding crossing $J_{1u} = 25 \sim J_{2g} = 24$ range. The upper energy component has lifetime larger than that of the lower one after the avoiding crossing and *vice versa*.

4.3.3 Rydberg-IP State Interaction

As it has been mentioned in Sect. 3.1, IP states are arranged between valence and Rydberg states. Heterogeneous interactions and avoiding crossing can occur at the range of high vibrational levels of IP states. The avoiding crossing of IP and Rydberg state *PECs* can occur on the outer Coulombic branch, leading to predissociation to neutral products (see Sect. 4.2.2), whereas on the inner wall

Fig. 4.13 Luminescence lifetimes of the $1_u(^1D)$ and $2_g(^1D)$ mixing states as a function of the J_{1u} . The solid and dashed lines show the calculated lifetimes with assumption that the hyperfine coupling matrix element $H_{\text{hr}} = 0.0482$ $(59) \text{ cm}^{-1}$ [50]



resulting in double minima or shelf-states in some cases. Low-lying vibrational levels, which are localized near R_e , can be described in harmonic approximation, whereas the character of the IP state *PECs* in the range of high levels changes from Morse-like at the shorter range to Coulomb potential at the outer branch. In the latter case, a “heavy Rydberg” model is applicable for description of the vibrational structure. The well-known formula describing the energy of the Rydberg series follows from the Coulomb interaction between Rydberg electron and ion core. The same approach can be applied for IP states, the potential of which is determined primarily by the Coulomb interaction between ion I^+ and anion I^- .

The energy of the vibrational levels of IP states can be written as:

$$E_{nj} = E_{\infty} - \frac{Ry(\mu)}{(n - \delta_{nj})^2}, \quad (4.64)$$

where E_{∞} is an energy of the separated ions (dissociation energy of the IP state), $Ry(\mu)$ is the Rydberg constant for the reduced mass μ of ion pair $\text{I}^+ + \text{I}^-$, n is rovibrational quantum number, δ_{nj} is quantum defect, which depends on vibrational and rotational quantum numbers. For pure Coulomb interaction plus centrifugal potential, δ is equal zero and

$$n = v + J + 1 \quad (4.65)$$

With a known numbering of vibrational and rotational quantum numbers of levels, the quantum defect can be found. The quantum defect can be expanded

similar to Rydberg states of atoms [51] by inverse even powers of $(n - \delta_\infty)$, where δ_∞ is the quantum defect at ionization energy

$$\delta_{nJ} = \delta_{\infty J} + \frac{\delta'}{(n - \delta_\infty)^2} + \dots, \quad (4.66)$$

Taking into account Eq. (4.64) and introducing a binding energy $E_b = E_{nJ} - E_\infty$, the Eq. (4.66) can be rewritten as:

$$\delta(E_b) = \delta(0) + \delta_1 E_b + \delta_2 E_b^2 + \dots \quad (4.67)$$

Pan and Mies [51] performed quantal calculations for LiI and confirmed that high vibrational levels near the dissociation limit form a Rydberg-like series with large negative quantum defects. They showed also that the dependence (4.67) is primarily linear in the near-dissociation range. Any deviation from the linear behavior of the $\delta(E_b)$ indicates the presence of perturbations.

Such vibrational analysis was performed for several first-tier IP states (DO_u^+ , EO_g^+ and $D'2_g$) of I_2 and other dihalogen molecules, the vibrational structure of which is well known for a large number of vibrational levels [52]. It was shown that analysis of $\delta(E_b)$ can be useful tool for revealing of avoiding crossing or other perturbations. This approach allowed to correct the numbering of some vibrational levels determined earlier [16].

Strong perturbations were found in the vibrational structure of the D state. Sudden change in $\delta(E_b)$ gradient was found at $E_b \approx -14500 \text{ cm}^{-1}$ ($T \approx 57670 \text{ cm}^{-1}$) which reflects the beginning of a perturbation region (Fig. 4.14). In this range, homogeneous and heterogeneous interactions result in avoiding crossing or weaker perturbations [22]. Figure 4.14 shows absolute positions of the Rydberg state vibrational levels. The energy of the $X[3/2]_c 6p \ 0_u^+$, $v = 0-2$ vibrational levels are equal to 58953, 59237 and 59449 cm^{-1} , respectively [53, 54], but the influence of the two latter levels was found in the $\delta(E_b)$ dependence. As noted by the authors of [53], the perturbations in the IP states caused by the $v = 3, 4$ vibrational levels of the $X[3/2]_c 6p; 1_u$ Rydberg state is seen (Fig. 4.14).

Renumbering of vibrational levels of the EO_g^+ and $D'2_g$ IP states allows to make more smooth dependence of the $\delta(E_b)$. However, this is not a major avoided crossing, but weak perturbations, which caused by Rydberg states remain. The «heavy Rydberg» approach predicts perturbations of the $D', v_D = 250-340$ ($E = 56500-59500 \text{ cm}^{-1}$) that is confirmed experimentally. In the $(2 + 1)$ REMPI spectra at this energy range [16], series of Rydberg vibrational bands ($\Delta E \sim 240 \text{ cm}^{-1}$) were found with superimposed series of closed spaced vibrational bands ($\Delta E \sim 20 \text{ cm}^{-1}$) (Fig. 4.15). The authors suggested that it is caused by vibronic interaction between the $X[3/2]_c 5d \ 2_g$ Rydberg state and the $D'2_g$ IP state. Each Rydberg vibrational level couples with a series of D' vibrational manifold by homogeneous interaction. In another energy range, 62500–64000 cm^{-1} the same effect observed due to coupling of the $X[3/2]_c 7s \ 1_g$, and $\beta 1_g$ states.

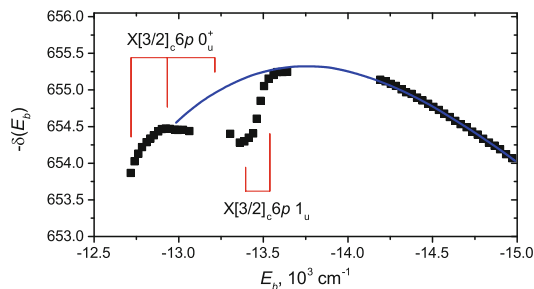


Fig. 4.14 The quantum defect of the $I_2(D)$ state $\delta(E_b)$ plotted at $E_b = 14000\text{--}15000\text{ cm}^{-1}$. Cubic extrapolation is shown by solid line [52]. Absolute positions of the Rydberg state vibrational levels are shown

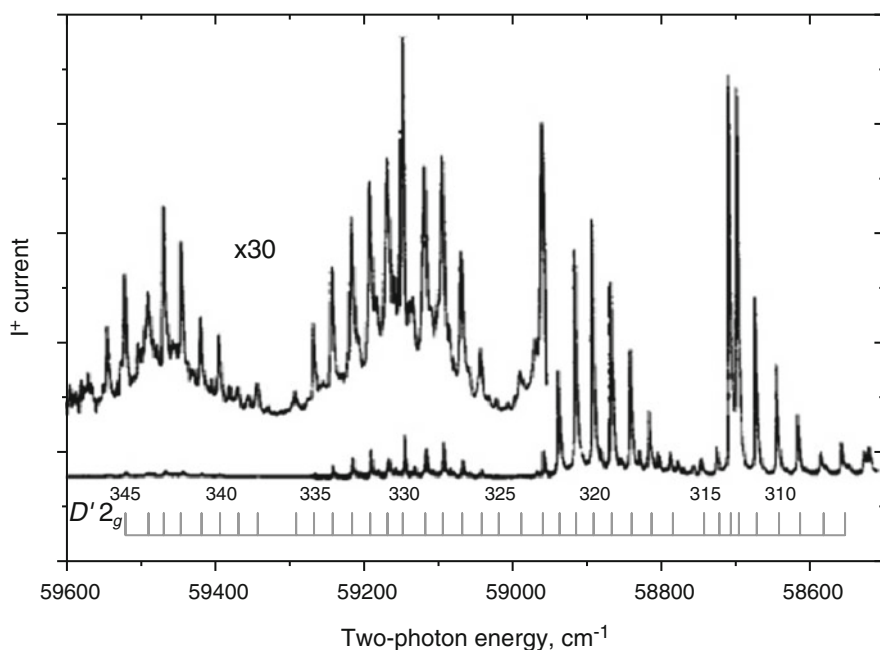


Fig. 4.15 The I^+ spectrum in the energy range $58500\text{--}59600\text{ cm}^{-1}$ [16]. Positions of the $D' 2_g$ vibrational levels are shown

In the diabatic description, the matrix elements H_{12} were determined for the $X [3/2]_c 7s 1g \sim \beta 1_g$ ($250 \pm 30\text{ cm}^{-1}$) and $X [3/2]_c 5d 2_g \sim D' 2_g$ ($450 \pm 150\text{ cm}^{-1}$) coupled states by solving the two-state coupling problem [16].

The value $H_{12} = 107(1)\text{ cm}^{-1}$ was obtained for the $X [1/2]_c 6p 0_u^+$ (RO_u^+) and FO_u^+ coupled states in the $\nu_F = 200\text{--}250$ range [55]. The electronic matrix element of interaction was estimated also for the $X [3/2]_c 5d 1g \sim \beta 1_g$ coupling states at the

Table 4.1 The matrix elements of the Rydberg~IP coupling

Coupled states	H_{12}, cm^{-1}	Configuration	References
$X[3/2]_c 7s 1g$	250 ± 30	$[2430]7s^1 + {}^3\Pi_1$	[16]
$\beta 1_g$		$[2242]{}^3\Sigma_1^- ([1432]{}^3\Pi_1)$	
$X[3/2]_c 5d 1_g$	>400	$[2430]5d_\sigma^1 + {}^3\Pi_1/5d_\pi^3 \Sigma_1^\pm$	[17]
$\beta 1_g$		$[2242]{}^3\Sigma_1^- ([1432]{}^3\Pi_1)$	
$X[3/2]_c 5d 2_g$	450 ± 150	$[2430]5d_\sigma^3 \Pi_2/5d_\pi^1 + {}^3\Delta_2$	[16]
$D'2_g$		$[2242]{}^1\Delta_2 ([1432]{}^3\Pi_2)$	
$X[1/2]_c 6p 0_u^+$	107 ± 1	$[2430]6p^3 \Pi_0$	[55]
$F 0_u^+$		$[2332]{}^3\Sigma_0^- ([1342]{}^3\Pi_0)$	

Major electronic configurations are shown. Minor configurations are shown in parentheses

$v_{Ry} = 3$ level of the Rydberg state where the abnormally low values of both the rotational constant and vibration energy were found [17]. The interaction matrix elements are summarized in Table 4.1. It should be noted that all of these values are sufficiently lower than typical values, for example, the interaction of the $D \sim (2) {}^1\Sigma_u^+$ in Cl_2 , where $H_{12} \sim 2000 \text{cm}^{-1}$.

In the diabatic representation, the two-electron operator $1/r_{12}$ is responsible for coupling of the configurations, which differ by two spin-orbitals [56]. Alternatively, the electronic configuration remains unchanged, and occupied molecular orbital changes its character from atomic to Rydberg as R decreases. This effect was called by Mulliken as MO Rydbergization [57]. In both cases, the total spin should be preserved. Thus, the electrostatic interaction is available between the states of the same symmetry in Hund's case (a).

The major configuration of all these Rydberg states is $[2430]nl$, and the Rydberg states have ${}^3\Pi$ symmetry. The dominant configurations of IP states at short internuclear separations were first derived by Mulliken [58]: $[1441]{}^1\Sigma (D 0_u^+)$, $[2332]{}^3\Sigma_0^- (F 0_u^+)$, $[2242]{}^3\Sigma_1(\beta 1_g)$ and $[2242]{}^1\Delta_2 (D'2_g)$. None of the dominant configurations can be responsible for Rydberg ~ IP homogeneous interaction. Minor contributions to wavefunctions of IP states have other MO configurations, which dominate at the more long distances and are discussed in Chap. 3. For example, the $D'2_g$ state has a minor configuration $[1432]{}^3\Pi_g$ and can be responsible for the Rydberg ~ IP vibronic coupling. The authors of [16] showed that all cases of such coupling mentioned above occur due to admixture of minor configurations to the IP states and the appropriate electronic matrix elements are of intermediate values. On the other hand, the $D \sim (2) {}^1\Sigma_u^+$ interaction in Cl_2 molecule is available due to major configurations $D [1441]$ and $[2430]4p$ states, and the coupling matrix element has a large value. The Franck-Condon factors for the high IP vibration levels and the Rydberg levels near the potential minimum are small, and no significant perturbations were observed.

Other perturbations of the Rydberg states were also observed that was exhibited in the intensity borrowing, Rydberg ~ Rydberg interaction [59]. However, detailed studies were carried out only partially.

References

1. Baklanov, K.I., Petrov, A.N., Titov, A.V., Kozlov, M.G.: Progress toward the electron electric-dipole-moment search: Theoretical study of the PbF molecule. *Phys. Rev. A*. **82**, 60501–60504 (2010). <https://doi.org/10.1103/PhysRevA.82.060501>
2. Landau, L.D., Lifshitz, E.M.: *Quantum mechanics* (3rd Edn, Revised and Enlarged). Pergamon, Oxford (1977)
3. Pique, J.P., Hartmann, F., Churassy, S., Bacis, R.: Hyperfine interactions in homonuclear diatomic molecules and u-g perturbations. I. Theory. *J. Phys.* **47**, 1909–1916 (1986). <https://doi.org/10.1051/jphys:0198600470110190900>
4. Jewsbury, P.J., Ridley, T., Lawley, K.P., Donovan, R.J.: Parity mixing in the valence states of I₂ probed by optical-optical double-resonance excitation of ion-pair. *J. Mol. Spectrosc.* **157**, 33–49 (1993). <https://doi.org/10.1006/jmsp.1993.1003>
5. Akopyan, M.E., Lukashov, S.S., Maslennikova, Y.D., Poretsky, S.A., Pravilov, A.M.: Hyperfine coupling of the iodine $E0_g^+$, $v_E = 19$ and $\gamma 1_u, v_\gamma = 18$ ion-pair states. *J. Phys. B At. Mol. Phys.* **40**, 1173–1181 (2007). <https://doi.org/10.1088/0953-4075/40/6/008>
6. Vigué, J., Broyer, M., Lehmann, J.C.: Natural hyperfine and magnetic predissociation of the I₂ B state I. — Theory. *J. Phys. Fr.* **42**, 937–947 (1981)
7. Tellinghuisen, J.: Potentials for weakly bound states in I₂ from diffuse spectra and predissociation data. *J. Chem. Phys.* **82**, 4012–4016 (1985). <https://doi.org/10.1063/1.448841>
8. Teichteil, C., Pelissier, M.: Relativistic calculations of excited states of molecular iodine. *Chem. Phys.* **180**, 1–18 (1994). [https://doi.org/10.1016/0301-0104\(93\)E0395-C](https://doi.org/10.1016/0301-0104(93)E0395-C)
9. de Jong, W.A., Visscher, L., Nieuwpoort, W.C.: Relativistic and correlated calculations on the ground, excited, and ionized states of iodine. *J. Chem. Phys.* **107**, 9046–9058 (1997). <https://doi.org/10.1063/1.475194>
10. Vigué, J., Broyer, M., Lehmann, J.C.: Natural hyperfine and magnetic predissociation of the I₂ B state III. — Experiments on magnetic predissociation. *J. Phys.* **42**, 961–978 (1981). <https://doi.org/10.1051/jphys:01981004207096100>
11. Martínez, E., Martínez, M.T., Castaño, F.: Iodine B³Π(0_u⁺) state predissociation: evaluation of the interaction mechanisms for predissociated levels of the B state. *J. Mol. Spectrosc.* **128**, 554–563 (1988). [https://doi.org/10.1016/0022-2852\(88\)90170-1](https://doi.org/10.1016/0022-2852(88)90170-1)
12. Huber, K.P., Herzberg, G.: *Molecular spectra and molecular structure*. Springer, Boston (1979)
13. Broyer, M., Vigué, J., Lehmann, J.C.: Direct evidence of the natural predissociation of the I₂ B state through systematic measurements of lifetimes. *J. Chem. Phys.* **63**, 5428–5431 (1975). <https://doi.org/10.1063/1.431275>
14. Pique, J.P., Hartmann, F., Bacis, R., Churassy, S., Koffend, J.B.: Hyperfine-induced ungerade-gerade symmetry breaking in a homonuclear diatomic molecule near a dissociation limit: ¹²⁷I₂ at the ²P_{3/2} – ²P_{1/2} limit. *Phys. Rev. Lett.* **52**, 267–270 (1984). <https://doi.org/10.1103/PhysRevLett.52.267>
15. Pique, J.P., Hartmann, F., Churassy, S., Bacis, R.: Hyperfine interactions in homonuclear diatomic molecules and u-g perturbations. II. Experiments on I₂. *J. Phys.* **47**, 1917–1929 (1986). <https://doi.org/10.1051/jphys:0198600470110191700>
16. Lawley, K.P., Ridley, T., Min, Z., Wilson, P.J., AlKahali, M.S.N., Donovan, R.J.: Vibronic coupling between Rydberg and ion-pair states of I₂ investigated by (2 + 1) resonance enhanced multiphoton ionization spectroscopy. *Chem. Phys.* **197**, 37–50 (1995)
17. Kvaran, Á., Wang, H., Jóhannesson, G.H., Yench, A.J.: REMPI spectra of I₂. The [²Π_{3/2}]_c 5d lg Rydberg state and interactions with ion pair states. *Chem. Phys. Lett.* **222**, 436–442 (1994). [https://doi.org/10.1016/0009-2614\(94\)00387-4](https://doi.org/10.1016/0009-2614(94)00387-4)

18. Mulliken, R.S.: The halogen molecules and their spectra. J-J-like coupling. Molecular ionization potentials. *Phys. Rev.* **46**, 549–571 (1934). <https://doi.org/10.1103/PhysRev.46.549>
19. Watanabe, K.: Ionization potentials of some molecules. *J. Chem. Phys.* **26**, 542–547 (1957). <https://doi.org/10.1063/1.1743340>
20. Myer, J.A.: Absorption cross section and photoionization yield of I₂ between 1050 and 2200 Å. *J. Chem. Phys.* **52**, 716–718 (1970). <https://doi.org/10.1063/1.1673044>
21. O’Grady, B.V., Donovan, R.J., Shobatake, K., Hiraya, A.: Fluorescence from ion-pair and Rydberg states of I₂. *Chem. Phys. Lett.* **122**, 612–616 (1985)
22. Hiraya, A., Shobatake, K., Donovan, R.J., Hopkirk, A.: Vacuum ultraviolet fluorescence excitation spectrum of I₂. *J. Chem. Phys.* **88**, 52–57 (1988). <https://doi.org/10.1063/1.454485>
23. Donovan, R.J., Ridley, T., Lawley, K.P., Wilson, P.: Two-colour optical double resonance ionisation spectrum of jet-cooled I₂: observation of the $f^{\prime}0_g^{+}$ (¹D) ion-pair state. *Chem. Phys. Lett.* **196**, 173–177 (1992). [https://doi.org/10.1016/0009-2614\(92\)85949-B](https://doi.org/10.1016/0009-2614(92)85949-B)
24. Donovan, R.J., Flood, R.V., Lawley, K.P., Yench, A.J., Ridley, T.: The resonance enhanced (2 + 1) multiphoton ionization spectrum of I₂. *Chem. Phys.* **164**, 439–450 (1992)
25. Ridley, T., De Vries, M., Lawley, K.P., Wang, S., Donovan, R.J.: The field-ionization of near-dissociation ion-pair states of I₂. *J. Chem. Phys.* **117**, 7117–7121 (2002). <https://doi.org/10.1063/1.1503777>
26. Kvaran, A., Yench, A.J., Kela, D.K., Donovan, R.J., Hopkirk, A.: Vibrationally resolved excitation functions for direct ion-pair (I⁺ + I⁻) formation from photodissociation of I₂. *Chem. Phys. Lett.* **179**, 263–267 (1991). [https://doi.org/10.1016/0009-2614\(91\)87035-A](https://doi.org/10.1016/0009-2614(91)87035-A)
27. Bogomolov, A.S., Grüner, B., Kochubei, S.A., Mudrich, M., Baklanov, A.V.: Predissociation of high-lying Rydberg states of molecular iodine via ion-pair states. *J. Chem. Phys.* **140**, 124311–124319 (2014). <https://doi.org/10.1063/1.4869205>
28. von Vangerow, J., Bogomolov, A.S., Dozmorov, N.V., Schomas, D., Stienkemeier, F., Baklanov, A.V., Mudrich, M.: Role of ion-pair states in the predissociation dynamics of Rydberg states of molecular iodine. *Phys. Chem. Chem. Phys.* **18**, 18896–18904 (2016). <https://doi.org/10.1039/C6CP02160C>
29. Saute, M., Aubert-Frécon, M.: Calculated long-range potential-energy curves for the 23 molecular states of I₂. *J. Chem. Phys.* **77**, 5639–5646 (1982). <https://doi.org/10.1063/1.443770>
30. Ishiwata, T., Yotsumoto, T., Motohiro, S.: Optical–optical double resonance spectroscopy of I₂ through the parity mixed valence states. *Bull. Chem. Soc. Jpn.* **74**, 1605–1610 (2001). <https://doi.org/10.1246/bcsj.74.1605>
31. Motohiro, S., Nakajima, S., Ishiwata, T.: Perturbation-facilitated optical–optical double resonance spectroscopy of the $h0_u^{-}$ (³P₁) and $H1_u$ (³P₁) ion-pair states of I₂. *J. Chem. Phys.* **117**, 187–196 (2002). <https://doi.org/10.1063/1.1481391>
32. Motohiro, S., Nakajima, S., Aoyama, K., Kagi, E., Fujiwara, H., Fukushima, M., Ishiwata, T.: Analysis of the 0_g^{-} (³P₁)–B ¹3 Π(0_u⁻) system of I₂ by perturbation-facilitated optical–optical double resonance. *J. Chem. Phys.* **117**, 9777–9784 (2002). <https://doi.org/10.1063/1.1516790>
33. Baturo, V.V., Cherepanov, I.N., Lukashov, S.S., Poretsky, S.A., Pravilov, A.M., Zhironkin, A. I.: Heterogeneous and hyperfine interactions between valence states of molecular iodine correlating with the I(²P_{1/2}) + I(²P_{1/2}) dissociation limit. *J. Chem. Phys.* **144**, 184310–184318 (2016). <https://doi.org/10.1063/1.4948630>
34. Baturo, V.V., Cherepanov, I.N., Lukashov, S.S., Poretsky, S.A., Pravilov, A.M.: Spectroscopic constants and potential energy curves of some iodine valence ungerade weakly bound states. *J. Phys. B Atomic Mol. Phys.* **055101**(8pp), 48 (2015). <https://doi.org/10.1088/0953-4075/48/5/055101>
35. Akopyan, M.E., Baturo, V.V., Lukashov, S.S., Mikheev, L.D., Poretsky, S.A., Pravilov, A.M., Vasyutinskii, O.S.: Hyperfine interaction in molecular iodine between the 0_g^{+} , 1_u and 0_u^{-} states correlating with the I(²P_{1/2}) + I(²P_{1/2}) dissociation limit. *J. Phys. B Atomic Mol. Phys.* **48**, 25102. (14pp) (2015). <https://doi.org/10.1088/0953-4075/48/2/025102>

36. Stephan-Rosbach, K.-H.; Comes F.J.: new I₂ emission from iodine molecule atom recombination reaction. *Chem. Phys.* **80**, 121–128 (1983). [https://doi.org/10.1016/0301-0104\(83\)85173-8](https://doi.org/10.1016/0301-0104(83)85173-8)
37. Exton, R.J., Balla, R.J.: ArF laser excitation, collisional transfer, and quench-free fluorescence in I₂/foreign gas mixtures. *J. Quant. Spectrosc. Radiat. Transf.* **86**, 267–283 (2004). <https://doi.org/10.1016/j.jqsrt.2003.08.006>
38. Ridley, T., Lawley, K.P., Donovan, R.J.: Observation of three weakly bound valence states of I₂. *J. Chem. Phys.* **127**, 154306–154307 (2007). <https://doi.org/10.1063/1.2795722>
39. Akopyan, M.E., Baturo, V.V., Lukashov, S.S., Poretsky, S.A., Pravilov, A.M.: Spectroscopic constants and the potential energy curve of the iodine weakly bound 0_g⁺ state correlating with the I(²P_{1/2}) + I(²P_{1/2}) dissociation limit dissociation limit. *J. Phys. B Atomic Mol. Phys.* **46**, 055101. (9pp) (2013). <https://doi.org/10.1088/0953-4075/46/5/055101>
40. Akopyan, M.E., Baturo, V.V., Lukashov, S.S., Poretsky, S.A., Pravilov, A.M.: Spectroscopic constants and potential energy curve of the iodine weakly bound 1_u state correlating with the I(²P_{1/2}) + I(²P_{1/2}) dissociation limit dissociation limit. *J. Phys. B Atomic Mol. Phys.* **025101** (7pp), 48 (2015). <https://doi.org/10.1088/0953-4075/48/2/025101>
41. Perrot, J.P.P., Femelat, B., Broyer, M., Chevaleyre, J.: Ω doubling in 1 g state and electronic transition moments for B0_u⁺ towards 0_g⁺ and 1_g(³P₂) states of iodine. *Mol. Phys.* **61**, 97–108 (1987). <https://doi.org/10.1080/00268978700101011>
42. Ishiwata, T., Motohiro, S., Kagi, E., Fujiwara, H., Fukushima, M.: Optical-optical double-resonance spectroscopy of the 1_u(³P₂) and 2_u(³P₂) states of I₂ through the A³Π(1_u) State. *Bull. Chem. Soc. Jpn.* **73**, 2255–2261 (2000). <https://doi.org/10.1246/bcsj.73.2255>
43. Kagi, E., Yamamoto, N., Fujiwara, H., Fukushima, M., Ishiwata, T.: Optical-optical double resonance spectroscopy of the 1_g(³P₁)-A³Π(1_u)-X¹Σ_g⁺ transition of I₂. *J. Mol. Spectrosc.* **216**, 48–51 (2002). <https://doi.org/10.1006/jmsp.2002.8676>
44. Motohiro, S., Ishiwata, T.: Optical-optical double resonance spectroscopy of the H1_u(³P₁)-A³Π_u-X¹Σ_g⁺ transition of I₂. *J. Mol. Spectrosc.* **204**, 286–290 (2000). <https://doi.org/10.1006/jmsp.2000.8229>
45. Motohiro, S., Umakoshi, A., Ishiwata, T.: Perturbation-facilitated optical-optical double-resonance spectroscopy of the 1_u(¹D) and 2_u(¹D) ion-pair states of I₂ through the parity mixing intermediate state. *J. Mol. Spectrosc.* **208**, 213–218 (2001). <https://doi.org/10.1006/jmsp.2001.8379>
46. Baturo, V.V., Lukashov, S.S., Poretsky, S.A., Pravilov, A.M., Vasyutinskii, O.S.: Mixing of the D0_u⁺ and 82_u ion-pair states of iodine molecule. *Chem. Phys. Lett.* **638**, 244–248 (2015). <https://doi.org/10.1016/j.cplett.2015.08.047>
47. Knöckel, H., Richter, H., Siese, M., Tiemann, E.: Hyperfine structure of the lowest 0+g and 1g ion pair states of I₂. *Mol. Phys.* **68**, 917–930 (1989). <https://doi.org/10.1080/00268978900102631>
48. Koffend, J.B., Bacis, R., Broyer, M., Pique, J.P., Churassy, S.: C.W. Optical-optical double resonance in I₂: hyperfine structure in the E0_g⁺ – B0_u⁺ system. *Laser Chem.* **1**, 343–355 (1983). <https://doi.org/10.1155/LC.1.343>
49. Perrot, J.P., Broyer, M., Chevaleyre, J., Femelat, B.: Extensive study of the 1_g(³P₂) ion pair state of I₂. *J. Mol. Spectrosc.* **98**, 161–167 (1983). [https://doi.org/10.1016/0022-2852\(83\)90211-4](https://doi.org/10.1016/0022-2852(83)90211-4)
50. Nakano, Y., Ukeguchi, H., Ishiwata, T.: Observation and analysis of the 2_g(¹D) ion-pair state of I₂: the g/u mixing between the 1_u(¹D) and 2_g(¹D) states. *J. Chem. Phys.* **121**, 1397–1404 (2004). <https://doi.org/10.1063/1.1756134>
51. Pan, S., Mies, F.H.: Rydberg-like properties of rotational-vibrational levels and dissociation continuum associated with alkali-halide charge-transfer states. *J. Chem. Phys.* **89**, 3096 (1988). <https://doi.org/10.1063/1.454966>
52. Gallagher, T.F.: *Rydberg Atoms*. Cambridge University Press, Cambridge (1994)

53. Donovan, R.J., Lawley, K.P., Ridley, T.: Heavy Rydberg behaviour in high vibrational levels of some ion-pair states of the halogens and inter-halogens. *J. Chem. Phys.* **142**, 1–10 (2015). <https://doi.org/10.1063/1.4921560>
54. Venkateswarlu, P.: Vacuum ultraviolet spectrum of the iodine molecule. *Can. J. Phys.* **48**, 1055–1080 (1970)
55. Ridley, T., Beattie, D.A., Cockett, M.C.R., Lawley, K.P., Donovan, R.J.: A re-analysis of the vacuum ultraviolet absorption spectrum of I₂, Br₂, and ICl using ionization energies determined from their ZEKE-PFI photoelectron spectra. *Phys. Chem. Chem. Phys.* **4**, 1398–1411 (2002). <https://doi.org/10.1039/b109555m>
56. Hoy, A.R., Jaywant, S.M., Brand, J.C.D.: A rotationally-resolved Rydberg transition of I₂. *Mol. Phys.* **60**, 749–759 (1987). <https://doi.org/10.1080/00268978700100511>
57. Lefebvre-Brion, H., Field, R.W.: Chapter 5 – Interpretation of the perturbation matrix elements. In: Field, H.L.-B.W. (ed.) *The spectra and dynamics of diatomic molecules*, pp. 275–346. Academic, San Diego (2004)
58. Mulliken, R.S.: Rydberg states and Rydbergization. *Acc. Chem. Res.* **9**, 7–12 (1976). <https://doi.org/10.1021/ar50097a002>
59. Mulliken, R.S.: Iodine revisited. *J. Chem. Phys.* **55**, 288–309 (1971). <https://doi.org/10.1063/1.1675521>
60. Sjödin, A.M., Ridley, T., Lawley, K.P., Donovan, R.J.: Observation of a substantially-bound excited-core Rydberg state in I₂ by optical triple resonance. *Chem. Phys. Lett.* **416**, 64–69 (2005). <https://doi.org/10.1016/j.cplett.2005.09.029>

Chapter 5

Collision-Induced Processes in Iodine Molecule

5.1 Background

Exchange of translational, rotational and vibrational energy of diatomic molecules in collisions with colliding partners (atoms or molecules) are well currently investigated. Translational-translational ($T \leftrightarrow T$), rotational-translational ($R \leftrightarrow T$) and vibrational-translational ($V \leftrightarrow T$) energy transfer processes in broad class of molecules have been thoroughly studied and discussed many years ago (see e.g [1, 2] and references). Electronic deactivation of electronically excited molecules and collision-induced predissociation have been discussed in the literature widely. The term “quenching” is often used. It means “net electronic deactivation” including electronic deactivation, and collision-induced predissociation [3].

$T \leftrightarrow T$ Processes It has been shown that $T \leftrightarrow T$ energy transfer processes are very fast, so a time of fully translational thermalization of “hot” molecules “A” in a bath “B” is close to a the time interval between successive collisions [1].

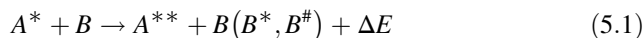
$R \leftrightarrow T$ and $T \leftrightarrow R$ Processes The time of thermalization of rotationally hot molecules depends strongly on the value of rotational quantum. For ground state hydrogen molecules (the rotational constant $B_e = 61 \text{ cm}^{-1}$), ~ 200 collisions are needed for the onset of an equilibrium rotational distribution at bath temperature $\sim 300 \text{ K}$, whereas for the ground state iodine molecules ($B_e \approx 0.04 \text{ cm}^{-1}$) an equilibrium rotational distribution is set after a few collisions only. One should note that the selection rules for a rotational quantum number change, $\Delta J - \text{even}$, and $\Delta J - \text{odd}$ are valid for homonuclear and heteronuclear diatomic molecules, respectively [1, 2, 4]. According to the adiabatic principle (see [1] and references), for massive molecules with low rotational constants, $R \leftrightarrow T$ exchange can be described in the framework of classical mechanics. In this case, $R \leftrightarrow T$ processes with large ΔJ are possible.

$V \rightarrow T$ and $T \rightarrow V$ Processes Probability (P) of $V \rightarrow T$ (vibrational relaxation) and $T \rightarrow V$ (vibrational excitation) transition per a collision depends very strongly on the value of vibrational quantum. Therefore, it is very low ($P_{1,0} \sim 10^{-8}$) for N_2

ground state molecules in $N_2(X, v_X = 1) + N_2(X, v_X = 0)$ collisions ($\omega_e = 2358 \text{ cm}^{-1}$) and much higher for the $Cl_2(X, v_X = 1) + Cl_2(X, v_X = 0)$ collisions ($\omega_e = 557 \text{ cm}^{-1}$) ($P_{1,0} \sim 2 \cdot 10^{-5}$) (see e.g [1, 2] and references). Probabilities of the $V \leftrightarrow T$ increase with a vibrational quantum number of the state, so it can be close to 1 near dissociation limit. The Δv – any propensity rule is valid for energy transfer from vibrational levels corresponding to low vibrational quanta. For very low vibrational quanta transitions with large Δv , $\Delta E_{v,v+1} \approx kT$, become possible.

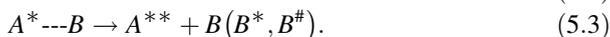
One should note that “pure” $V \leftrightarrow T$ processes are impossible. They are always accompanied by $T \leftrightarrow T$ and $R \leftrightarrow T$ energy transfer due to high probabilities of the latter.

Electronic Deactivation This term means a collision-induced transition to other electronic states of a particle (atom or molecule), i.e. $E \rightarrow E'$ energy transfer which excludes reverse $E \leftarrow E'$ process since rather large energy ΔE losses in the former. Rate constants of electronic deactivation



(the labels * and # mean electronic and rovibrational excitation, respectively, the excitation energy of A^{**} is less than that of A^*) can be large if:

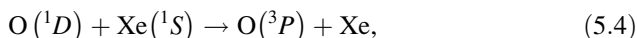
- Excited complex ($A^* \cdots B$) is formed in the collision of electronically excited particle A^* with colliding partner B (atom or molecule) which predissociates fast to $A^{**} + B(B^*, B^\#)$.



The rate constant of predissociation ($k_{5,3}$) has to be comparable or higher than that of complex dissociation ($k_{5,2}$) (see [5–9] and references). This model is called as “collision complex model”.

- Quasi-resonant energy transfer process occurs, i.e. $\Delta E \approx kT$ in process (5.1) (see [1, 10–13] and references).

Well known examples of the first type of electronic deactivation are deactivation of oxygen atoms in the first excited state, $O(^1D)$, in collisions with $B = Xe$ and ground state molecules N_2 , CO , O_2 , CO_2 , for example [6],



$k_{5,4} = 7 \cdot 10^{-11} \text{ cm}^3/\text{s}$. Bound $XeO(a^1\Sigma^+, b^1\Pi)$ states are formed in the collisions of excited $O(^1D)$ atom with Xe ground state atom; they predissociate rather fast due to the strong spin-orbit coupling of heavy Xe atom. Colliding partners N_2 , CO , O_2 , CO_2 have much weaker spin-orbit couplings, but three-atomic complexes possess a much higher lifetime (see [5–9] and references). The rate constant of $O(^1D)$ atom deactivation in collisions with He atom is extremely low

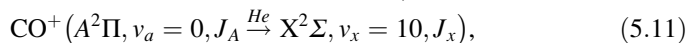
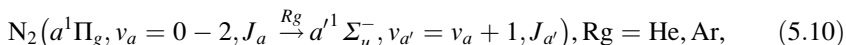
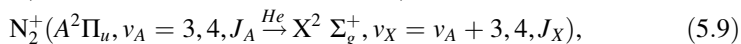
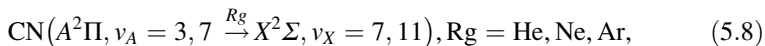
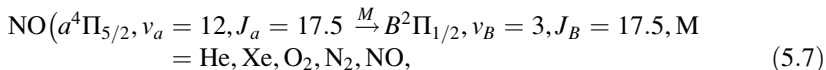
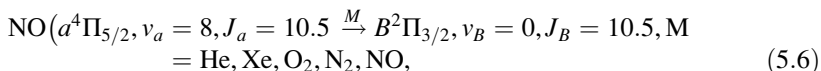
since HeO states correlating with the $O(^1D) + He(^1S)$ are repulsive. The probability of nonadiabatic transition is extremely low in this case due to high Massey parameter [1],

$$\zeta = \frac{1/\tau}{\Delta E/\hbar}. \quad (5.5)$$

Quasi-resonant energy transfer processes are occurred in collisions of $N_2(A^3\Sigma_u^+)$ with $CO(X^1\Sigma_g^+)$ [10], $N_2(X^1\Sigma_g^+)$ [12] and $N_2(A^3\Sigma_u^+, B'^3\Sigma_u^-, B^3\Pi_g)$ with $Xe(^1S)$ [13].

Collision-Induced Predissociation Spontaneous predissociation has been discussed in Chap. 4. When electronically excited molecule collides with a colliding partner, which perturbs the former, *collision-induced* predissociation can occur. In this case, predissociation channels, strongly forbidden for spontaneous predissociation, can be allowed. This type of processes is fairly well investigated experimentally in the iodine molecule BO_u^+ state (see Sect. 5.3.1). Unfortunately, there are no theoretical models for collision-induced predissociation having a predictive character in the literature (see [13–19]).

Collision-Induced Nonadiabatic Transitions Between Bound States Perturbations induced by a collision $A^* + B$ can result in non-adiabatic transitions between rovibronic levels of the A bound states. These effects are very specific regarding nature of colliding partners and their rovibronic states [18–20]. Some state-to-state collision-induced nonadiabatic transitions (CINATs) namely,



have been studies with rather high state resolution (see [18–21] and references).

Processes (5.6 and 5.7) are examples of so-called “perturbation facilitated” [18] or “perturbation assisted” CINATs, occurred between states which may be mixed in unperturbed, “free” or isolated, molecule. The perturbation facilitated CINATs are well described in framework of so-called “gateway” model [18, 19, 22, 23], if a collision is “sudden”, i.e. collision duration and perturbation matrix element of the “initial” (i) and “final” (f) mixed states in free molecule are small:

$$\tau_{coll} \cdot V_{i,f} \leq \hbar. \quad (5.13)$$

($V_{i,f} \ll 1 \text{ cm}^{-1}$ for $\tau_{coll} \approx 3 \text{ ps}$). Besides, a collision has to be weak, i.e. energy gap between the states is independent of $A^* - B$ distance (see [18] and references). The gateway model is valid if mixing coefficients in a free molecule $C_{i,f}$ is low due to extremely low perturbation matrix element $V_{i,f}$. The processes (5.6) and (5.7) for $M = \text{He}$ answer this condition due to extremely low FCF of the initial and final states. For $M = \text{Xe}, \text{O}_2, \text{N}_2, \text{NO}$, this model is invalid since $V_{i,f} > 1 \text{ cm}^{-1}$, and more complex model have to be used [22].

According to gateway model, the cross-section for a CINAT between rovibronic levels J_1, J_2 of electronic states $|1\rangle, |2\rangle$ is

$$\sigma_{1,J_1,2,J_2} \approx \sigma_{i,J_i,i,J_f} \cdot C_{i,f}^2 + \sigma_{f,J_i,f,J_f} \cdot C_{i,f}^2 \quad (5.14)$$

where σ_{i,J_i,i,J_f} is $R-T$ cross-section.

The (5.9) and (5.10) CINATs are typical so-called “perturbation-irrelevant” [18] processes since $u \leftrightarrow g$ nonadiabatic transitions are strongly forbidden in a free homonuclear diatomic molecule.

Models which describe some of experimental features observed in studies processes (5.8), (5.9), (5.10) and (5.11) have been created. They reproduce selection and propensity rules and cross-sections for *near resonant* CINATs but are strict invalid for *off-resonant* CINATs (see [18–20] and references). M. Alexander [21] discussed process (5.12) in the framework of interaction between permanent dipole moment of N_2O and transition electric dipole between CaO electronic states.

5.2 Rotational, Vibrational and Rovibrational Energy Transfer in Iodine Molecule

R-T Processes Data on cross-section (rate constants) of “pure” $R - T$ processes in $\text{I}_2(B0_u^+)$ state are given in Steinfeld’s compilation [3] (see [24], also). Analysis of these data shows that cross-sections of the processes under discussion are $\sigma_{R-T} \approx 4 \cdot 10^{-15} \text{ cm}^2$ for colliding partners $M = \text{Rg}, \text{I}_2(X)$, independent of rotational quantum number for $J_B > 15$. Total, for all final rotational states, rate constants $k_{R-T} = \sigma_{R-T} \cdot V \approx 1.5$ ($M = \text{I}_2(X), \text{Xe}$) – 6 ($M = \text{He}$) in units $10^{-10} \text{ cm}^3/\text{s}$ ($V = 2.2 \cdot 10^4 \text{ cm/s}$ ($M = \text{I}_2, \text{Xe}$) – $12.5 \cdot 10^4 \text{ cm/s}$ ($M = \text{He}$)) are mean relative velocities of the $\text{I}_2(B) - M$ colliding partners). Many rotational states are populated in the processes, especially for high initial rotational levels.

V-T + R-T Processes Vibrational distribution among final vibronic levels have been studied at several initial $\text{I}_2(B, v_B)$ levels, $v_B = 43$ for $M = \text{I}_2(X), \text{Xe}$ and $v_B = 15, 25, 43$ for $M = \text{He} - \text{Ar}$ [3]. They are rather wide, $\Delta v \approx 10$ for $v_B \geq 15$. Total, for all final vibronic levels, rate constants $k_{V-T} \approx 5 \cdot 10^{-11} \text{ cm}^3/\text{s}$ for $v_B = 43$,

$M = I_2(X)$, Xe and $\approx 1.5 \cdot 10^{-10} \text{ cm}^3/\text{s}$, $M = \text{He}$. Data for other rare gases are contradictory [3]. To estimate k_{V-T} rate constants for other B state vibronic levels, one can use empirical models, for example, mean probability of $V-T$ process $\langle P_{v+1,v} \rangle$ is:

$$\langle P_{v+1,v} \rangle = a \left(kT/\Delta E + \exp[-b \Delta E/kT] \right)$$

Here, a , b are adjustable parameters which should be fitted to describe experimental data, $\Delta E = E_i - E_f$ [25].

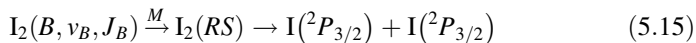
As it is mentioned in Sect. 5.1, the $V-T$ processes are always accompanied by $R \leftrightarrow T$ energy transfer. Analysis of the data given in [3] shows [26] that population of rovibronic levels formed due to from the $V-T + R-T$ processes can be estimated as a product of those for $V-T$ and $R-T$ processes discussed in this Section and [3].

5.3 Collision-Induced Nonadiabatic Processes in Iodine Molecule

5.3.1 Collision-Induced Predissociation of the $I_2(B0_u^+)$ State

The $I_2(B0_u^+)$ state is the only one among iodine molecule valence and IP states in which spontaneous predissociation was detected and studied (see Sect. 3.1). Mechanisms of spontaneous predissociation of Rydberg states are unknown in detail up to the present because of their complication. Only in recent works [27, 28] time-resolved experiments allowed to demonstrate directly the role of IP states as an intermediate gates in predissociation.

Quenching of the $I_2(B0_u^+)$ state in collisions with various partners were studied repeatedly (see [3] and references). It is obviously that the principal channel of the quenching at least for $M \neq I_2(X)$ is collision-induced predissociation (CIP)



(RS means repulsive state (states)), since electronic deactivation of the $I_2(B, v_B, J_B)$ molecules in collisions with He, e.g., is impossible (see Sect. 1). The CIP rate constant for $M = I_2(X)$, $k_{5.15}(I_2(X)) \approx 4 \cdot 10^{-10} \text{ cm}^3/\text{s}$ and is independent of v_B . The $k_{5.15}(\text{Rg})$ values smoothly increase with v_B . For Rg = He, e.g., $k_{5.15}(\text{He}) \approx 5 \cdot 10^{-12} \text{ cm}^3/\text{s}$ ($v_B = 6$) – $10^{-10} \text{ cm}^3/\text{s}$ ($v_B = 50$), see [3] and references. The CIP rate constant for each RS has to oscillate with v_B due to oscillation of Franck-Condon densities (FCD s) for B/RS states (see [27, 28] and references). Therefore, it is very likely that RS are *gerade* $a1_g, a'0_g^+$ and $(1)2_g$ states correlating with the *aa* limit (see Fig. 1.1). Oscillations of Franck-Condon densities for the RS states are out of phase, so total $FCD(B/RS) = f(v_B)$ function can be smooth (see [29] and references). As to *ungerade* states, the $C1_u$ is the only state which intersects the B state. The $FCD(B/C) = f(v_B)$ function oscillates (see Fig. 4.3 and [28, 30]). Therefore, process (5.15) cannot occur due to the $B \sim C$ collision-induced coupling.

5.3.2 Collision-Induced Nonadiabatic Transitions between the Ion-Pair States

5.3.2.1 Background

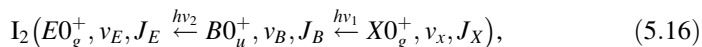
The history of studies of CINATs in the iodine IP states has been described in [31]. These processes and states attracted many scientific groups due to an observation of the $I_2(D'2_g \rightarrow A'2_u)$ lasing after optical $D0_u^+ \leftarrow X0_g^+$ transition (see Fig. 1.1) or an excitation of the $I_2 + M$ mixtures $M = Rg, CF_4, SF_6$, by high-energy electronic beams. It was believed that population of the D state accompanied by collision-induced energy transfer to the low vibronic level of the D' state (see [32] and references). Hydrogen lamp/monochromator system or ArF lasers were utilized for the optical excitation, and many vibronic levels of the D state were populated. Besides, all the studies were carried out at high M pressures, i.e. under *multiple-collision* conditions. Nevertheless, kinetic analyzes of experimental data were carried out in a “one-level one-way” approximation, and reverse processes were neglected. Therefore, the rate constants reported in these studies (see [32–34] and references) represents only average effective parameter and cannot be used for a description of CINATs in iodine molecule (see analysis in [31, 35]).

Application of the OODR technique has made a possible population of selected rovibronic levels of the IP states. Some versions of this technique are successfully utilized for study spectroscopic characteristics of valence and IP states (see Chap. 2). First observation of CINATs at *single-collision* condition was carried out in 1993 [36]. However, in this and two subsequent papers [37, 38] vibrational state distributions resulted in the $E \xrightarrow{M} D$ CINAT were only reported for collisions with $I_2(X)$ and some other colliding partners, $M = N_2, CO_2$. No data on CINAT rate constants were reported.

The first data on the $E, v_E, J_E \approx 55 \xrightarrow{I_2} D, v_D$ CINAT rate constants and D state vibrational level populations were published in 1999 [39] for wide, $v_E = 8–55$, vibronic level range.

5.3.2.2 Overview of Experimental Methods. State-of-the-Art

Standard two-step two-color, $h\nu_1 + h\nu_2$, OODR excitation scheme is utilized for population of selected rovibronic levels of the *gerade* $I_2(E0_g^+, f0_g^+)$ state, for example,



To populate selected rovibronic levels of other IP states, $D'2_g, \beta1g, D0_u^+, \gamma1_u, \delta2_u$, e.g., the authors employed three-step three-color, $h\nu_1 + h\nu_f + h\nu_2$, excitation scheme ($\lambda_f = 10644.0 \text{ \AA}$ is fundamental harmonic of the Nd:YAG laser) via $B0_u^+$

and $0_g^+, 1_u, 0_u^-$ (bb) states correlating with the ab and bb dissociation limits, respectively,

$$\text{I}_2(D0_u^+, \nu_D, J_D \xleftarrow{h\nu_2} 0_g^+, \nu_0, J_0 \xleftarrow{h\nu_f} B0_u^+, \nu_B, J_B \xleftarrow{h\nu_1} X0_g^+, \nu_X, J_X), \quad (5.17)$$

for example (see Chap. 2 for details).

The partial rate constants $k^M(i, \nu_i \rightarrow f)$ for the CINAT process

$$\text{I}_2(i, \nu_i) \xrightarrow{M} \text{I}_2(f) \quad (5.18)$$

are determined from the integrated luminescence intensities $I(f \rightarrow \nu)$ of the bands corresponding to the $\text{I}_2(f \rightarrow \nu)$ emissions as

$$\frac{I(f \rightarrow \text{val})}{I(i, \nu_i \rightarrow \text{val})} = \frac{k^M(i, \nu_i \rightarrow f)[M] + k^{\text{I}_2(X)}(i, \nu_i \rightarrow f)[\text{I}_2(X)]}{k_{i-\text{val}}(\nu_i)} \cdot \frac{k_{f-\text{val}}}{\sum_{k_{f-\text{val}}}}. \quad (5.19)$$

where $\Sigma -$ is a summation over all available $f \rightarrow \text{val}$ transitions.

Here,

- i, f are initial (optically populated) and final populated in a CINAT IP states, luminescence spectrum from which to the appropriate valence state, val , is measured,

$$\begin{aligned} & \text{I}_2(i, \nu_i \rightarrow \text{val}) + h\nu \\ & \text{I}_2(f, \nu_f \rightarrow \text{val}) + h\nu \end{aligned} \quad (5.21)$$

- $k_{i-\text{val}}(\nu_i)$ and $k_{f-\text{val}}$ are Einstein coefficients of transitions (5.21) for the optically and collisionally populated vibronic levels, respectively (see Sect. 3.3 for details),
- $k^M(i, \nu_i \rightarrow f)$ and $k^{\text{I}_2(X)}(i, \nu_i \rightarrow f)$ are partial rate constants of CINAT (5.18) for M and $\text{I}_2(X)$,
- Σ is a summation over all available $f \rightarrow \text{val}$ transitions.

Pressure dependences of the ratio (5.19) are measured at the constant iodine pressure and the M pressures which correspond single-collision condition, usually, $p_M = 0\text{--}2$ Torr. Only the linear low-pressure portion $\frac{I(f \rightarrow \text{val})}{I(i, \nu_i \rightarrow \text{val})} = \varphi(p_M)$ functions are used to obtain the rate constants. In this pressure range, secondary processes due to subsequent collisions can be safely neglected.

The vibrational distributions $P(i, \nu_i; \nu_f)$ of the final states are determined as

$$P(i, \nu_i; \nu_f) = \frac{k^M(i, \nu_i \rightarrow f, \nu_f)}{k^M(i, \nu_i \rightarrow f)}.$$

Measurements of the $f, \nu_f \rightarrow \text{val}$ luminescence spectra with high spectral resolution in pure iodine vapor and then in mixture with M are needed. The luminescence spectra are fit by simulations, in which populations of the ν_f levels are used as adjustable parameters. The spectrum obtained in pure iodine vapor is used to obtain

the $P(i, v_i; v_f)$ for pure iodine. These distributions are utilized for simulation of the spectrum measured in a mixture. Then the $P(i, v_i; v_f)$ for nonadiabatic transitions induced by collisions with M are determined by subtracting the I_2 contribution.

The uncertainty of the $k^M(i, v_i \rightarrow f)$ rate constants (10–20%, usually) accumulates the uncertainties of the experimental spectra and calibration of the condenser/monochromator/PMT system, mainly. Uncertainties of the measured vibrational level populations are larger and vary from 10 to 100% depending on the population.

To understand a mechanism of population of final states and determine radiative lifetimes of the optically populated states and their quenching rate constants, it is advantageous to measure temporal behaviors of luminescence intensities of initial and final states (see [40] and references).

5.3.2.3 Theoretical Models

Three models were utilized by the authors with colleagues for analysis of CINAT mechanisms. Simple one-dimensional model potentials:

$U_{\text{eff}}(R) = 4\epsilon \left[(R_0/R)^{12} - (R_0/R)^6 \right] - \frac{C_n}{R^n} + \frac{M^2}{2\mu R^2}$. were used in the first works [41–43] to understand the mechanism of non-resonant non-adiabatic transitions corresponding to large Massey parameter (5.5). Here [1, 44]:

R are the $I_2(\text{IP}) - M$ distances,

- ϵ - are the depths of the Lennard-Jones (6–12) potentials,

R_0 are the distances between colliding partners, where $U_{\text{eff}}(R) = 0$.

$M = \mu V b_e$ are the angular momenta of the relative motion of colliding particles, with reduced mass μ ,

$b_e = (\sigma_2/\pi)^{1/2}$ are the effective impact parameters of the processes under study,

$V = 12.5$ (M = He), 4.2 (M = Ar), 5.0 (M = N₂), 3.1 (M = CF₄), 2.2 (M = I₂) (in units of 10⁴ cm/s) are mean velocities of relative motions of the partners.

The first term in this E_q . is the Lennard-Jones (6–12) potential and the last term is the orbital kinetic energy of the collision pair. The term $-C_n/R^n$ corresponds to the first nonvanishing term of the multipole expansion of potential energy operator (see Sect. 5.3.2.5 for details).

Electrostatic model and semiclassical Born approximation (see [18, 21, 45, 46] and references) was utilized to describe nonadiabatic transition between the $I_2(\text{IP})$ states induced by collision partners possessing permanent electric dipole, quadrupole or transition electric dipole moments [31, 47–49] (see Sects. 3.2.5, 3.2.6 and 3.2.7 for details).

Some versions of quantum scattering calculations implementing diatomic-in-molecules (DIM) and long-range (LR) perturbation theories were used for analysis of dynamics and mechanisms of nonadiabatic transitions induced in $I_2(\text{IP})$ by collisions with rare gas atoms [49–51] and CF₄, SF₆ molecules possessing transition electric dipole moments [52] (see details in Sects. 3.2.4 and 3.2.5).

Let us discuss them in detail.

Isolated Diatomic Molecule Wavefunction The Hamiltonian for isolated diatomic iodine molecule is

$$\hat{H}_{I_2} = \frac{-\hbar^2}{2M} \frac{d^2}{dr^2} + \frac{(\hat{j} - \hat{j}^e)^2}{2Mr^2} + \hat{H}^e(r, \mathbf{r}^e). \quad (5.23)$$

Here M is the reduced mass of the molecule, r is the internuclear distance, \hat{j} is the total angular momentum of the molecule, composed of the electronic angular momentum \hat{j}^e and the angular momentum of the nuclei rotation. $\hat{H}^e(r, \mathbf{r}^e)$ is the electronic Hamiltonian for fixed internuclear distance r , \mathbf{r}^e are electronic coordinates.

In the adiabatic approximation the solution of Schrödinger equation with Hamiltonian (5.23) is the product of electronic $|n\Omega\omega\sigma\rangle$, rotational $|jm\Omega\rangle$, and vibrational $|vj\rangle$ wavefunctions:

$$|n\Omega\omega\sigma vjm\rangle = |n\Omega\omega\sigma\rangle |jm\Omega\rangle |vj\rangle, \quad (5.24)$$

where, according to Hund case (c) coupling scheme, $\Omega(m)$ is the projection of the total electronic angular momentum on the molecular (laboratory) axis, σ is the inversion parity and $\omega = u$ or g specifies the symmetry with respect to permutation of identical nuclei, v is the vibrational quantum number. $|n\Omega\omega\sigma\rangle$ is the eigenfunction of the electronic Hamiltonian $\hat{H}^e(r, \mathbf{r}^e) |n\Omega\omega\sigma\rangle = V_{n\Omega\omega\sigma}(r) |n\Omega\omega\sigma\rangle$. The vibrational wave function satisfies the following Schrödinger equation:

$$\left(\frac{-\hbar^2}{2M} \frac{d^2}{dr^2} + \frac{\hbar^2(j(j+1) - \Omega^2)}{2Mr^2} + V_{n\Omega\omega\sigma}(r) \right) |vj\rangle = \epsilon_{n\Omega\omega\sigma vj} |vj\rangle. \quad (5.25)$$

The rotational wave function is proportional to Wigner function.

$|jm\Omega\rangle = \sqrt{j(j+1)/4\pi} D_{M\Omega}^j(\alpha, \beta, \gamma = 0)$. The nonadiabatic perturbation $\hat{W} = \hat{W}_1 + \hat{W}_2$ has the following matrix elements

$$\begin{aligned} & \langle n\Omega\omega\sigma vjm | \hat{W}_1 | n'\Omega'\omega'\sigma'v'j'm' \rangle = \\ & \delta_{\Omega\Omega'} \delta_{\omega\omega'} \delta_{\sigma\sigma'} \delta_{jj'} \delta_{mm'} \left\langle vj \left| \left\langle n\Omega\omega\sigma \left| \frac{d}{dr} \right| n'\Omega'\omega'\sigma' \right\rangle \frac{-\hbar^2}{M} \frac{d}{dr} \right| v'j' \right\rangle + \\ & \delta_{\Omega\Omega'} \delta_{\omega\omega'} \delta_{\sigma\sigma'} \delta_{jj'} \delta_{mm'} \left\langle vj \left| \frac{\hbar^2}{2Mr^2} \left\langle n\Omega\omega\sigma \left| \hat{j}_x^e{}^2 + \hat{j}_y^e{}^2 \right| n'\Omega'\omega'\sigma' \right\rangle \right| v'j' \right\rangle \times \\ & \langle n\Omega\omega\sigma vjm | \hat{W}_2 | n'\Omega \pm 1 \omega' \sigma' v' j' m' \rangle \\ & = \delta_{\omega\omega'} \delta_{jj'} \delta_{mm'} \sqrt{(J \pm \Omega + 1)(J \mp \Omega)} \left\langle vj \left| \frac{-\hbar^2}{2Mr^2} \left\langle n\Omega\omega\sigma \left| \hat{J}_{\mp}^e \right| n'\Omega \pm 1 \omega' \sigma' \right\rangle \right| v'j' \right\rangle \end{aligned}$$

Isolated Spherical Top Polyatomic Molecule Wavefunction The Hamiltonian for a spherical top polyatomic molecule is

$$\hat{H}_A = \hat{T}(Q) + \hat{H}_A^e(Q, \mathbf{r}^e) + \hat{W}_A(Q, \mathbf{r}^e), \quad (5.26)$$

where $\hat{T}(Q)$ is the nuclear kinetic energy operator, Q denotes the internal nuclear coordinates, $\hat{H}_A^e(Q, \mathbf{r}^e)$ is the electronic Hamiltonian for fixed nuclear coordinates Q , $\hat{W}_A(Q, \mathbf{r}^e)$ includes rotational energy and electronic-vibrational-rotational interactions [53]. In the following consideration, we will consider molecule A in its ground electronic state and neglect the rotation. The latter is achieved by replacing the spherical top rotational wavefunction $\sqrt{(2j_A + 1)/8\pi^2} D_{MK}^{j_A}(\alpha, \beta, \gamma)$ by the constant value $\sqrt{1/8\pi^2}$ corresponding to $j_A = M = K = 0$ quantum numbers of the ground rotational state, where \hat{j}_A is the total angular momentum of the molecule. In this approximation the solution of Schrödinger equation with Hamiltonian (5.26) is the product of electronic $|f\rangle$ and vibrational $|v_A\rangle$ wavefunctions:

$$|fv_A\rangle = |f\rangle|v_A\rangle. \quad (5.27)$$

As for diatomic molecule, the electronic wavefunction is the eigenfunction of the electronic Hamiltonian $\hat{H}_A^e(Q, \mathbf{r}^e) |f\rangle = V_A(Q) |f\rangle$. The vibrational wave function is solution of the Schrödinger equation with electronic potential $V_A(Q)$:

$$(\hat{T}(Q) + V_A(Q))|v_A\rangle = \epsilon_{v_A}|v_A\rangle. \quad (5.28)$$

Scattering Equations Collisions of molecules or atoms can be accompanied by changing of internal states of both colliding partners. (In this book, we do not consider chemical reactions). Various possible states are referred to as channels function. Those which are allowed (forbidden) by the energy conservation law are called *open (closed) channels*. In this section, we consider collisions between I_2 and a spherical top molecule A in its ground rotational and electronic state. The only difference from collision with rare gas atoms (Rg) in its ground state is that the transitions between the different vibrational levels of the A molecule are included. Therefore, equations obtained in this section can be applied for $I_2 + \text{Rg}$ collisions by omitting vibrational quantum number v_A and vibrational variables Q of the molecule A .

In collisions between I_2 and a spherical top molecule, the channel functions

$$|n\Omega\omega\sigma v j m\rangle |fv_A\rangle = |n\Omega\omega\sigma\rangle |j m \Omega\rangle |v j\rangle |fv_A\rangle, \quad (5.29)$$

(that diagonalize the Hamiltonians of isolated particles) are products of the free particles wavefunctions introduced above. Energies of the channels

$$\epsilon_{n\Omega\omega\sigma v j v_A} = \epsilon_{n\Omega\omega\sigma v j} + \epsilon_{v_A} \quad (5.30)$$

are sums of the free particles energies. Initial states of colliding particles referred to as the entrance channel. Inelastic as well as elastic scattering cross-sections for all

possible open channels can be obtained by solving the time-independent Schrödinger equation

$$\hat{H}\Psi(\mathbf{R}, \mathbf{r}, Q, \mathbf{r}^e) = E \Psi(\mathbf{R}, \mathbf{r}, Q, \mathbf{r}^e) \quad (5.31)$$

with wavefunction asymptotically represented as the sum of the incident plane wave for entrance channel and outgoing spherical waves for output channels [54]

$$\begin{aligned} \Psi(\mathbf{R}, \mathbf{r}, Q, \mathbf{r}^e) \\ \xrightarrow{R \rightarrow \infty} \frac{1}{\sqrt{k_{n_0\Omega_0\omega_0\sigma_0\nu_0j_0m_0}}} |n_0\Omega_0\omega_0\sigma_0\nu_0j_0m_0\rangle |f\nu_{A0}\rangle e^{iRz k_{n_0\Omega_0\omega_0\sigma_0\nu_0j_0m_0}} + \\ \sum_{n\Omega\omega\sigma\nu jm_A} \frac{f_{n\Omega\omega\sigma\nu jm_A \leftarrow n_0\Omega_0\omega_0\sigma_0\nu_0j_0m_0}(\tilde{\theta}, \tilde{\varphi})}{\sqrt{k_{n\Omega\omega\sigma\nu jm_A}}} |n\Omega\omega\sigma\nu jm\rangle |f\nu_A\rangle e^{iRk_{n\Omega\omega\sigma\nu jm}}, \end{aligned} \quad (5.32)$$

where R is the center-of-mass separation of the colliding particles, $n_0\Omega_0\omega_0\sigma_0\nu_0j_0m_0$ indexes refer to the fixed asymptotic state before the collision (entrance channel),

$$k_{n\Omega\omega\sigma\nu jm_A} = \frac{1}{\hbar} \sqrt{2\mu(E - \epsilon_{n\Omega\omega\sigma\nu jm_A})} \geq 0 \quad (5.33)$$

is the wave vector, f is the scattering amplitude, the summation in Eq. (5.32) includes open channels only. The degeneracy-averaged integral cross sections are defined as

$$\frac{\sigma_{n\Omega\omega\sigma\nu jm_A \leftarrow n_0\Omega_0\omega_0\sigma_0\nu_0j_0m_0}}{2j_0 + 1} = \frac{1}{\sum_{m, m_0}} \int_0^{2\pi} d\tilde{\varphi} \int_0^\pi |f_{n\Omega\omega\sigma\nu jm_A \leftarrow n_0\Omega_0\omega_0\sigma_0\nu_0j_0m_0}(\tilde{\theta}, \tilde{\varphi})|^2 \sin \tilde{\theta} d\tilde{\theta} \quad (5.34)$$

The Hamiltonian for the $I_2 + A$ system is

$$\hat{H} = \frac{-\hbar^2}{2\mu} \frac{d^2}{dR^2} + \frac{\hat{l}^2}{2\mu R^2} + \hat{H}_{I_2} + \hat{H}_A + \hat{V}(R, r, \cos \theta, Q, \mathbf{r}^e), \quad (5.35)$$

where \hat{l} is the orbital angular momentum for the collision, μ is the reduced mass of the colliding particles, \hat{V} is the interaction potential, θ is the angle between \mathbf{R} and \mathbf{r} vectors. $\hat{V}(R, r, \cos \theta, Q, \mathbf{r}^e)$ is the $I_2 + A$ interaction potential operator, which vanishes at the infinite separation R . The total angular momentum $\hat{\mathbf{J}} = \hat{\mathbf{l}} + \hat{\mathbf{j}}$ is conserved, therefore it is convenient to expand $\Psi(\mathbf{R}, \mathbf{r}, Q, \mathbf{r}^e)$ in terms of total angular momentum eigenfunctions

$$|j l \Omega J M\rangle = \sum_{m, m_l} (-1)^{j-l+M} \sqrt{2J+1} \begin{pmatrix} j & l & J \\ m & m_l & -M \end{pmatrix} |lm_l\rangle |jm\Omega\rangle, \quad (5.36)$$

where $(:::)$ is a 3-j symbol, M is the projection of \mathbf{J} on the laboratory axis, and $|lm_l\rangle$ is the spherical function, m_l is the projection of $\hat{\mathbf{l}}$ on the laboratory axis. Expansion of $\Psi(\mathbf{R}, \mathbf{r}, Q, \mathbf{r}^e)$ is [55]

$$\frac{\Psi(\mathbf{R}, \mathbf{r}, \mathbf{Q}, \mathbf{r}^e)}{\sqrt{4\pi}} = \sum_{J, M, l_0} (-1)^{j_0 - l_0 + M} i^{l_0} \sqrt{2l_0 + 1} \begin{pmatrix} j_0 & l_0 & J \\ m_0 & 0 & -M \end{pmatrix} \Phi_{n_0 \Omega_0 \omega_0 \sigma_0 \nu_0 j_0 \nu_{A0} l_0}^{JM} \quad (5.37)$$

$$\begin{aligned} \Phi_{n_0 \Omega_0 \omega_0 \sigma_0 \nu_0 j_0 \nu_{A0} l_0}^{JM}(\mathbf{R}, \mathbf{r}, \mathbf{Q}, \mathbf{r}^e) = \\ \sum_{n \Omega \omega \sigma \nu j \nu_A l} F_{n \Omega \omega \sigma \nu j \nu_A l}^{J n_0 \Omega_0 \omega_0 \sigma_0 \nu_0 j_0 \nu_{A0} l_0}(\mathbf{R}) |n \Omega \omega \sigma\rangle |v j\rangle |f \nu_A\rangle |j l \Omega J M\rangle \end{aligned} \quad (5.38)$$

Each $\Phi_{n_0 \Omega_0 \omega_0 \sigma_0 \nu_0 j_0 \nu_{A0} l_0}^{JM}(\mathbf{R}, \mathbf{r}, \mathbf{Q}, \mathbf{r}^e)$ satisfy the same Schrödinger Eq. (5.31)

$$\hat{H} \Phi_{n_0 \Omega_0 \omega_0 \sigma_0 \nu_0 j_0 \nu_{A0} l_0}^{JM}(\mathbf{R}, \mathbf{r}, \mathbf{Q}, \mathbf{r}^e) = E \Phi_{n_0 \Omega_0 \omega_0 \sigma_0 \nu_0 j_0 \nu_{A0} l_0}^{JM}(\mathbf{R}, \mathbf{r}, \mathbf{Q}, \mathbf{r}^e) \quad (5.39)$$

as the whole wavefunction $\Psi(\mathbf{R}, \mathbf{r}, \mathbf{Q}, \mathbf{r}^e)$. Substitution of Eq. (5.38) into Eq. (5.39) leads to the system of close-coupled equations (CC model) for $F_{n \Omega \omega \sigma \nu j \nu_A l}^{J n_0 \Omega_0 \omega_0 \sigma_0 \nu_0 j_0 \nu_{A0} l_0}(\mathbf{R})$:

$$\begin{aligned} & \left(\frac{d^2}{dR^2} - \frac{l(l+1)}{R^2} + k_{n \Omega \omega \sigma \nu j \nu_A}^2 \right) F_{n \Omega \omega \sigma \nu j \nu_A l}^{J n_0 \Omega_0 \omega_0 \sigma_0 \nu_0 j_0 \nu_{A0} l_0}(\mathbf{R}) \\ &= \frac{2\mu}{\hbar^2} \sum_{n' \Omega' \omega' \sigma' \nu' j' \nu'_A l'} \langle j' l' \Omega' J' M' | V_{n' \Omega' \omega' \sigma' \nu' j' \nu'_A, n \Omega \omega \sigma \nu j \nu_A}(\mathbf{R}, \theta) | j l \Omega J M \rangle \\ & \times F_{n' \Omega' \omega' \sigma' \nu' j' \nu'_A l'}^{J n_0 \Omega_0 \omega_0 \sigma_0 \nu_0 j_0 \nu_{A0} l_0}(\mathbf{R}), \end{aligned} \quad (5.40)$$

where

$$V_{n' \Omega' \omega' \sigma' \nu' j' \nu'_A, n \Omega \omega \sigma \nu j \nu_A}(\mathbf{R}, \theta, \mathbf{r}, \mathbf{Q}) = \langle n' \Omega' \omega' \sigma' | \hat{V}(\mathbf{R}, \mathbf{r}, \cos \theta, \mathbf{Q}, \mathbf{r}^e) | n \Omega \omega \sigma \rangle, \quad (5.41)$$

$$V_{n' \Omega' \omega' \sigma' \nu' j' \nu'_A, n \Omega \omega \sigma \nu j \nu_A}(\mathbf{R}, \theta) = \langle f \nu'_A | \langle v' j' | V_{n' \Omega' \omega' \sigma' \nu' j' \nu'_A, n \Omega \omega \sigma \nu j \nu_A}(\mathbf{R}, \theta, \mathbf{r}, \mathbf{Q}) | v j \rangle | f \nu_A \rangle. \quad (5.42)$$

Evaluation of the matrix elements $V_{n' \Omega' \omega' \sigma' \nu' j' \nu'_A, n \Omega \omega \sigma \nu j \nu_A}(\mathbf{R}, \theta)$ is described in [56, 57].

To satisfy asymptotic condition (5.32), functions $F_{n \Omega \omega \sigma \nu j \nu_A l}^{J n_0 \Omega_0 \omega_0 \sigma_0 \nu_0 j_0 \nu_{A0} l_0}(\mathbf{R})$ have to be asymptotically represented as the sum of the ingoing wave for entrance channel and outgoing waves for other open (including entrance) channels [54]

$$\begin{aligned} & \frac{F_{n \Omega \omega \sigma \nu j \nu_A l}^{J n_0 \Omega_0 \omega_0 \sigma_0 \nu_0 j_0 \nu_{A0} l_0} \xrightarrow{R \rightarrow 0} 0}{F_{n \Omega \omega \sigma \nu j \nu_A l}^{J n_0 \Omega_0 \omega_0 \sigma_0 \nu_0 j_0 \nu_{A0} l_0} \xrightarrow{R \rightarrow \infty}} \\ &= \frac{1}{\sqrt{k_{n_0 \Omega_0 \omega_0 \sigma_0 \nu_0 j_0 \nu_{A0}}}} \delta_{n_0 n} \delta_{\Omega_0 \Omega} \delta_{\omega_0 \omega} \delta_{\sigma_0 \sigma} \delta_{\nu_0 \nu} \delta_{j_0 j} \delta_{\nu_{A0} \nu_A} \delta_{l_0 l} e^{-i(R k_{n_0 \Omega_0 \omega_0 \sigma_0 \nu_0 j_0 \nu_{A0}} - l_0 \pi / 2)} \\ & - \frac{S_{n \Omega \omega \sigma \nu j \nu_A l \leftarrow n_0 \Omega_0 \omega_0 \sigma_0 \nu_0 j_0 \nu_{A0} l_0}^J}{\sqrt{k_{n \Omega \omega \sigma \nu j \nu_A}}} e^{i(R k_{n \Omega \omega \sigma \nu j \nu_A} - l \pi / 2)} \end{aligned} \quad (5.43)$$

where $S_{n \Omega \omega \sigma \nu j \nu_A l \leftarrow n_0 \Omega_0 \omega_0 \sigma_0 \nu_0 j_0 \nu_{A0} l_0}^J$ is S -matrix. Then degeneracy-averaged integral cross sections (5.34) are given by [55]

$$\sigma_{n\Omega\omega\sigma\nu j_{v_A} \leftarrow n_0\Omega_0\omega_0\sigma_0\nu_0 j_0 v_{A0}} = \frac{\pi/(2j_0 + 1)}{k_{n_0\Omega_0\omega_0\sigma_0\nu_0 j_0 v_{A0}}^2} \sum_J (2J + 1) \sum_{ll_0} \left| \delta_{n_0 n} \delta_{\Omega_0 \Omega} \delta_{\omega_0 \omega} \delta_{\sigma_0 \sigma} \delta_{\nu_0 \nu} \delta_{j_0 j} \delta_{v_{A0} v_A} \delta_{l_0 l} - S_{n\Omega\omega\sigma\nu j_{v_A} \leftarrow n_0\Omega_0\omega_0\sigma_0\nu_0 j_0 v_{A0} l_0}^J \right|^2 \quad (5.44)$$

Equation (5.44) provides fully state-resolved cross sections. Usually the rotational summed cross sections

$$\sigma_{n\Omega\omega\sigma\nu v_A \leftarrow n_0\Omega_0\omega_0\sigma_0\nu_0 v_{A0}} = \sum_{j_0} P_{j_0} \sigma_{n\Omega\omega\sigma\nu j_{v_A} \leftarrow n_0\Omega_0\omega_0\sigma_0\nu_0 j_0 v_{A0}} \quad (5.45)$$

are of interest in an experiment. Here P_{j_0} is a weight factor corresponding to the population of different rotational states of I_2 .

EVCC-IOS Approximation Numerical solution of the system (5.40) is very difficult due to a large number of coupled scattering channels. If the rotational spacing in a molecule is small compared to the collision energy, and the interaction potential is short-ranged, then rotational degrees of freedom of I_2 can be treated within the infinite-order sudden (IOS) approximation [56, 58]. This approximation reduces greatly the dimension of the close-coupled (CC) system by neglecting all rotational channels:

$$\left(\frac{d^2}{dR^2} - \frac{\bar{l}(\bar{l} + 1)}{R^2} + k_{n\Omega\omega\sigma\nu \bar{j}_{v_A}}^2 \right) F_{n\Omega\omega\sigma\nu v_A}^{\bar{j}}(R, \theta) = \frac{2\mu}{\hbar^2} \sum_{n' \Omega' \omega' \sigma' \nu' v'_A} V_{n' \Omega' \omega' \sigma' \nu' v'_A, n\Omega\omega\sigma\nu v_A}(R, \theta) F_{n' \Omega' \omega' \sigma' \nu' v'_A}^{\bar{j}}(R, \theta) \quad (5.46)$$

Here \bar{l} is the effective average value of the orbital angular momentum operator that parameterizes the IOS approximation, and \bar{j} has the same meaning for the average value of the rotational angular momentum set to its initial value. The radial functions $F_{n\Omega\omega\sigma\nu v_A}^{\bar{j}}(R, \theta)$ depend parametrically on the θ angle. The system of Eq. (5.46) is solved at fixed θ values, and the scattering S -matrix $S(\theta)$ is defined by the standard IOS boundary conditions similar to those given by Eq. (5.43). The expression for the total S -matrix which defines the full set of the cross sections (5.44) is [58]

$$S_{n\Omega\omega\sigma\nu j_{v_A} \leftarrow n_0\Omega_0\omega_0\sigma_0\nu_0 j_0 v_{A0} l_0}^J = i^{l+l_0-2\bar{l}} \langle j l \Omega J M | S_{n\Omega\omega\sigma\nu v_A \leftarrow n_0\Omega_0\omega_0\sigma_0\nu_0 v_{A0}}^{\bar{j}}(\theta) | j_0 l_0 \Omega_0 J M \rangle \quad (5.47)$$

Exponential Distorted Wave IOS Approximation The system of close-coupled equations (5.46) can be further simplified if the interaction between channels is small. In the exponential distorted wave (EDW) IOS approximation [59, 60] Eq. (5.46) are uncoupled by neglecting the off diagonal matrix elements $V_{n'\Omega' \omega' \sigma' v'_A, n\Omega\omega\sigma v_A}(R, \theta)$:

$$\left(\frac{d^2}{dR^2} - \frac{\bar{l}(\bar{l}+1)}{R^2} - \frac{2\mu}{\hbar^2} V_{n\Omega\omega\sigma v_A, n\Omega\omega\sigma v_A}(R, \theta) + k_{n\Omega\omega\sigma v_A}^2 \right) F_{n\Omega\omega\sigma v_A}^{\bar{l}\bar{j}}(R, \theta) = 0. \quad (5.48)$$

The standard asymptotic conditions are applied for solutions of Eq. (5.25):

$$F_{n\Omega\omega\sigma v_A}^{\bar{l}\bar{j}}(R, \theta) \xrightarrow{R \rightarrow 0} 0, \\ F_{n\Omega\omega\sigma v_A}^{\bar{l}\bar{j}}(R, \theta) \xrightarrow{R \rightarrow \infty} \sin \left(k_{n\Omega\omega\sigma v_A} R - \pi \bar{l} / 2 + \eta_{n\Omega\omega\sigma v_A}^{\bar{l}\bar{j}}(\theta) \right). \quad (5.49)$$

Thus large diabatic $V_{n\Omega\omega\sigma v_A, n\Omega\omega\sigma v_A}(R, \theta)$ potentials are taken into account on all orders in the EDW-IOS approximation. Then interactions between channels are taken into account in first order perturbation approximation giving S-matrix

$$S_{n\Omega\omega\sigma v_A \leftarrow n_0\Omega_0\omega_0\sigma_0 v_0 v_{A0}}^{\bar{l}\bar{j}}(\theta) = e^{i\eta_{n\Omega\omega\sigma v_A}^{\bar{l}\bar{j}}(\theta)} e^{iA_{n\Omega\omega\sigma v_A, n_0\Omega_0\omega_0\sigma_0 v_0 v_{A0}}^{\bar{l}\bar{j}}(\theta)} e^{i\eta_{n_0\Omega_0\omega_0\sigma_0 v_0 v_{A0}}^{\bar{l}\bar{j}}(\theta)},$$

where

$$A_{n\Omega\omega\sigma v_A, n_0\Omega_0\omega_0\sigma_0 v_0 v_{A0}}^{\bar{l}\bar{j}}(\theta) = \frac{2(\delta_{n_0 n} \delta_{\Omega_0 \Omega} \delta_{\omega_0 \omega} \delta_{\sigma_0 \sigma} \delta_{v_0 v} \delta_{v_{A0} v_A} - 1)}{(k_{n\Omega\omega\sigma v_A} k_{n_0\Omega_0\omega_0\sigma_0 v_0 v_{A0}})^{1/2}} \\ \int_0^\infty F_{n\Omega\omega\sigma v_A}^{\bar{l}\bar{j}}(R, \theta) \frac{2\mu}{\hbar^2} V_{n\Omega\omega\sigma v_A, n_0\Omega_0\omega_0\sigma_0 v_0 v_{A0}} F_{n_0\Omega_0\omega_0\sigma_0 v_0 v_{A0}}^{\bar{l}\bar{j}}(R, \theta) dR.$$

Rate Constant Vibrationally-resolved and rotationally-summed rate constants for a temperature T can be obtained by the formula

$$k_{n\Omega\omega\sigma v_M \leftarrow n_0\Omega_0\omega_0\sigma_0 v_0 v_{M0}}(T) = \left(\frac{8}{T\pi\mu k_B} \right)^{1/2} \int_0^\infty \frac{E_c \sigma_{n\Omega\omega\sigma v_M \leftarrow n_0\Omega_0\omega_0\sigma_0 v_0 v_{M0}}(E_c)}{T k_B} e^{-\frac{E_c}{T k_B}} dE_c, \quad (5.50)$$

where k_B is the Boltzmann constant, $E_c = \frac{\hbar^2 k_{n_0\Omega_0\omega_0\sigma_0 v_0 v_{M0}}^2}{2\mu}$ is the collision energy.

In some experiments only the summed over the final vibrational levels of partner M and I_2 rate constants are determined. They are

$$k_{n\Omega\omega\sigma v \leftarrow n_0\Omega_0\omega_0\sigma_0 v_0} = \sum_{v_M} k_{n\Omega\omega\sigma v v_M \leftarrow n_0\Omega_0\omega_0\sigma_0 v_0 v_{M0}}$$

$$k_{n\Omega\omega\sigma \leftarrow n_0\Omega_0\omega_0\sigma_0} = \sum_{v_M v} k_{n\Omega\omega\sigma v v_M \leftarrow n_0\Omega_0\omega_0\sigma_0 v_0 v_{M0}}.$$

Evaluation of the rate constant using Eq. (5.50) may require calculation of cross sections at many energy values. In case the calculation of the cross section energy dependence required for Eq. (5.50) is a very computationally demanding different models for the energy dependence can be used. In the hard sphere (HS) model, it is assumed that cross sections are independent of E_c :

$$\sigma(E_c) \approx \sigma_0 = \text{const.} \quad (5.51)$$

Substituting Eq. (5.51) into Eq. (5.50), one gets

$$k_{n\Omega\omega\sigma v \leftarrow n_0\Omega_0\omega_0\sigma_0 v_0}^{\text{HS}}(T) = \left(\frac{8Tk_B}{\pi\mu}\right)^{1/2} \sigma_0. \quad (5.52)$$

In the modified hard sphere (MHS) model [61] it is assumed that $\sigma(E_c)$ has the threshold behavior

$$\sigma(E_c) = \begin{cases} 0, & \text{if } E_c < E_0 \\ \sigma_0 \left(1 - \frac{E_0}{E_c}\right), & \text{if } E_c \geq E_0. \end{cases} \quad (5.53)$$

The integral in Eq. (5.50) can be analytically calculated with function (5.53) giving

$$k_{n\Omega\omega\sigma v \leftarrow n_0\Omega_0\omega_0\sigma_0 v_0}^{\text{MHS}}(T) = \left(\frac{8Tk_B}{\pi\mu}\right)^{1/2} \sigma_0 e^{-\frac{E_0}{T k_B}}. \quad (5.54)$$

MHS model is convenient if the $\sigma(E_c)$ function monotonically increases with E_c . In a case of decreasing functions the HS model should be used instead.

IDIM PT1 Model To evaluate matrix elements (5.41) the first-order intermolecular diatomics-in-molecule perturbation theory (IDIM PT1) model can be applied. First, consider the model for $\text{I}_2 + \text{Rg}$ system. Then the matrix elements (5.41) read

$$V_{n'\Omega'\omega'\sigma', n\Omega\omega\sigma}(R, \theta, r) = \langle \text{Rg} | \langle n'\Omega'\omega'\sigma' | \hat{V}(R, r, \cos \theta, \mathbf{r}^e) | n\Omega\omega\sigma \rangle | \text{Rg} \rangle, \quad (5.55)$$

where vibrational variables Q are omitted (see above). The model was successfully applied for description of the IP states of the first two tiers (see Sect. 5.3.2.4). In the

IDIM PT1 model, the electronic Hamiltonian (last three terms in Eq. (5.35)) is separated into the zero-order term

$$\hat{H}_0 = \hat{H}_{I_2} + \hat{H}_{Rg} \quad (5.56)$$

and perturbation

$$\begin{aligned} \hat{V}_{DIM} = & \hat{H}_{RgI_a}(R_a) - \hat{H}_{I_a} - \hat{H}_{Rg} + \hat{H}_{RgI_b}(R_b) - \hat{H}_{I_b} - \hat{H}_{Rg} = \hat{V}_{RgI_a}(R_a) + \\ & \hat{V}_{RgI_b}(R_b), \end{aligned} \quad (5.57)$$

where indexes a, b distinguish iodine centers, $R_{a(b)}$ is $Rg - I_{a(b)}$ separation, $\hat{V}_{RgI_{a(b)}}$ is $Rg + I_{a(b)}$ interaction potential operator, which vanishes at the infinite separation $R_{a(b)} \rightarrow \infty$. Electronic basis functions are represented as the product of I_2 wave function (3.8) within the asymptotic model and wave function of inert gas $|Rg\rangle$:

$$|n\Omega\omega\sigma, j^e\rangle |Rg\rangle = \frac{1}{\sqrt{2}} (|j^e\Omega\rangle_a |00\rangle_b |Rg\rangle + p |00\rangle_a |j^e\Omega\rangle_b |Rg\rangle). \quad (5.58)$$

Matrix elements of the \hat{V}_{DIM} on the basis set (5.58) are

$$\begin{aligned} V_{n'\Omega'\omega'\sigma', n\Omega\omega\sigma}^{DIM}(R, \theta) = & \langle Rg | \langle n'\Omega'\omega'\sigma', j'^e | \hat{V}_{DIM} | n\Omega\omega\sigma, j^e \rangle | Rg \rangle = \\ & \frac{1}{2} \langle Rg | \langle j'^e\Omega' | \hat{V}_{RgI}(R_a) | j^e\Omega \rangle | Rg \rangle + \frac{pp'}{2} \langle Rg | \langle j'^e\Omega' | \hat{V}_{RgI}(R_b) | j^e\Omega \rangle | Rg \rangle + \\ & \frac{\delta_{\Omega\Omega'} \delta_{j^e j'^e}}{2} \langle Rg | \langle 00 | \hat{V}_{RgI}(R_b) | 00 \rangle | Rg \rangle + \frac{\delta_{\Omega\Omega'} \delta_{j^e j'^e}}{2} pp' \langle Rg | \langle 00 | \hat{V}_{RgI}(R_a) | 00 \rangle | Rg \rangle, \end{aligned} \quad (5.59)$$

where the same as for $R_{a(b)}$ indexes $a(b)$ are supposed for wave functions. Note, that due to the pp' factor in front of second and fourth terms on the right-hand side of Eq. (5.59) the coupling connecting states of the same parity ω (including diagonal matrix elements) are symmetric with respect to the permutation of iodine nuclei, whereas connecting states of opposite parities ω are antisymmetric. The key feature of the IDIM PT1 model is that the matrix elements (5.59) can be represented as functions of *nonrelativistic* diatomic potentials V_{Π} , V_{Σ} of states ${}^3\Pi$, ${}^3\Sigma^-$ correlating with the limit $I^+({}^3P) - Rg$ and V_- of the state ${}^1\Sigma^+$ correlating with the limit $I^-({}^1S) - Rg$ [62]. In the asymptotic model, the nonrelativistic wave functions of $I^\pm - Rg$ systems are

$$|l^e \tilde{\Lambda} S^e \Sigma\rangle | \mathbf{Rg}\rangle, \quad (5.60)$$

where $l^e(S^e)$ are the orbital (spin) momentum, $\tilde{\Lambda}$ is the projection of the orbital momentum on the internuclear axis $I_{a(b)} - \mathbf{Rg}$, Σ is the spin projection quantum number. In the nonrelativistic approximation, the spin quantization axis is arbitrary. It is more convenient to choose it coinciding with the I – I internuclear axis of the iodine molecule as for the total electronic momentum in the basis set (5.58). Wave functions of ${}^3\Pi$, ${}^3\Sigma^-$, ${}^1\Sigma^+$ states are $|1 \pm 11\Sigma\rangle | \mathbf{Rg}\rangle$, $|101\Sigma\rangle | \mathbf{Rg}\rangle$, and $|0000\rangle | \mathbf{Rg}\rangle$ respectively. Since $|l^e = 0\tilde{\Lambda} = 0S^e = 0\Sigma = 0\rangle \equiv |j^e = 0\Omega = 0\rangle$ the last two matrix elements on the right-hand side of Eq. (5.59) can be immediately calculated:

$$\langle \mathbf{Rg} | \langle 00 | \hat{V}_{\mathbf{RgI}}(R_{a(b)}) | 00 \rangle | \mathbf{Rg} \rangle = V_-(R_{a(b)}). \quad (5.61)$$

The matrix of $\hat{V}_{\mathbf{RgI}}$ on the basis set (5.60) has simple diagonal form and is independent of the spin projection quantum number Σ :

$$\langle 1\tilde{\Lambda}' 1\Sigma' | \hat{V}_{\mathbf{RgI}}(R_{a(b)}) | 1\tilde{\Lambda} 1\Sigma \rangle = \delta_{\Sigma'\Sigma} \tilde{V}_{\tilde{\Lambda}'\tilde{\Lambda}}(R_{a(b)}), \quad (5.62)$$

$$\tilde{\mathbf{V}}(R_{a(b)}) = \begin{pmatrix} V_{\Pi}(R_{a(b)}) & 0 & 0 \\ 0 & V_{\Sigma}(R_{a(b)}) & 0 \\ 0 & 0 & V_{\Pi}(R_{a(b)}) \end{pmatrix} \quad (5.63)$$

The quantization axis for the total electronic momentum in (5.58) and the orbital momentum in (5.60) are different. The transformation from $I_{a(b)} - \mathbf{Rg}$ axis to I – I one is given by the Wigner rotation matrix $\mathbf{D}(\boldsymbol{\alpha} = 0, \boldsymbol{\beta}_{a(b)}, \boldsymbol{\gamma} = 0) = \mathbf{d}(\boldsymbol{\beta}_{a(b)})$:

$$|1\Lambda 1\Sigma\rangle = \sum_{\tilde{\Lambda}} \tilde{d}_{\tilde{\Lambda}\Lambda}^{1\sim}(\beta_{a(b)}) |1\tilde{\Lambda} 1\Sigma\rangle, \quad (5.64)$$

where $\beta_{a(b)}$ is the angle between $I_{a(b)} - \mathbf{Rg}$ and I – I axis, Λ is the projection of the orbital momentum on the internuclear axis I – I. Then, accounting for the explicit form of $\tilde{d}_{\tilde{\Lambda}\Lambda}^{1\sim}(\beta_{a(b)})$, matrix of $\hat{V}_{\mathbf{RgI}}$ on the basis set (5.64) is

$$\langle \mathbf{Rg} | \langle 1\Lambda' 1\Sigma' | \hat{V}_{\mathbf{RgI}}(R_{a(b)}) | 1\Lambda 1\Sigma \rangle | \mathbf{Rg} \rangle = \delta_{\Sigma'\Sigma} V_{\Lambda'\Lambda}(R_{a(b)}), \quad (5.65)$$

$$\begin{aligned}
\mathbf{V}(R_{a(b)}) &= \mathbf{d}^T(\beta_{a(b)}) \tilde{\mathbf{V}}(R_{a(b)}) \mathbf{d}(\beta_{a(b)}) = \\
&\begin{pmatrix} \frac{1 + \cos(\beta_{a(b)})}{2} & \frac{\sin(\beta_{a(b)})}{\sqrt{2}} & \frac{1 - \cos(\beta_{a(b)})}{2} \\ -\frac{\sin(\beta_{a(b)})}{\sqrt{2}} & \cos(\beta_{a(b)}) & \frac{\sin(\beta_{a(b)})}{\sqrt{2}} \\ \frac{1 - \cos(\beta_{a(b)})}{2} & -\frac{\sin(\beta_{a(b)})}{\sqrt{2}} & \frac{1 + \cos(\beta_{a(b)})}{2} \end{pmatrix} \\
&\times \begin{pmatrix} V_{\Pi}(R_{a(b)}) & 0 & 0 \\ 0 & V_{\Sigma}(R_{a(b)}) & 0 \\ 0 & 0 & V_{\Pi}(R_{a(b)}) \end{pmatrix} \\
&\times \begin{pmatrix} \frac{1 + \cos(\beta_{a(b)})}{2} & -\frac{\sin(\beta_{a(b)})}{\sqrt{2}} & \frac{1 - \cos(\beta_{a(b)})}{2} \\ \frac{\sin(\beta_{a(b)})}{\sqrt{2}} & \cos(\beta_{a(b)}) & -\frac{\sin(\beta_{a(b)})}{\sqrt{2}} \\ \frac{1 - \cos(\beta_{a(b)})}{2} & \frac{\sin(\beta_{a(b)})}{\sqrt{2}} & \frac{1 + \cos(\beta_{a(b)})}{2} \end{pmatrix} \quad (5.66) \\
&= \begin{pmatrix} V_{\Pi}(R_{a(b)}) & 0 & 0 \\ 0 & V_{\Pi}(R_{a(b)}) & 0 \\ 0 & 0 & V_{\Pi}(R_{a(b)}) \end{pmatrix} \\
&+ (V_{\Sigma}(R_{a(b)}) - V_{\Pi}(R_{a(b)})) \\
&\times \begin{pmatrix} \frac{\sin^2(\beta_{a(b)})}{2} & \frac{\sin(\beta_{a(b)}) \cos(\beta_{a(b)})}{\sqrt{2}} & -\frac{\sin^2(\beta_{a(b)})}{2} \\ \frac{\sin(\beta_{a(b)}) \cos(\beta_{a(b)})}{\sqrt{2}} & \cos^2(\beta_{a(b)}) & -\frac{\sin(\beta_{a(b)}) \cos(\beta_{a(b)})}{\sqrt{2}} \\ -\frac{\sin^2(\beta_{a(b)})}{2} & -\frac{\sin(\beta_{a(b)}) \cos(\beta_{a(b)})}{\sqrt{2}} & \frac{\sin^2(\beta_{a(b)})}{2} \end{pmatrix},
\end{aligned}$$

where indexes in matrices are in the order $\Lambda = 1, \Lambda = 0, \Lambda = -1$. Finally, using the transformation

$$|j^e \Omega\rangle = \sum_{\Lambda \Sigma} C_{1\Lambda 1\Sigma}^{j^e \Omega} |1\Lambda 1\Sigma\rangle \quad (5.67)$$

where $C_{1\Lambda 1\Sigma}^{j^e \Omega}$ are Clebsch-Gordan coefficients, for first two matrix elements on the right hand side of Eq. (5.59) we have

$$\begin{aligned}
&\langle \mathbf{Rg} | \langle j^e \Omega' | \hat{V}_{\mathbf{RgI}}(R_{a(b)}) | j^e \Omega \rangle | \mathbf{Rg} \rangle = \\
&\sum_{\Lambda \Sigma \Lambda' \Sigma'} C_{1\Lambda' 1\Sigma'}^{j^e \Omega'} C_{1\Lambda 1\Sigma}^{j^e \Omega} \langle \mathbf{Rg} | \langle 1\Lambda' 1\Sigma' | \hat{V}_{\mathbf{RgI}}(R_{a(b)}) | 1\Lambda 1\Sigma \rangle | \mathbf{Rg} \rangle = \\
&\sum_{\Lambda \Sigma \Lambda' \Sigma'} C_{1\Lambda' 1\Sigma'}^{j^e \Omega'} C_{1\Lambda 1\Sigma}^{j^e \Omega} \delta_{\Sigma' \Sigma} V_{\Lambda' \Lambda}(R_{a(b)}) = \sum_{\Lambda \Sigma \Lambda'} C_{1\Lambda' 1\Sigma}^{j^e \Omega'} C_{1\Lambda 1\Sigma}^{j^e \Omega} V_{\Lambda' \Lambda}(R_{a(b)}) = \quad (5.68) \\
&\sum_{\Lambda \Lambda'} C_{1\Lambda' 1(\Omega-\Lambda)}^{j^e \Omega'} C_{1\Lambda 1(\Omega-\Lambda)}^{j^e \Omega} V_{\Lambda' \Lambda}(R_{a(b)}) = \\
&\sum_{\Lambda} C_{1(\Omega'-\Omega+\Lambda) 1(\Omega-\Lambda)}^{j^e \Omega'} C_{1\Lambda 1(\Omega-\Lambda)}^{j^e \Omega} V_{(\Omega'-\Omega+\Lambda) \Lambda}(R_{a(b)}).
\end{aligned}$$

Eqs. (5.59, 5.61, 5.66 and 5.68) give diabatic potential curves and coupling between them for the first two tiers of IP states. Let us consider some examples. For diabatic potential curve of the $D'2_g$ ($j^e = 2, \Omega = 2, p = 1$) state Eqs. (5.68 and 5.66) give

$$\begin{aligned} \langle \mathbf{Rg} | \langle j^e = 2\Omega = 2 | \hat{V}_{\mathbf{RgI}}(R_{a(b)}) | j^e = 2\Omega = 2 \rangle | \mathbf{Rg} \rangle &= C_{1111}^{22} C_{1111}^{22} V_{11} \\ &= V_{\Pi}(R_{a(b)}) + 1/2 \left(V_{\Sigma}(R_{a(b)}) - V_{\Pi}(R_{a(b)}) \right) \sin^2(\beta_{a(b)}). \end{aligned}$$

Then Eqs. (5.59 and 5.61) give

$$\begin{aligned} \langle \mathbf{Rg} | \langle D' | \hat{V}_{\text{DIM}} | D' \rangle | \mathbf{Rg} \rangle &= \\ \frac{1}{2} \sum_{\alpha=a,b} V_{\Pi}(R_{\alpha}) + 1/2 \left(V_{\Sigma}(R_{\alpha}) - V_{\Pi}(R_{\alpha}) \right) \sin^2(\beta_{\alpha}) + V_{-}(R_{\alpha}) \end{aligned}$$

For coupling between the $\beta(j^e = 2, \Omega = 1, p = 1)$ and $E(j^e = 2, \Omega = 0, p = 1)$ states, Eqs. (5.68 and 5.66) give

$$\begin{aligned} \langle \mathbf{Rg} | \langle j^e = 2\Omega' = 1 | \hat{V}_{\mathbf{RgI}}(R_{a(b)}) | j^e = 2\Omega = 0 \rangle | \mathbf{Rg} \rangle &= \\ = C_{1110}^{21} C_{1010}^{20} V_{10} + C_{1011}^{21} C_{1(-1)11}^{20} V_{0(-1)} &= \\ = \frac{1}{2} \sqrt{1/6} \left(V_{\Sigma}(R_{a(b)}) - V_{\Pi}(R_{a(b)}) \right) \sin(\beta_{a(b)}) \cos(\beta_{a(b)}) \end{aligned}$$

and from Eqs. (5.59 and 5.61)

$\langle \mathbf{Rg} | \langle \beta | \hat{V}_{\text{DIM}} | E \rangle | \mathbf{Rg} \rangle = \frac{1}{4} \sqrt{1/6} \sum_{\alpha=a,b} \left(V_{\Sigma}(R_{\alpha}) - V_{\Pi}(R_{\alpha}) \right) \sin(\beta_{\alpha}) \cos(\beta_{\alpha})$. For coupling between the $f(j^e = 0, \Omega = 0, p = 1)$ and $D(j^e = 2, \Omega = 0, p = -1)$ states, Eqs. (5.68 and 5.66) give

$$\begin{aligned} \langle \mathbf{Rg} | \langle j^e = 0 \Omega' = 0 | \hat{V}_{\mathbf{RgI}}(R_{a(b)}) | j^e = 2 \Omega = 0 \rangle | \mathbf{Rg} \rangle &= \\ = C_{111(-1)}^{00} C_{111(-1)}^{20} V_{11} + C_{1(-1)11}^{00} C_{1(-1)11}^{20} V_{(-1)(-1)} &+ \\ + C_{1010}^{00} C_{1010}^{20} V_{00} &= \\ = \frac{\sqrt{2}}{6} \left(V_{\Sigma}(R_{a(b)}) - V_{\Pi}(R_{a(b)}) \right) \left(1 - 3 \cos^2(\beta_{a(b)}) \right). \end{aligned}$$

Then $\langle \mathbf{Rg} | \langle f | \hat{V}_{\text{DIM}} | D \rangle | \mathbf{Rg} \rangle = v_a - v_b$, where

$v_{a(b)} = \frac{\sqrt{2}}{12} \left(V_{\Sigma}(R_{a(b)}) - V_{\Pi}(R_{a(b)}) \right) \left(1 - 3 \cos^2(\beta_{a(b)}) \right)$. High-quality *ab initio* potentials V_{Π} , V_{Σ} , V_{-} are available from Ref. [63]. All potentials can be presented in the form

$$V(R_{\alpha}) = V_{\text{SR}}(R_{\alpha}) - f(R_{\alpha}) V_{\text{LR}}(R_{\alpha}), \quad (5.69)$$

where $V_{\text{SR}}(R_{\alpha})$ and $V_{\text{LR}}(R_{\alpha})$ are short-range and long-range parts, f is the switching function which provides their smooth connection. The long-range part has the form

$$V_{\text{LR}}(R_\alpha) = \frac{D_4}{R^4} + \frac{D_6}{R^6} + \frac{D_8}{R^8} \quad (5.70)$$

where D_n coefficients include both induction and dispersion terms,

$$D_n = \frac{1}{2}\alpha_{n/2-1} + C_n \quad (5.71)$$

where $C_4 = 0$, $\alpha_1, \alpha_2, \alpha_3$ are static dipole, quadrupole and octupole polarizabilities of Rg, respectively.

The induction interaction is a result of the interaction between charged particle I^\pm and Rg atom. It is clear that in the case of the interaction between Rg and neutral molecule I_2 this interaction is artificial, and should be eliminated. The modified potentials used in the IDIM PT1 model acquire the form

$$V^*(R_\alpha) = V_{\text{SR}}(R_\alpha) - f(R_\alpha) \left(\frac{c_6}{R^6} + \frac{c_8}{R^8} \right). \quad (5.72)$$

Another correction to the IDIM PT1 model is related with giant transition dipole moment, $d_{n\Omega u\sigma_j^e, n\Omega g\sigma_j^e}(r) = n\Omega\omega = u\sigma, j^e |d_z| n\Omega\omega = g\sigma, j^e$, between IP states of opposite permutation symmetry and the same tier [45]. The transition dipole moment $d_{n\Omega u\sigma_j^e, n\Omega g\sigma_j^e}(r)$ play the same role for the dispersion interaction of each state $|n\Omega\omega = g\sigma, j^e\rangle$, $|n\Omega\omega = u\sigma, j^e\rangle$ as the permanent one of polar diatomics.

$$V^{(2)}_{n\Omega g\sigma_j^e, n\Omega g\sigma_j^e}(R, \theta) = V^{(2)}_{n\Omega u\sigma_j^e, n\Omega u\sigma_j^e}(R, \theta) = -\frac{1}{2}d_{n\Omega u\sigma_j^e, n\Omega g\sigma_j^e}(r)\alpha_1 \frac{(1 + 3\cos^2\theta)}{R^6} \quad (5.73)$$

The second order correction (5.73) should be added to the diabatic potential of each $|n\Omega\omega = g\sigma, j^e\rangle$, $|n\Omega\omega = u\sigma, j^e\rangle$ state calculated within the IDIM PT1 model. It can be shown that no correction for the diabatic coupling is required.

The short-range IDIM PT1 model treats spherical top molecules as an effective atom without internal degrees of freedom and is therefore essentially the same as that described above [57]. The elimination of artificial induction interaction is also similar to Rg + I_2 case. The difference is that the transitions between different *vibrational* levels of the spherical top molecule (explicitly included to close-coupled equations) by dipole-dipole interaction should be taken into account. This leads to the first order correction to matrix element (5.42)

$$V^1_{n\Omega\omega'\sigma'j'v'_A, n\Omega\omega\sigma v_A}(R, \theta) = -\frac{2}{3} \frac{\langle v'_j | d_{n\Omega\omega'\sigma_j^e, n\Omega\omega\sigma_j^e}(r) | v_j \rangle \langle v'_A | d(Q) | v_A \rangle}{R^3} \cos \theta, \quad (5.74)$$

where $v'_A |d(Q)|v_A$ is vibrational transition dipole moment of the spherical top molecule A. Note, that $v'_A |d(Q)|v_A = 0$ if $v'_A = v_A$. The second-order correction

related to transitions between different *electronic* levels of the molecule is given by the same Eq. (5.73)

The IDIM PT1 model properly takes into account the symmetry of the problem. These symmetry properties are typical for all the states involved and can be summarized as follows [31]:

1. Transitions between all states within the tier are allowed; electronic coupling matrix elements are *symmetric* and *antisymmetric* with respect to iodine nuclear inversion and provide selection rules $\Delta J = 0, \pm 2, \dots$ and $\Delta J = \pm 1, \pm 3, \dots$ for transitions between the states of the *same* and *opposite* inversion parity w , respectively.
2. The maximum couplings connect the states of the same j , Ω , and opposite inversion parity

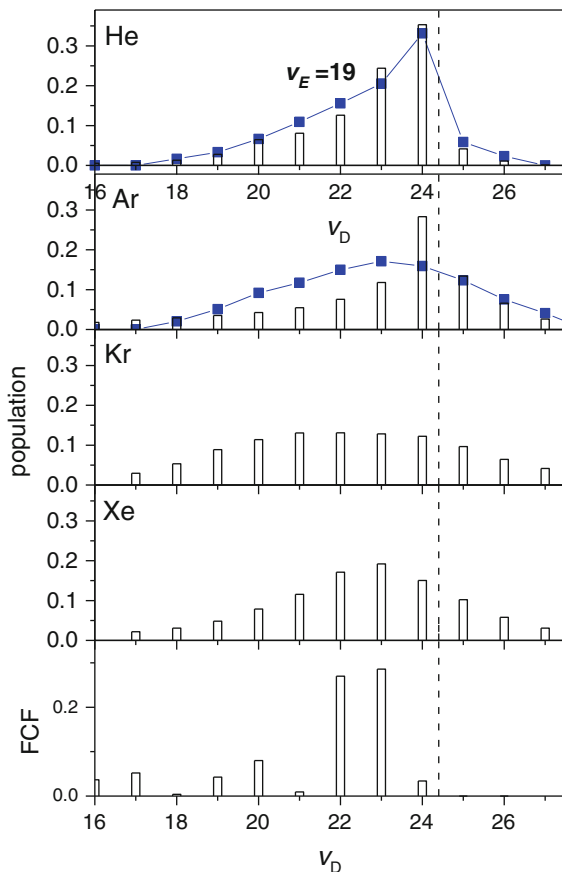
5.3.2.4 Collisions with Rare Gas Atoms

The majority of experimental studies concerns CINATs from the *gerade* $I_2(E0_g^+)$ state [41–43, 47, 48, 50, 52, 64–70]. The nonadiabatic transitions from the $I_2(f0_g^+)$ state induced by collisions with $I_2(X)$ and Rg = He, Ar, Kr, Xe [49, 67, 70], as well as from *ungerade* $I_2(D0_u^+)$ states induced by collisions with $I_2(X)$ and Rg = He, Ar, Xe [51, 69] have also been studied. The mechanism of population of the iodine first tier ion-pair states following optical population of rovibronic levels of four $I_2(E0_g^+, D0_u^+, \beta1_g$ and $D'2_g)$ states in the presence of Ar atoms has been investigated in [40].

The $I_2(E0_g^+ \xrightarrow{Rg} D0_u^+)$ CINATs. The $I_2(E \xrightarrow{Rg} D)$ CINAT rate constants lie in the (10–20), (4–7), (3–8) and (0–1) (units, 10^{-11} cm³/s) interval for Rg = He, Ar, Kr and Xe, respectively in the $v_E = 8–40$ range [31, 35, 41, 43] and (4–6.4) and (2–3.2) (units, 10^{-11} cm³/s) interval for Rg = He, Ar, respectively in the $v_E = 0–2$ range [65, 66]. CINAT cross-sections, $\sigma = k/V$, are *appr.* independent of Rg nature, with the exception of Rg = Xe, for which reactive quenching leading to $XeI(A, X) + I(^2P_j)$ formation is the dominant channel in the $I_2(IP) + Xe$ collisions (see [70]). Calculations were performed by the EVCC-IOS (6×6) method (see Sect. 5.3.2.3) where all six electronic states of the first IP tier were included. Rate constant was calculated within the HS approximation (5.52) for the $E_c = 300$ cm⁻¹ collision energy. Wide vibrational and rotational distributions are typical for the $I_2(E \xrightarrow{Rg} D)$ CINATs (see Fig. 5.1), and width of the distributions increases with Rg masses. There is no correlation between the population of the $I_2(D, v_D)$ vibronic levels and *FCFs*.

The $I_2(E0_g^+ \xrightarrow{Rg} D'2_g, \beta1_g, \gamma1_u, \delta2_u)$ CINATs. The *D* state vibronic levels are mainly populated (> 90% probability) in collisions with He atoms in the $v_E \approx 8–40$ range, and luminescence in $D \rightarrow X$, $D \rightarrow a'$ and $D \rightarrow 0_g^+$ (*ab*) transitions, $\lambda \approx 2700–3300$ Å, 3300–4000 Å and 4300–4700 Å, respectively (for $v_D \approx 18$) occur. However, according to [64, 65] the $D'2_g$ and $\beta1_g$ state are populated in these collisions with high, > 30%, probabilities at $v_E \approx 0, 1, 2$. In presence of Ar, Kr, Xe, luminescence bands, which can be ascribed to transitions from the $D'2_g, \beta1_g, \gamma1_u,$

Fig. 5.1 Measured (bars) and calculated by the EVCC-IOS (6×6) method (squares) population of the $I_2(D, v_D)$ vibronic levels populated in the $I_2(E, v_E = 19, J_E \approx 55 \xrightarrow{Rg} D, v_D)$ CINAT, Rg = He, Ar, Kr, Xe. The vertical line indicates energetic position of the initial, $v_E = 19$, level [50]. Franck-Condon factors between the $v_E = 19$ and v_D vibronic levels are shown on lower panel



$\delta 2_u$ states, occur, and integral intensity of these bands is higher than that of corresponding to the D state (see [40, 50], Fig. 5.2) and Table 5.1. Wide vibrational and rotational distributions are typical for the $I_2(E \xrightarrow{Rg} D' 2_g, \beta 1_g, \gamma 1_u, \delta 2_u)$ CINATs, also.

The $I_2(D 0_u^+ \xrightarrow{Rg} E 0_g^+, D' 2_g, \beta 1_g, \gamma 1_u, \delta 2_u)$ CINATs. In presence of all, Rg = He, Ar, Xe, colliding partners CINAT channel to the all the first tier IP states occur. Total CINAT rate constants to the β, γ, δ and, maybe, D' states is higher than that of corresponding to the E state (see Table 5.2). It is shown in [40] that the $D, v_D = 18 \xrightarrow{Ar} D'$ and $E, v_E = 13 \xrightarrow{Ar} D'$ CINATs do not occur. Therefore, one can believe that these CINATs do not occur at other vibronic level of the E and D states and, maybe, in collisions with other Rg.

Wide vibrational and rotational distributions are typical for the $I_2(D \xrightarrow{Rg} E, D', \beta, \gamma, \delta)$ CINATs, also (see Fig. 5.3).

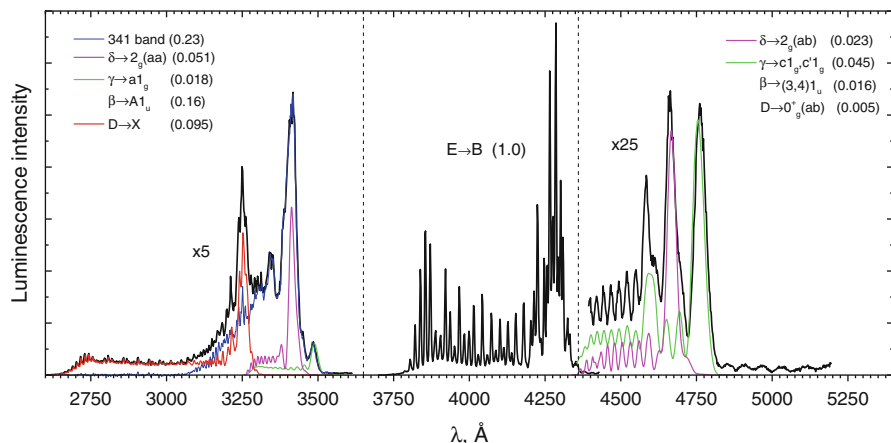


Fig. 5.2 Luminescence spectrum observed after optical population of the $I_2(E,13,49)$ rovibronic state. Spectral resolution FWHM = 4 Å. $p_{I_2} = 270$ mTorr, $p_{Ar} = 4$ Torr. Experimental spectrum, simulations of the $D \rightarrow X$, $\gamma \rightarrow a1_g$, c, c' , $\delta \rightarrow 2_g(aa)$, $2_g(ab)$ spectra as well as differences between experimental and simulated $D \rightarrow X$ spectra in the 2600–3300 Å spectral range are shown as black, red, green, purple and dark blue lines. Estimations of ratios of partial intensities of optical transitions from the $I_2(E)$ to valence states correlating with the first dissociation limit of the valence states (aa) as well as $I_2(D, \delta$ and γ) states to valence states correlating with the second dissociation limit of the valence states (ab) to that of from the E state are given [40]

Population of the Iodine First Tier IP States from Quasi-Resonant Rovibronic Levels of the $I_2(E, D, \beta$ and D') States The principal goal of that study [40] was to determine, do CINATs between IP states of the same parity with respect to permutation of identical nuclei, $E0_g^+$, $D'2_g$, $\beta1_g$ occur, or these states are populated due to optical transitions in the ArI_2 vdW complexes accompanied by their dissociation and/or predissociation which produce $Ar + I_2(D', \beta)$ fragments (see Sect. 6.4).

Rate constants of population of the first tier IP states from the optically populated ($I_2(E, \nu_E = 13$, $D, \nu_D = 18$, $\beta, \nu_\beta = 19$ and $D'2_g, \nu_{D'} = 23$) vibronic states are given in Table 5.3).

Detailed analysis of the data obtained [40] has shown that D' state is not involved in CINATs with other IP states of the first tier. One of the possible explanations has been assumed that the $ArI_2(IP)$ complexes formed in collisions or products of their dissociation/predissociation are responsible for luminescence at the $\lambda_{lum}^{max} \approx 3410$ Å band (see Sect. 6.4.3.3).

The $I_2(f0_g^+ \xrightarrow{Rg} IP)$ CINATs. The $I_2(f0_g^+ \xrightarrow{Rg} F0_u^+)$ channel is dominant for collisions with $Rg = He, Ar, Kr, Xe$ [49]. No emission from other, $g0_g^-, h0_g^-, G1_g$ and $H1_u$, states of the second tier was observed. CINATs to the first tier IP states have very low probability, and rather strong luminescence in the $\lambda_{lum} = 350$ – 500 nm spectral range observed for $Rg = Xe$ is, most likely, due to transitions in XeI_2 vdW complexes (see Sect. 6.4). The $I_2(f \xrightarrow{Rg} F)$ CINAT rate constants lie in the (3–7.1),

Table 5.1 Partial, $k(E, v_E \xrightarrow{M} f)$, and total rate constants, $\sum k(E, v_E \xrightarrow{M} f)$, (in units of $10^{-11} \text{ cm}^3/\text{s}$) for the CINATs from the E, v_E level to the D, D', β, γ , and δ IP states in collisions with I_2 , He, Ar, Kr, Xe. The values calculated using the EVCC-IOS (6×6) method are given in parentheses (see [40, 50])

M	$k(E, v_E \xrightarrow{M} f)$	$\sum k(E, v_E \xrightarrow{M} f)$				
	D	D'	β	γ	δ	
$v_E = 8^a$						
I_2	60 ± 15	≤ 1.5	≤ 1.5	≤ 2	≤ 1	60 ± 15
He	10.0 ± 2.5	1.0 ± 0.4	≤ 0.1	< 0.1	11.0 ± 2.5	
	(4.8)	(0.29)	(0.29)	(0.23)	(0.17)	(5.8)
Ar	7 ± 2	8 ± 2	1.0 ± 0.5	0.9 ± 0.5	17 ± 3	
	(2.3)	(0.9)	(1.2)	(2.4)	(2.4)	(9.2)
Kr	3.6 ± 1.1	9 ± 3	1.3 ± 0.4	1.2 ± 0.5	15 ± 4	
Xe	≤ 0.2	11 ± 3	2.0 ± 0.6	2 ± 1	15 ± 4	
$v_E = 19^b$						
I_2	52 ± 6	≤ 0.3	≤ 0.3	≤ 0.8	≤ 0.5	52 ± 6
He	19 ± 3	≤ 0.2	≤ 0.2	≤ 0.4	≤ 0.2	20 ± 3
	(12.3)	(0.7)	(0.7)	(0.3)	(0.6)	(14.6)
Ar	7.0 ± 2.3	≤ 0.1	10 ± 3	1.0 ± 0.4	2.4 ± 0.8	22 ± 7
	(6.2)	(1.2)	(1.7)	(6.1)	(2.2)	(17.4)
Kr	8.5 ± 2.0	4.5 ± 1.5	9 ± 2	3 ± 2	3.0 ± 1.5	28 ± 9
Xe	1.0 ± 0.4	3 ± 1	5 ± 1	2.0 ± 0.7	1.0 ± 0.5	12 ± 4

^aOnly the sum of the CINAT rate constants for the D' and β states is determined experimentally

^bRate constants given in [50] have been corrected according to data of [40]

(2.6–5.3), (2.5–3.9) and (1.3–2.4) (units, $10^{-10} \text{ cm}^3/\text{s}$) interval for Rg = He, Ar, Kr and Xe, respectively in the $v_f = 8$ –17 range. Wide vibrational and rotational distributions are observed in the $\text{I}_2(f \xrightarrow{\text{Rg}} F)$ CINATs for Rg = Ar – Xe (Fig. 5.4).

CINATs from other second tier IP states was not studied. The authors estimated only the rate constants of total decay of the $G1_g$ and $g0_g^-$ states in collisions with $\text{I}_2(X)$ and Ar; they are less than $10^{-11} \text{ cm}^3/\text{s}$.

Total rate constants for the $\text{I}_2(f \xrightarrow{\text{Rg}} F)$ CINAT are not sensitive to the resonance conditions. Vibrational distributions exhibit clear dependence on the energy gap and $FCFs$ between initial and final levels only for He, but not for heavier rare gases.

Theoretical Analysis of the Experimental Data Obtained The following principal features have been found out for the non-adiabatic transitions induced by collisions with rare gas atoms:

1. Transitions connecting the states correlating with different dissociation limits have low probabilities;
2. All the states of the first tier with the exception of the $D'2_g$ are involved in CINATs, whereas the “parallel” $\Omega_g \leftrightarrow \Omega_u$ transitions with $\Delta\Omega = 0$ are dominant for Rg = He;

Table 5.2 Partial $k(D, v_D \xrightarrow{M} f)$ and total, $\sum k(D, v_D \xrightarrow{M} f)$, rate constants (in units of $10^{-11} \text{ cm}^3/\text{s}$) for the CINAT's from the D , v_D levels to the first-tier IP states in collisions with $\text{I}_2(X)$ and Rg atoms. The theoretical values obtained using the EVCC-IOS (6×6) method for $v_D = 6, 8$ and 13 are given in parentheses (see [51]). Rate constants for E, D' and β states and $v_D = 6, 8$ and 13 are overestimated, probably (see discussion in [40])

M	$k(D, v_D \xrightarrow{M} f)$	$\sum k(D, v_D \xrightarrow{M} f)$				
	E	D'	β	γ	δ	
$v_D = 6$						
I_2	7 ± 2	$\leq 0.2^a$	$\leq 0.2^b$	7 ± 2		
He	0.8 ± 0.2 (0.43)	3.0 ± 0.6^a (3.45)	≤ 0.04 (4.96)	< 0.04 (0.002)	3.8 ± 0.7 (0.005)	(8.8)
Ar	0.6 ± 0.1 (0.66)	23 ± 5^a (4.34)	≤ 0.01 (15.8)	≤ 0.01 (0.23)	23 ± 5 (0.40)	(21.4)
Xe	0.4 ± 0.1	16 ± 3^a	≤ 0.01	≤ 0.01	16 ± 3	
$v_D = 8$						
I_2	9 ± 2	$\leq 0.3^a$	$\leq 0.3^b$	9 ± 2		
He	2.2 ± 0.4 (0.95)	2.3 ± 0.5^a (3.96)	≤ 0.04 (4.93)	≤ 0.04 (0.01)	4.5 ± 0.7 (0.08)	(9.93)
Ar	1.2 ± 0.2 (0.97)	15.7 ± 2.8^a (5.44)	≤ 0.2 (15.1)	≤ 0.2 (0.40)	17 ± 3 (3.76)	(25.7)
Xe	1.1 ± 0.2	12 ± 2	≤ 0.13	≤ 0.13	≤ 0.13	13 ± 2
$v_D = 13$						
I_2	6.3 ± 1.3	$\leq 0.2^a$	$\leq 0.2^b$	6.3 ± 1.3		
He	2.8 ± 0.6 (2.00)	2.8 ± 0.7^a (4.32)	0.3 ± 0.1 (5.05)	≈ 0.5 (0.05)	6.4 ± 1.2 (0.53)	(11.95)
Ar	1.8 ± 0.4 (1.65)	$18 \pm 4^{a,b}$ (6.68)	2.8 ± 0.8 (15.3)	$\approx 6^b$ (0.73)	29 ± 6 (4.45)	(28.8)
Xe	1.8 ± 0.4	$14 \pm 4^{a,b}$	2.7 ± 0.8	2.6 ± 0.7^b	21 ± 5	
$v_D = 18$						
I_2	69 ± 14	$\leq 2^a$	$\leq 2^b$	69 ± 14		
He	$\leq 1.0^c$	3.5 ± 0.7^d	4.0 ± 1.5			
Ar	3.1 ± 0.3	≤ 0.5	29 ± 3	≤ 2	6 ± 1	35
Xe	1.8 ± 0.4	$\approx 9^b$	5 ± 1	11 ± 4^b	27 ± 5	

^a Only the sum of the rate constants to the D' and β states was determined

^b Rate constants given in [51] have been corrected to ratio of Einstein coefficients $\delta \rightarrow 2_g(aa)/\delta \rightarrow 2_g(aa)$ presented in [40]

^c It is difficult to determine the rate constants due to strong overlapping of the $E \rightarrow B$ and $D \rightarrow a'$ spectra

^d Only the sum of the rate constants to the D', β, γ and δ states was determined

^e Only the sum of the rate constants to the γ and δ states was determined

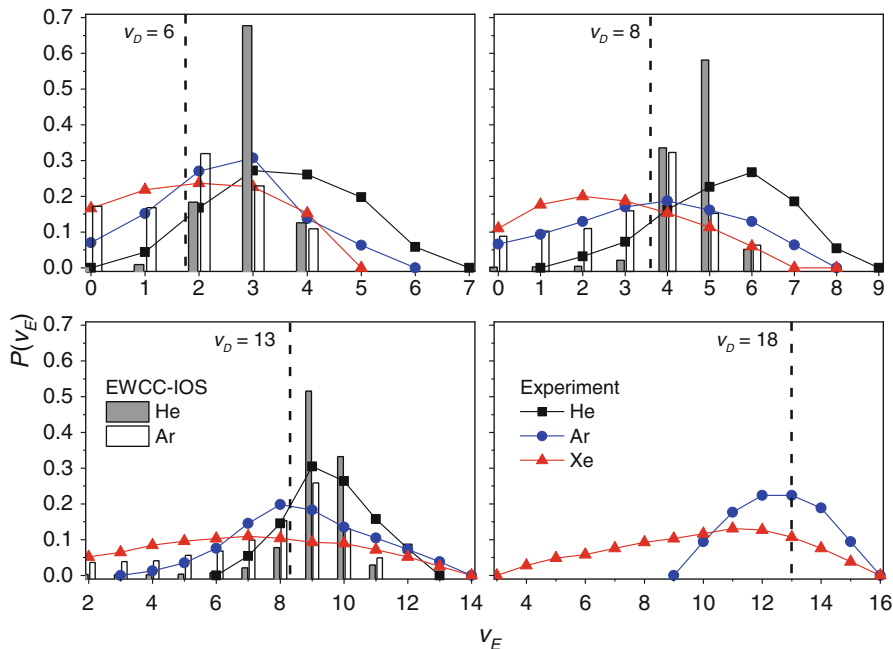


Fig. 5.3 Experimental and calculated using the EVCC-IOS (6×6) method V_D s for the $D \rightarrow E$ CINAT in collisions with He, Ar and Xe atoms. Vertical dashed lines indicate the positions of the initial v_D level [51]

Table 5.3 Rate constants of population of the iodine first tier IP states, $k(E,13,49 \xrightarrow{Ar} IP)$, $k(D,18,48 \xrightarrow{Ar} IP)$, $k(\beta,19,47 \xrightarrow{Ar} IP)$ and $k(D',23,48 \xrightarrow{Ar} IP)$, in units of $10^{-10} \text{ cm}^3/\text{s}$. Total, for all observed CINATs, rate constants (k_{CINAT}) are also given [40]

State	$E0_g^+$	$D0_u^+$	$\lambda_{lum}^{max} \approx 3410 \text{ \AA}^b$	$\delta 2_g$	$\gamma 1_u$	k_{CINAT}
$E,13,49$	–	0.44(4)	0.40(4) ^c	0.24(2)	0.22(2)	1.3
$D,18,48$	0.31(3)	–	2.9(3) ^c	0.6(1)	≤ 0.2	4.0
$\beta,19,47$	0.21(4)	0.5(1)	3.2(7) ^a	0.7(2)	≤ 0.2	4.8
$D',23,48$	≤ 0.05	≤ 0.1	≤ 0.1	≤ 0.01	$\leq 10^{-3}$	≤ 0.2

^arate constant of collisional population of the states which are responsible for luminescence at the $\lambda_{lum}^{max} \approx 3410 \text{ \AA}$ band with exception of those from the $\beta,19,47$ and δ states

^brate constant for the states which are responsible for luminescence at the $\lambda_{lum}^{max} \approx 3410 \text{ \AA}$ bands under the assumption that they are populated in CINATs

^cthe D' state is populated in the CINAT with very low probabilities

3. Vibrational distributions of the states populated in a CINAT are broad and depend on R_g ;
4. CINAT rate constants depend weakly on vibrational quantum numbers of optically populated states
5. Broad rotational distributions occur at the states populated in CINATs.

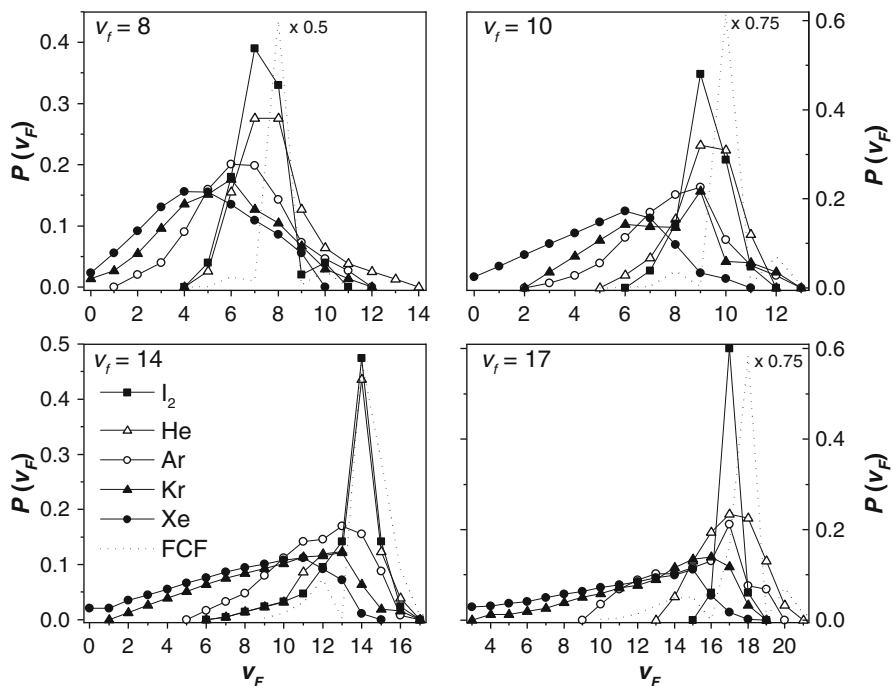


Fig. 5.4 Measured vibrational distributions $P(v_F)$ after exciting four different f, v_f levels. Dashed lines represent Franck–Condon factors [49]

An analysis has explained some of the features given above.

Experimental as well as theoretical results show that total, for all final vibronic levels, rate constants do not show any dependence on energy gap between initial and nearest final vibronic levels and smoothly increases with initial vibrational excitation. All the electronic states of the first tier except the $D'2_g$ one are populated in CINATs from E, D states in a statistical way for Rg = Ar – Xe, whereas the “parallel” $E \leftrightarrow D$ ($\Omega_g \leftrightarrow \Omega_u$) transitions with $\Delta\Omega = 0$ are dominant for Rg = He. Only the “parallel” transition $f \rightarrow F$ is observed for CINAT from f for all Rg atoms except Xe. The VDs for transitions from all studied states E, D, f are similar. It is resonant for He and broad for other Rg atoms. The large difference of the CINAT branching ratios is explained by the different behavior of the potential curves. The dipole polarizability of the He atom is $0.2 \cdot 10^{-24} \text{ cm}^3$, whereas for Ar–Xe they are about one order of magnitude larger, $1.6 - 4.0 \cdot 10^{-24} \text{ cm}^3$ [44]. Since the dipole polarizability determines the magnitude of the long-range interaction (see Eq. 5.73), the depth of the He–I₂ potential curve is much smaller than the mean thermal energy at 300 K, while the Ar–I₂ interaction strength approaches 240 cm^{-1} (see Sect. 6.4.3). Also, the mean collision velocity is smaller for heavier Rg atoms. Both factors increase the mean collision time and favor statistical population of the CINAT channels for Rg = Ar – Xe. The “parallel” coupling between states with the same f^e, Ω and opposite inversion parity ω is enhanced by the pairwise potential

curve V_- of ${}^1\Sigma^+ (I^- ({}^1S) - Rg)$ (see Eqs. 5.59 and 5.61). The latter circumstance has notable influence on CINAT dynamic for $Rg = He$. Using Eqs. (5.59, 5.61, 5.66 and 5.68), one can verify that interaction with Rg couples all the states from the first tier, whereas f and F states from the second tier correlating with the $I({}^3P_0) + I^-({}^1S)$ limit are uncoupled from other four states correlating with the $I({}^3P_1) + I^-({}^1S)$ limit. It turns out that f as well as F state coupled to all states of the first tier, though transitions from f to first tier states were not observed.

One sees in Figs. 5.1 and 5.3 that the $E \rightarrow D$ CINAT accompanied by positive vibrational energy transfer, whereas for the $D \rightarrow E$ CINAT there is negative vibrational energy transfer. The $f \rightarrow F$ transition show more pronounced propensity for the population of the nearest vibrational levels (Fig. 5.4). This is explained by the specific patterns of the $FCFs$. The splitting between E and D states is about five vibrational quanta, whereas that of between f and F states is one quantum, only. Moreover, the difference in equilibrium distances is 0.02 Å for the f, F states and 0.06 Å for the E, D states. The FCF patterns for the $f \rightarrow F$ transitions are more sharply peaked, and the final vibronic levels with maximum Franck–Condon overlap are near the levels closest in energy (Fig. 5.5).

5.3.2.5 Collisions with Molecules Possessing Permanent Electric Quadrupole Moments

Substantial difference between CINAT characteristics for Rg and molecules possessing permanent quadrupole moments, $M = I_2, N_2, CO_2$, is observed. It is the consequence of various characters of long-range interaction between collision partners. The long-range, $\sim R^{-4}$, interaction between the $I_2(E0_g^+ - D0_u^+)$ or $I_2(f0_g^+ - F0_u^+)$ transition electric dipole moment and the permanent electric quadrupole moments of M ($\Theta \approx 10, = 1.5$ and 4.2 , in units $10^{-26} esu$, for $I_2(X), N_2$ and CO_2 , respectively, [45, 71, 72]) is strong in these cases (R is the distance between centers of mass of the colliding partners). For rare gas atoms, the first non-vanishing term of multipole expansion of the interaction potential corresponds to short-range, $\sim R^{-6}$, dispersion one [31, 41–43, 47].

The $I_2(0_g^+ \xrightarrow{I_2(X)} 0_u^+)$ CINATs. In pure iodine vapor, the $I_2(E0_g^+ \xrightarrow{I_2(X)} D0_u^+)$ and $I_2(D0_u^+ \xrightarrow{I_2(X)} E0_g^+)$ CINATs are dominant due to large $I_2(X)$ permanent electric quadrupole moment. The $I_2(f \xrightarrow{I_2(X)} F)$ CINAT is the only, that it has been occurred [70]. Let us discuss these processes at first.

The $I_2(E, \nu_E \xrightarrow{I_2(X)} D, \nu_D)$ CINATs have been studied in detail in [39, 41, 42, 47, 50, 51, 64, 67, 69] (see [31], also). The $I_2(D, \nu_D \xrightarrow{I_2(X)} E, \nu_E)$ CINATs have been studied in [69]. The principal features obtained are as follows (see Figs. 5.6 and 5.7):

- The $u \leftrightarrow g$ and $\Delta\Omega = 0$ propensity rules are valid in these cases;
- CINAT total, for all D state vibronic levels, rate constants exhibit sharp maxima as functions of ν_E , and near-resonant CINATs have highest total rate constants.

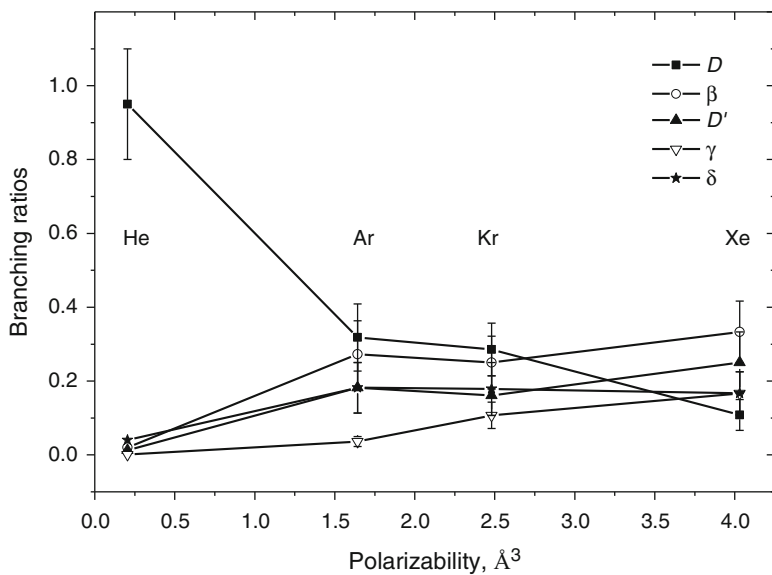


Fig. 5.5 Branching ratios of $I_2(E, 19^{Rg} \rightarrow IP)$ CINAT channels as a function of $Rg = He, Ar, Kr, Xe$ polarizability

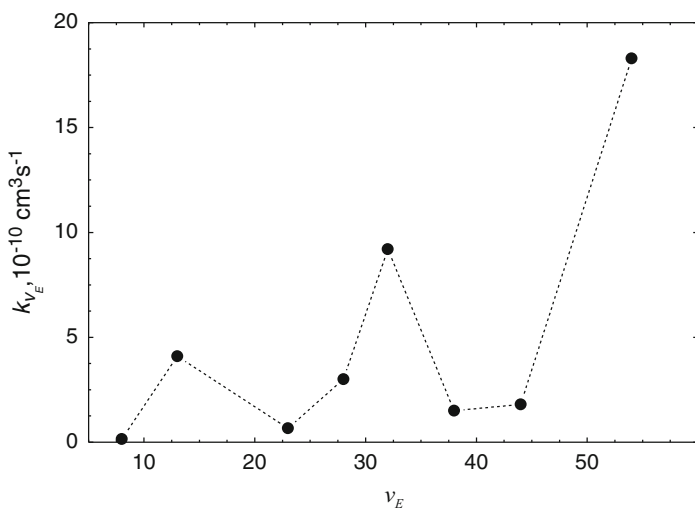


Fig. 5.6 Total, for all v_D , rate constants of the $I_2(E, v_E \xrightarrow{I_2(X)} D, v_D)$ CINATs [69]

Near-resonant $0 \text{ cm}^{-1} \leq |\Delta E| \leq 20\text{--}25 \text{ cm}^{-1}$, long-range, rate constants $\sim (4\text{--}18) \cdot 10^{-10} \text{ cm}^3/\text{s}$, and non-resonant, $|\Delta E| \geq 25 \text{ cm}^{-1}$, rate constants $\sim (0.7\text{--}2) \cdot 10^{-10} \text{ cm}^3/\text{s}$ CINATs occur (Fig. 5.6). The former is called as “approach-induced non-adiabatic transitions” in [39]. Vibronic states nearest to the initial ones are mainly populated in the near-resonant CINATs. Similar resonant character of the rate constant dependence has been observed in [39], but rate constants in this work are **over-evaluated** (see discussion in [69]);

- The $\Delta J = \pm 1$ and “ ΔJ – large” propensity rules are valid in near-resonant and non-resonant CINATs, respectively;
- The $E, v_E \xrightarrow{I_2(X)} D, v_D$ and $E, v_E \xleftarrow{I_2(X)} D, v_D$ CINAT rate constants are similar;
- There are no distinct correlations between populations of vibronic states (VDs) and FCFs of initial and final vibronic levels (see Fig. 5.7 e.g). The VDs “try” to follow the trend in the FCFs with the initial states, but energy gap law, $P \sim \exp\left(-\frac{|\Delta E|}{\beta}\right)$ (β – is a variable parameter, usually, $\beta = kT$) (see [18, 43] and references) “prevents” this trend [65].
- The near-resonant CINATs are governed by the permanent $I_2(X)$ quadrupole – $I_2(E\text{-}D)$ transition dipole interaction;
- Rate constants of non-resonant processes correspond to small impact parameters. In these cases, the CINATs are provided by orbiting of the $I_2(E \text{ or } D)$ and $I_2(X)$ colliding partners due to dispersion, $-C_6/R^6$, interaction [42, 43]. The orbiting leads to a population of several vibronic states in non-adiabatic transitions from the initial to final I_2 states. Cross-section of the complex formation is $\sigma_c \approx 80 \text{ \AA}^2$ [42]. CINAT rate constants depending on long-range, transition

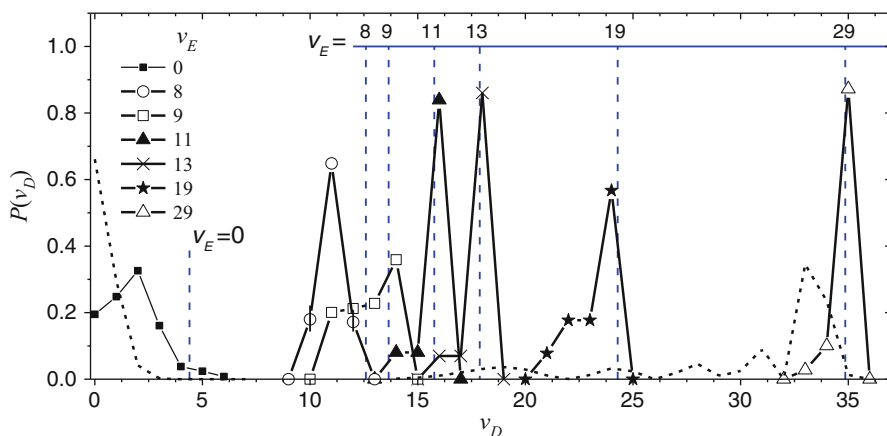


Fig. 5.7 Vibrational distributions (VD) for the $I_2(E, v_E \xrightarrow{I_2(X)} D, v_D)$ CINATs measured in [65] ($v_E = 0$) and [39]. The positions of the initial levels are marked by vertical dashed lines. Dotted lines represent the FC factor distributions for $v_E = 0$ and 29. Vibrational quantum numbers of the initially populated vibrational levels of the E state are marked [31]

$I_2(E-D)$ dipole – permanent $I_2(X)$ quadrupole, $-C_4/R^4$, interaction [51, 70] decreases strongly in this case due to large energy mismatch.

Very similar features have been observed for the

$$I_2(f0_g^+ \xrightarrow{I_2(X)} F0_u^+)$$

CINAT (see Fig. 5.8). They have been explained in the framework of the electrostatic model (see below).

The $I_2(E0_g^+ \xrightarrow{M} D0_u^+, D'2_g, \beta1_g, \delta2_u, \gamma1_u)$ CINATs, $M = N_2, CO_2$. In these cases nonadiabatic transitions to the β, D', δ and γ states are also observed (Table 5.4).

Integrated, for all states of the tier, rate constants depend weakly on v_E for $M = N_2, CO_2$. Vibrational distributions corresponding to the $I_2(E, v_E, J_E \xrightarrow{M} D, v_D, J_D)$ CINATs, look as sharp maxima superimposed with rather broad distribution (Fig. 5.8), similar to those observed for Ar (see Sect. 5.3.2.4).

The former is caused by the interaction between the $I_2(E-D)$ transition electric dipole and the permanent electric quadrupole of M, as in the case of $M = I_2(X)$, and the latter by the dispersion one (see above). Sums of the partial rate constants corresponding to dispersion interaction can be estimated as 70% ($v_E = 8$), 80% ($v_E = 13$) and 90% ($v_E = 19$) ($M = N_2$) and 40% ($v_E = 8$), 35% ($v_E = 13$) and 25% ($v_E = 19$) ($M = CO_2$) of the integrated $I_2(E \xrightarrow{M} D)$ ones. Relative populations corresponding to the dispersion interaction were calculated as sums of populations

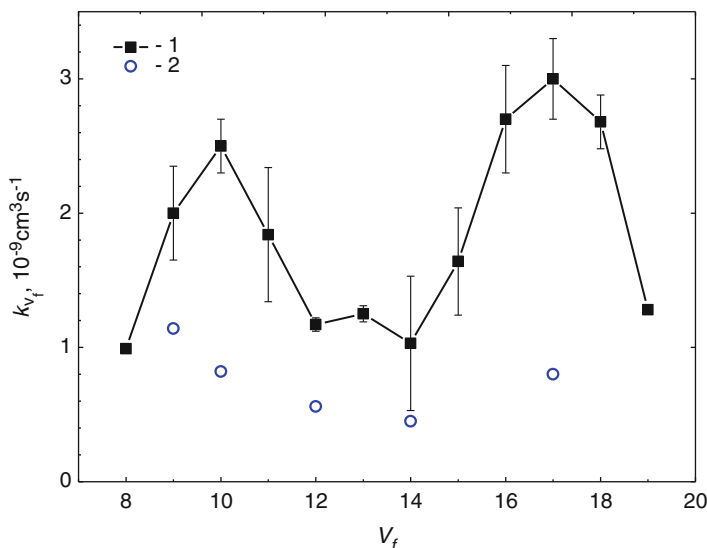


Fig. 5.8 The total (1) rate constant of the $I_2(f0_g^+ \xrightarrow{I_2(X)} F0_u^+)$ CINAT and that of nonresonant transitions (2) plotted as functions of the v_f number. Transitions to all v_f levels (curve 1) and v_f levels except the nearest ones (curve 2) are taken into account [70]

Table 5.4 Partial $I_2(E \xrightarrow{M} D)$, $I_2(E \xrightarrow{M} \beta)$, $I_2(E \xrightarrow{M} D')$, $I_2(E \xrightarrow{M} \gamma)$, $I_2(E \xrightarrow{M} \delta)$ and $I_2(E \xrightarrow{M} D + D' + \beta + \gamma + \delta)$ CINAT rate constants, k_{tot} , for $M = N_2, CO_2$ for $E, v_E = 8, 13, 19; J_E \approx 55$. All units are in $10^{-10} \text{ cm}^3/\text{s}$ [47]

M	v_E	$k_{E \rightarrow D}$	$k_{E \rightarrow \beta}$	$k_{E \rightarrow D'}$	$k_{E \rightarrow \gamma}$	$k_{E \rightarrow \delta}$	k_{tot}
N_2	8	3.9 ± 0.5	3.1 ± 0.9	0.9 ± 0.3	0.21 ± 0.06	0.50 ± 0.15	8.6 ± 2.5
	13	5.1 ± 0.8	3.9 ± 0.9	1.0 ± 0.3	0.2 ± 0.06	0.75 ± 0.2	11 ± 2.3
	19	6.1 ± 0.9	2.9 ± 0.9	0.7 ± 0.2	0.24 ± 0.07	0.56 ± 0.2	10.5 ± 2.2
CO_2	8	3.5 ± 0.5	4.0 ± 1.2	1.9 ± 0.6	0.17 ± 0.05	0.13 ± 0.04	9.7 ± 2.4
	13	6.5 ± 0.9	4.5 ± 1.4	1.4 ± 0.4	0.31 ± 0.09	0.34 ± 0.10	13.1 ± 1.9
	19	9.1 ± 1.4	4.0 ± 1.2	<0.1	0.17 ± 0.05	0.31 ± 0.09	13.9 ± 2.8

of the levels lying on the dotted lines of Fig. 5.9. These lines are drawn through the symbols of the levels which cannot be populated due to interaction between the $I_2(E-D)$ transition electric dipole and the permanent electric quadrupole of N_2 . Partial rate constants corresponding to these types of interaction are presented in columns 3 and 4, respectively, of Table 5.5.

There are significant differences of the VD s for N_2 and CO_2 . In the latter case, there are additional maxima corresponding to the energy loss of $630\text{--}710 \text{ cm}^{-1}$ or 7–8 vibrational quanta for $v_E = 8, 19$ (see Fig. 5.9). The energy loss is close to excitation energy of $CO_2 \nu_2 e_{1u}$ vibrational mode (667 cm^{-1}). As it shown in the next Sect., the sharp maximum in VD s, $P(v_D)$, of the $E, v_E = 19, J_E \xrightarrow{CO_2} D, v_D = 17, J_D$ transition is caused by the interaction of the $I_2(E-D)$ transition electric dipole and $CO_2(01^1 0 \leftarrow 000) \nu_2 e_{1u}$ transition electric dipole. Partial rate constant corresponding to this type of interaction is presented in column 5 of Table 5.5.

There are two CO_2 IR active vibrational modes that can be excited, namely, $CO_2(01^1 0 \leftarrow 000) \nu_2 e_{1u}$ (667 cm^{-1}) and $CO_2(001^0 \leftarrow 000) \nu_3 a_{1u}$ (2349 cm^{-1}) [73]. The CINAT induced by the $I_2(E-D)$ transition electric dipole – $CO_2(001^0 \leftarrow 000)$ transition electric dipole is impossible for $v_E \leq 19$. The energy loss of iodine molecule corresponding to ν_2 mode excitation, ($\Delta v_D \approx 7$) become apparent in the case of $v_E = 8, 19$ (Fig. 5.9). This transition is the most pronounced for the $v_E = 19$ level since it is resonant one. The small energy mismatch ($\Delta E = -10 \text{ cm}^{-1}$) compensated by the rotational energy change in $CO_2 (J-1 \leftarrow J = 10, 12, 14)$ transitions. The maximum of the $CO_2(X)$ thermal rotational distribution occurs at $J = 16$. One cannot observe the dipole – dipole induced transition for the $v_E = 13$ level, probably, due to three reasons:

- energy mismatch is rather large, $\Delta E = -30 \text{ cm}^{-1}$, for the $v_E = 13, v_D = 11$ combination corresponding to minimal energy difference,
- FC factor for this combination is 2.7 times less than that of for the $v_E = 19, v_D = 17$ one,
- R, P branches of the $CO_2(010 \leftarrow 000)$ transition 2 times less intensive than Q one for high rotational levels, and only the former can compensate this energy mismatch. It is very complicated to record such slight population of the levels.

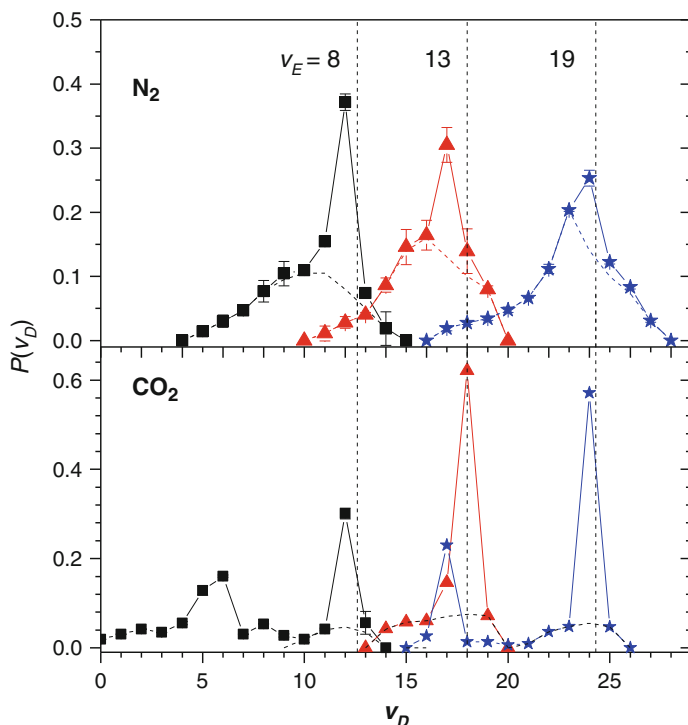


Fig. 5.9 Populations of the $I_2(D, v_D, J_D)$ vibronic levels formed from selected rovibrational levels $I_2(E, v_E, J_E \approx 55)$ in nonadiabatic transitions induced by collisions with $M = N_2$ and CO_2 . The vibrational quantum numbers of initially populated v_E levels are shown. Vertical dotted lines show energetic positions of the optically populated $v_E, J_E = 55$ rovibrational levels relative to the $v_D, J_D = 54$ ones. Sums of relative populations are equal to 1 for each initial v_E level. Dotted lines show VDs corresponding to dispersion interaction (see below) [47]

Table 5.5 Partial $I_2(E \xrightarrow{M} D)$ rate constants corresponding to the $I_2(E-D)$ transition electric dipole – M permanent electric quadrupole, k_{d-q} , dispersion, k_{dis} , and $I_2(E-D)$ transition electric dipole – M transition electric dipole, k_{d-d} , interactions for $M = N_2, CO_2$ and $E, v_E = 8, 13, 19; J_E \approx 55$. All units are in $10^{-10} \text{ cm}^3/\text{s}$ [47]

M	v_E	k_{d-q}	k_{dis}	k_{d-d}
N_2	8	1.5	2.4	–
	13	1.1	4.0	–
	19	0.8	5.3	–
CO_2	8	1.0	2.5	–
	13	3.6	2.9	≤ 0.05
	19	4.7	2.0	2.4

There is broad $\nu_D^{\max} = 6$ “band” at the D state VD for $M = \text{CO}_2$ and $\nu_E = 8$ (Fig. 5.9), that can be assigned to the ν_2 mode excitation. The energy mismatch for this combination is $\Delta E = -50 \text{ cm}^{-1}$ and cannot be compensated by the CO_2 rotational energy change. The FC factor of this combination is only 2.7 times larger than that of $\nu_E = 13$, $\nu_D = 11$ one. It is incomprehensible, can one explain this “band” by using of the dipole – dipole interaction. It can be caused by other terms of multipole expansion, probably (see below).

Electrostatic Model for the $I_2(0_g^+ \xrightarrow{M} 0_u^+)$ CINATs, $M = I_2(X), N_2, \text{CO}_2$ A transparent semiquantitative interpretation of CINAT with collision partners possessing permanent electric multipole moments relied upon the *electrostatic model* suggested for the first time by Alexander [21]. The model was successfully used by Lawley [45] and in the author’s laboratory (see [31, 47, 70] and references therein) to analyze CINATs. In this model, the diabatic couplings between IP states are determined by the long-range multipole expansion.

The potential energy operator in the case of interaction between two diatomic molecules is expanded in the standard multipolar series (see, e.g., [21]):

$$U(R) = \sum_{l_1 l_2} U_{l_1 l_2} / R^{l_1 + l_2} \quad (5.75)$$

where l_1 (l_2) is the l -th electric multipole rank of the excited (unexcited) collision partner, $l = l_1 + l_2$, $U_{l_1 l_2}$ are orientation dependent coefficients.

The transition probability of the process:

$$I_2(i, \nu_i, J_i) + I_2(X0_g^+, \nu_X, J_X) \rightarrow I_2(j, \nu_j, J_j) + I_2(X, \nu'_X, J'_X) \quad (5.76)$$

where i and j are initial and final IP states for fixed impact parameter b , V is a velocity of relative motion and Hunds case (c) (specification of the electronic states by the quantum number of the projection along the interatomic axis Ω) is (see [21, 70]).

$$P_{ij} = \sum_{l_1 l_2} \frac{1}{\hbar^2 V^2 b^{2l}} \left[\langle j | Q_{\Delta\Omega_1}^{l_1} | i \rangle \langle \nu_i | \nu_j \rangle^2 \langle X, \nu' | Q_{\Delta\Omega_2}^{l_2} | X, \nu \rangle^2 \right] \cdot C_{l_1 l_2} R_l(\xi), \quad (5.77)$$

$$C_{l_1 l_2} = \frac{2^{2l+1} [(l-1)!]^2}{(2l_1+1)!(2l_2+1)!} \langle J_i \Omega_i l_1 \Delta \Omega_{ij} | J_j \Omega_j \rangle^2 \langle J_X \Omega_X l_2 \Delta \Omega_X | J'_X \Omega_2 \rangle^2 \quad (5.78)$$

Here, Q_m^l is the component of l -th electric multipole operator, $\langle J_i \Omega_i l_1 \Delta \Omega_{ij} | J_j \Omega_j \rangle$, $J_X \Omega_X = 0 l_2 \Delta \Omega_X | J'_X \Omega_2 = 0$ are Clebsch-Gordan coefficients, $R_l(\xi)$ are the resonance functions of Massey parameter $\xi = \frac{\Delta E_{5.76} b}{\hbar V}$, $\Delta E_{5.76}$ is the energy difference between final and initial states in process (5.76), $\langle \nu_i | \nu_j \rangle^2$ is FCF . The Eq. (5.77) is valid within Franck-Condon approximation.

If one take into consideration *only the first* nonvanishing term of the multipole expansion of interaction energy operator (5.75) for $I_2(i) + I_2(X)$ system corresponding *transition dipole – permanent quadrupole* interaction, then $l_1 = 1$, $l_2 = 2$, $Q^1 = \mu$ (dipole

moment operator), $Q^2 = Q$ (quadrupole moment operator). In this case the transition probability and Clebsch-Gordan coefficients are:

$$P_{ij} = \sum_{l_1 l_2} \frac{1}{\hbar^2 V^2 b^{2.3}} [\langle j | \mu | i \rangle^2 \langle v_i | v_j \rangle^2 \langle X, v' | Q | X, v \rangle^2] \cdot C_{12} R_l(\xi), \quad (5.77a)$$

$$C_{12} = \frac{32}{45} \langle J_i \Omega_i l_1 \Delta \Omega_{ij} J_j \Omega_j \rangle^2 \langle J_X \Omega_X l_2 \Delta \Omega_X J'_X \Omega_2 \rangle^2 \quad (5.78a)$$

Matrix element $\langle j | \mu | i \rangle$ is nonvanishing one only for *optically allowed* transitions $g \leftrightarrow u$, $\Delta \Omega = 0, \pm 1$, $0^+ \leftrightarrow 0^+$, $0^- \leftrightarrow 0^-$ [4]. According to Lawley's estimation [45], the transition dipole moment $0_g^+ | \mu | 0_u^+$ is giant (~ 25 D) for transitions between the states of the *same tier*, and vanishes for the transitions between the states of *different tiers* in the model of separated atoms (see Sect. 3.1), since transitions between the $1^+(\ ^3P_2, \ ^3P_1, \ ^3P_0, \ ^1D$ and $\ ^1S)$ states are forbidden. The perpendicular transitions with $\Delta \Omega \neq 0$ are also forbidden in the framework of this model [45]. The resonance function of dipole-quadrupole interaction is [46]

$$R_3(\xi) = \exp(-2\xi)(1 + 1.98\xi + 2.182\xi^2 + 1.533\xi^3 + 0.933\xi^4 + 0.785\xi^5)$$

The function $R_3(\xi) \approx 1.0 \pm 0.2$ in the range $\xi = 0-3$, which corresponds to $\Delta E' = \Delta E_{ff} + \Delta E_X \leq 1 \text{ cm}^{-1}$ at $b = 30 \text{ \AA}$ and $V = 2.2 \cdot 10^4 \text{ cm/s}$ ($I_2 - I_2$ collision). A deficit of the energy in the $I_2(f, v_f, J_f) \rightarrow I_2(F, v_F, J_F = J_f \pm 1)$ transition can be compensated by its surplus in the $I_2(X, v_X, J_X) \rightarrow I_2(X, v'_X, J'_X)$ one, and vice versa. It was shown in [47] that rotational transition $\Delta J(N_2(X)) = +2$ allowed in electrostatic model can compensate an energy mismatch, so $R(\xi) \approx 1$.

Experimental data given above for both first and second tiers (see [31, 39, 42, 47, 69, 70], also) agree qualitatively with these propensity rules:

- The $0_g^+ \xleftrightarrow{M} 0_u^+$ transitions between the states of the same tier is the main channel of CINATs;
- the $0_g^+ \xrightarrow{M} 0_u^+$ transition between the states of different tiers has not been observed.

The rotational propensity rules are governed by the requirement on nonzero values of Clebsch-Gordan coefficients in (5.78), and 6 channels $J_i - J_j = \pm 1$, $J'_X - J_X = 0, \pm 2$ are opened in the $0_g^+ \xleftrightarrow{M} 0_u^+$ CINATs [18, 21]. It was shown in [37] that the $I_2(E, v_E = 1, J_E = 25) \xrightarrow{I_2(X)} I_2(D, v_D, J_D = J_E \pm 1)$ transitions are the most probable, and probabilities of the $\Delta J = \pm 3$ channels *appr.* 30 times less. The same feature was obtained in [45] for the $I_2(f0_g^+ \xrightarrow{I_2(X)} F0_u^+)$ CINAT.

The cross-section of a collision-induced process in the first Born approximation is determined by the equation:

$$\sigma_{ij} = \pi b_c^2 + \int_{b_c}^{\infty} P_{ij}(b) db \quad (5.79)$$

where cut-off impact parameter b_c is determined from

$$P_{ij} = 0.5 \quad (5.80)$$

equality [46].

An estimation for the one of open channels of the near resonant $I_2(f0_g^+, v_f = 17 \xrightarrow{I_2(X)} F0_u^+, v_F = 17)$ CINAT obtained in [70], $\sigma_{fF} \approx 3000 \text{ \AA}^2$ agrees satisfactorily with experimental data, $\sigma_{fF} = k_{5.74}/V = 1500 \text{ \AA}^2$ (see Fig. 5.8), $V = 2.2 \cdot 10^4 \text{ cm/s}$ is mean velocity of $I_2 - I_2$ relative motion [42].

The $I_2(E, v_E, J_E \xrightarrow{M} D', v_D, J_{D'})$ and β, v_β, J_β CINATs. We did not observe a population of the β and D' states in the CINAT if $M = I_2$. In the case of $M = N_2, CO_2$ both states are populated, so both molecules act similar to rare gases, i.e. as structureless partners.

The probability of the $E \xrightarrow{M} \beta$ CINAT is about 4 times larger than that of $E \xrightarrow{M} D'$ one (Table 5.4). Vibrational distributions for the β state near the position of initially populated v_E levels are very wide as in the case of Rg (Fig. 5.10). They correspond to the dispersion interaction.

Very intriguing is the presence of the low energy β state vibrational levels in $P(v_\beta)$ corresponding to loss of about 7 vibrational quanta $590-720 \text{ cm}^{-1}$ in the $E, v_E \xrightarrow{CO_2} \beta, v_\beta$ CINAT. The presence of low energy β state vibrational levels cannot be attributed to the interaction between the $I_2(E-\beta)$ transition electric dipole and the $CO_2(01^10 \leftarrow 000)$ transition electric dipole in the first-order of semiclassical perturbation theory since $\langle \beta 1_g | \mu | E 0_g^+ \rangle = 0$ [47]. Excitation of the $CO_2 \nu_2 e_{1u}$ (667 cm^{-1}) decreases energy mismatches up to $\Delta E' = -6 \text{ cm}^{-1}, -78 \text{ cm}^{-1}$ и $+54 \text{ cm}^{-1}$ for $v_E = 8, 13, 19$, respectively. At the two later levels, the energy differences cannot be compensated by the CO_2 rotational energy change. This feature can be due to polarization interaction accompanied by quasi-resonance excitation of CO_2 collision partner.

One should note that it is impossible to describe the spectra in the $\lambda = 3300-3550 \text{ \AA}$ range completely by using the populations of the β state depicted in Fig. 5.10b; it is necessary to use v_β levels corresponding to loss up to 14 vibrational quanta of the β state (Fig. 5.10c).

5.3.2.6 Collisions with Molecules Possessing Permanent Electric Dipole Moments

According to the electrostatic model discussed in previous Sect., the $I_2(0_g^+ \xleftrightarrow{M} 0_u^+)$ CINATs have to be the most probable if M possesses a permanent electric dipole moment. In this case, long-range interaction between the $I_2(E-D)$ transition electric dipole and the permanent electric dipole of M , $\sim R^{-3}$, is dominant. For these collision partners, rate constants of quasi-resonant CINATs have to be huge, and VDs have to be narrow if energy mismatches have not compensated by rotational transitions in a colliding partner. Studies carried out in $M + H_2O$ [67-69] (dipole moment is $\mu_{H_2O} = 1.6 \text{ D}$ [73, 74]), acetone, CH_3COCH_3 and CD_3I [48] (acetone and

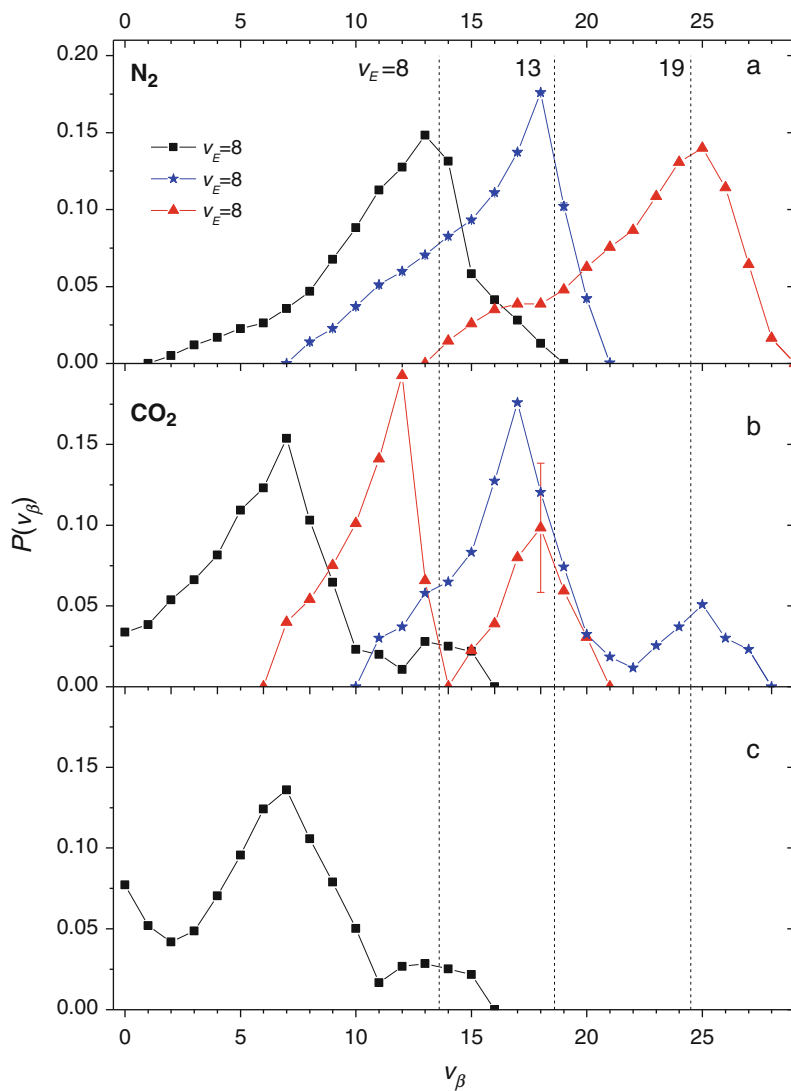


Fig. 5.10 Populations of the $I_2(\beta, v_\beta, J_\beta)$ vibronic levels formed from selected rovibrational levels $I_2(E, v_E, J_E \approx 55)$ in nonadiabatic transitions induced by collisions with $M = \text{N}_2$ (a) and CO_2 (b). It is supposed that energy loss cannot be higher than corresponding to the $\text{CO}_2(v_2e_{1u}) \approx 667 \text{ cm}^{-1}$ vibrational mode excitation. The same as in Fig. 5.10 (b), $v_E = 8$, utilized to describe all the $\lambda = 3300\text{--}3550 \text{ \AA}$ range completely (c). The vibrational quantum numbers of initially populated v_E levels are shown. Vertical dotted lines show energetic positions of the optically populated $v_E, J_E = 55$ rovibronic levels relative to the $v_\beta, J_\beta = 54$ ones. Sums of populations are equal to 1 for each initial v_E level

Table 5.6 The $k(E, v_E \xrightarrow{H_2O} D, v_D)$ and $k(D, v_D \xrightarrow{H_2O} E, v_E)$ CINAT rate constants in units of $10^{-10} \text{ cm}^3/\text{s}$ obtained in [67, 69]

$E, 8, 52$			$D, 13, 55$	
D	$\lambda_{lum}^{max} \approx 3400 \text{ \AA}^a$	E	$\lambda_{lum}^{max} \approx 3400 \text{ \AA}^a$	
36 ± 6^3	35^b	4.0 ± 0.5^c	$27 + 4^c$	–
$E, 13, 25$			$D, 18, 28$	
D			E	
20 ± 3^c	43^b	4.0 ± 0.5^c	9.4 ± 1.6^c	4.0 ± 0.5^c

^a–rate constants for the states which luminescence occurs at $\lambda_{lum}^{max} \approx 3400 \text{ \AA}$, if they are populated in CINATs

^b– $J_E = 55 \pm 1$ rotational states were populated in this work, [67]

^c[69]

Table 5.7 Partial $k^M(i, v_E)$ ($i = D, D' + \beta, \gamma, \delta$) and total $I_2(E \xrightarrow{M} D + D' + \beta + \gamma + \delta)$, $k_{tot}^M(v_E)$, CINAT rate constants for $M = \text{CD}_3\text{I}$ and $(\text{CO}_3)_2\text{CO}$ [48]. All values are in $10^{-10} \text{ cm}^3/\text{s}$

M	v_E	$k^M(D, v_E)$	$k^M(D' + \beta, v_E)$	$k^M(\gamma, v_E)$	$k^M(\delta, v_E)$	$k_{tot}^M(v_E)$
CD_3I	8	1.00 ± 0.15	0.44 ± 0.13	<0.05	<0.03	1.44 ± 0.28
	13	11.7 ± 1.7	0.36 ± 0.11	0.12 ± 0.04	<0.03	12.2 ± 1.9
	19	5.7 ± 0.9	0.94 ± 0.3	0.56 ± 0.17	<0.03	7.2 ± 1.4
Acetone	8	2.6 ± 0.3	0.66 ± 0.20	≤ 0.1	3.3 ± 0.5	
	13	15.5 ± 2.3	0.73 ± 0.20	0.29 ± 0.09	<0.03	16.5 ± 2.6
	19	18.2 ± 2.7	0.88 ± 0.26	0.72 ± 0.20	<0.03	19.8 ± 3.2

CD_3I dipole moments is 2.93 D and 1.65 D, respectively [75–77]) confirm these expectations (Tables 5.6 and 5.7).

The $I_2(E, v_E, J_E \xrightarrow{H_2O} D, v_D, J_D)$ CINATs are resonant for all populated vibronic levels due to rotational transitions in H_2O molecules [69], vibrational populations are broad (Fig. 5.11), and total rate constants are large even for $E, v_E = 8$, though energy mismatch between the $E, v_E = 8$ and nearest $D, v_D = 12, 13$ vibronic levels are large, $\Delta E > 30 \text{ cm}^{-1}$ (see Fig. 5.10).

In the case of $M = \text{CD}_3\text{I}$ and $(\text{CO}_3)_2\text{CO}$, rotational excitation of the collision partners can also compensate the energy mismatch between initial and final rovibrational levels, but vibrational population profile are much narrower (Fig. 5.12).

Dispersion interactions accompanied by quasi-resonance excitation of the collision partner vibrational modes are also occurred at $v_E = 8$ vibronic level. They lead to population of low, $v_E \leq 10$ vibronic states [48].

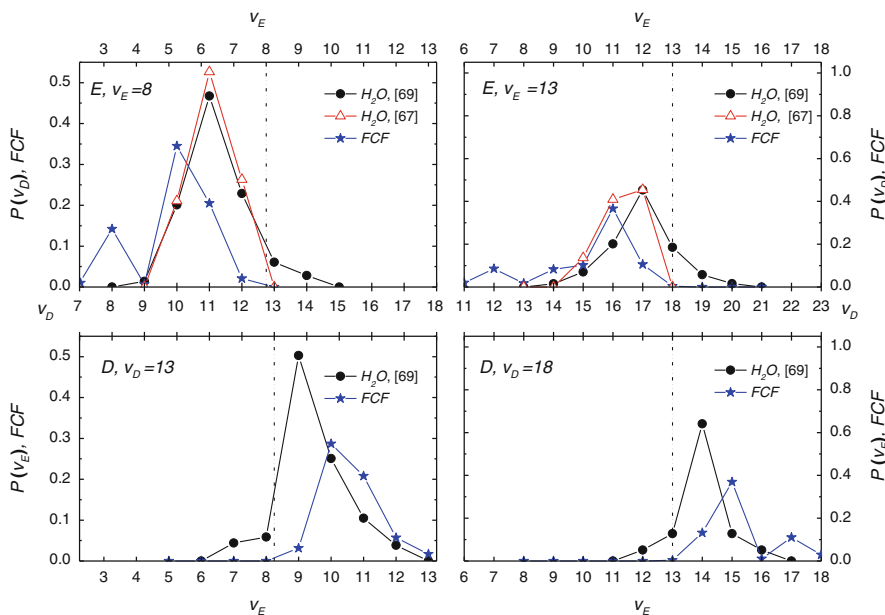


Fig. 5.11 Vibrational populations for the $I_2(E, v_E \xrightarrow{M} D, v_D)$ CINATs in collisions with $M = H_2O$ [69]. Vertical dashed lines indicate the positions of the initial v_E levels. All the VD s are normalized to their sums. FCF s between optically and collisionally populated vibronic levels are also shown

5.3.2.7 Collisions with Molecules Possessing Transition Electric Dipole Moments

According to the electrostatic model, the leading term of electrostatic expansion for collisions with molecules possessing infrared transition electric dipole moments corresponds to $E-D$ transition electric dipole moment – IR transitions electric dipole moment, $\sim R^{-3}$, interactions. Similar interactions are observed for $M = CO_2$ (Sect. 3.2.5) and CD_3I , $(CH_3)_2CO$ (Sect. 3.2.6). These CINATs have been studied for $M + CF_4$, SF_6 in details [31, 41, 52, 57].

Collisions with both partners produce very efficient electronic energy transfer with the total rate constant of order of $10^{-9} \text{ cm}^3/\text{s}$. The total CINAT probability is predominantly associated to the transitions that lead to dipole allowed $\nu_3 = 1283 \text{ cm}^{-1}$ (CF_4), 948 cm^{-1} (SF_6) and $\nu_4 = 631 \text{ cm}^{-1}$ (CF_4), 615 cm^{-1} (SF_6) excitations of the partner. As a result, CF_4 and SF_6 partners are efficient for I_2 vibrational energy loss (Table 5.8).

The VD s for the D state reveal broad features corresponding to CINATs in which the partner acts as a structureless particle, and narrow maxima formed by the CINATs assisted by excitations of the dipole allowed ν_3 and ν_4 vibrational modes of the partner (see Fig. 5.13).

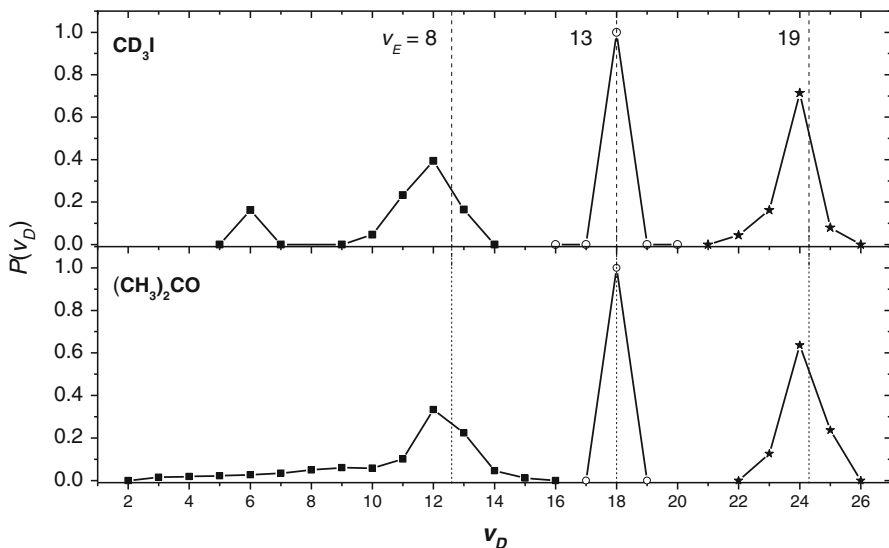


Fig. 5.12 Relative populations of the $\text{I}_2(D, v_D, J_D)$ vibronic levels formed from selected rovibronic levels $\text{I}_2(E, v_E = 8, 13, 19, J_E \approx 55)$ in non-adiabatic transitions induced by collisions with $\text{M} = \text{CD}_3\text{I}$ and $(\text{CH}_3)_2\text{CO}$. The vibrational quantum numbers of initially populated v_E levels are shown. Vertical dotted lines show energetic positions of the optically populated $v_E, J_E = 55$ rovibronic levels relative to the $v_D, J_D = 54$ ones. Sums of relative populations are equal to 1 for each initial v_E level [48]

Table 5.8 Partial and total $k^M(v_E)$ CINAT rate constants ($10^{-10} \text{ cm}^3/\text{s}$), $\text{M} = \text{CF}_4, \text{SF}_6$. First row – experiment, second row – theory. Theoretical $k^M(D; v_E)$ constants calculated using CC(6) model are given in parentheses [52]

M	v_E	$k^M(D; v_E)$	$k^M(\beta; v_E)$	$k^M(D'; v_E)$	$k^M(\gamma; v_E)$	$k^M(\delta; v_E)$	$k^M(v_E)$
CF_4	8	3.5 ± 0.5	3.6 ± 1.1	2.3 ± 0.7	< 0.1	< 0.1	9.4
		2.6 (3.3)	2.6	2.3	0.3	0.3	8.2
	13	3.4 ± 0.5	4.2 ± 1.3	2.8 ± 0.8	0.2	0.2	10.8
		8.9 (13.9)	1.1	3.0	0.8	1.3	15.1
	19	3.3 ± 0.5	5.5 ± 0.8^a	0.3	0.3	9.4	
		(4.0)	–	–	–	–	–
SF_6	8	13.0 ± 1.9	1.5 ± 0.4	1.4 ± 0.4	$< 0.2^a$	15.9	
		6.2 (5.4)	4.8	3.8	0.1	0.1	15.1
	13	3.3 ± 0.5	8.3 ± 1.2^a	$< 0.2^a$	11.6		
		(6.9)	–	–	–	–	–
	19	4.6 ± 0.7	8.2 ± 0.2^a	0.1	0.1	13.0	
		(1.4)	–	–	–	–	–

^aSum for two transitions

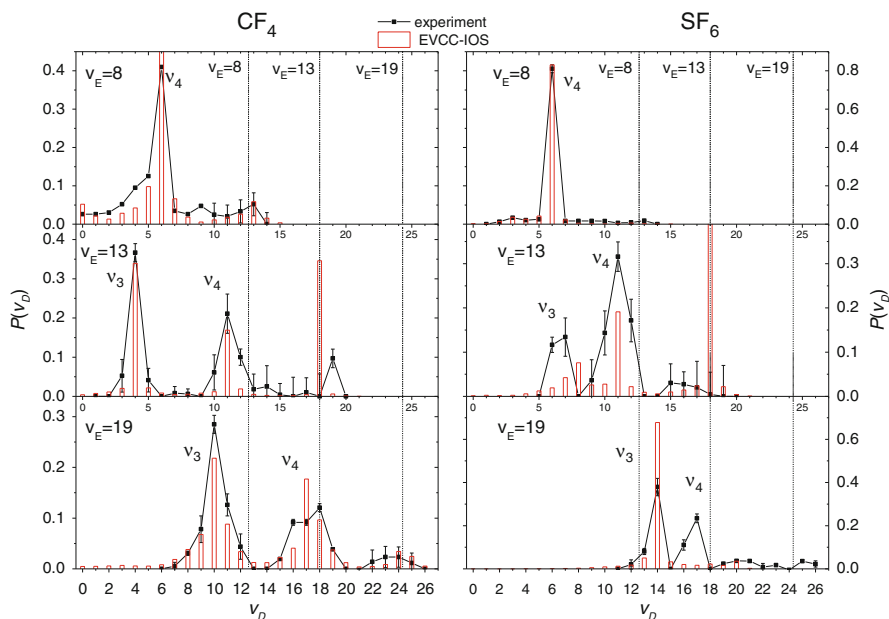


Fig. 5.13 Vibrational distributions in the $E^M \rightarrow D$ CINAT channel. Lines and squares represent the experiment, vertical bars – theory (see [52])

According to the theoretical analysis, the former originates from transitions induced by short-range couplings, the latter – from assisted electrostatic transitions induced by the long-range interaction of two transition dipoles. Vibrational distributions for other channels, first of all the D' and β , exhibit the same features despite no direct electrostatic transitions can lead to partner's vibrational excitation (Fig. 5.14).

The corresponding CINATs are interpreted within the post-collision mechanism [52]. Qualitatively, it implies that, during a single collision, the long-range transitions to D, v_3 and D, v_4 channels are followed by the short-range transitions to other electronic states which cannot change the state of the partner. The propensity of the assisted electrostatic transitions to near-resonant energy transfer makes overall CINAT dynamics sensitive to the accidental variations of the resonance defects, or energy gaps between initial and closest final levels. They alter both the branching ratio and the total CINAT rate. The CINATs to the D' and β states dominate among the transitions to the D state.

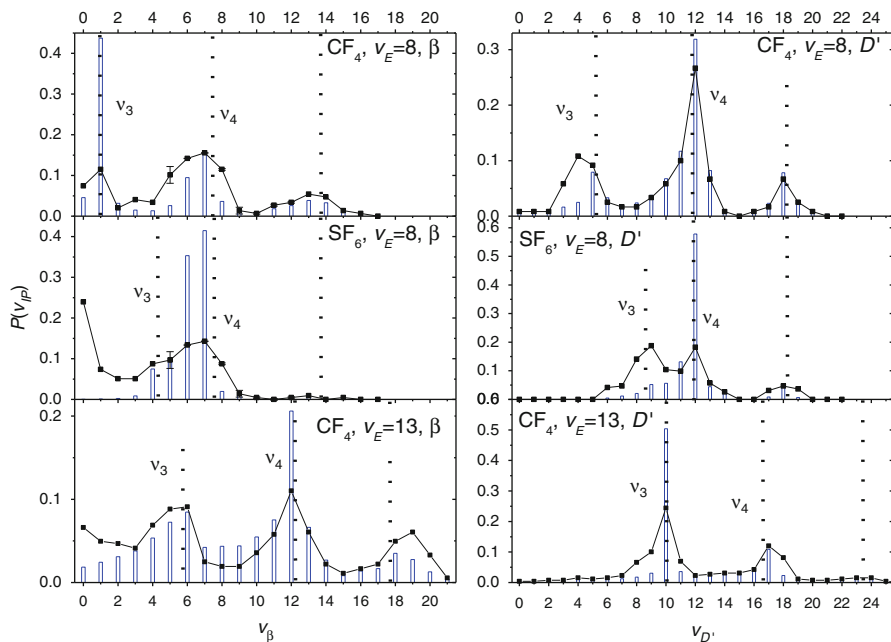


Fig. 5.14 Vibrational distributions in the D' and β CINAT channels. The legends are the same as in Fig. 5.13

5.3.2.8 CINATs in the Third Tier

The $2_u(1D_2), v_{2u} = 3, 5, 7 \xrightarrow{I_2(X)} 2_g(1D_2)$ CINATs similar to those observed in the 1-st and 2-nd tier and following $u \leftrightarrow g$, $\Delta\Omega = 0$ propensity rules have been studied in [78]. The VDs trend to FCFs, so $2_g, v_{2g}$ vibrational states lying up to $\sim 400 \text{ cm}^{-1}$ higher than the initial $2_u, v_{2u}$ states are populated with $(2-4) \cdot 10^{-10} \text{ cm}^3/\text{s}$ rate constants.

5.3.2.9 Conclusions

The following principal features have been found for the nonadiabatic transitions between IP states induced by collisions with rare gas atoms, molecules possessing permanent electric quadrupole and dipole moments and transition electric dipole moments:

Rare Gas Atoms

- CINAT cross-sections, $\sigma = k/V$, are *appr.* independent on Rg nature, with the exception of Rg = Xe, for which reactive quenching is the dominant channel in the $I_2(E) + \text{Xe}$ collisions.

- The “parallel” $E \leftrightarrow D$ ($\Omega_g \leftrightarrow \Omega_u$) transitions with $\Delta\Omega = 0$ are dominant for $Rg = He$. For $Rg = Ar - Xe$, all the electronic states of the first tier are populated in CINATs from the E states in a statistical way, and total, for β , D , γ and δ states, rate constant is higher than that of corresponding to the D state.
- Vibrational populations of the final states depend on Rg . It is resonant and narrow for He and broad for other Rg atoms.
- CINAT rate constants smoothly increase with initial vibrational excitation of the E state;
- The large difference of the CINAT branching ratios is explained by the different behavior of the potential curves. The dipole polarizability of the He atom is $0.2 \cdot 10^{-24} \text{ cm}^3$, whereas for $Ar - Xe$ they are about one order of magnitude larger, $(1.6 - 4.0) \cdot 10^{-24} \text{ cm}^3$. Since the dipole polarizability determines the magnitude of the long-range interaction, the depth of the $He - I_2 PES$ is much smaller than the mean thermal energy at 300 K, while the $Ar - I_2$ interaction strength approaches 240 cm^{-1} . In addition, the mean collision velocity is smaller for heavier Rg atoms. Both factors increase the mean collision time and favor statistical population of the CINAT channels for $Rg = Ar - Xe$.

Molecules Possessing Permanent Electric Quadrupole Moments

- The long-range, $\sim R^{-4}$, interaction between the $I_2(E0_g^+ - D0_u^+)$ or $I_2(f0_g^+ - F0_u^+)$ transition electric dipole moment and the permanent electric quadrupole moments of M is strong in these cases (R is the distance between centers of mass of the colliding partners). In pure iodine vapor, the $I_2(0_g^+ \xleftrightarrow{I_2(X)} 0_u^+)$ are dominant due to large $I_2(X)$ permanent electric quadrupole moment. The $u \leftrightarrow g$ and $\Delta\Omega = 0$ propensity rules are valid in these cases;
- Total, for all D state vibronic levels rate constants exhibits sharp maxima as function of v_E , and near-resonant CINATs have highest total rate constants. Vibronic states nearest to the initial ones are mainly populated in the near-resonant CINATs. The $\Delta J = \pm 1$ and “ $\Delta J - \text{large}$ ” propensity rules are valid in near-resonant and non-resonant CINATs, respectively;
- The $E, v_E \xrightarrow{I_2(X)} D, v_D$ and $D, v_E \xleftarrow{I_2(X)} E, v_D$ CINAT rate constants are similar;
- There are no distinct correlations between VDs of a state populated in CINATs and $FCFs$ of initial and final vibronic levels, though VDs “try” to follow the trend in the $FCFs$ with the initial states, but energy gap law, $P \sim \exp\left(-\frac{|\Delta E|}{\beta}\right)$ (β – is a variable parameter, usually, $\beta = kT$) (see [18, 43] and references) “prevents” this trend [65].
- Rate constants of non-resonant processes correspond to small impact parameters. In these cases, the CINATs are provided by orbiting of the $I_2(E \text{ or } D)$ and $I_2(X)$ colliding partners due to dispersion, $\sim C_6/R^6$, interaction [42, 43]. The orbiting leads to population of several vibronic states in non-adiabatic transitions from the initial to final I_2 states.

- For $M = N_2, CO_2$, the $I_2(0_g^+ \xrightarrow{M} D0_u^+, D'2_g, \beta1_g, \delta2_u, \gamma1_u)$ CINATs are also occurred.

Molecules Possessing Permanent Electric Dipole Moments

In this case, long-range interaction between the E - D transition electric dipole and the permanent electric dipole of M , $\sim R^{-3}$, is dominant, and the $I_2(0_g^+ \xleftrightarrow{M} 0_u^+)$ CINATs have to be the most probable. For these collision partners, rate constants of quasi-resonant CINATs have to be huge, and VD s have to be narrow, if energy mismatches have not compensated by rotational transitions in a colliding partner.

Molecules Possessing Transition Electric Dipole Moments

In this case, the leading term of electrostatic expansion corresponds to E - D transition electric dipole moment–vibrational transitions electric dipole moment, $\sim R^{-3}$, interactions. Collisions with these partners produce very efficient electronic energy transfer with the total rate constant of the order of $10^{-9} \text{ cm}^3/\text{s}$. The total CINAT probability is predominantly associated with the transitions that lead to dipole allowed excitations of the partner. As a result, these partners are efficient for I_2 vibrational energy loss.

References

1. Kondratiev, V.N., Nikitin, E.E.: Gas-Phase Reactions: Kinetics and Mechanism. Springer-Verlag, Berlin/Heidelberg/New York (1981)
2. Gordiets, B.F., Osipov, A.I., Shelepin, L.L.: Kinetic Processes in Gases and Molecular Lasers. Nauka, Moscow (1980.) (English translation: Gordon and Breach, New York (1987))
3. Steinfeld, J.I.: Rate data on inelastic collision processes in the diatomic halogen molecules. J. Phys. Chem. Ref. Data. **13**, 445–553 (1984)
4. Herzberg, G.: Molecular Spectra and Molecular Structure: I. Spectra of Diatomic Molecules, Krieger (1989)
5. Raper, O.F.: DeMore: reaction of $O(^1D)$ with CO. J. Chem. Phys. **40**, 1053–1057 (1964)
6. Tully, J.C.: Collision complex model for spin-forbidden reactions: quenching of $O(^1D)$ by N_2 . J. Chem. Phys. **61**, 61–68 (1974)
7. Pravilov, A.M., Sidorov, I.I., Skorokhodov, V.A.: Mechanism and kinetics of photorecombination of $O(^1D)$ with Xe. Sov. J. Chem. Phys. **3**, 793–807 (1985)
8. Pravilov, A.M., Protopopov, S.V., Sidorov, I.I., Skorokhodov, V.A.: Photorecombination of $O(^1D)$ with CO. Sov. J. Chem. Phys. **3**, 2010–1023 (1985)
9. DeMore, W.B., Margitan, J.J., Molina, M.J., Watson, R.T., Golden, D.H., Hampson, R.F., Kurilo, M.J., Howard, C.J., Raviskara, A.R.: Chemical kinetics and photochemical data for use in stratospheric modeling. Evaluation No.7, pp. 85–37. JPL Pub Jet Propulsion Lab, Pasadena. 217 pp
10. Deperasinska, I., Beswick, J.A., Tramer, A.A.: Distorted wave calculation for electronic energy transfer in molecular collisions. Application to the $N_2(A^3\Sigma_u^+) + CO(X^1\Sigma_g^+) \rightarrow N_2(X^1\Sigma_g^+) + CO(a^3\Pi)$ system. J. Chem. Phys. **71**, 2477–2487 (1979)
11. Adv. Chem. Phys. XLVII: Photosensitive Chemistry. In: Jortner, J., Levine, R.D., Rice, S.A. (eds.) part 2 (1981)
12. Pravilov A.M., Smirnova L.G., Vilesov A.F.: The mechanism of $N_2(B^3\Pi_g)$ deactivation by N_2 . Chem. Phys. Lett. **144**, 469–472 (1988)

13. Vilesov, A.F., Privilov, A.M., Smirnova, L.G.: Excitation of Xe in active nitrogen. *Opt. Spectrosc. (USSR, Engtransl)*. **65**, 443–445 (1988)
14. Hagege, J., Roberge, P.C., Vermeil, C.: Collision-induced predissociation in the gas phase. Photolysis of methanol at 1849 Å. *Trans. Faraday Soc.* **64**, 3288–3299 (1968)
15. Bendazzoli, G.L., Raimondi, M., Garetz, B.C., George, T.F., Morokuma, K.: Semiclassical study of collision-induced predissociation. Comparison of Landau-Zener model with the method of analytic continuation. *Theor. Chim. Acta. (Berl)*. **44**, 341–350 (1977)
16. Tully, J.C.: Nonadiabatic processes in molecular collisions. In: Miller, W.H. (ed.) *Dynamics of Molecular Collisions, Part B*, 217. Plenum Press, New York (1976)
17. Tully, J.C.: Molecular dynamics with electronic transitions. *J. Chem. Phys.* **93**, 1061–1071 (1990)
18. Lefebvre-Brion, H., Field, R.W.: *Perturbation in the Spectra of Diatomic Molecules*. Academic, New York (1986)
19. Lefebvre-Brion, H., Field, R.W.: *The Spectra and Dynamics of Diatomic Molecules*. Elsevier, Amsterdam (2004)
20. Dagdigian, P.J.: State-resolved collision-induced electronic transitions. *Annu. Rev. Phys. Chem.* **48**, 95–123 (1997)
21. Alexander, M.A.: Dipolar model for collisional energy transfer between dark and radiating excited electronic states: $\text{CaO}(A^1\Pi, a^3\Pi) + \text{N}_2\text{O} \leftrightarrow \text{CaO}(A^1\Sigma^+) + \text{N}_2\text{O}$. *J. Chem. Phys.* **76**, 429–444 (1982)
22. Ottinger, C., Vilesov, A.F.: Intramolecular collisional transfer in $\text{NO}(a^4\Pi \rightarrow B^2\Pi, b^4\Sigma^-)$: gateway-type, resonant versus direct, nonresonant mechanisms. *J. Chem. Phys.* **100**, 1805–1814 (1994)
23. Gelbart, W.M., Freed, K.F.: Intramolecular perturbations and the quenching of luminescence in small molecules. *Chem. Phys. Lett.* **18**, 470–475 (1973)
24. Steinfeld, J.I.: Rate data on inelastic collision processes in the diatomic halogen molecules. 1986 supplement. *J. Phys. Chem. Ref. Data.* **16**, 903–910 (1987)
25. Dreiling, T.D., Setser, D.W.: State-to-state relaxation processes for $\text{XeCl}(B,C)$. *J. Chem. Phys.* **75**, 4360–4378 (1981)
26. Akopyan, M.E., Lukashov, S.S., Poretsky, S.A., Privilov, A.V.: Ion-pair states in the complexes of iodine molecule with rare gases. *Russ. J. Phys. Chem.* **83**, 116–124 (2009)
27. Dalby, F.W., Levy, C.D.P., Vanderlinde, J.: Vibrational and rotational dependence of electric field induced predissociation of I_2 . *Chem. Phys.* **85**, 23–29 (1984)
28. Tellinghuisen, J.: Potentials for weakly bound states in I_2 from diffuse spectra and predissociation data. *J. Chem. Phys.* **82**, 4012–4016 (1985)
29. Buchachenko, A., Halberstadt, N., Lepetit, B., Roncero, O.: Ar^+I_2 : a model system for complex dynamics. *Int. Rev. Phys. Chem.* **22**, 153–202 (2003)
30. Tellinghuisen, J.: The Franck-Condon principle in bound-free transitions In: *Advances in Chemical Physics*, vol. **60**, pp. 299–369 (1985)
31. Tscherbul, N.V., Buchachenko, A.A., Akopyan, M.E., Poretsky, S.A., Privilov, A.M., Stephenson, T.A.: Collision-induced non-adiabatic transitions between the ion-pair states of molecular iodine: a challenge for experiment and theory. *Phys. Chem. Chem. Phys.* **6**, 3201–3214 (2004.) (Invited Article)
32. Zuev, V.S., Mikheev, L.D.: *Photochemical Lasers*. Harwood Academic Publishers, Chur (1991)
33. Kvaran, Á., Ósk, S., Jónsdóttir, S.O., Thorgeirsson, T.E.: Mechanism of vibrational relaxation and intersystem crossing within excited ion-pair states of I_2 . *Proc. Indian. Acad. Sci.* **103**, 417–428 (1991)
34. Exton, R., Balla, R.J.: ArF excitation, collision transfer, and quench-free fluorescence in I_2 /foreign gas mixtures. *J. Quant. Spectrosc. Rad. Tranf.* **86**, 267–283 (2004)
35. Lukashov, S.S., Poretsky, S.A., Privilov, A.M.: Optical population of free iodine molecule ion-pair states and their $\text{RgI}_2(\text{IP})$ complexes via RgI_2 vdW complexes of valence states correlating with the third dissociation limit. *Chem. Phys.* **336**, 109 (2007)

36. Ubachs W., Aben I., Milan J.B., Somsen G.S., Stuiiver A.G., Hogervorst W.: Radiative and collisional relaxation of a single rovibrational quantum state of I_2 : $E(0_g^+), v=8, J=56$. *Chem. Phys.* **174**, 285–295 (1993)
37. Inard D., Cerny D., Nota M., Bacis R., Churassy S., Skorokhodov V.: $E0_g^+ \rightarrow A1_u$ and $E0_g^+ \rightarrow B''1_u$ laser-induced fluorescence in molecular iodine recorded by Fourier-transform spectroscopy. *Chem. Phys.* **243**, 305–321 (1999)
38. Teule R., Stolte S., Ubachs W., Aben I., Milan J.B., Somsen G.S., Stuiiver A.G., Hogervorst W.: Collision-induced $E(0_g^+) - D(0_u^+)$ state-to-state energy transfer in I_2 . *Laser Chem.* **18**, 111–128 (1999)
39. Akopyan M.E., Bibinov N.K., Kokh D.B., Pravilov A.M., Stepanov M.B., Vasyutinskii O.S.: The “approach-induced” $I_2(E0_g^+ \xleftrightarrow{I_2(X)} D0_u^+)$ transition. *Chem. Phys.* **242**, 263–272 (1999)
40. Akopyan, M.E., Baturo, V.V., Lukashov, S.S., Poretsky, S.A., Pravilov, A.M.: Non-adiabatic transitions between first tier ion-pair states of I_2 induced by collisions with Ar atoms. *Chem. Phys.* **462**, 3–11 (2015)
41. Akopyan M.E., Bibinov N.K., Kokh D.B., Pravilov A.M., Sharova O.L., Stepanov M.B.: The approach-induced $I_2(E0_g^+ \xrightarrow{M} D0_u^+)$ transition, $M = He, Ar, I_2, N_2, CF_4$. *Chem. Phys.* **263**, 459–470 (2001)
42. Bibinov N.K., Malinina O.L., Pravilov A.M., Sharova O.L., Stepanov M.B., Zakharova A.A.: The “approach-induced” and collision-induced $I_2(E0_g^+ \xleftrightarrow{I_2(X)} D0_u^+)$ transition from low, $v_E = 8-23$ vibronic levels of the $I_2(E)$ state. *Chem. Phys.* **277**, 179–189 (2002)
43. Akopyan M.E., Pravilov A.M., Stepanov M.B., Zakharova A.A.: The collision-induced $I_2(E0_g^+ \xrightarrow{M} D0_u^+)$ transition, $M = He, Ar, N_2, CF_4$. *Chem. Phys.* **287**, 399–410 (2003)
44. Hirschfelder, J.O., Curtis, C.F., Bird, R.B.: *Molecular Theory of Gases and Liquids* (Appendix, Table 1c). Wiley, New York. (1954)
45. Lawley, K.: Dispersion and polarization forces associated with the ion-pair states of diatomic molecules. *Chem. Phys.* **127**, 363–371 (1988)
46. Derouard, J., Sadeghi, N.: Resonant excitation of Li atoms to the (2^2P) state by collisions with $Li_2^*(A^1\Sigma_u^+, v', J')$ molecules. *Chem. Phys. Lett.* **111**, 353–359 (1984)
47. Akopyan M.E., Lukashov S.S., Khadikova E.I., Nikandrova E.A., Poretsky S.A., Pravilov A.M., Torgashkova A.S.: Non-adiabatic $E \rightarrow M D, D', \beta, \gamma, \delta$ transitions in the first ion-pair tier of molecular iodine induced by collisions with I_2, N_2, CO_2 . *Chem. Phys.* **342**, 173–183 (2007)
48. Akopyan, M.E., Lukashov, S.S., Maslennikova, Y.D., Poretsky, S.A., Pravilov, A.M., Torgashkova, A.S.: Non-adiabatic transitions from the $I_2(E)$ induced by the transition dipole moment of $I_2(E-D)$ and the electric dipole moment of collision partners. *Chem. Phys. Lett.* **458**, 29–34 (2008)
49. Akopyan M.E., Novikova I.Yu., Poretsky S.A., Pravilov A.M., Smolin A.G., Tscherbul T.V., Buchachenko A.A.: Collision-induced non-adiabatic transitions in the second-tier ion-pair states of iodine molecule: experimental and theoretical study of the $I_2(f0_g^+)$ collisions with rare gas atoms. *J. Chem. Phys.* **122**, 204318–204312 (2005)
50. Akopyan M.E., Buchachenko A.A., Lukashov S.S., Poretsky S.A., Pravilov A.M., Suleimanov Yu.V., Torgashkova A.S., Tscherbul T.V.: Non-adiabatic $E \rightarrow D, D', \beta, \gamma, \delta$ transitions in the first ion-pair tier of molecular iodine induced by collisions with I_2, He, Ar, Kr, Xe . *Chem. Phys. Lett.* **436**, 1–6 (2007)
51. Akopyan M.E., Khadikova E.I., Lukashov S.S., Poretsky S.A., Pravilov A.M., Buchachenko A.A., Suleimanov Yu.V.: Dynamics and mechanism of non-adiabatic transitions from the ungerade $I_2(D0_u^+)$ state induced by collisions with iodine ground state molecules and rare gas atoms. *J. Chem. Phys.* **133**, 244304–244310 (2010)
52. Akopyan M.E., Khadikova E.I., Lukashov S.S., Poretsky S.A., Pravilov A.M., Torgashkova A.S., Buchachenko A.A., Suleimanov Yu.V.: Dynamics and mechanism of the $E \rightarrow D, D', \beta, \gamma, \delta$

- non-adiabatic transitions induced in molecular iodine by collisions with CF_4 and SF_6 molecules. *J. Chem. Phys.* **129**, 114309–114309 (2008)
53. Watson, J.K.G.: Simplification of the molecular vibration-rotation Hamiltonian. *Mol. Phys.* **100**, 47–54 (2002)
54. Landau, L.D., Lifshitz, E.M.: *Quantum Mechanics*, 3rd edn. Pergamon, Oxford (1977)
55. Kouri, D.J.: In: Bernstein, R.B. (ed.) *Atom-Molecule Collision Theory*. Plenum, New York (1979)
56. Tscherbil T.V., Buchachenko A.A.: Quantum scattering equations for non-adiabatic transitions in collisions between a Hund case (c) diatomic molecule and a structureless atom with application to $\text{I}_2(E0_g^+)$ + Ar. *J. Phys. B Atomic Mol. Phys.* **37**, 1605–1619 (2004)
57. Suleimanov, Y.V., Buchachenko, A.A.: Electronic to vibrational energy transfer assisted by interacting transition dipole moments: a quantum model for the nonadiabatic $\text{I}_2(E) + \text{CF}_4$ collisions. *J. Phys. Chem. A* **111**, 8959–8967 (2007)
58. Parker, G.A., Pack, R.T.: Rotationally and vibrationally inelastic scattering in the rotational IOS approximation. Ultrasimple calculation of total (differential, integral, and transport) cross sections for nonspherical molecules. *J. Chem. Phys.* **68**, 1585–1601 (1978)
59. Balint-Kurti, G.G.: In: Buckingham, A.D., Coulson, C.A. (eds.) *International Review of Science*, vol. 1, pp. 286–326. Butterworth, London (1975)
60. Wickham-Jones, C.T., Balint-Kurti, G.G., Novak, M.M.: Distorted wave calculations of the vibrational relaxation of CO in collision with He atoms. *Chem. Phys.* **117**, 1–8 (1987)
61. Chernyi, G.G., Losev, S.A., Merchet, S.O., Potapkin, B.V.: *Physical and Chemical Processes in Gas Dynamics: Cross Sections and Rate Constants*, vol. 1. AIAA, Reston (2002)
62. Tscherbil, T.V., Zaitsevskii, A.V., Buchachenko, A.A., Stepanov, N.F.: Analytic potential surfaces and diabatic interaction matrix elements between electronic states in the inert gas atom-halogen molecule system: Ion-pair states. *Russ. J. Phys. Chem.* **77**, 511–520 (2003)
63. Buchachenko, A.A., Tscherbil, T.V., Klos, J., Szczesniak, M.M., Chalasinski, G., Webb, R., Viehland, L.A.: Interaction potentials of the RG–I anions, neutrals, and cations (RG=He, Ne, Ar). *J. Chem. Phys.* **122**, 194311–194319 (2005)
64. Fecko C.J., Freedman M.A., Stephenson T.A.: Collision-induced electronic energy transfer from $v=0$ of the $E(0_g^+)$ ion-pair state in I_2 : collisions with $\text{I}_2(X)$. *J. Chem. Phys.* **115**, 4132–4138 (2001)
65. Fecko C.J., Freedman M.A., Stephenson T.A.: Collision-induced electronic energy transfer from $v=0$ of the $E(0_g^+)$ ion-pair state in I_2 : collisions with He and Ar. *J. Chem. Phys.* **116**, 1361–1369 (2002)
66. Chandra, P.P., Stephenson, T.A.: Franck-Condon effects in collision-induced electronic energy transfer: $\text{I}_2(E;v=1-2) + \text{He}$, Ar. *J. Chem. Phys.* **121**, 2985–2991 (2004)
67. Ridley, T., Lawley, K.P., Donovan, R.J.: Long-range collisional energy transfer between charge-transfer (ion-pair) states of I_2 , induced by H_2O and $\text{I}_2(X)$. *J. Chem. Phys.* **131**, 234302–234312 (2009)
68. Ridley T, Lawley K.P., Donovan R.J., A. Ross: Efficient long-range collisional energy transfer between the $E0_g^+(^3P_2)$ and $D0_u^+(^3P_2)$ ion-pair states of I_2 , induced by H_2O , observed using high-resolution Fourier transform emission spectroscopy. *J. Chem. Phys.* **135**, 114302–114308 (2011)
69. Akopyan M.E., Baturo V.V., Lukashov S.S., Poretsky S.A., Pravilov A.M.: Non-adiabatic transitions from $\text{I}_2(E0_g^+ \text{ and } D0_u^+)$ states induced by collisions with $M = \text{I}_2(X0_g^+)$ and H_2O . *J. Chem. Phys.* **136**, 234302–234311 (2012)
70. Akopyan M.E., Chinkova I.Yu., Fedorova T.V., Poretsky S.A., Pravilov A.M.: The collision-induced non-adiabatic transitions from the $f0_g^+$ state of the iodine ion-pair second tier. *Chem. Phys.* **302**, 61–67 (2004)
71. Weast, R.C. (ed.): *Handbook of Chemistry and Physics*, 45th edn, (1968)
72. Graham, C., Imrie, D.A., Raab, R.E.: Measurement of the electric quadrupole moments of CO_2 , CO , N_2 , Cl_2 and BF_3 . *Mol. Phys.* **93**, 49–56 (1998)

73. Sharma, R.D., Brau, C.A.: Energy transfer in near-resonant molecular collisions due to long-range forces with application to transfer of vibrational energy from ν_3 mode of CO_2 to N_2 . *J. Chem. Phys.* **50**, 924–930 (1969)
74. Herzberg, G.: *Molecular Spectra and Molecular Structure: Infrared and Raman Spectra of Polyatomic Molecules*. Nostrand, Princeton (1967)
75. Housecroft, C.E., Sharpe, A.G.: *Inorganic Chemistry*, 4rd edn. Pearson Education, Harlow (2012)
76. Dorosh, O., Kisiel, Z.: Electric dipole moments of acetone and of acetic acid measured in supersonic expansion. *Acta Phys. Pol. A.* **112**, S9–104 (2007)
77. Gadhi, J., Wlodarczak, G., Legrand, J., Demaison, J.: The dipole moments of methyl bromide and methyl iodide. *Chem. Phys. Lett.* **156**, 401–404 (1989)
78. Hoshino, S., Nakano, Y., Araki, M., Ishiwata, T., Tsukiyama, K.: Collision induced state-to-state energy transfer dynamics between the 2_u ($^1\text{D}_2$) and 2_g ($^1\text{D}_2$) ion-pair states of I_2 . *Phys. Chem. Chem. Phys.* **18**, 14292–14298 (2016)

Chapter 6

Van der Waals Complexes of Iodine Molecules

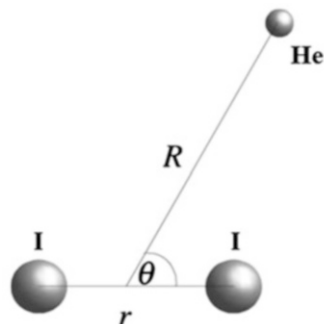
6.1 General

Van der Waals (vdW) complexes are weakly-bound molecular species in which the dominant attractive contribution are weak intermolecular attractions, the dispersion interaction, in particular (see [1–3] and references). Therefore, interactions in such complexes including rare gases-halogen ones have been among the most intensively studied intermolecular forces.

Population and decay of vdW complexes in the gas phase play a fundamental role in the kinetics and dynamics of excited molecular electronic states. They are responsible for radiative emission and energy transfer in the atmosphere, energy pooling and conversion in laser media, relaxation phenomena in chemiluminescence processes, plasma formation, and in many other situations, where electronically excited states are involved. Description of these processes is significant for understanding mechanisms of non-adiabatic transitions in weakly-bound complexes of any molecules and clusters. Determination of propensity rules is necessary for the development of dynamic description in vdW complexes. An understanding of population and decay of vdW complexes is also essential for interpretation and modeling of various photoinitiated processes in liquids and solids, where the role of intermolecular interaction is greatly magnified through the formation of solvation shell(s) and multiple collisions between a molecule and a solvent. One should note that decay of vdW complexes has much in common with vibrational relaxation and electronic predissociation induced by collisions with atoms and molecules which, for the case of I₂ molecules, have been discussed in Chap. 5.

An energy of a vdW bond is minimal, less than several hundred cm⁻¹ [1] (dissociation energies of the complexes increase from He to Kr (and Xe, probably) due to an increase of polarizability, see Sect. 5.3.2.4). Therefore, to observe and study vdW complexes, it is required a cooling vapor of atoms or molecules to sufficiently low temperatures by utilizing supersonic molecular beam technique.

Fig. 6.1 *T*-shaped ($\Theta = 90^\circ$), free-rotor ($360^\circ > \theta > 0^\circ$) and linear ($\Theta = 0, 180^\circ$), RgI₂ vdW complex



The first pioneering work devoted to studies of halogen molecule vdW complexes in supersonic molecular beam was published in 1976 by D.H. Levy and his team [4]. Nevertheless, this field of chemical physics and molecular spectroscopy is trendy at present. One of the most thoroughly studied groups of vdW complexes are complexes consisting of homonuclear halogens (hereafter, X₂) or interhalogens (XY) and rare gas atoms, RgX₂(X0_g⁺, B0_u⁺, E0_g⁺), RgXY(0⁺, 1). Decades of experimental and theoretical papers devoted to vdW complexes have been published (see [5–12] and references). A large amount of experimental and theoretical data have been obtained, and spectroscopic characteristics of the RgI₂(X, B) states have been determined. Three conformers of RgI₂ complexes have been observed and studied. These are *T*-shaped (*C*_{2v} symmetry group), linear (*C*_{∞v} symmetry group) RgI₂(X, B) complexes which vibrational wave functions are localized at $\Theta = 90^\circ$, 0 and 180°, respectively, as well as “free-rotor” or bending complexes which vibrational wave functions are delocalized over $\Theta = 0 - 360^\circ$ (Fig. 6.1).

Dynamics of the RgI₂(B) state electronic predissociation (*EP*), vibrational predissociation (*VP*) involving intramolecular vibrational relaxation (redistribution) (*IVR*), and cage effect have been studied rather well. As to RgI₂(IP) complexes, series of researches in which indirect spectroscopic and kinetic proofs of their existence in gas phase at a room temperature was performed in 2004–2012 (see [13–18] and references). However, it is impossible to obtain spectroscopic characteristics of these species under such conditions. It becomes possible only at temperatures of about 1 K using a supersonic molecular beam technique. Recent studies of the RgI₂(IP) complexes (see below) show that the RgI₂(E0_g⁺, β1_g ← B0_u⁺) optical transitions occur, only. No RgI₂(D0_u⁺, D'2_g ← B0_u⁺) transitions allowed in the *C*_{2v} and *C*_{∞v} symmetry groups are observed. Therefore, Rg atoms do not perturb significantly homonuclear iodine molecule, i.e. act as “spectator” (see below).

6.2 Overview of Experimental Methods. State-of-the-Art

Bound excited X_2 , XY valence states are perturbed by repulsive states, and predissociation of the complexes to Rg and halogen atoms occurs. Therefore, the only methods of studies spectroscopic characteristics and dynamics of these complexes at the supersonic molecular bands are the following:

- intracavity laser spectroscopy [19–21];
- measurements of luminescence spectra of halogens (interhalogens) which are the products of vibrational predissociation of the complexes; a loss of several vibrational quanta occurs in these processes (see [4, 19–24] and references);
- the pump-probe method when $RgHal_2(B, v_B)$ complex VP products, *e.g.*, produced due to absorption of a pump laser photon by a complex are excited to the gerade (g), $Hal_2(E0_g^+)$, for example. The IP state are populated by a probe laser photon, and luminescence of this IP state are monitored during measurement of excitation spectra (see [15–29] and references). Action spectra can also be measured: wavelength of probe radiation is fixed and that of pump radiation scan (see [28, 29] and references);
- luminescence depletion techniques [28];
- velocity-map imaging method [10, 30].
- Below, experimental set-up designed and manufactured by the author's group will be we described. This experimental setup exhibits unique sensitivity and possibilities for investigation of weakly-bound complexes of halogens with rare gases ($RgHal_2$) and molecules ($MHal_2$) using laser-induced luminescence spectroscopy techniques.

It allows to measure:

- excitation and action spectra for transitions between valence and IP states of complexes,
- luminescence spectra of the $RgHal_2(IP)$, $MHal_2(IP)$ complex predissociation products, $Hal_2(IP)$, as well as $RgHal_2(IP)$, $MHal_2$ themselves (if it occurs),
- determine vibrational distributions in each IP state,
- relative probabilities of vibrational and electronic predissociation as well as complex binding energies [31, 32],
- determine binding energies of ground and intermediate state complexes, as well as their spectroscopic characteristics.

6.2.1 Design and Characteristics of the Set-Up Utilized in the Author's Group

6.2.1.1 Supersonic Jet

Numerous papers, reviews, and books have been devoted to the nature of cooling in supersonic jets and design of supersonic valves since pioneering work of Kantrowitz and Grey [33] (see [34–40], e.g.).

As the gas expands from a valve nozzle, the effect of extensive cooling in the translational and internal degrees of freedom is produced due to binary collisions in which of stationary gas thermal (random translational and internal) energy is transformed into kinetic energy of ordered motion of particles. The velocity of particle random motion and translation temperature, as well as rotational and vibrational temperatures, decreases due to $T - T$ and $R, V-T$ energy transfer processes (see Sect. 5.2) as low as ~ 0.05 , 0.5 and 50 K, respectively [4]. Gas-dynamics convergent-divergent (de Laval nozzle) or convergent nozzles were utilized in first experiments to produce supersonic beams (see [33–38] and references). It has been shown nevertheless (see [36] and references) that beam flux (particle/s) can increase up to 20% if one deletes divergent part of a nozzle. Therefore, the authors use standard no cone (axisymmetric) Series 9 pulse valve equipped with IOTA ONE pulse driver (Parker Hannifin Corporation) in their practice.

Below, estimations of principal parameters of a jet which correspond to experimental conditions realized in first studies [31, 32] will be presented. Information given in the literature (see [34–40] and references) has been utilized.

1. Mass flow

$$m = \left(\frac{2}{\gamma - 1} \right)^{\frac{1}{\gamma - 1}} \sqrt{\frac{2\gamma}{\gamma + 1}} \sqrt{(\gamma + 1)R/M \cdot T_0 A^* \rho_0}. \quad (6.1)$$

Here,

$\gamma = C_p/C_v$ is the adiabatic index (the specific heat ratio), $\gamma = 5/3$ and $7/5$ for monoatomic and diatomic gases, respectively (see [38] and references);

$R = 8.3144598 \text{ J}\cdot\text{mol}^{-1}\cdot\text{K}^{-1}$ is molar gas constant;

M is molar mass;

A^* is a nozzle throat square; for axisymmetric nozzle diameter $D = 0.5$ mm, the authors usually use, $A^* = 2.5 \cdot 10^{-3} \text{ cm}^2$;

T_0 and ρ_0 are a temperature of the nozzle (stagnation temperature) and gas density in a gas reservoir.

The authors usually use helium as a carrier gas with backing pressure $p_{He} \approx 2\text{--}30$ atm. One can estimate helium flow as $\sim 10^{21}$ atom/s for $p_{He} = 30$ atm and a valve duration and frequency of the opening $\tau \approx 200 \text{ }\mu\text{s}$ and 10 Hz, respectively. The

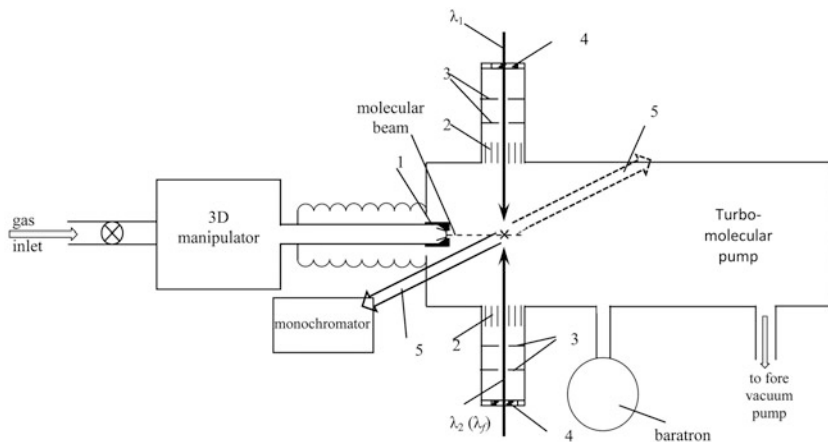


Fig. 6.2 Schematic of the supersonic molecular beam setup: 1 – pulse valve equipped with removable nozzle, 2 – honeycomb blackened light traps, 3 – blackened diaphragms, 4 – fused silica windows, 5 – luminescence outputs for measurements of integral luminescence intensity (a glass filter/photomultiplier tube) and spectral measurements ($f/2.5$ condenser/ $f/2.5$ monochromator/PMT system)

Pfeiffer HiPace 1500 UC turbomolecular pump (pumping speed 1350 l/s for He) is utilized to evacuate ~ 50 l expansion chamber (Figs. 6.2 and 6.3).

2. Sonic speed is

$$a = \sqrt{\frac{\gamma k T}{m}}, \quad (6.2)$$

$k = 1.38 \cdot 10^{-16}$ erg/K is Boltzmann constant, m is molar weight (g).

For He at the reservoir ($\gamma = 1.67$, $m = 6.68 \cdot 10^{-24}$ g) and $T_0 = 300$ K, sonic speed is $a_0 = 1.12 \cdot 10^5$ cm/s.

At a **nozzle throat section**, the sonic speed is $a^* = \sqrt{\frac{2}{\gamma+1}} a_0 = 0.87 a_0$.

At an expansion chamber, the local sonic speed is $a = a_0 \left(1 + \frac{\gamma-1}{2} M^2\right)^{-1/2}$;
here M is Mach number.

3. Mach number M is

$$M = u/a; \quad (6.3)$$

here, u is stream flow velocity.

M value for Rg atoms can be calculated as:

$$M(x) = 3.2(x/D)^{2/3}. \quad (6.4)$$

Fig. 6.3 Photo of the experimental setup utilized in [31, 32]



For x/D value (x is a distance from a nozzle origin to a zone of observation) $x/D = 20$ (typical value in [19]), M is $M \approx 24$, and $a \approx 0.07 a_0$. One should take into account that adiabatic cooling occurs if particle concentration in a jet large enough for fast $R, V-T$ and $T-T$ energy transfer processes.

4. Helium temperature is equal to

$$T = T_0 \left(1 + \frac{\gamma - 1}{2} M^2 \right)^{-1} \quad (6.5)$$

at $M \geq 4$. At $M = 24$ and $T_0 = 300$ K, helium temperature is $T \approx 1.5$ K. Translational temperature of iodine molecule is ~ 10 times less [4]. The rotational and vibrational temperatures can be determined experimentally. An analysis of the literature data and those obtained in the author's group shows that they depend on a reservoir pressure.

5. Helium concentration at a jet is

$$[\text{He}] = [\text{He}]_0 \left(1 + \frac{\gamma - 1}{2} M^2\right)^{-1/(\gamma - 1)} \quad \text{at } M \geq 4 \quad (6.6)$$

At $p_{\text{He}} = 30 \text{ atm}$ ($[\text{He}]_0 = 8.07 \cdot 10^{20} \text{ cm}^{-3}$) and $x/D = 20$, $[\text{He}] = 3 \cdot 10^{17} \text{ cm}^{-3}$.

6. Dimension of the jet for $M \geq 4$

$$r = \left[\frac{27}{256} \gamma^{1/2} \tau \left(1 + \frac{\gamma - 1}{2} M^2\right)^{3/2} D^2 \sqrt{\frac{R}{MT_0}} \right]^{1/3} \quad (6.7)$$

For helium, $M = 24$, $\tau = 200 \text{ нс}$, $D = 0.5 \text{ mm}$ and $T_0 = 300 \text{ K}$, $r \approx 2.5 \text{ cm}$.

It is essential that ratio of Mach numbers of massive and light species, $M_{\text{I}_2}/M_{\text{He}}$, for example, is proportional to $\sqrt{m_{\text{I}_2}/m_{\text{He}}}$. Collisions of iodine molecules and $\text{RgI}_2(X)$ complexes with helium atoms during expansion tend to accelerate massive component velocity along the jet axis but are less effective for the perpendicular component. This leads to decreasing of translational temperature and considerable enrichment of the massive seed gases near the jet axis (see [39, 40] and references).

6.2.1.2 The System of Preparation of Gas Mixtures

The system used allows forming many-component gas mixtures consisting of carrier gas (helium, usually), rare or molecular gas seeded and a halogen gas. The principal units of the system are (see Fig. 6.4):

- ~1.5-liter gas reservoir,
 - the circulation pump used for gas mixing similar to that of shown in Fig. 3.29 in [41],
 - the $p \leq 1 \text{ atm}$ and $p \leq 100 \text{ atm}$ manometer, used for a measurement of seeding rare or molecular gas pressures and total pressure of a gas mixture, respectively,
 - the reducer gear, which allows maintaining constant gas pressure in the flow.
- Gas pressures in the reservoir and before the nozzle (backing pressure) were $p \leq 70$ and $\leq 30 \text{ atm}$, usually. The rotational and vibrational temperature of iodine molecules were ~1 and 50 K at $x \approx 5 \text{ mm}$ distance [31]. To increase the temperatures and, hence, populations of hot rovibrational mode, we decrease backing pressure up to several bars.

In the case, when weakly-bound complexes of iodine with rare gases (RgI_2) or molecules (MI_2) are studied, the He/Rg or He/M mixtures are passed via bubbler packed with a mixture of iodine crystals and Teflon facing heated up to 75 °C (iodine vapor pressure $p_{\text{I}_2} \approx 10 \text{ Torr}$). The inlet line and pulse valve are held at ~85 °C. In the cases, when chlorine complexes are studied, the He/Rg/Cl_2 or He/M/Cl_2 mixtures are prepared. The $[\text{I}_2]/[\text{He}]$ ratio in the jet as high as $2 \cdot 10^{-4}$ and much higher near the jet axes, so $[\text{I}_2] \gg 6 \cdot 10^{13} \text{ cm}^{-3}$ (see above).

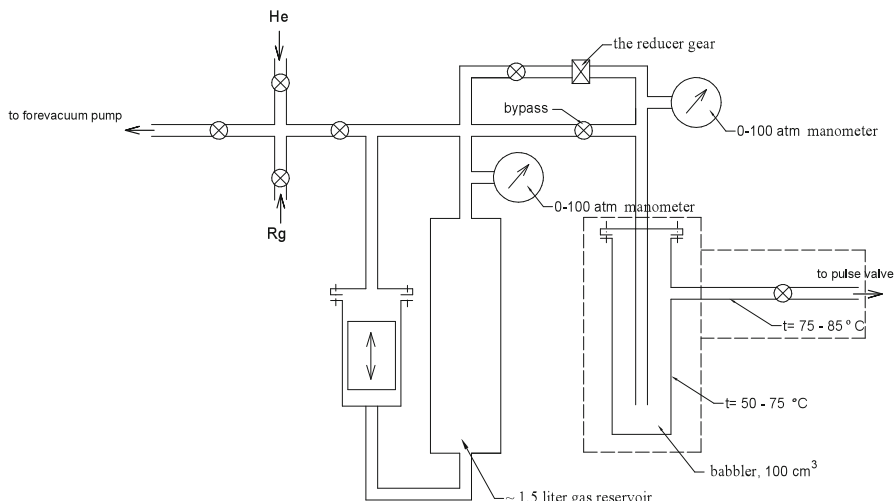
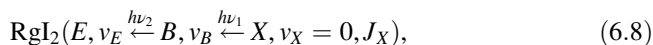


Fig. 6.4 The system of gas mixture preparation

6.2.1.3 An Estimation of Concentrations of the Complexes

Let us estimate concentrations of the $\text{RgI}_2(B)$ and $\text{RgI}_2(IP)$ complexes if $[\text{RgI}_2(X)] = 10^{13} \text{ cm}^{-3}$ ($[\text{RgI}_2(X)]/[\text{I}_2(X)] \approx 0.2$ [19]). It is assumed that experimental conditions similar to described in [31, 32] are realized.

Two tunable dye TDL90 lasers ($h\nu_1$ and $h\nu_2$) pumped by YG981C Nd:YAG ($h\nu_f$) (Quatel) are utilized for a population of the $\text{RgI}_2(B)$ and $\text{RgI}_2(E)$ complexes, respectively. A time duration of the dye laser pulses is $\tau_{\text{pulse}} \approx 8 \text{ ns}$, and spectral width of dye laser emission is $\sim 0.07 \text{ cm}^{-1}$. The $\text{RgI}_2(B, \nu_B)$ and $\text{RgI}_2(E, \nu_E)$ complexes are populated by the $h\nu_1$ and $h\nu_2$ laser beam, respectively.



The $h\nu_1$ and $h\nu_2$ laser pulse energies in the chamber are $\sim 4 \text{ mJ/pulse}$ and $(0.1-1) \text{ mJ/pulse}$ depending on λ_2 value, usually. The $h\nu_1$ and $h\nu_2$ beams are focused using spherical and cylindrical lenses, sometimes, respectively, so dimensions of the beams at $\sim 5 \text{ mm}$ downstream the nozzle pinhole are 2 mm and $0.2 \times 6 \text{ mm}$.

1. Relative population of the $\text{RgI}_2(X, \nu_X = 0, J_X \approx 5)$ rovibronic state is approximately 0.5 at $T_{\text{rot}} \approx 2 \text{ K}$, and $[\text{RgI}_2(X, \nu_X = 0, J_X \approx 5)] \approx 5 \cdot 10^{12} \text{ cm}^{-3}$. There are $\sim 8 \cdot 10^{10}$ $\text{RgI}_2(X, \nu_X = 0, J_X \approx 5)$ complexes in the $h\nu_1$ laser beam waist (cylinder 0.5 cm length and 0.2 cm diameter).

The

$$M_{h\nu_1} = \frac{10^{16}}{0.03 \cdot 10^{-8}} \approx 3 \cdot 10^{25} \text{ photon}/(\text{cm}^2 \cdot \text{s}) \quad (6.9)$$

photon emittance corresponds to 4 mJ/pulse energy at $\lambda_1 = 500 \text{ nm}$

2. One can suppose, that absorption cross-section of the $\text{RgI}_2(X, \nu_X, J_X)$ complexes is approximately the same as that of $\text{I}_2(X, \nu_X, J_X)$ molecules. The latter can be estimate using Einstein coefficients of the $\text{I}_2(B, \nu_B, J_B \rightarrow X, \nu_X, J_X)$ transition [42]. For $\text{I}_2(B, 19 \rightarrow X, 0)$ it is equal $2.4 \cdot 10^4 \text{ s}^{-1}$, and $\sigma_{B, 20 \leftarrow X, 0} \approx 10^{-14} \text{ cm}^2$, e.g., at the center of the Doppler contour.

Ratio of the $B, \nu_B \xleftarrow{h\nu_1} X, \nu_X = 0, J_X$ pumping rate $\sigma M_{h\nu_1}$ to pumping reverse time $\sigma M_{h\nu_1} \tau_{pulse}$ is equal to $\sim 3 \cdot 10^3 \gg 1$. Therefore, there is saturation in the $B, \nu_B, J_B \xleftrightarrow{h\nu_1} X, \nu_X = 0, J_X$ transition, and $[B, \nu_B, J_B] = [X, 0, J_X]$.

3. Rate of the $E, \nu_E \xleftarrow{h\nu_2} B, \nu_B$ transition, $\sigma M_{h\nu_2} \approx 10^{-13} \cdot 3 \cdot 10^{24} \text{ photon/s} = 3 \cdot 10^{11} \text{ s}^{-1}$, is ~ 15 times larger than rate of the $\text{RgI}_2(B)$ complex decay, if its lifetime is $\sim 50 \text{ ps}$ (see Sect. 6.4). Therefore, $[\text{Rg}(E, \nu_E, J_E)] = [\text{Rg}(B, \nu_B, J_B)]$, and $1/4$, namely, $\sim 2 \cdot 10^{10} \text{ RgI}_2(X, \nu_X = 0, J_X)$ complexes in the laser beam waist are “relocated” to complex IP state.
4. Let us estimate electron flow from a photomultiplier tube (PMT) photocathode, if one uses a $f/2.5$ condenser/ $f/2.5$ monochromator/PMT system. Let a condenser diameter is 6 cm and photoemission quantum yield is 0.1. In this case, the part of light emitted from the waist which gets to the monochromator entrance slit is *appr.* equal to

$$\frac{\pi 3^2}{4\pi(2.5 \cdot 6)^2} = 0.01,$$

and the electron flow is

$$\sim 2 \cdot 10^{10} \cdot 0.01 \cdot 0.1 = 2 \cdot 10^7 \text{ e/pulse.}$$

If a spectrum width is 100 nm, and one measures spectrum with FWHM = 0.2 nm, the electron flow is huge.

Experiments confirm estimations presented above [31, 32]. The $h\nu_2$ laser radiation is produced by mixing of the TDL laser fundamental output and fundamental harmonic of the YG981C laser in KDP crystal, $1/\lambda_2 = 1/\lambda' + \nu_f^i$ (λ' and ν_f^i are generation wavelengths of the TDL laser and wavenumbers of fundamental harmonics of the YG981C laser, respectively). The fundamental YG981C laser harmonic consists of 4 spectral components: $\nu_f^1 = 9395.12 \pm 0.02 \text{ cm}^{-1}$, $\nu_f^2 = 9393.53 \pm 0.07 \text{ cm}^{-1}$ and $\nu_f^3 = 9396.67 \pm 0.10 \text{ cm}^{-1}$ with relative intensities of

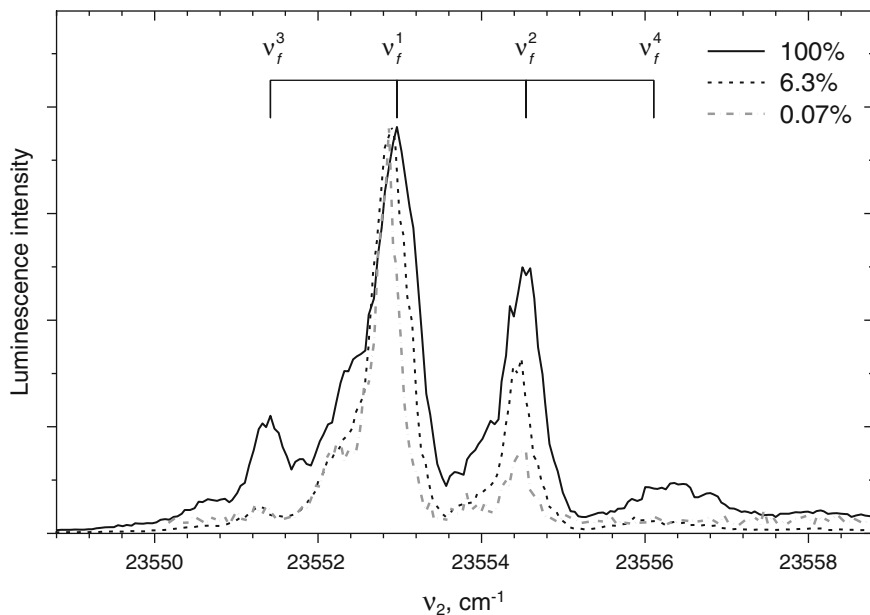


Fig. 6.5 Dependences of four components of the excitation band corresponding to the $\text{HeI}_2(E,0 \leftarrow B,19 \leftarrow X,0)$ excitation pathway on abatement of the $h\nu_2$ laser radiation intensity. Positions of the excitation bands of the luminescence corresponding to the spectral components of fundamental YG981C laser harmonic are shown [32]

about 1: 0.3: 0.05, and a very weak line with the frequency of $\nu_f^4 = 9392.04 \text{ cm}^{-1}$. Therefore, the $h\nu_2$ laser radiation consists of 4 spectral components, also. There are four components with comparable intensities at the $\text{I}_2(E, \nu_E = 0,1 \leftarrow B,18$ and β , $\nu_\beta = 5-7 \leftarrow B,18)$ transition excitation spectra in free iodine molecules as well as excitation bands in the HeI_2 complexes corresponding to the 4 spectral components of the Nd:YAG laser generation. Studies of dependences of these four components on intensity of $h\nu_2$ laser radiation in the chamber show that the high four spectral components observed are comparable in intensity due to saturation at the $\text{HeI}_2(E,0 \xleftrightarrow{h\nu_2} B,19)$ transitions even at weakest component corresponding to $\nu_f^4 = 9392.04 \text{ cm}^{-1}$ (Fig. 6.5).

6.3 Theoretical Models

The first-order intermolecular diatomics-in-molecule perturbation theory (IDIM PT1) model described in Sect. 5.3.2.3 can also be applied for vdW complexes of iodine molecules and rare gases. Similarly to the interaction of rare gases with iodine molecules in the ion pair states, the simple analytical formulas for diabatic

PES s of valence $RgI_2(X)$ [43] and $RgI_2(B)$ [44] states, U_X and U_B respectively, can be obtained:

$$U_X = \langle Rg | \langle X | \hat{V}_{DIM} | X \rangle | Rg \rangle = \sum_{\alpha=a,b} \left(V_{\Sigma}(R_{\alpha}) \cos^2(\beta_{\alpha}) + V_{\Pi}(R_{\alpha}) \sin^2(\beta_{\alpha}) \right), \quad (6.10)$$

$$U_B = \langle Rg | \langle B | \hat{V}_{DIM} | B \rangle | Rg \rangle = \frac{1}{4} \sum_{\alpha=a,b} \left(3V_{\Sigma}(R_{\alpha}) + V_{\Pi}(R_{\alpha}) - \left(V_{\Sigma}(R_{\alpha}) - V_{\Pi}(R_{\alpha}) \right) \cos^2(\beta_{\alpha}) \right), \quad (6.11)$$

where V_{Π} , V_{Σ} are *nonrelativistic* diatomic potentials of states ${}^2\Pi$, ${}^2\Sigma^+$ correlating with the limit

$I({}^2P) - Rg$, $\beta_{a(b)}$ is the angle between $I_{a(b)} - Rg$ and $I - I$ axes, indexes a , b distinguish iodine centers. Beyond the IDIM PT1 model, the high-level *ab initio* calculations by multi-reference configuration interaction and coupled-cluster methods briefly described below are available.

Multi-reference Configuration Interaction Method The most straightforward *ab initio* method beyond the Hartree-Fock approximation is the configuration interaction (CI) method [45]. In this method wave function is a linear combination of determinants which generated by selecting occupied spin-orbitals. The type of CI where all determinants are used is called the full CI method. This is the exact method in a given basis set. However, the possible number of determinants which can be generated in the full CI method is extremely large and this method is not tractable for many-electron systems using reasonable basis set. Therefore approximate schemes with selected configurations are usually used. In the most popular multi-reference CI (MR-CI) method the wave function is written as a *linear* expansion

$$\Psi^{MR-CI} = \hat{C} \Psi_M, \quad (6.12)$$

where

$$\hat{C} = 1 + \hat{C}_1 + \hat{C}_2 + \hat{C}_3 + \dots, \quad (6.13)$$

$$\hat{C}_1 = \sum_b \sum_r c_b^r a_b^+ a_r, \quad (6.14)$$

$$\hat{C}_2 = \sum_{b>c} \sum_{r>s} c_{bc}^{rs} a_s^+ a_c a_r^+ a_b, \text{ etc}, \quad (6.15)$$

Ψ_M is a multi-reference wave function which is usually a solution of the multi-configurational self-consistent field method, a_b , a_r^+ are the electron annihilation and creation operators. The expansion coefficients c_b^r , $c_{bc}^{rs} \dots$ are founded by diagonalization of the Hamiltonian matrix computed on the selected determinants for roots of interest. The most popular is the approximation $\hat{C} \approx 1 + \hat{C}_1 + \hat{C}_2$ resulting in MR-CI with single and double (MR-CISD) excitations method.

A method is said to be size-consistent if the computed energy of the composite system $A + B$ at an infinite distance from each other gives the same energy as if the

method is applied to A and B separately. The natural, from a physical point of view, requirement of size-consistency is not valid, however, for the MR-CISD method until the full-CI limit is reached. To correct the MR-CI method to be approximately size consistent, the so called ‘‘Davidson correction’’ is applied that never leads, however, to the exact size-consistency. Some advantage of the MR-CI method is that it can be used for calculations of the ground as well as excited states.

Coupled-Cluster Method In the single-reference coupled-cluster (CC) method [46] the wave function is written as the *exponential* expansion

$$\Psi^{\text{CC}} = \exp(\hat{T})\Psi_0, \quad (6.16)$$

where

$$\hat{T} = \hat{T}_1 + \hat{T}_2 + \hat{T}_3 + \dots \quad (6.17)$$

is the excitation operator,

$$\hat{T}_1 = \sum_b \sum_r t_b^r a_r^+ a_b, \quad (6.18)$$

$$\hat{T}_2 = \sum_{b>c} \sum_{r>s} t_{bc}^{rs} a_s^+ a_c a_r^+ a_b, \text{ etc.}, \quad (6.19)$$

Ψ_0 is a single-reference wave function. The wave function and energy are functions of *cluster amplitudes* $t_b^r, t_{bc}^{rs} \dots$ to be found iteratively from a non-linear set of coupled-cluster equations. Of course in real calculations \hat{T} is not an infinite series and truncation of \hat{T} has to be made. The truncation $\hat{T} \approx \hat{T}_1 + \hat{T}_2$ gives the CC method with single and double excitation (CCSD model). Applying the approximation $\hat{T} \approx \hat{T}_1 + \hat{T}_2 + \hat{T}_3$ one gets the CC method with single, double and triple (CCSDT model) excitations. Similarly, more accurate approaches where \hat{T} is truncated at a later step are introduced. In the simplest case of the closed-shell system, Ψ_0 is a single Hartree-Fock determinant, indices b, c, \dots denote occupied Hartree-Fock spin-orbitals and r, s, \dots unoccupied spin-orbitals. In this case indices for occupied and unoccupied spin-orbitals do not overlap, therefore \hat{T}_i operators commute with each other, and we can write

$$\begin{aligned} \exp(\hat{T}) &= \hat{T}_1 + \hat{T}_2 + \hat{T}_3 \\ &+ \dots \frac{1}{2!} \hat{T}_1^2 + \hat{T}_1 \hat{T}_2 + \frac{1}{3!} \hat{T}_1^3 + \frac{1}{4!} \hat{T}_1^4 + \frac{1}{2!} \hat{T}_1^2 \hat{T}_2 + \hat{T}_1 \hat{T}_3 + \frac{1}{2!} \hat{T}_2^2 + \dots \end{aligned} \quad (6.20)$$

One sees that already in the CCSD method higher than double excitations appear due to the so-called *disconnected* (like $\frac{1}{2!} \hat{T}_2^2$) terms which are the product of the *connected* clusters \hat{T}_i . Within many body perturbation theory, it can be shown (*factorization lemma*) that for exact wave function, the disconnected terms are product of the connected ones exactly in the same way as in Eq. (6.20). Thus the

exponential ansatz (6.16) has the correct connected cluster structure of the exact wave function but only connected cluster amplitudes are independent parameters. This makes the CC method to be a very efficient computational tool. Moreover, it is not difficult to see that due to the exponential representation for the wave function (6.16) the CC is a size-extensive method. Even truncated $\hat{T} \approx \hat{T}_1 + \hat{T}_2$ generates an infinite number of disconnected clusters. From the perturbation theory, the CCSD energy is correct up to the fourth order (where the contribution from connected triple amplitudes appear) but many contributions are included to infinite order. Usually, the CCSD model recovers up to 95% of the correlation energy of the full CI limit in a given basis if Hartree-Fock configuration dominates the wave function. Further improvement of accuracy is possible within CCSDT and higher CC methods. However, the CCSDT method is too expensive in calculations of three-atomic potential surfaces. In this case, the most commonly used method for preserving triple excitations is to calculate them within perturbation theory using converged single and double cluster amplitudes from the CCSD method. This method, denoted as CCSD(T), is inexpensive enough to be widely used in calculations of vdW complexes of iodine molecules.

Unfortunately, there are serious limitations for the CC method. The nonlinearity in the coupled-cluster equations requires applying iterative procedures which may not converge. Only the lowest state of each symmetry can be studied.

For open-shell systems, limited by the single reference approach, calculated by the restricted (RHF) or unrestricted (UHF) Hartree-Fock methods Ψ_0 can be used. The corresponding CC methods are referred to as RCC and UCC. In the UHF method, the wave function is a single determinant and CC equations are essentially the same as for closed-shell case. Generally speaking, in the RHF method wave function is a linear combination of Slater determinants, that makes CC equations for RHF-based reference more complicated. In turn, CC wave function (6.16) with UHF-based Ψ_0 , in general, is not a spin eigenfunction. Though, it was shown that this is not a problem for the CC energy. Usually, the RCCSD(T) and UCCSD(T) methods give very close energies. To the best of our knowledge, multi-reference CC approaches were not yet applied for studies of vdW complexes of an iodine molecule.

Bound State Calculations In the *adiabatic* approximation, the rovibrational Hamiltonian of RgI₂vdW complexes in the Jacobi coordinate system has the form

$$\hat{H} = \frac{-\hbar^2}{2\mu} \frac{d^2}{dR^2} + \frac{\hat{\mathbf{l}}^2}{2\mu R^2} + \frac{-\hbar^2}{2M} \frac{d^2}{dr^2} + \frac{\hat{\mathbf{j}}^2 - \Omega^2}{2Mr^2} + V_{I_2}(r) + V(R, r, \cos \theta), \quad (6.21)$$

where

- M is the reduced mass of the I_2 molecule,
- μ is the reduced mass of the Rg + I_2 system,
- θ is the angle between \mathbf{R} and \mathbf{r} vectors (see Fig. 6.1),
- $\hat{\mathbf{j}}$ is the angular momentum of the I_2 molecule, composed of the electronic angular momentum $\hat{\mathbf{j}}^e$ and the angular momentum of the nuclei rotation,

- Ω is the projection of \hat{j} on the \mathbf{r} vector,
- \hat{l} is the orbital angular momentum associated with the \mathbf{R} vector.

$V_{I_2}(r)$ is the I_2 potential function for a given electronic state with quantum numbers $n, \Omega, \omega, \sigma$ (see paragraph *Isolated diatomic molecule wavefunction* in Sect. 5.3.2.3 for more details). $V(R, r, \cos\theta)$ is the adiabatic Rg + I_2 interaction potential. It is given by Eq. (5.55).

with $n = n', \Omega = \Omega', \omega = \omega', \sigma = \sigma'$ and has to be calculated by an *ab initio* method (CCSD(T) or MR-CI, for example). Bound states energies and wavefunctions can be obtained by solving the time-independent Schrödinger equation

$$\hat{H}\Psi_n(\mathbf{R}, \mathbf{r}) = E_n\Psi_n(\mathbf{R}, \mathbf{r}) \quad (6.22)$$

with asymptotic conditions (compare with Eq. 5.32)

$$\Psi_n(\mathbf{R}, \mathbf{r}) \xrightarrow{r \rightarrow \infty, R \rightarrow \infty} 0, \quad (6.23)$$

where index n enumerates bound states. Since the interaction of Rg with I_2 is weak, a good approximation to Eqs. 6.21 and 6.22 is to use the vibrationally averaged Hamiltonian [47]

$$\hat{H}_v = \frac{-\hbar^2}{2\mu} \frac{d^2}{dR^2} + \frac{\hat{l}^2}{2\mu R^2} + B_v \hat{j}^2 + E_{I_2}(v) + V_{vv}(R, \cos\theta) \quad (6.24)$$

$$\hat{H}_v \Psi_{vm}(\mathbf{R}) = E_{vm} \Psi_{vm}(\mathbf{R}) \quad (6.25)$$

$$\Psi_{vm}(\mathbf{R}) \xrightarrow{R \rightarrow \infty} 0, \quad (6.26)$$

where

$$V_{vv}(R, \cos\theta) = \langle v | V(R, r, \cos\theta) | v \rangle, \quad (6.27)$$

$$B_v = \left\langle v \left| \frac{1}{2Mr^2} \right| v \right\rangle, \quad (6.28)$$

$|v\rangle$ is vibrational wavefunctions of the I_2 molecule. In the approximation (6.24 and 6.25) bound states of Rg I_2 vdW complexes are classified by two quantum numbers, v which enumerates vibrational states of the I_2 molecule and m which enumerates vdW modes (for a given vibrational state of the I_2 molecule). Due to the interaction between different vibrational channels $|v\rangle$ (which is neglected in Eqs. 6.24 and 6.25) all bound states of Eq. (6.25) with $E_{vm} > E_{I_2}(v=0)$ are, in fact, quasi-bound (or resonance) states with finite lifetimes. In scattering calculations (see Sect. 5.3.2.3) quasi-bound states manifest as resonances in elastic (as well as inelastic) cross-section $\sigma(E)$, where the width of the resonance, Γ , is related to the lifetime, τ , accordingly

$$\tau = \frac{\hbar}{\Gamma} \quad (6.29)$$

An alternative way to calculate vdW complexes' lifetime is to use imaginary optical potential. In this method, energy gets additional imaginary contribution $-\frac{i\Gamma}{2}$. Then the lifetime is given by Eq. (6.29).

6.4 The RgI₂ vdW Complexes

The valence state HeI₂(*X*, *B*) and ArI₂(*X*, *B*) complexes are the most popular among the RgI₂ ones, though the first experimental data concerning the HeI₂(*E*) complexes were published in 2006 [8]. More detailed studies of the RgI₂(IP) complexes have been carried out in the author's group (see Sect. 6.4.1.3).

In this Sect., we will discuss spectroscopic characteristics of ground *X*, valence *B* and ion-pair state vdW complexes (dissociation and binding energies, topologies of PESs, energies of vdW levels) and data on the RgI₂(*B* and *E* states) decay. We will begin our description with the simplest, HeI₂, object.

6.4.1 The HeI₂ vdW Complexes

It is now installed that *T*-shaped, linear HeI₂(*X*) and free-rotor vdW complexes as well as He_{*n*}I₂(*X*) (*n* = 2, 3) clusters are formed in a supersonic beam, though it was believed up to 2004 that *T*-shaped HeI₂(*X*) complex existed, only. The linear HeI₂(*X*) and then HeI₂(*B*) vdW complexes were predicted theoretically in [47, 48], respectively. Experimentally, the linear HeI₂(*X*) complex was observed in [8]. All the He_{*n*}I₂(*B*, *v_B* ← *X*, 0) (*n* = 1–3) excitation bands are blue-shifted relative to I₂(*B*, *v_B* ← *X*, 0) bands, and spectral separations between maxima of the I₂(*B*, *v_B* = 13–26 ← *X*, 0) and He_{*n*}I₂(*B*, *v_B* = 13–26 ← *X*, 0) bands are ~*n*·3.7 cm⁻¹ [4, 19]. The spectral separation between maxima of the I₂(*B*, 32 ← *X*, 0) and linear HeI₂(*B*, 32 ← *X*, 0) bands is ~10 cm⁻¹ [8]. Besides, continuum, ~16 cm⁻¹ blue-shifted relative to I₂(*B*, *v_B* ← *X*, 0) band and corresponding to bound-free transitions of the HeI₂(*X*, 0) linear complex, was observed in [8].

6.4.1.1 The HeI₂(*X*) Complexes

Theoretical and experimental data on dissociation energies of the *T*-shaped and linear HeI₂(*X*, *v_X* = 0) complexes, topology of PES and energies of vdW levels are given in several papers (see [8, 47, 49–51] and references). The principal results obtained are as follows (Table 6.1):

Table 6.1 Spectroscopic parameters of the RgI_2 complexes, $Rg = He, Ne, Ar, Kr$

HeI₂								
	<i>T</i> -shaped				Linear (free-rotor)			
	D_e^a , cm ⁻¹	R_e^b , Å	D_0^c , cm ⁻¹	R_0^d , Å	D_e , cm ⁻¹	R_e , Å	D_0^c , cm ⁻¹	R_0 , Å
<i>X</i>	38.92 [50]	3.84 [8]	15.51 [50] 16.6 [8]	4.36 [50]	44.28 [50]	4.83 [50] 4.89 [8]	15.72 [50] 16.3 [8]	5.34 [50]
<i>B</i>	29.48 [48]	3.96 [48]	12.33 [48] 12.8 [8]	4.58 [48]			6 [6, 32, 44]	
<i>E</i>	33.2 [52]	4.1 [52]	16.85 [52] 16.7(6) [8] 14.0(1) [32]				10.3 [53]	
NeI₂								
<i>X</i>	89 [54]	3.78 [54]	72.4–74.7 [55] 65.3 [28] 69.62 [54] 64 [56]		91 [54]	4.91 [54]	68 [54]	5.01 [54]
<i>B</i>			65.0–67.1 [55] 57.6 [28]					
<i>E</i>			73 [56]					
ArI₂								
<i>X</i>	235 [57]	3.96 [57]	212 [57] 240.5 [10]		268 [57]	5.05 [57]	237.8 [57]	
<i>B</i>		3.83 [44]	227 [12] 226.5 [10]				250.3 [10]	
<i>E</i>			410–415 (see [58])					
KrI₂								
<i>X</i>			320 [58]					
<i>B</i>			307 [58]					
<i>E</i>			663–683 [58]					

The UCCSD(T), RCCSD(T) and MR-CI methods were used in theoretical calculations, carried out in [48, 50, 54, 57, 52], respectively

^aPotential well depths

^bEquilibrium distance corresponding to potential well depths

^cBinding energies of the lowest vdW levels corresponding to the *T*-shaped or linear (free-rotor) complexes

^dEquilibrium distance corresponding to $n = 0$ vdW levels

- potential well depths are $D_e^{X,0} = 44.28 \text{ cm}^{-1}$ (linear) and 38.92 cm^{-1} (*T*-shaped) [50];
- equilibrium distance values $R_e^{X,0} = 4.83 \text{ Å}$ [50], 4.89 Å [8] (linear) and 3.84 Å [8] (*T*-shaped);

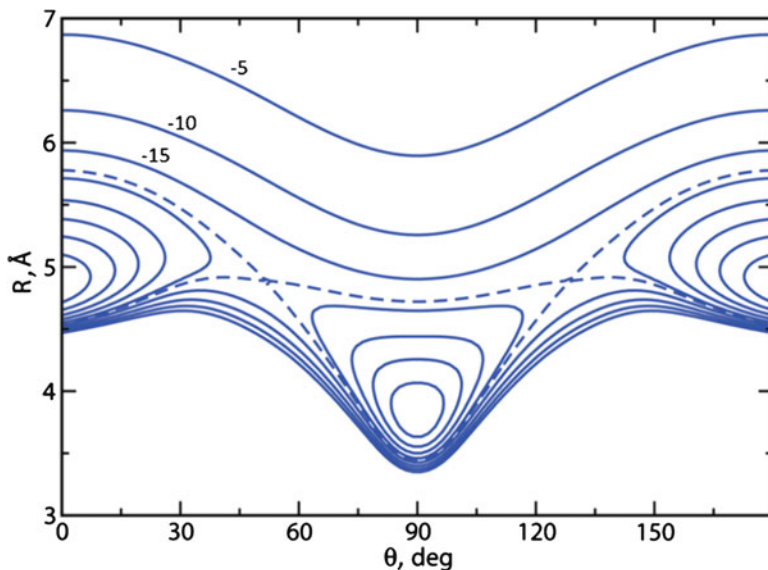


Fig. 6.6 Contour plots of the vibrationally averaged $V_{v,v}(R, \theta)$ potential (see Eq. 6.27) of the $\text{HeI}_2(X)$ complex for $v_X = 0$, in the (θ, R) plane. Contour intervals are of 5 cm^{-1} and for energies from -40 to 0 cm^{-1} . The dashed line corresponds to the energy of -18.43 cm^{-1} of the barrier between the linear and bent isomers [50]

- binding energies of $n_X = 0$ vdW level are $D_0^{X,0} = 15.72 \text{ cm}^{-1}$ [50], 16.3 cm^{-1} [8] (linear) and 15.51 cm^{-1} [50], 16.6 cm^{-1} [8] (*T*-shaped);
- equilibrium distance values are $R_0^{X,0} = 5.34 \text{ \AA}$ (linear) and 4.36 \AA (*T*-shaped) [50];
- the degenerate $n_X = 0, 1$ ($E = -15.72 \text{ cm}^{-1}$) vdW levels are localized in the linear well, whereas $n_X = 2$ one ($E = -15.51 \text{ cm}^{-1}$) is localized in the *T*-shaped well (Figs. 6.6 and 6.7). The $n_X \geq 3$ levels ($E \geq -8.3 \text{ cm}^{-1}$) are spread over all θ values [50].

6.4.1.2 The $\text{HeI}_2(B)$ Complexes

Theoretical, calculated by the UCCSD(T) method, and experimental data on dissociation energies of the *T*-shaped and linear $\text{HeI}_2(B)$ complexes, the topology of PES and energies of vdW levels are given in [8, 48].

The principal results obtained are as follows:

- potential well depth of the *T*-shaped $\text{HeI}_2(B,0)$ complex is $D_e^{B,0} = 29.48 \text{ cm}^{-1}$ [48];
- equilibrium distance values of the *T*-shaped $\text{HeI}_2(B,0)$ complex is $R_e^{B,0} = 3.96 \text{ \AA}$ [48];

- binding energy of $n_B = 0$ vdW level of the $\text{HeI}_2(B,0)$ complex is $D_0^{B,0} = 12.33 \text{ cm}^{-1}$ [48] and that of $n_B = 0$ vdW level of the $\text{HeI}_2(B, \nu_B = 19\text{--}23)$ complex is $\sim 12.8 \text{ cm}^{-1}$ [8];
- equilibrium distance values of the T -shaped $\text{HeI}_2(B,0)$ complex $R_0^{B,0} = 4.58 \text{ \AA}$ [48];
- the $n_B = 0$ vdW level of the $\text{HeI}_2(B,0)$ complex ($E = -12.33 \text{ cm}^{-1}$) is localized in the T -shaped configuration, whereas $n_B = 1\text{--}6$ ($E = -8.36 \text{--} -2.34 \text{ cm}^{-1}$) wave functions are spread over all θ values [48] (see Fig. 6.7 a, also). It can be assumed that similar features occur at the $\text{HeI}_2(B, \nu_B = 19\text{--}23)$ complex [8]. One should note that the $\text{HeI}_2(B,0 \leftarrow X,0)$ transition is impossible due to extremely

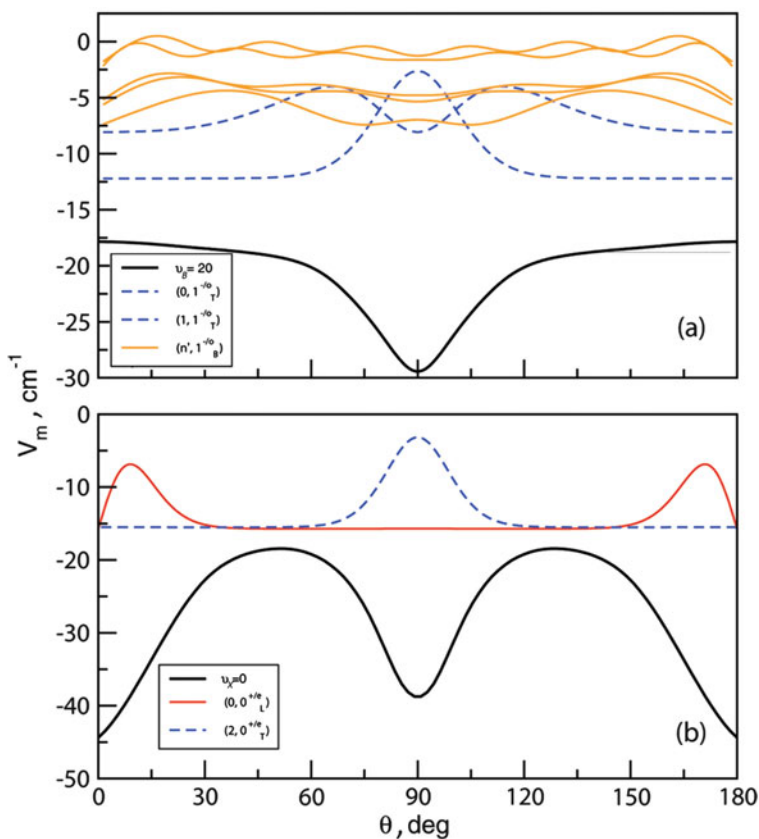


Fig. 6.7 Minimum energy path of the vibrationally averaged $V_{v,v}$ potentials, for (a) $\text{HeI}_2(B,20)$ and (b) $\text{HeI}_2(X,0)$ as a function of angle θ . The angular probability distributions of the two lowest-energy intermolecular vdW levels with $J_X = 0$ ($p_X = +1, j_X = \text{even}$) for the $\text{HeI}_2(X,0)$ PES and $J_B = 1$ ($p_B = -1, j_B = \text{odd}$) for the $\text{HeI}_2(B,20)$ PES are superimposed. For each eigenstate, the zero probability corresponds to its energy value. Solid lines indicate bent/free-rotor states, where $n_B \geq 2$ (a), solid line is for the state localized in the linear $\text{HeI}_2(X,0)$ well (b), and dashed lines correspond to the ones localized in T -shaped wells (a,b) [50]

low *FCFs*. Therefore, data obtained in [8] for the HeI₂(*B*, *v_B* = 19–23) complexes are of great interest for experimentalists.

Analysis of the data presented in this and previous Sect. shows that the HeI₂(*B*, *v_B*, *n_B* = 0 ← *X*, 0, *n_X* = 2) transition occurs in the *T*-shaped configuration. According to CCSD(T) calculations [48, 50], the HeI₂(*B*, *v_B*, *n_B* ≥ 1 ← *X*, 0, *n_X* = 0, 1) bound-bound transitions should occur in the free-rotor configuration, and the blue shift relative to I₂(*B*, *v_B* ← *X*, 0) band has to be ~10 cm⁻¹. The same shift was obtained in [32] (see Fig. 6.8). The bound-free transitions of the HeI₂(*X*, 0) linear complex is ~16 cm⁻¹ blue-shifted relative to I₂(*B*, *v_B* ← *X*, 0) band [8].

A lot of works are devoted to studies of the HeI₂(*B*, *v_B*) decay (see [4, 6, 59–63] and references). At present, it can be considered as established the following features of the HeI₂(*B*, *v_B*) decay:

- Vibrational predissociation of the *T*-shaped HeI₂(*B*, *v_B* = 13–26) complexes occurs, and the Δ*v_B* = 1 channel is the principal one (rate of the Δ*v_B* = 2 *VP* is ~30 times less than that of Δ*v_B* = 1 one) (see [6, 60] and references). The Δ*v_B* = 0 *VP* has been observed in [55], but nobody confirms this feature since.
- quantum yield of luminescence of the *T*-shaped HeI₂(*B*, *v_B* = 13–26) *VP* product population is independent of *v_B* within ~±10% uncertainty (see [6, 19] and

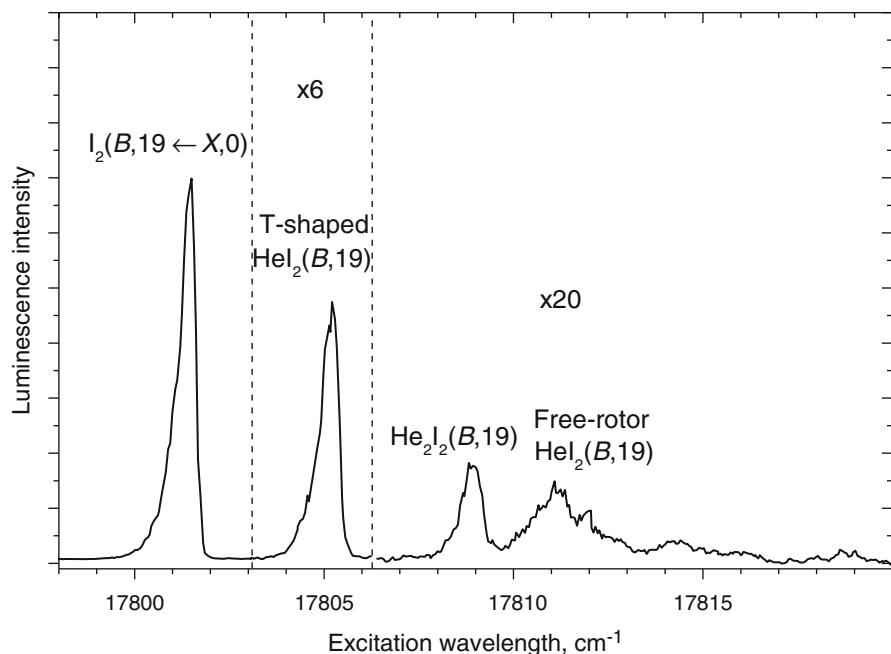
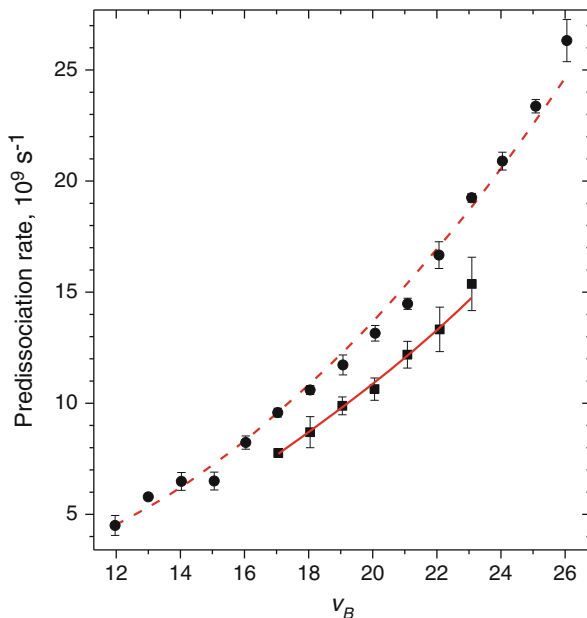


Fig. 6.8 Excitation spectra of luminescence of the I₂(*B*, 19) and products of *VP* of the HeI₂(*B*, 19) complexes. The PMT FEU100 + KS10 glass filter, λ > 600 nm, was used. Positions of the bands corresponding to the transition to the *T*-shaped and linear HeI₂(*B*, 19) complexes are shown [32]

Fig. 6.9 Theoretical fits (6.30) of the real-time VP rates (dashed line) and the experimental linewidth deduced VP rates (open squares) [59] for HeI_2 . The real-time data [61] are shown as filled triangles [59]



references). This feature, maybe, due to the fact that the rate of EP of the complexes is much less than that of VP .

- VP rate increases with v_B in the $v_B = 13$ – 23 range (Fig. 6.9) according to Eq. (6.30)

$$1/\tau = Av_B^2 + Bv_B^3 \text{ s}^{-1} \quad (6.30)$$

- $A = 2.09 \cdot 10^7$, $B = 6.56 \cdot 10^5$, for $12 < v_B < 26$ according to data of [48].
- Calculations performed in [57] shows that VP rate increases ~ 3.5 times with $n_B = 0, 2$. According to [58], this feature takes place for $n_B = 4$, only.
- the bound-free $\text{HeI}_2(B, v_B \leftarrow X, 0)$ transitions of the linear complex leads to direct dissociation of the $\text{HeI}_2(B, v_B)$ complex, $\Delta v_B = 0$ [8].

6.4.1.3 The T -shaped $\text{HeI}_2(\text{IP})$ Complexes

MR-CI calculations of PES and energies of vdW levels of the $\text{HeI}_2(E, v_E = 0, n_E)$ complexes [52] has shown as follows:

- potential well depth of the T -shaped $\text{HeI}_2(E, 0)$ complex is $D_e^{E,0} = 33.2 \text{ cm}^{-1}$;
- equilibrium distance values of the T -shaped $\text{HeI}_2(E, 0)$ complex is $R_e^{E,0} = 4.1 \text{ \AA}$;
- binding energies of the $n_E = 0$ vdW level are $D_0^{E,0} = 16.85 \text{ cm}^{-1}$, and this level is localized at T -shaped configuration;

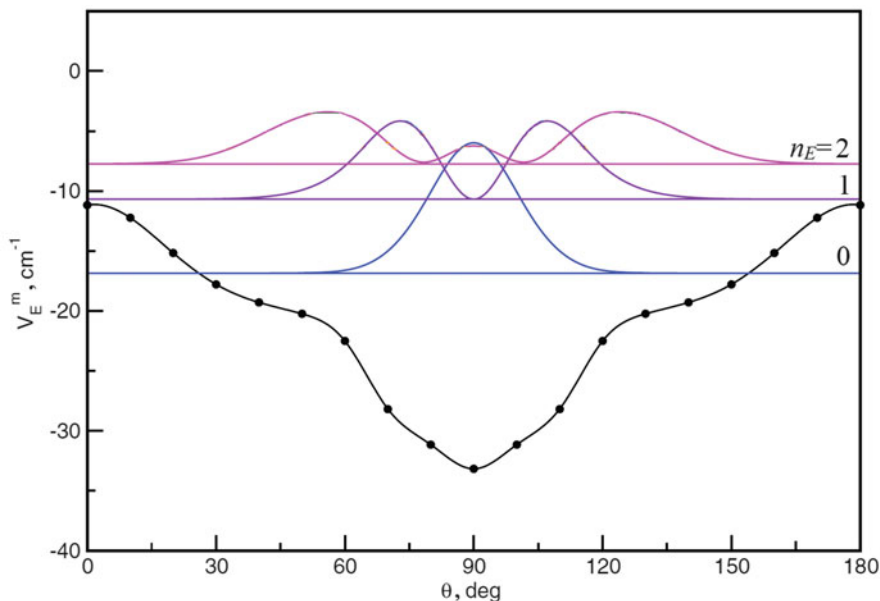


Fig. 6.10 Minimum energy path, V_E^m , of the $\text{HeI}_2(E,0)$ state as a function of θ . The energies and angular probability distributions of the lowest three bound intermolecular vdW levels for $J=0$ are also displayed [52]

- the $n_E = 1$ level ($E = -10.68 \text{ cm}^{-1}$ relative to the dissociation limit) is localized around $\theta = 70^\circ$ and 110° , and $n_E \geq 2$ levels ($E \geq -7.74 \text{ cm}^{-1}$) show oscillatory character over all Θ values (Fig. 6.10).

The first experimental data on the energy of the $\text{HeI}_2(E)$ *T*-shaped and linear vdW complexes were obtained in [8] by the group of R.A. Loomis. They measured excitation spectra of luminescence in the $\lambda_{\text{lum}} \approx 338\text{--}345 \text{ nm}$, where $\text{I}_2(E \rightarrow A1_u, C1_u, \beta1_g \rightarrow A1_u, \text{ and } D'2_g \rightarrow A'2_u)$ transitions could occur, at excitation wavelength range corresponding to the $\text{HeI}_2(E, \nu_E = 1, n_E \leftarrow B, 23, n_B = 0, 3)$ transitions. The origin of the luminescence in the $\lambda_{\text{lum}} \approx 338\text{--}345 \text{ nm}$ spectral range was not discussed. Transitions from the $n_B = 0$ and 3 vdW levels have to be corresponded to *T*-shaped and free-rotor conformers of the complex, respectively (see Sect. 6.4.1.2). The authors determined the energies of the *T*-shaped $\text{HeI}_2(E, \nu_E = 1, n_E = 0, 1)$ complex (-16.7 and -13.8 cm^{-1} , respectively) as well as those of the linear $\text{HeI}_2(E, \nu_E = 1, n_E = 0\text{--}2)$ one, as they believed ($-16.7, -13.8$ and -10 cm^{-1}).

More detailed studies of spectroscopic characteristics of the $\text{HeI}_2(E, \nu_E = 0\text{--}2, n_E)$ *T*-shaped complex as well as its *VP* and *EP* were carried in the author's group [32]. The complexes were populated in the

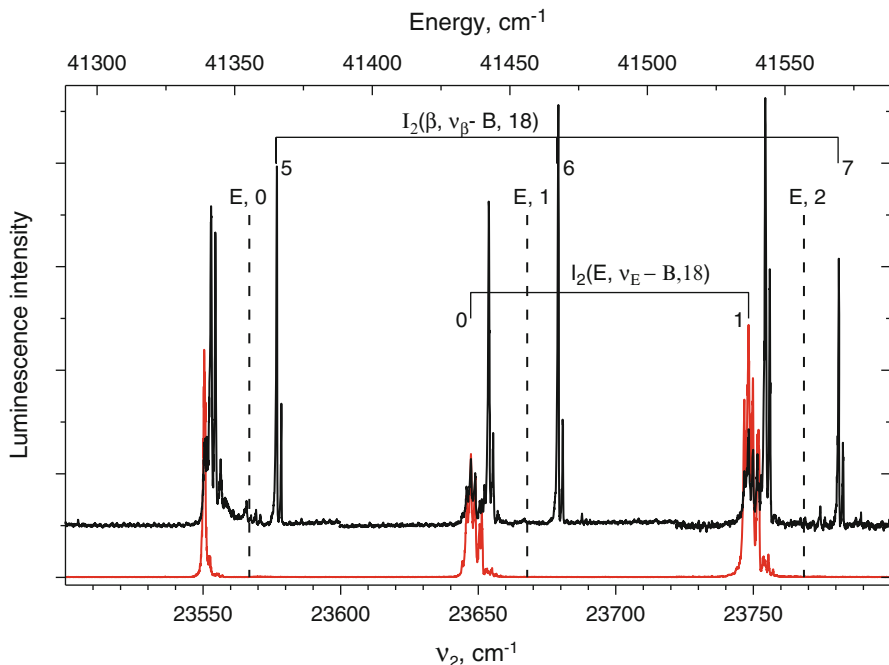
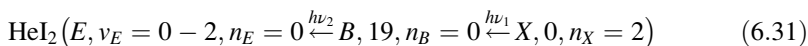


Fig. 6.11 Excitation spectra of luminescence in the $E \rightarrow B$ transition, (lower line) and the UV spectral range, $\lambda_{\text{lum}} \approx 2600\text{--}3800 \text{ \AA}$ (upper line) at $\nu_1 = 17804.94 \text{ cm}^{-1}$ (T -shaped $\text{HeI}_2(B, 19 \leftarrow X, 0)$ transition, see Fig. 6.7). The $E \rightarrow B$ transition was monitored at $\lambda_{\text{lum}} = 4274 \text{ \AA}$ and 4303 \AA in the $\nu_1 = 23,500\text{--}23,725$ and $23,725\text{--}23,800 \text{ cm}^{-1}$, spectral range, respectively. Dissociation limits of the $\text{HeI}_2(E, \nu_E = 0\text{--}2)$ complexes) are marked out by broken lines. Assignments of the $\text{I}_2(E, \nu_E = 0, 1 \leftarrow B, 18)$ and $\beta, \nu_\beta = 5\text{--}7 \leftarrow B, 18)$ transitions are shown [32]



excitation pathway in the ($41285\text{--}41,585 \text{ cm}^{-1}$) energy range. The $n_E = 0$, $n_B = 0$ and $n_X = 2$ levels are localized at the T -shaped configuration (see above). Population of the $n_E \geq 1$ levels were not observed, probably, due to low $FCFs$ of the $\text{HeI}_2(E, 0, n_E \geq 1 \leftarrow B, 19, n_B = 0)$ transitions between the T -shaped and bending (free-rotor) isomers (Figs. 6.11 and 6.12).

Three groups of the excitation bands located lower than the dissociation limits of the $\text{HeI}_2(E, \nu_E = 0\text{--}2)$ complexes, $\nu_2 = 23566.8$, 23667.8 and 23768.4 cm^{-1} , respectively consist of the band in which the $E \rightarrow B$ luminescence prevails ($\text{I}_2(E, \nu_E)$ bands) and both $E \rightarrow B$ and $D \rightarrow X$ luminescence occur ($\text{HeI}_2(E, \nu_E)$ bands) (see Figs. 6.11 and 6.12).

Intensities of the $D \rightarrow X$ transitions are $< 10^{-2}$ of that of $E \rightarrow B$ at the $\text{I}_2(E, \nu_E = 0, 1, 2)$ bands. Detailed analysis shows that these bands are ascribed to two-photon transitions, $\text{I}_2(E, \nu_E, J_E \xleftarrow{h\nu_2 + h\nu_1} X, 0, J_X)$ ($g - g$, $\Delta J = \pm 2$) in a free iodine

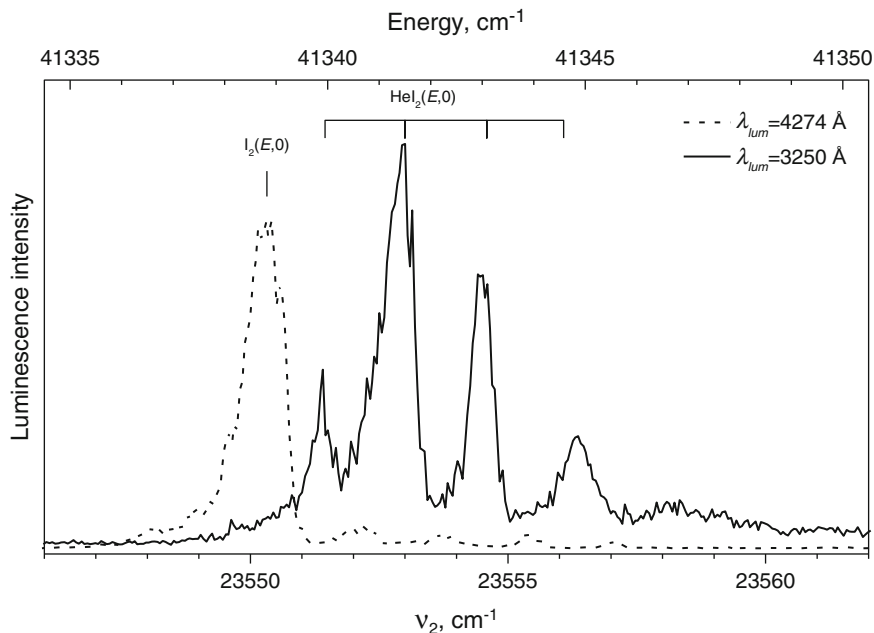


Fig. 6.12 Excitation spectra of luminescence at the $\lambda_{lum} = 4274 \pm 5 \text{ \AA}$, ($E \rightarrow B$ transition, dotted line) and $\lambda_{lum} = 3250 \pm 5 \text{ \AA}$ ($D \rightarrow X$ transition, solid line) at the 1-st group; $\nu_1 = 17804.94 \text{ cm}^{-1}$. Positions of the excitation bands of the luminescence corresponding to the spectral components of fundamental YG981C laser harmonic are shown. The $\lambda_{lum} = 3250 \pm 5 \text{ \AA}$ excitation bands (1B) are saturated [32] (see Sect. 6.2.1.2)

molecule. The $\text{HeI}_2(E, \nu_E = 0, 1, 2)$ bands are assigned to the T -shaped $\text{HeI}_2(E, \nu_E = 0, 1, 2, n_E = 0 \xleftarrow{h\nu_2} B, 19, n_B = 0)$ transitions, respectively. Transitions to other $\text{HeI}_2(\text{IP})$ complexes are not observed in the energy range under study, though all these transitions are allowed in the C_{2v} point group [64]. Therefore, one can assume that He atom behaves as “spectator” (see [7] and references), and propensity rules for the $\text{HeI}_2(\text{IP} - B)$ transitions are the same as selection rule for the isolated I_2 molecule (see Chap. 3).

The $\text{HeI}_2(E)$ complex energy is $(17788.5 + \nu_2) \text{ cm}^{-1}$ (upper x -axis in Fig. 6.11). The energy gaps, ΔE , between origins of the bands $(17788.5 + \nu_2)$ and $\text{I}_2(E, \nu_E)$ energies are binding energies of the $\text{HeI}_2(E, \nu_E = 0, 1 \text{ and } 2, n_E = 0)$ complexes. They are equal to 13.9(1), 14.0(1) and 14.0(1) cm^{-1} , respectively, $\sim 2.8 \text{ cm}^{-1}$ less than those obtained in [8, 52].

The $\text{I}_2(E, \nu_E = 0 \rightarrow B, E, \nu_E = 0, 1 \rightarrow B \text{ and } E, \nu_E = 0-2 \rightarrow B)$ transitions are observed at the $\text{HeI}_2(E, \nu_E = 0, 1 \text{ and } 2)$ bands, respectively. Intensities of the $E \rightarrow B$ and $D \rightarrow X$ luminescence are comparable at them (Fig. 6.13), and I_{E-B}/I_{D-X} are equal to 0.14(1), 0.55(8) and 0.61(9), respectively.

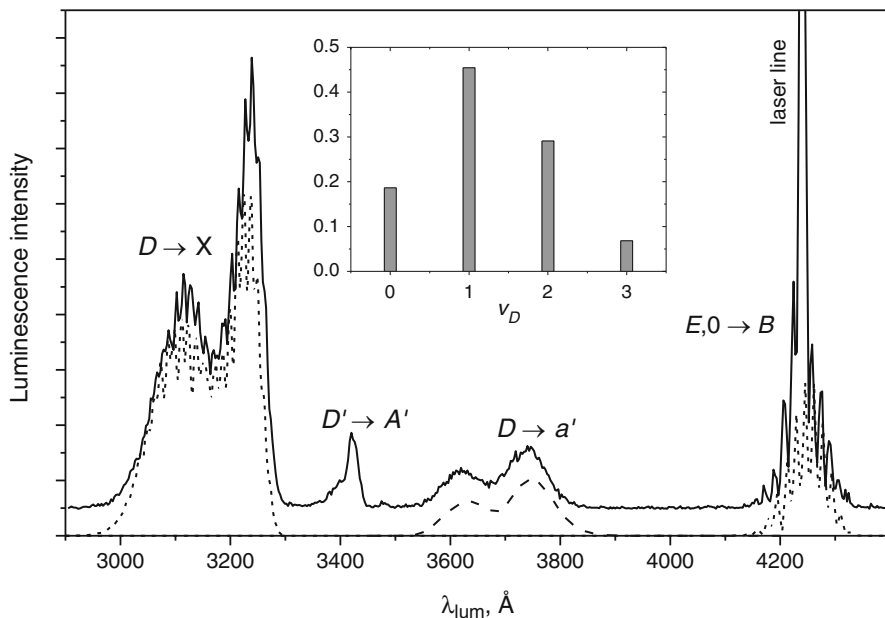


Fig. 6.13 Experimental (solid line) and simulated (broken line) luminescence spectra in the $\lambda_{lum} = 2900\text{--}4400$ Å spectral range at $1B, \nu_2 = 23552.9$ cm^{-1} , band; $\nu_1 = 17804.94$ cm^{-1} , T -shaped $\text{HeI}_2(B, 19 \leftarrow X, 0)$ transition. Spectral resolution FWHM = 10 Å. Experimental spectrum is offset for clarity. Populations of the D, v_D vibronic levels are given in the inset [32]

The principal channel of the $\text{HeI}_2(E, 0, n_E = 0)$ state decay is electronic predissociation. Weak $D' \rightarrow A'$ luminescence, $I_{D'A'}/I_{D-X} = 0.05$, was also observed at the $\text{HeI}_2(E, \nu_E = 0)$ band. The $\text{HeI}_2(E, \nu_E = 1, 2, n_E = 0)$ complexes undergo vibrational ($\Delta v = -1$) as well as electronic $\text{HeI}_2(E, \nu_E = 1, 2, n_E = 0 \rightarrow D, v_D$ and $D', v_{D'})$ predissociations, and rate of VP are 1.2 and 1.6 times larger for the $\nu_E = 1, 2$, respectively, than those of EP . One should note, that the $\text{HeI}_2(E0_g^+ \leftrightarrow D0_u^+)$ non-adiabatic transition is forbidden at the C_{2v} symmetry group ($\text{HeI}_2(A_1 \leftrightarrow B_2)$). It may be allowed due to vibronic or rotational perturbations. The similar features occur for the $\text{ArI}_2(B0_u^+)$ EP which is due to perturbation by the $\text{ArI}_2(a1_g, a'0_g^+$ and $(1)2_g$) states (see Sect. 6.4.3.2 and [7]) and in the $\text{I}_2(E0_g^+ \xrightarrow{He} D0_u^+)$ CINATs. For He, this CINAT is the principal channel. It is due to strong long-range electrostatic interaction and follows $u \leftrightarrow g$ propensity rule (see Sect. 5.3.2.4).

The $\text{HeI}_2(E, 0, n_E = 0)$ state lies 13.9 cm^{-1} below the dissociation limit and cannot dissociate. The $\text{HeI}_2(E, 0, n_E = 0 \rightarrow D, v_D < 4$ and $D', v_{D'} < 10)$ electronic predissociations observed in the experiments are available only. Nevertheless, luminescence, which can be ascribed to the $\text{I}_2(E, 0 \rightarrow B)$ transition, is observed at the $\text{HeI}_2(E, \nu_E = 0)$ band. One can say the same about the $E, \nu_E = 1 \rightarrow B$ and $E, \nu_E = 2 \rightarrow B$ transitions at the $\text{HeI}_2(E, \nu_E = 1, 2)$ band. Explanation of this feature is as follows: origin of this luminescence is the $\text{HeI}_2(E, \nu_E, n_E)$ complexes.

One can believe that EP of the $\text{HeI}_2(E, \nu_E, n_E)$ is rather slow process, and VP channels mentioned above are energetically unavailable. Therefore, radiative decays of these complexes are the principal channels.

The binding energy obtained in [32] is $\sim 2.8 \text{ cm}^{-1}$ less than those obtained in [8, 52]. The excitation band assigned in [8] as corresponding to the $n_E = 0$ ($n^\dagger = 0$ [8]), should be ascribed to two-photon transition in a free iodine molecule, in fact. In this case, ($n^\dagger = 1$ [8]) is $n_E = 0$, and D_0^1 has to be equal to $\sim 13.8 \text{ cm}^{-1}$, similar to data obtained in [32]. The $n^\dagger = 2$ [8, 52] ($n_E = 1$ [53]) level corresponds to linear (free-rotor) configuration (see the next Sect).

6.4.1.4 The Free-Rotor HeI₂(IP) Complexes

These studies were carried out at the $\nu_1 = 17,811 \text{ cm}^{-1}$ band, free-rotor $\text{HeI}_2(B, 19, n_B \leftarrow X, 0, n_X)$ transition [53] (see Fig. 6.8). Survey excitation spectra of luminescence in the $\text{I}_2(E \rightarrow B)$ transition and UV spectral range, $\lambda_{\text{lum}} \approx 2600\text{--}3800 \text{ \AA}$ measured at $\nu_1 = 17811.0 \text{ cm}^{-1}$, maximum of the $\text{HeI}_2(B, 19 \leftarrow X, 0)$ transition in the linear (free-rotor) isomer, are presented in Fig. 6.14.

The mean free-rotor $\text{HeI}_2(E, \nu_E = 0\text{--}6, n_E)$ binding energy of the lowest observed vdW levels to which the $\text{HeI}_2(E, \nu_E, n_E \leftarrow B, 19, n_B)$ transitions occur is 10.3 cm^{-1} (Table 6.2) similar to that of the $n^\dagger = 2$ [8, 52]. Therefore, one can believe that it is lowest vdW level of the linear (free-rotor) configuration, $n_E = 1$.

One should note that binding energies presented in Table 6.2 contradict to the data of [52].

The $\text{I}_2(D \rightarrow X, E \rightarrow B)$ and very weak luminescence, $\lambda_{\text{lum}}^{\text{max}} \approx 342 \text{ nm}$, branching ratios ~ 0.03 and 0.02 at $\nu_E = 0$ and 6 bands, respectively, occurs (Fig. 6.15).

6.4.2 The NeI₂ vdW Complexes

The linear and T -shaped $\text{NeI}_2(X)$ vdW complexes as well as $\text{He}_n\text{I}_2(X)$ ($n = 2\text{--}6$) clusters are formed in a supersonic beam (see [28] and references). All the $\text{Ne}_n\text{I}_2(B, \nu_B \leftarrow X, 0)$ ($n = 1\text{--}6$) excitation bands are blue-shifted relative to $\text{I}_2(B, \nu_B \leftarrow X, 0)$ bands, and spectral separations between maxima of the $\text{I}_2(B, \nu_B = 13\text{--}26 \leftarrow X, 0)$ and $\text{Ne}_n\text{I}_2(B, \nu_B = 13\text{--}26 \leftarrow X, 0)$ bands are $\sim n \cdot (6.1\text{--}7.0) \text{ cm}^{-1}$ [28].

6.4.2.1 The NeI₂(X) Complexes

Data on basic spectroscopic characteristics of the $\text{NeI}_2(X, 0)$ state are given in Table 6.1. PES of the state has two minima corresponding to T -shaped ($D_e^{X,0} = 89 \text{ cm}^{-1}$) and linear ($D_e^{X,0} = 91 \text{ cm}^{-1}$) isomers. The $n_X = 0, 3, 6$ (energies relative the dissociation limit are $-69, -58$ and -51 cm^{-1}) of the T -shaped and

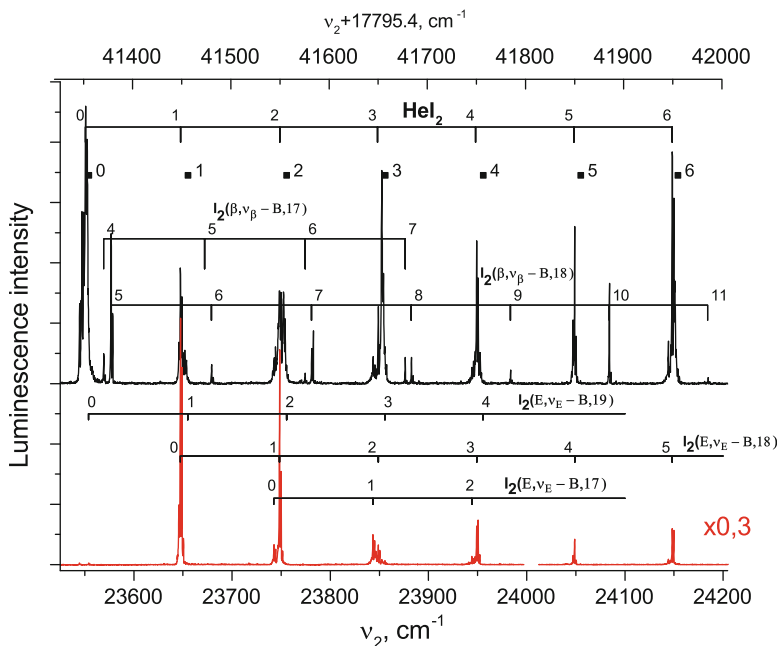


Fig. 6.14 Excitation spectra of luminescence in the $E \rightarrow B$, $\lambda_{\text{lum}} \approx 4284 \text{ \AA}$, (lower line) and UV spectral range, $\lambda_{\text{lum}} \approx 2600\text{--}3800 \text{ \AA}$ (upper line) measured at $\nu_1 = 17811.0 \text{ cm}^{-1}$, maximum of the free-rotor $\text{HeI}_2(B, 19 \leftarrow X, 0)$ band. Energy of transitions to the $\text{I}_2(E, \nu_E = 0\text{--}6, J_E = 0)$ states corresponding to the most intense spectral $\nu_f^1 = 9395.12 \text{ cm}^{-1}$ component (see Sect. 6.2.1.2) are marked out. Assignments of the $\text{I}_2(E, \nu_E = 0\text{--}5 \leftarrow B, \nu_B = 17, 18)$ and $\beta, \nu_\beta = 5\text{--}7 \leftarrow B, \nu_B = 17, 18)$ transitions are shown. Groups of excitation bands of the $\text{I}_2(\text{IP} \rightarrow \text{valence states})$ luminescence corresponding to the $\text{HeI}_2(E, \nu_E = 0\text{--}6, n_E)$ complex states are marked out as 0–6 [53]

the $n_X = 1, 2, 4, 5$ (energies relative to the dissociation limit are -68.56 and -55.15 cm^{-1}) of the linear isomers are stable due to high (energies relative to the dissociation limit are -49 cm^{-1}) isomerization barrier between them. As obtained in RCCSD(T) calculations, the $n_X = 0\text{--}2$ states are near-degenerated [54].

6.4.2.2 The $\text{NeI}_2(B)$ Complexes

According to data of [28], the T -shaped, linear and delocalized $\text{NeI}_2(B, \nu_B = 32\text{--}38)$ isomers are populated in the $\text{NeI}_2(B, \nu_B \leftarrow X, 0)$ transitions from single vdW level (“zero-point level”) at rather high $\text{NeI}_2(X, 0)$ complex rotational and vibrational temperatures (Mach number is $M \approx 9$ for $x/D = 12.5$, see Sect. 6.2.1.1). The similar data have been obtained in the author’s group [56] (Fig. 6.16).

Table 6.2 The free-rotor HeI₂($E, v_E = 0-6, n_E$) complex binding energies

v_E	I ₂ ($E, v_E = 0-6, J_E = 0$) transition energy, cm ⁻¹	Energy, cm ⁻¹	HeI ₂ (E, v_E, n_E) binding energy, cm ⁻¹	$v_D^{max}/b.r.$	$v_E^{max}/b.r.$
0	41355.3	41345.9 (C) ^a	9.4	4/ 0.97	-
		41345.5 (B)	9.8		
		41345.0 (A)	10.3		
1	41456.3	41446.84 (C)	9.5	-	-
		41446.45 (B)	9.9		
		41445.53 (A)	10.3		
2	41556.9	41547.43 (C)	9.5	6/ 0.33	1/ 0.67
		41547.0 (B)	9.9		
		41546.55 (A)	10.4		
3	41657.0	41647.6 (C)	9.4	7/ 0.27	2/ 0.73
		41647.18 (B)	9.8		
		41646.78 (A)	10.2		
4	41756.8	41952.37 (C)	9.4	-	-
		41476.97 (B)	9.8		
		41746.54 (A)	10.3		
5	41856.2	41846.77 (C)	9.4	-	-
		41846.35 (B)	9.9		
		41845.93 (A)	10.3		
6	41955.2	41945.71 (C)	9.5	10/ 0.21	5/ 0.77
		41945.38 (B)	9.8		

Maximal vibrational number (v_{IP}^{max}) of a I₂(IP) state populated in the linear HeI₂(E, v_E, n_E) VP and EP as it has been determined by simulation of the luminescence spectra measured at the HeI₂($E, v_E, n_E = 0 \leftarrow B, 19, n_B$) bands. The ratios of integrated partial intensity from selected IP state to the sum of all integrated intensities (branching ratios, *b.r.*) of the HeI₂(E, v_E, n_E) VP and EP product formation and maximal vibronic state (v_{IP}^{max}) populated are also given [53]

^aA, B, C are excitation bands observed from lowest to highest wavenumber values

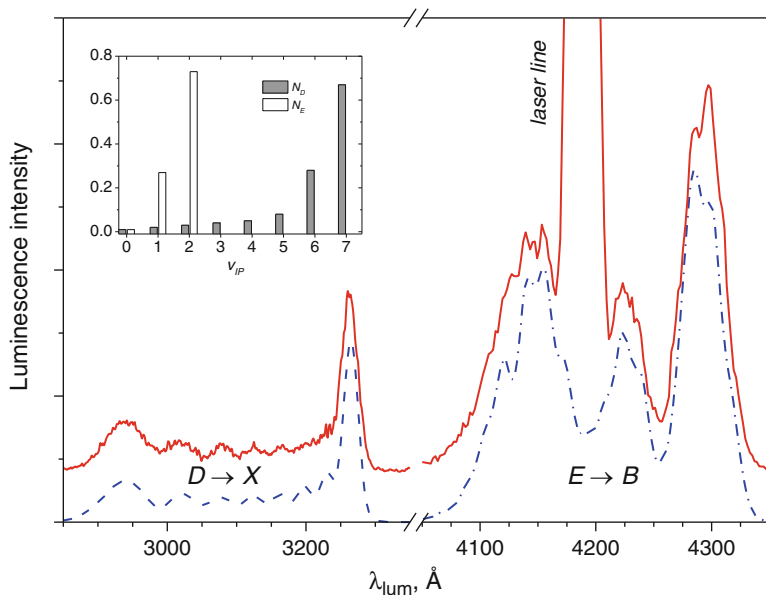


Fig. 6.15 Experimental (solid line) and simulated (dashed line) luminescence spectra in the $\lambda_{lum} = 2800\text{--}4400\text{ \AA}$ spectral range at the 3-rd group of bands, $\nu_2 = 23852.4\text{ cm}^{-1}$. Spectral resolution FWHM = 20 \AA . Experimental spectrum is offset for clarity. Populations of the D, ν_D and E, ν_E vibronic levels are given in the inset. The λ_2 laser lines are marked [53]

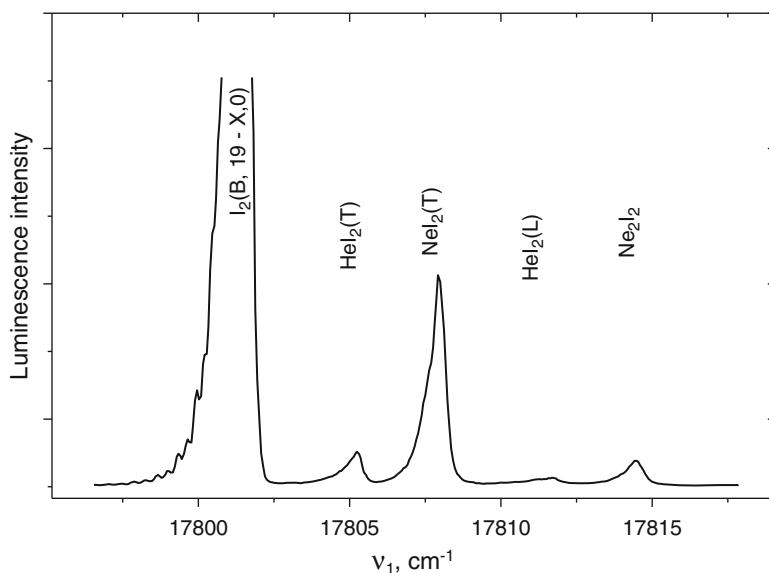


Fig. 6.16 Excitation spectra of luminescence of the $I_2(B,19)$ and products of VP of the $HeI_2(B,19)$, $NeI_2(B,19)$, $HeNeI_2(B,19)$ and $Ne_2I_2(B,19)$ complexes. The PMT FEU100 + KS10 glass filter, λ > 600 nm, was used [56]

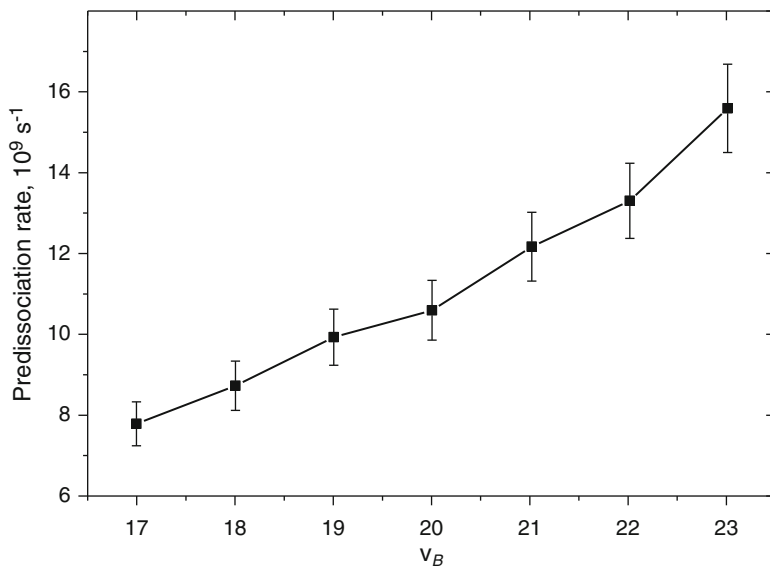


Fig. 6.17 The vibrational predissociation rate for $\text{NeI}_2(B, v_B)$ complexes shown as a function of the v_B [61]

The “zero-point level” is delocalized sampling both the T -shaped and linear configurations (see [65], also). This level is the near-degenerate $n_X = 0$ –2 states [54], probably (see previous Sect.). Binding energy of the $\text{NeI}_2(B, v_B \approx 36)$ complexes is $57.6 \pm 1 \text{ cm}^{-1}$ and $\omega_e^B \approx 20.7 \text{ cm}^{-1}$ [28].

Vibrational distributions obtained for VP products of rather low $\text{NeI}_2(B, v_B = 13$ –26) T -shaped isomer populated at low, $T_{rot} \approx 0.5 \text{ K}$ and $T_{vib} \approx 50 \text{ K}$ (see [4, 55, 66]) temperatures differ dramatically from those obtained for $\text{NeI}_2(B, v_B = 32$ –38) [28]. The $\Delta v_B = 1$ VP channel is the principal one for the $v_B = 13$ –26 levels; the probability of the population of the $v_B - 1$ levels is ~ 0.94 for $v_B = 21, 22$ and that of $v_B - 2$ is ~ 0.05 . For high $v_B = 32$ –38, the probability of population of the $v_B - 1$ levels decreases with v_B and become closed for $v_B = 37$, and the $v_B \leq 35$ vibronic states can be only populated due to intramolecular vibrational redistribution (IVR , see Sect. 6.4.3.2 for details) [28]. Wide vibrational distribution, up to $v_B - 7$, were also observed for the T -shaped and linear $\text{NeI}_2(B, 34)$ isomers. Seven vdW vibrational levels assigned to T -shaped, linear and delocalized $\text{NeI}_2(B, 34)$ isomers, as well as continuum-like bands of the $\text{NeI}_2(B, 34 \leftarrow X, 0)$ transition in the $(-4 - + 47.6 \text{ cm}^{-1})$ interval from the $\text{NeI}_2(B, 34, n_B = 0 \leftarrow X, 0)$ band were identified in [28].

According to all literature data concerning the $\text{NeI}_2(B, v_B)$ complexes [28, 55], the principal channel decay of these complexes is VP , and its rate increases with v_B (Fig. 6.17).

6.4.2.3 The T -shaped $\text{NeI}_2(\text{IP})$ Complexes

Survey excitation spectra of luminescence in the $\text{I}_2(E \rightarrow B)$ transition and UV spectral range, $\lambda_{\text{lum}} \approx 2600\text{--}3800 \text{ \AA}$ measured at $\lambda_1 = 5615.49 \text{ \AA}$ ($\nu_1 = 17807.9 \text{ cm}^{-1}$), T -shaped $\text{NeI}_2(B, 19 \leftarrow X, 0)$ transition are presented in Fig. 6.18.

One sees seven groups of the excitation bands located lower than the dissociation limits of the $\text{NeI}_2(E, \nu_E = 0\text{--}6)$ complexes (zero, 1-st and so on groups) in Fig. 6.18. One of these groups is given in Fig. 6.19 as an example. The $\text{NeI}_2(\text{IP})$ complex term energy relative to that of the $\text{I}_2(X, \nu_X = 0, J_X = 0)$ is given at upper x -axis in Fig. 6.18). The energy gaps, ΔE , between those of transitions to the $\text{NeI}_2(E, \nu_E = 0\text{--}6, n_E = 0)$ complexes (see caption to Fig. 6.18) and energy of transitions to the $\text{I}_2(E, \nu_E = 0\text{--}6, J_E = 0)$ states are binding energies of the $\text{NeI}_2(E, \nu_E = 0\text{--}6, n_E = 0)$ complexes (Table 6.3).

The $\text{NeI}_2(E, \nu_E, n_E = 0)$ binding energy is $D_0^{E, \nu_E} \approx 73 \text{ cm}^{-1}$. Energies of the $\text{I}_2(\text{IP}, \nu_{\text{IP}}, J_{\text{IP}} = 5)$ rovibronic levels of the first-tier iodine molecule IP states, $\text{IP} = D', \beta, D, E, \gamma, \delta$ and calculated relative to that of $\text{I}_2(X, 0, 4)$ and positions of $\text{NeI}_2(E, \nu_E, n_E \leftarrow B, 19, n_B = 0)$ vibrational progression terms are given in Fig. 6.20.

The EP and VP channels are possible if energy of a $\text{NeI}_2(E, \nu_E, n_E)$ term is larger than that of corresponding $\text{I}_2(E, \nu_E, n_E)$ dissociation limit. Nevertheless, luminescence in the $\lambda_{\text{lum}} = 4100\text{--}4400 \text{ \AA}$ spectral range similar to the $\text{I}_2(E, 0 \rightarrow B, \nu_B)$ and $\text{I}_2(E, 1 \rightarrow B, \nu_B)$ ones has been observed in the $E, \nu_E = 0$ and $\nu_E = 1$ band groups, respectively, though they are energetically forbidden (see Fig. 6.21 as an example). Similar “energetically forbidden” transitions have been observed at all band groups studied.

6.4.3 The ArI_2 vdW Complexes

The $\text{ArI}_2(B0_u^+)$ vdW complex has received special attention of both experimentalists and theoreticians due to very rich dynamics, VP including IVR , EP and “caging”. The interpretation of these processes leads to many puzzles, controversies, and surprises. These processes compete, so that it is difficult to distinguish them in experiments. From the theoretical point of view, competing processes should be taken into account simultaneously, which can make the problem computationally intractable [7].

Theoretical and experimental studies of spectroscopic characteristics of the $\text{ArI}_2(X, B)$ complexes, dynamics of the $\text{ArI}_2(B)$ decay and caging both below and above $\text{I}_2(B)$ dissociation limit carried out up to 2003 are reviewed in detail in [7]. In the cases, if there are no more recent data, information from the papers discussed in [7] will be used below.

The T -shaped and linear $\text{ArI}_2(X)$ vdW complexes as well as $\text{Ar}_n\text{I}_2(X)$ ($n = 2, 3$) clusters are formed in a supersonic beam. All the $\text{Ar}_n\text{I}_2(B, \nu_B \leftarrow X, 0)$ ($n = 1\text{--}3$) excitation bands are blue-shifted relative to $\text{I}_2(B, \nu_B \leftarrow X, 0)$ bands, and spectral

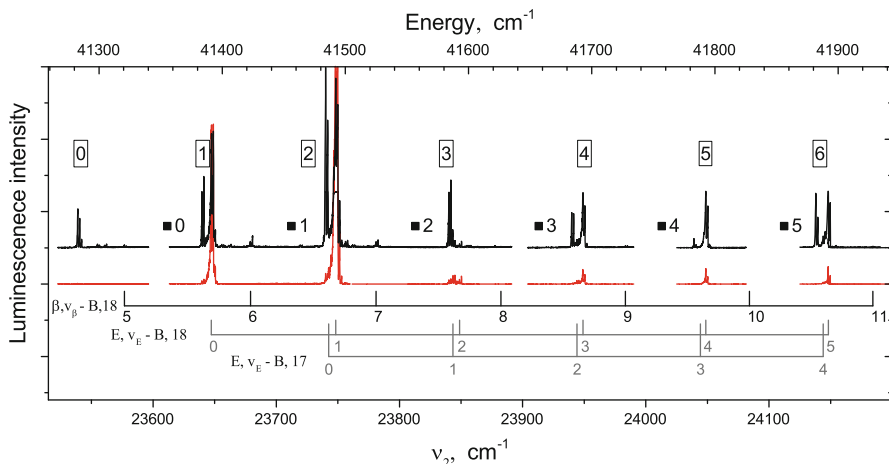


Fig. 6.18 Excitation spectra of luminescence in the $E \rightarrow B$, $\lambda_{\text{lum}} \approx 4284 \text{ \AA}$, (lower line) and UV spectral range, $\lambda_{\text{lum}} \approx 2600\text{--}3800 \text{ \AA}$ (upper line) measured at $\lambda_1 = 5615.49 \text{ \AA}$ ($\nu_1 = 17807.9 \text{ cm}^{-1}$, T -shaped $\text{NeI}_2(B, 19 \leftarrow X, 0)$ transition). The energy of transitions to the $\text{I}_2(E, \nu_E = 0\text{--}6, J_E = 0)$ states are marked out. Assignments of the $\text{I}_2(E, \nu_E \leftarrow B, \nu_B = 17, 18$ and $\beta, \nu_\beta \leftarrow B, \nu_B = 17)$ transitions are shown. Groups of excitation bands of the $\text{I}_2(\text{IP} \rightarrow \text{valence states})$ luminescence corresponding to the $E, \nu_E = 0\text{--}6$ states are marked out as 0–6 in frames [56]

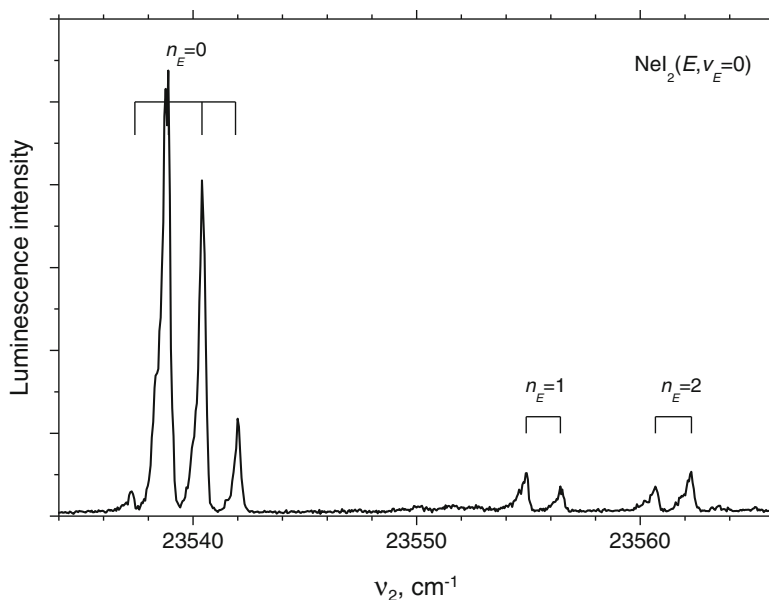


Fig. 6.19 Excitation spectra of luminescence in the in the $\nu_2 = 23522\text{--}23583 \text{ cm}^{-1}$ ($E, \nu_E = 0$ group) corresponding to the $E \rightarrow B$, $\lambda_{\text{lum}} \approx 4284 \text{ \AA}$, (red, gray line) and UV spectral range, $\lambda_{\text{lum}} \approx 2600\text{--}3800 \text{ \AA}$ (black line) at $\nu_1 = 17807.9 \text{ cm}^{-1}$. Assignments of the transitions observed are shown [56]

Table 6.3 The T -shaped $\text{NeI}_2(E, v_E = 0-6)$ complex binding energies (see the text for details)

v_E	$\text{I}_2(E, v_E = 0-6, J_E = 0)$ transition energies, cm^{-1}	$\text{NeI}_2(E, v_E, n_E)$ energies ^b , cm^{-1}	$\text{NeI}_2(E, v_E, n_E)$ ^b binding energies, cm^{-1}	v_D^{max}/br	v_β^{max}/br	v_E^{max}/br	v_γ^{max}/br
0	41355.3	41282.7 ($n_E = 0$)	72.6	3/ 0.58	5/ 0.04	0/ 0.38	–
		41298.7 ($n_E = 1$)	56.6	3/ 0.61	5/ 0.04	0/ 0.35	
		41304.4 ($n_E = 2$)	50.9	3/ 0.65	5/ 0.04	0/ 0.31	
1	41456.3	41383.4	72.9	4/ 0.31	5/ 0.02	1/ 0.67	–
2	41556.9	41483.9	73.0	5/ 0.43	6/ 0.08	2/ 0.49	–
3	41657.0	41583.9	73.1	6/ 0.34	7/ 0.05	3/ 0.54	0/ 0.07
4	41,756,8	41683.6	73.2	7/ 0.38	8/ 0.07	4/ 0.40	1/ 0.05
5	41856.2	41782.9	73.3	7/ 0.37	9/ 0.07	5/ 0.51	1/ 0.03
6	41955.2	41881.8	73.4	9/ 0.49	10/ 0.10	6/ 0.38	2/ 0.02

Maximal vibrational number ($v_{\text{IP}}^{\text{max}}$) of a $\text{I}_2(\text{IP})$ state populated at the $\text{NeI}_2(E, v_E, n_E)$ VP and EP and the branching ratios (br)^a of the $\text{NeI}_2(E, v_E, n_E)$ VP and EP product formation and maximal vibronic state ($v_{\text{IP}}^{\text{max}}$) populated are given [56]

^a br is ratio of integrated partial intensity from selected IP state to the sum of all integrated intensities

^bAll the data have been obtained for $n_E = 0$ except those for $v_E = 0$

separations between maxima of the $\text{I}_2(B, v_B = 13-26 \leftarrow X, 0)$ and $\text{Ar}_n\text{I}_2(B, v_B = 13-26 \leftarrow X, 0)$ bands are $\sim n \cdot 13.4 \text{ cm}^{-1}$ [7, 19].

6.4.3.1 The $\text{ArI}_2(X)$ Complexes

Most recent theoretical and experimental data on dissociation energies of the T -shaped and linear $\text{ArI}_2(X, v_X = 0)$ complexes, topology of PES and energies of vdW levels are presented in [57, 67] (theory, RCCSD(T) calculations), [10, 30, 68] (experiment). The principal results are as follows:

- the potential well depths are $D_e^{X,0} = 268 \text{ cm}^{-1}$ (linear) and 235 cm^{-1} (T -shaped) [57];
- the $R_e^{X,0}$ equilibrium distance values $R_e^{X,0} = 5.05 \text{ \AA}$ (linear) and 3.96 \AA (T -shaped) [57];
- binding energies of the $n_X = 0$ vdW level are $D_0^{X,0} = 237.8$ [57], 250(2) [68], 250.3(2.7) cm^{-1} [10] (linear) and 212 [57], 240.5(3.6) cm^{-1} [10] (T -shaped);

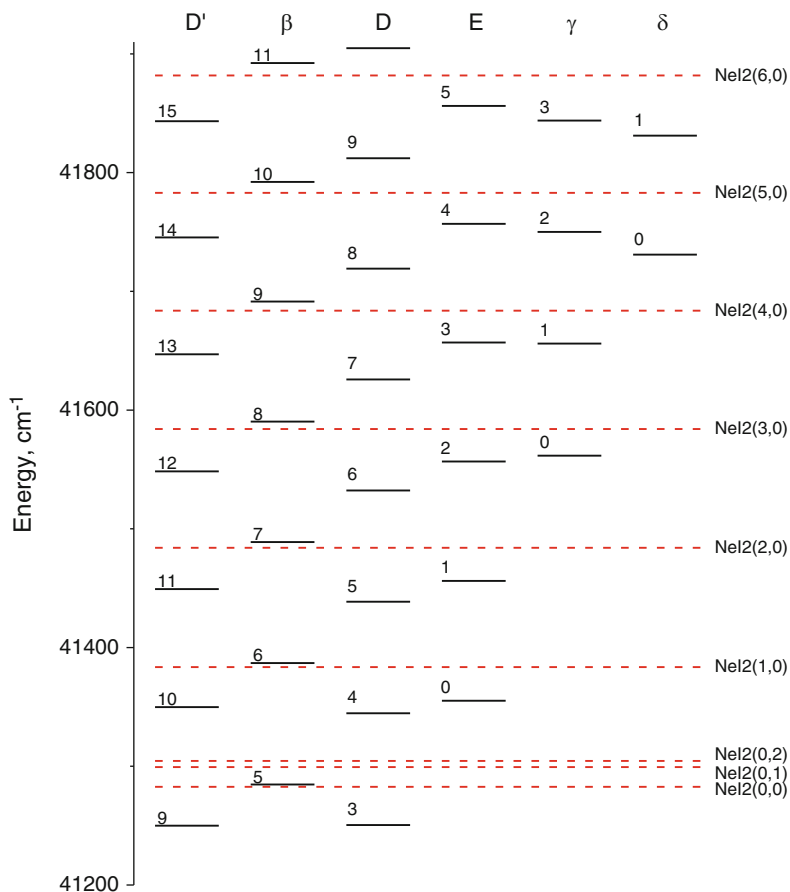


Fig. 6.20 Energies of the I₂(IP, v_{IP}, J_{IP} = 5) rovibronic levels of the first-tier iodine molecule IP states, IP = D', β, D, E, γ, δ and calculated relative to that of I₂(X,0,4). Vibrational quantum numbers of the states are indicated. Positions of NeI₂(E, v_E, n_E ← B, 19, n_B = 0) vibrational progression terms are also shown [56]

- the $R_e^{X,0}$ equilibrium distance values are $R_e^{X,0} = 5.05 \text{ \AA}$ (linear) and 3.96 \AA (*T*-shaped) [57];
- the $n_X = 0$ and 1 ($E = -237.8$ and -213.7 cm^{-1}) vdW levels are localized in the linear well, whereas $n_X = 2$ one ($E = -212 \text{ cm}^{-1}$) is localized in the *T*-shaped well (Fig. 6.22) One should note that similar feature is observed at the HeI₂(*X*) complex (see Sect. 6.4.1.1).
- the high, $E = 132 \text{ cm}^{-1}$ above the global (linear) minimum, isomerization barrier presents at $R \approx 4.92 \text{ \AA}$, $\Theta \approx 52.3^\circ$, and lowest vdW vibrational states are expected to be mostly localized in either linear ($n_X = 0, 1$) or *T*-shaped ($n_X = 2$) wells [57];
- the ω_e values are equal to 24.0 (linear) and 26.5 (*T*-shaped) cm^{-1} [57].

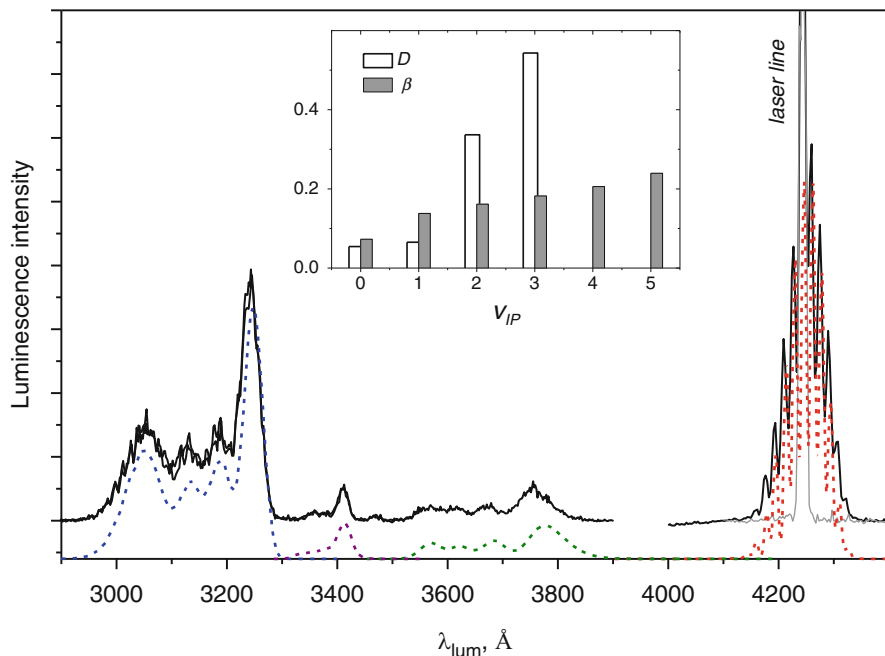


Fig. 6.21 Experimental (solid line) and simulated (broken line) luminescence spectra in the $\lambda_{lum} = 2900\text{--}4400$ Å spectral range at the zero group of bands, $\text{NeI}_2(E, 0, n_E = 0)$, $\nu_1 = 17807.9$ cm^{-1} , $\nu_2 = 23538.84$ cm^{-1} . Spectral resolution FWHM = 10 Å. Experimental spectrum is offset for clarity. Populations of the D, v_D and β, v_β vibronic states are given in the inset [56]

6.4.3.2 The $\text{ArI}_2(B)$ Complexes

Structure, energetic, and PESs of the T -shaped Isomer According to experimental data and results of calculations known to date, there is only one minimum in the $\text{ArI}_2(B)$ complex PES along the angular coordinate around the I_2 molecule which corresponds to the T -shaped isomer. The binding energy is $D_0^{B, v_B} \approx 227$ cm^{-1} for all studied v_B (Fig. 6.23, see [12] and references).

To the best of our knowledge, there are no results of *ab initio* calculations of the $\text{ArI}_2(B)$ PES in the literature, and the PES has been calculated using several versions of semiempirical diatomics-in-molecule (DIM) method [7]. The $R_e^{B, 0} = 3.83$ Å as well as ω_e values for stretching (~ 33.2 cm^{-1}) and bending (~ 18.5 cm^{-1}) modes have been calculated in [44]. Besides, it has been shown that $R_e^{B, 22}$ value lies in the 3.7–4.5 Å range; it is likely that $R_e^{B, 22} = 4.02$ Å and $R_e^{X, 0} = 4.00$ Å [44]. The latter is similar to the $R_e^{X, 0} = 3.96$ Å (T -shaped) [57]. An analysis of the literature data (see [7, 12, 30, 31, 44, 69] and references) has shown that the $\text{ArI}_2(B, v_B, n_B \leftarrow X, 0, n_X = 2)$ transitions in the T -shaped conformer occur for low n_B . Since

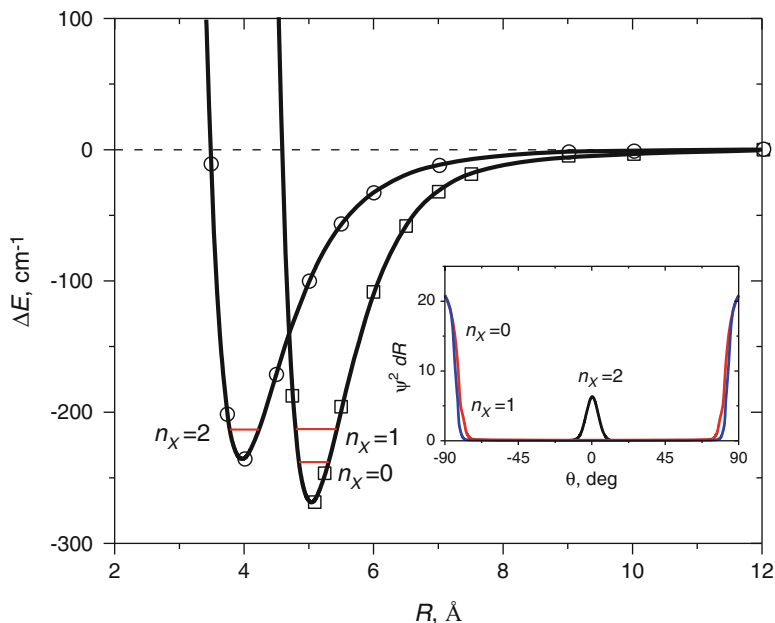


Fig. 6.22 Potential energy curves for the $\text{ArI}_2(X)$ complex. *Ab initio* results are indicated by open circles for linear isomer ($\Theta = 0^\circ$) and squares for T -shaped isomer ($\Theta = 90^\circ$). The $\int \Psi^2 dR$ distributions for the eigenfunctions corresponding to the $n_X = 0, 1, 2$ vibrational vdW levels are given in the insert [57]

both $\text{ArI}_2(X$ and $B)$ PESs are similar near the bottom of the T -shaped well, the Franck–Condon principle implies that the transition probability from the $n_X = 2$ level has to be largest for $n_B \approx 0$ and rapidly decreases with n_B ; transitions to the first three $n_B \approx 0$ –2 states are the strongest (see [7] and references).

The Photodecay Dynamics of the T-shaped Isomer: The Vibrational Predissociation Including Intramolecular Vibrational Redistribution and Electronic Predissociation All these channels of $\text{ArI}_2(B)$ decay are observed. Luminescence of the $\text{ArI}_2(B, v_B - \Delta v_B)$ lacks for the $v_B \leq 11$ levels since, as it assumed, rate of EP is much larger than that of VP (one should note ratio of rate constants of vibrational relaxation to electronic predissociation in the $\text{I}_2(B, v_B) + \text{Ar}$ collisions is approximately independent of v_B in the $v_B \approx 6$ –25 range [70]). The VP compete with the EP , and vibrational predissociation efficiencies, $\Delta v_B \geq 3$, show strong oscillations over the $v_B \approx 12$ –26 range for $n_B = 0$ [19, 20, 71]. Similar oscillations were observed for the $\text{ArI}_2(B, v_B, n_B = 1, 2 \leftarrow X, 0, n_X = 2)$ excitation pathway (see [20] and Fig. 6.24).

The $\text{ArI}_2(B)$ EP may be due to the $\text{ArI}_2(B - a1_g)$ coupling in the T -shaped isomer according to selection rule, and the EP rate has to oscillate with v_B due to oscillation of FCD for B/a states (see [7, 72] and references). According to data of [72], the

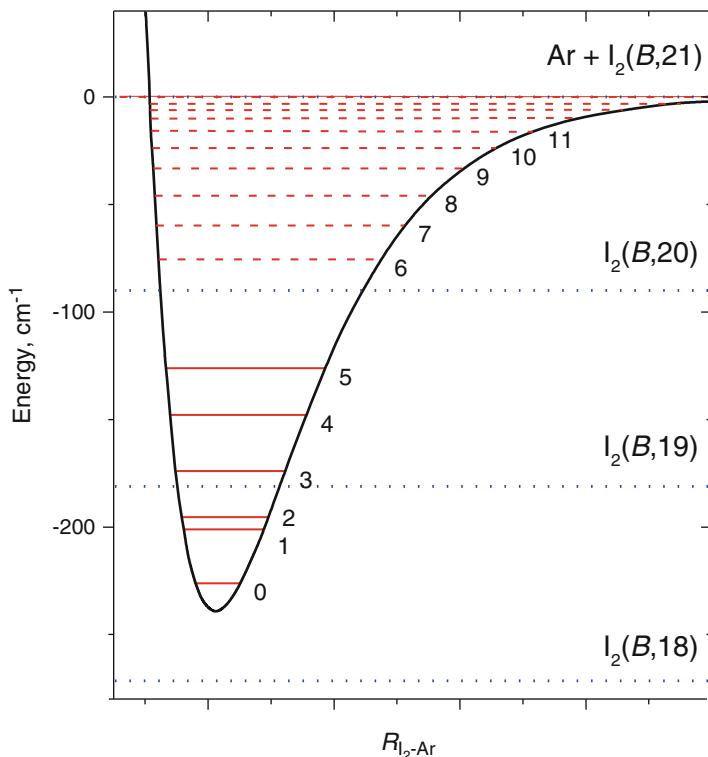


Fig. 6.23 Schematic of the $\text{ArI}_2(B, v_B = 21, n_{21})$ bound intermolecular vibrational levels. The levels marked as solid and dashed lines represent the states localized in the T -shaped well and those corresponding to the linear regions of the $\text{ArI}_2(B, v_B = 21, n_{21})$ PES, respectively. The $n_{21} = 0-3$, $3-5$ and ≥ 6 states decay via the $\Delta v_B = 3$, 2 and 1 channels, respectively. The $n_{21} = \geq 6$ energy levels likely resemble hindered, internal rotor states with the Ar atom delocalized about the I_2 molecule (see [12])

$\text{ArI}_2(B)$ EP is due to the $\text{ArI}_2(B - RS)$, $RS = a'0_g^+$, $a1_g$, $(1)2_g$ (and $C1_u$, in a less degree) coupling (see Sect. 5.3.1). The coupling with the $a'0_g^+$ and $(1)2_g$ states is valid since large amplitude vibration occurs at the $\text{ArI}_2(B, v_B)$ corresponding to non- T -shaped geometries. Oscillations of Franck-Condon densities for the RS states are out of phase, so total $FCD(B/RS) = f(v_B)$ function can be smooth (see [7, 72] and references).

The VPE oscillations are due to IVR in the sparse limit, corresponding to the case when half-widths of the bound $\text{ArI}_2(B, v_B, n_B)$ levels are less than a value of the vdW quantum. The IVR results from quasi-degeneracy between the initial excited state (“bright state”) $\text{ArI}_2(B, v_B, n_B^b)$ and intermediate zero-order “dark states” with less $\text{I}_2(B)$ vibrational excitation and more vdW bending and stretching energy, $\text{ArI}_2(B, v_{B-1}$ or $v_{B-2}, n_B^d \geq n_B^b)$. The vibrational coupling induced by the argon atom mixes these zero-order quasi-degenerate states, which leads to a population to the dark

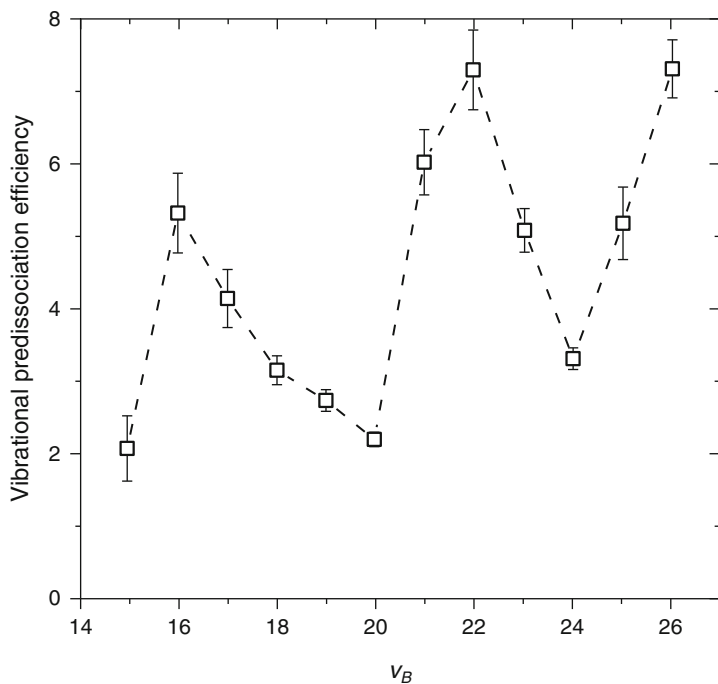


Fig. 6.24 Vibrational predissociation efficiencies (VPE) for the $\text{ArI}_2(B, v_B, n_B = 0 \leftarrow X, 0, n_X = 2)$ (T -shaped) transitions plotted as function of the v_B [20]

states. These, in turn, provide to the $\text{ArI}_2(B - RS)$ coupling [7, 73, 74]. The IVR leads to loss 4 $I_2(B, v_B)$ vibrational quanta at high v_B levels and bimodal rotational distribution of the $I_2(B, v_B - 3)$ VP product [5].

The information given above concerns the decay of the low, $n_B = 0-2$ states. At higher, $n_B = 3-5$ states, the $\Delta v_B = 2$ channel become energetically available. The $n_B \geq 6$ states corresponding to the linear regions of the $\text{ArI}_2(B, v_B, n_B)$ PES , likely resemble hindered, internal rotor states with the Ar atom delocalized about the I_2 molecule. The $\Delta v_B = 1$ channel becomes energetically available there (see [12] and Fig. 6.23).

The Photodecay Dynamics of the Linear Isomer According to Franck-Condon principle, the transition to the linear $\text{ArI}_2(B)$ isomer PES occur from the the $n_X = 0$ and 1 ($E = -237.8$ and -213.7 cm^{-1}) vdW levels localized in the linear well ($R_e^{X,0} = 5.05 \text{ \AA}$), see Sect. 6.4.3.1. The transitions occur to the left branch of the $\text{ArI}_2(B)$ PES , and continuum excitation spectra correspond to them [5, 7, 21, 30, 63, 69]. The $I_2(B \rightarrow X)$ luminescence intensity integrated over transitions of linear isomer is 2.1 times higher that total integrated luminescence intensity of the T -shaped isomer, though the intensities at any selected wavelength is ~ 15 times weaker than the peak intensity of the T -shaped isomer, since the excitation is continuum-like. Wide ranges of the $I_2(B, v_B - \Delta v_B)$ states (from $v_B = 12$ to 23 with maximal population at the $v_B = 18$ level for the $\text{ArI}_2(B, v_B = 26 \leftarrow X, 0)$ transition

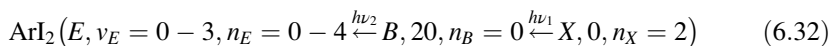
[21]) are populated. Rotationally cold $I_2(B, \nu)$ fragments, $T_{rot} \approx 5$ K, consistent with direct dissociation from a near-linear geometry are observed [5].

The One-Atom Cage Effect. This effect is subject to numerous studies since 1981, when Saenger *et al.* have found it [75] (see [76], also). When the $RgI_2(B)$ complex is above the $I_2(B)$ dissociation limit, large range of the $I_2(B, \nu_B)$ molecules ($23 \leq \nu_B \leq 49$ for $ArI_2(B)$ at $\lambda_{ex} = 488$ nm) is produced. Similar wide vibrational distributions than those of observed in VP were observed at the bound part of the $RgI_2(B)$ PES s, also. Many contradictory hypotheses have been discussed. Now, this effect is interpreted as the purely kinematic (ballistic) mechanism, i.e. it is due to the collision of the dissociating I atom with the argon atom near the linear configuration which leads to stabilization of a $I_2(B)$ molecule [5, 7, 20, 30].

6.4.3.3 The $ArI_2(IP)$ Complexes

To the best of our knowledge, there were no experimental or theoretical data on $ArI_2(IP)$ vdW until the work [31] in which the $ArI_2(E0_g^+)$ complexes have been observed and studied for the first time using the experimental setup and methods described in Sect. 6.2.

The complexes were populated in the



excitation pathway (T -shaped isomer) in the (~ 41250 – 41720 cm^{-1}) complex energy range.

Binding energy of the T -shaped $ArI_2(X, 0)$ is $D_0^X = (240.5 \pm 3.6)$ cm^{-1} Energy gap between maxima of transitions to the $I_2(B, 20)$ and $ArI_2(B, 20)$ is 14 cm^{-1} , and energy of the T -shape $ArI_2(B, 0)$ is $D_0^B = 226.5$ cm^{-1} (see Sect. 4.3.1). The $ArI_2(E)$ complex term energy (upper x -axis in Figure 6.25) relative to that of the $I_2(X, \nu_X = 0, J_X = 0)$ is $\nu_1 + \nu_2 - D_0^X = \nu_2 + 17905.9 - 240.5 = \nu_2 + 17665.4$ cm^{-1} . Four, $ArI_2(E, \nu_E = 0-3 \leftarrow B, 20)$ progressions corresponding to stretching vdW modes were found. The $ArI_2(E, \nu_E = 0-3 \leftarrow B, 20)$ transitions are the strongest in the spectral range under study. It follows the $\Delta\Omega = 0$ propensity rule. No progressions corresponding to transitions to other $ArI_2(IP)$ states have been found. Therefore, Ar atom, as $Rg = He, Ne$ and Kr (see Sect. 6.4.4) behaves as “spectator”, and propensity rules for the $ArI_2(IP - B)$ transitions are the same as for the isolated I_2 molecule (see Chap. 3) (Table 6.4).

Experimental luminescence spectra are simulated well as transitions in a free iodine molecule (see Fig. 6.26). Relative populations of the D, D' and β states as well as those of their vibronic levels depend significantly on ν_2 . The larger ν_2 value is, the higher vibronic levels of IP states which populated in EP of the $ArI_2(E, \nu_E)$ complexes and following VP of the $ArI_2(IP, \nu_{IP})$ complexes are [77].

Partial intensities of the $I_2(E \rightarrow B)$ transitions at each excitation lines corresponding to population of the $ArI_2(E)$ complexes are much less than those

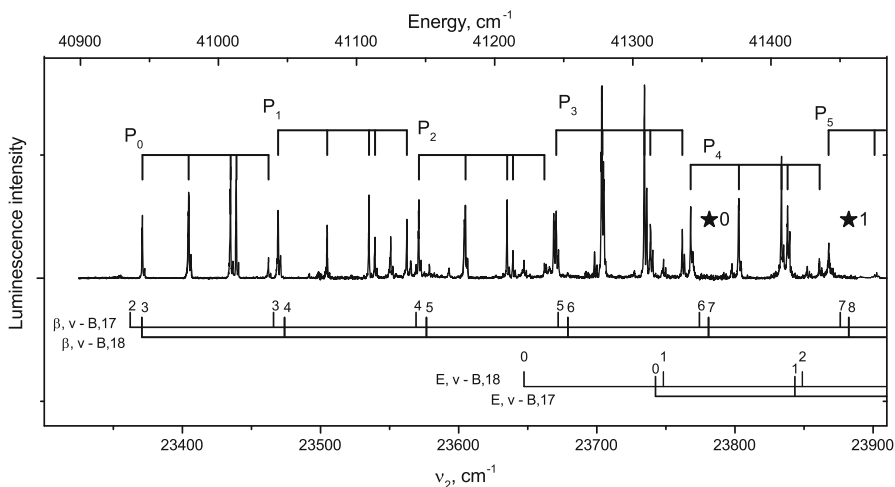


Fig. 6.25 Excitation spectra of luminescence in the $\lambda_{\text{lum}} \approx 2600\text{--}3800 \text{ \AA}$ spectral range in the He + Ar mixture; $\nu_1 = 17804.94 \text{ cm}^{-1}$. Dissociation limits of the $\text{RgI}_2(E, \nu_E)$ complexes are marked out by stars. Assignments of the transitions in free I_2 and discovered vibrational progressions correlating with the $\text{Ar} + \text{I}_2(E, \nu_E)$ limits are shown

Table 6.4 Energy gaps between adjacent terms of the progressions $P_i(j+1) - P_i(j)$ for ArI_2

	P_0	P_1	P_2	P_3	P_4
$P_v(1) - P_v(0), \text{ cm}^{-1}$	33.5(1)	35.5(1)	33.8(1)	33.5(1)	34.9(1)
$P_v(2) - P_v(1), \text{ cm}^{-1}$	30.3(1)	30.3(1)	30.1(1)	30.4(1)	31.0(1)
$P_v(3) - P_v(2), \text{ cm}^{-1}$	4.2(1)	4.4(1)	4.2(1)	4.3(1)	4.3(1)
$P_v(4) - P_v(3), \text{ cm}^{-1}$	23.3(1)	23.1(1)	22.8(1)	23.1(1)	23.3(1)
$D_0^E(\nu), \text{ cm}^{-1}$	410.4(2)	413.1(2)	411.8(2)	412.6(2)	415.0(2)

The binding energies of the $\text{ArI}_2(E, \nu_E = 0\text{--}4, n_E = 0)$ complexes, D_0^{E, ν_E} , are equal to differences between calculated dissociation limits of the $\text{ArI}_2(E, \nu_E = 0\text{--}7)$ complexes and the origins of the progressions discovered [77]

of the total $\text{I}_2(D \rightarrow X, \beta \rightarrow A$ and $D' \rightarrow A')$ transitions (Fig. 6.26). Therefore, the rate of VP of the $\text{ArI}_2(E, \nu_E = 0\text{--}3)$ complexes is ~ 10 times lower than those of EP to the $\text{ArI}_2(\text{other IP})$ states.

6.4.3.4 The Rydberg ArI_2 vdW Complexes

Mass-resolved one-color $(2 + 1)\text{REMPI}$ spectroscopy (see Sect. 2.1.7 and 3.4) was used to study the $X[1/2]_c 6s$ and $X[3/2]_c nd, n = 5, 6$, Rydberg states of the ArI_2 vdW complex in the $\sim 53000\text{--}55000 \text{ cm}^{-1}$ and $\sim 62250\text{--}64000 \text{ cm}^{-1}$ energy range, respectively. The long vibrational progression and the increased vibrational spacing, 240 cm^{-1} , over that of the ground electronic state, 214 cm^{-1} , is indicative

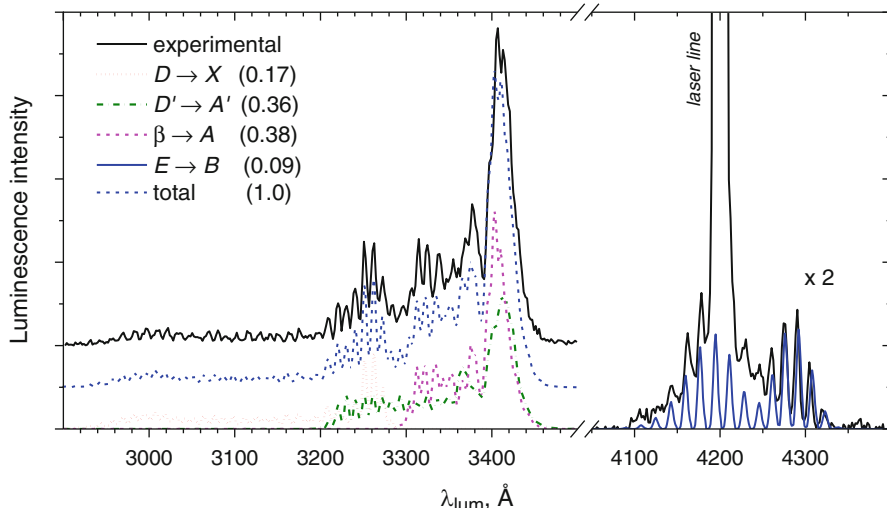


Fig. 6.26 Luminescence spectra in the $\lambda_{lum} = 2900\text{--}3500\text{ \AA}$ and $4100\text{--}4350\text{ \AA}$ spectral ranges at $\nu_2 = 23811.1\text{ cm}^{-1}$; $\nu_1 = 17905.9\text{ cm}^{-1}$ ($\text{ArI}_2(B,20 \leftarrow X,0)$ transition). Spectral resolution FWHM = 5 \AA . Partial luminescence intensities of the transitions are given [31]

of a reduction in equilibrium bond length upon excitation to the Rydberg state due to a removal of non-bonding with some antibonding character π_g electron. Two, *T*-shaped and linear isomers of the complexes were observed (see [78] and references).

6.4.4 The KrI_2 vdW Complexes

6.4.4.1 The $\text{KrI}_2(\text{IP})$ vdW Complexes

To the best of our knowledge, nobody observed luminescence of the products of the $\text{KrI}_2(B)$ complex *VP*, since its *EP* rate is much larger than that of *VP*, probably. The KrI_2 complexes have been studied in [19] (intracavity absorption spectroscopy), theoretically [9] and in rare-gas matrixes (see [9] and references). The $\text{KrI}_2(X$ and $B)$ well depths were estimated in [79] as 294 and 278 cm^{-1} , respectively. Dissociation energies and some spectroscopic constants of the $\text{KrI}_2(X)$ linear and *T*-shaped isomers had been calculated in [9] using the MP2 and CCSD(T) methods. It was shown in [19] that energy gap between the $\text{I}_2(B, \nu_B \leftarrow X, 0)$ and $\text{KrI}_2(B, \nu_B \leftarrow X, 0)$ bands is $\sim 13\text{ cm}^{-1}$. The same value has been obtained in [58] (see below).

Some spectroscopic characteristics of the $\text{KrI}_2(X, B, E)$ complexes as well as branching ratios of the $\text{KrI}_2(E)$ *VP* and *EP* decay channels and vibrational populations of the *VP* and *EP* products have been studied [58, 77] using the experimental setup and methods described in Sect. 6.2. The complexes were populated in the

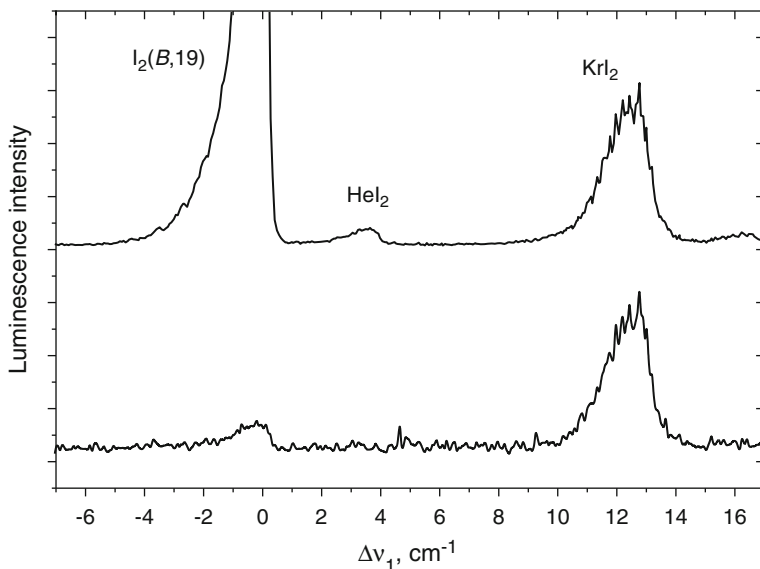
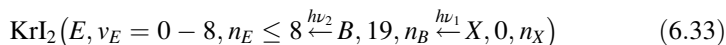


Fig. 6.27 Action spectra of luminescence of the $I_2(B,19)$ and products of VP of the $HeI_2(B,19)$, $KrI_2(B,19)$ complexes; $\lambda_{lum} = 4294 \text{ \AA}$ (lower spectrum) and $\lambda_{lum} \approx 2600\text{--}3800 \text{ \AA}$ (upper spectrum), $\nu_2 = 23933.3 \text{ cm}^{-1}$. Positions of the $HeI_2(B,19)$ and $KrI_2(B,19)$ bands are shown [58]



excitation pathway (T -shaped isomer) in the ($\sim 41000\text{--}41850 \text{ cm}^{-1}$) complex energy range.

The $KrI_2(B,19)$ band of action spectra is narrow and very similar to those of transitions in the $HeI_2(B, \nu_B)$ and $ArI_2(B, \nu_B)$ T -shaped complexes, and corresponds to transition in the T -shaped complex. Spectral separation between wavenumbers of this and the $I_2(B,19) h\nu_1 h\nu_1 X, 0$ transition is $\sim 13 \text{ cm}^{-1}$ (Fig. 6.27) similar to observed in [19].

Survey excitation spectra of luminescence in the UV spectral range, $\lambda_{lum} \approx 2600\text{--}3800 \text{ \AA}$ at $\nu_1 = 17814.39 \text{ cm}^{-1}$ measured at the He + Kr mixture and pure He are presented in Fig. 6.28. Luminescence at the $\lambda_{lum} \approx 2600\text{--}3800 \text{ \AA}$ spectral range corresponds to the $I_2(D \rightarrow X, \beta \rightarrow A$ and $D' \rightarrow A')$ transitions.

The $KrI_2(X, 0; B, 19$ and $E, \nu_E = 0\text{--}8, n_E = 0)$ binding energy are ~ 320 , ~ 307 and $\sim 663\text{--}683 \text{ cm}^{-1}$, respectively. The $KrI_2(IP)$ complex term energy (upper x-axis in Fig. 6.28) relative to that of the $I_2(X, \nu_X = 0, J_X = 0)$ is $\nu_1 + \nu_2 - D_0^X = \nu_2 + 17814.4 - 320 = \nu_2 + 17494.4$. Seven $I_2(E, \nu_E)$ vibrational quanta have to be lost for the $KrI_2(E, \nu_E, n_E) VP$. The $\omega_e = 34.7 \text{ cm}^{-1}$ value for $P_0(n_E)$ progression is larger than those of for $P_1(n_E) - P_7(n_E)$, and nature of this feature is unknown at the moment. Besides, energy interval between $P_1(0)$ and $P_0(0)$ terms, 93 cm^{-1} , is less than that of $I_2(E, 1 - E, 0)$, 101.1 cm^{-1} (see Appendix) due to perturbation caused by a Kr atom. The $I_2(E, \nu_E = 0\text{--}1)$, $I_2(D', \nu_{D'} = 3\text{--}10)$, $I_2(\beta, \nu_\beta = 0\text{--}6)$ and

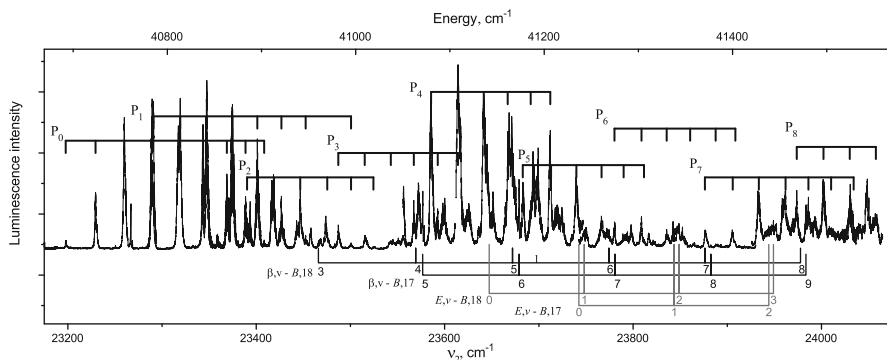


Fig. 6.28 Excitation spectra of luminescence in the UV spectral range, $\lambda_{\text{lum}} \approx 2600\text{--}3800 \text{ \AA}$ at $\nu_1 = 17814.39 \text{ cm}^{-1}$, ($\text{KrI}_2(B,19 \leftarrow X,0)$ transition) measured at the He + Kr mixture. Assignments of the $\text{I}_2(E,\nu_E \leftarrow B,\nu_B)$ and $\beta,\nu_\beta \leftarrow B,\nu_B$ transitions and discovered $\text{KrI}_2(E,\nu_E,n_E \leftarrow B,19,n_B)$ vibrational progressions correlating with the Kr + $\text{I}_2(E,\nu_E = 0\text{--}8)$ limits are shown [58]

$\text{I}_2(D,\nu_D = 4\text{--}5)$ are products of the $\text{KrI}_2(E,\nu_E = 0\text{--}8,n_E)$ *VP* and *EP*. The $\text{KrI}_2(E,\nu_E, n_E) \rightarrow \text{Kr} + \text{I}_2(\beta,\nu_\beta = 0\text{--}6)$ is the principal channel of the complex decay, branching ratios, $b.r. = 0.4\text{--}0.7$. The *VP* branching ratios is $b.r. \leq 0.23$.

The authors try to describe vibrational populations of the *VP* and *EP* products using the models of direct coupling of the initially excited bound level $\text{KrI}_2(E,\nu_E, n_E)$ with quasi-continuum states $\text{Kr} + \text{I}_2(\text{IP},\nu_{\text{IP}})$ (“direct *EP*”) or a sequential multistep process including *IVR* and non-adiabatic $\text{RgI}_2(E \rightarrow \text{IP})$ transition (“*EP* + *IVR*”) (see [80, 81] and references). The models are able to tend the main features of the vibrational population of the *EP* products, only.

6.4.4.2 The Rydberg KrI_2 vdW Complexes

Mass-resolved one-color (2 + 1)REMPI spectroscopy (see Sect. 2.1.7 and 3.4) was used to study the $X[3/2]_c 5d \Omega_g$ ($\Omega = 0, 2$) Rydberg states of the KrI_2 vdW complex in the $\sim 61900\text{--}63800 \text{ cm}^{-1}$ energy range [82]. Anharmonic progressions of the vdW stretching mode with $\omega_e = 49$ and 47 cm^{-1} values for the $X[3/2]_c 5d 0_g$ and $X[3/2]_c 5d 2_g$ states, respectively, were observed.

6.4.5 The XeI_2 vdW Complexes

Information on the XeI_2 vdW complexes is very scarce. They have been studied by intractivity absorption spectroscopy method [19], theoretically [9] and in rare-gas matrixes (see [9] and references). The $\text{XeI}_2(X$ and $B)$ well depths were estimated in

[80] as 348 and 330 cm^{-1} , respectively. Dissociation energies and some spectroscopic constants of the $\text{XeI}_2(X)$ linear and T -shaped isomers were calculated in [9] using the MP2 and CCSD(T) methods. It was shown in [19] that energy gap between the $\text{I}_2(B, v_B \leftarrow X, 0)$ and $\text{XeI}_2(B, v_B \leftarrow X, 0)$ is $\sim 13\text{ cm}^{-1}$.

The authors tried to “catch” XeI_2vdW complexes by the way which was successfully utilized for a study of the KrI_2 vdW complexes but failed. Maybe, it is due to very fast EP of the $\text{XeI}_2(B)$ complexes.

6.5 The Principal Features of Decay of the Electronically-Excited RgI_2 vdW Complexes Populated in Collisions and Optically

It is fascinating to analyze decay of the $\text{RgI}_2(B)$ and $\text{RgI}_2(E)$ vdW complexes which formed in $\text{Rg} + \text{I}_2$ collisions or optical transitions. These are:

- collision-induced predissociation (CIP) of the $\text{I}_2(B)$ molecules (see Sect. 5.3.1);
- collision-induced non-adiabatic transitions (CINATs) of the $\text{I}_2(E)$ molecules (see Sect. 5.3.2);
- electronic predissociation of the $\text{RgI}_2(B)$ complexes;
- electronic predissociation of the $\text{RgI}_2(E)$ complexes.

The $\text{RgI}_2(B)$ Complexes. The CIP rate constants for $\text{Rg} = \text{He} - \text{Xe}$ smoothly increase with v_B . For $\text{Rg} = \text{He}$, e.g., it is $\sim 5 \cdot 10^{-12}\text{ cm}^3/\text{s}$ ($v_B = 6$) – $10^{-10}\text{ cm}^3/\text{s}$ ($v_B = 50$) and increase in the He - Xe row due to increase of Rg polarizability. It has been established that the $\text{RgI}_2(B0_u^+)$ complex predissociates due to coupling with *gerade* $\text{RgI}_2(a1_g, a'0_g^+)$ and $(1)2_g$ repulsive states, see Sect. 5.3.1. Collision-induced

$\text{I}_2(B, v_B, J_B \xrightarrow{\text{Rg}} B, v_B \pm \Delta v_B, J_B \pm \Delta J_B)$ $V, R-T$ processes occur also. The authors could not optically populate the $\text{XeI}_2(E)$ complexes via the $\text{XeI}_2(B)$, probably, due to a high rate of EP of the latter, though relative ratios of rate constants of the CIP and $V, R-T$ processes do not differ dramatically on the Rg nature [70]. CIP rate is much less than that of $V, R-T$ processes for $\text{Rg} = \text{He}$, and quantum yield of the optically populated $\text{HeI}_2(B)$ VP is ~ 1 . Quantum yield of the optically populated $\text{ArI}_2(B, v_B)$ VP depends on v_B . For $\text{Rg} = \text{Kr}, \text{Xe}$, it is negligibly small.

The $\text{RgI}_2(E)$ Complexes. The experimental and theoretical studies clearly identify two mechanisms for CINAT between the IP states of iodine molecule – “*approach-induced*” for collisions with molecular partners possessing large electric permanent quadrupole moments, permanent dipole moment, transition dipole moment, and more common “*collision-induced*” one for collisions with rare gas atoms.

The following principal features have been found out for the non-adiabatic transitions induced by collisions with rare gas atoms:

- CINAT cross-sections, $\sigma = k/V$, are *appr.* Independent of Rg nature, except Rg = Xe, for which reactive quenching is the dominant channel in the $I_2(E) + Xe$ collisions.
- The “parallel” $E \leftrightarrow D$ ($\Omega_g \leftrightarrow \Omega_u$) transitions with $\Delta\Omega = 0$ are dominant for Rg = He. For Rg = Ar – Xe, all the electronic states of the first tier are populated in CINATs from the E states in a statistical way and total, for all β , D' , γ and δ states, rate constant is higher than that of corresponding to the D state.
- Vibrational populations of the final states depend on Rg. It is resonant and narrow for He and broad for other Rg atoms.
- CINAT rate constants smoothly increases with initial vibrational excitation of the E state;
- The large difference of the CINAT branching ratios is explained by the different behavior of the potential curves. The dipole polarizability of the He atom is $0.2 \cdot 10^{-24} \text{ cm}^3$, whereas for Ar – Xe, they are about one order of magnitude larger, $1.6 - 4.0 \cdot 10^{-24} \text{ cm}^3$. Since the dipole polarizability determines the magnitude of the long-range interaction, the depth of the He- I_2 PES is much smaller than the mean thermal energy at 300 K, while the Ar- I_2 interaction strength approaches 240 cm^{-1} . Also, the mean collision velocity is smaller for heavier Rg atoms. Both factors increase the mean collision time and favor statistical population of the CINAT channels for Rg = Ar – Xe.

The following principal features have been found after study of the optically populated $RgI_2(E)$ complexes:

- The binding energies of the $RgI_2(X, B \text{ and } E)$ complexes increase in the He – Kr row, $D_0^X \approx 16$ (He), 64 (Ne), 240 (Ar), 320 (Kr); $D_0^B \approx 12.5$ (He), 57 (Ne), 227 (Ar), 307 (Kr); $D_0^E \approx 14.0$ (He), 73 (Ne), 410 (Ar), 670 (Kr), units, cm^{-1} . It is due to increase of polarizability in this row (Fig. 6.29).
- The EP is the principal channel of the $RgI_2(E)$ decay, Rg = Ar, Kr. For He, Ne probabilities of the VP and EP are comparable. Relative probabilities of different EP channels depend on Rg: the He + $I_2(D)$ channel is the principal for light, He, Ne, atoms and of minor importance for Ar, Kr, for which Rg + $I_2(\beta)$ channel is the principal. The Rg + $I_2(D')$ channel has a appreciable probability for Ar and Kr.
- The propensity rule for optical transitions in the RgI_2 vdW complexes, $u - g$, is the same as selection rule for a homonuclear diatomic molecule, i.e. Rg acts as a “spectator”, and $RgI_2(D0_u^+, D'2_g \leftarrow B0_u^+)$ transitions allowed in the C_{2v} and $C_{\infty v}$ symmetry groups are not observed.
- One should note, that the $HeI_2(E0_g^+ \leftrightarrow D0_u^+)$ non-adiabatic transition is forbidden at the C_{2v} symmetry group ($HeI_2(A_1 \leftrightarrow B_2)$). It may be allowed due to vibronic or rotational perturbations. The similar features occur for the $ArI_2(B0_u^+)$ EP which is due to perturbation by the $ArI_2(a1_g, a'0_g^+)$ and $(1)2_g$ states and in

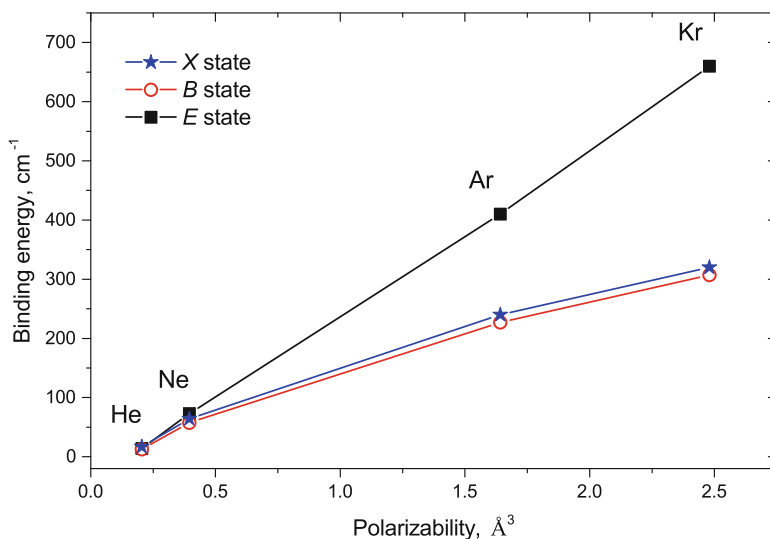


Fig. 6.29 Binding energies of the $RgI_2(X, B$ and $E)$ vdW complexes as functions of the Rg polarizability

- the $I_2(E0_g^+ \xleftrightarrow{He} D0_u^+)$ CINATs. For He, the latter is the principal channel which follows $u \leftrightarrow g$ propensity rule due to high long-range electrostatic interaction.
- The T -shaped $RgI_2(E \rightarrow B)$, $Rg = He, Ne$, luminescence occur.

References

1. Blaney, B.L., Ewing, G.E.: Van der Waals molecules. *Annu. Rev. Phys. Chem.* **27**, 553–586 (1976)
2. Glossary of terms used in physical organic chemistry (IUPAC Recommendations 1994). *Pure Appl. Chem.* **66**, 1077–1184 (1994)
3. IUPAC: Compendium of Chemical Terminology. In: McNaught, A.D., Wilkinson, A. (eds.) *The Gold Book*, 2nd edn. Blackwell Scientific Publications, Oxford (1997)
4. Smalley, R.E., Levy, D.H., Wharton, L.: The fluorescence excitation spectrum of the HeI_2 van der Waals complex. *J. Chem. Phys.* **64**, 3266–3275 (1976)
5. Burroughs, A., Heaven, M.C.: Dissociation dynamics of $I_2(B)$ -Ar: Rotational population distributions of $I_2(B,v)$ fragments from T-shaped and linear complexes. *J. Chem. Phys.* **114**, 7027–7035 (2001)
6. Rohrbacher, A., Halberstadt, N., Janda, K.C.: The dynamics of noble gas-halogen molecules and clusters. *Annu. Rev. Phys. Chem.* **51**, 405–433 (2000)
7. Buchachenko, A.A., Halberstadt, N., Lepetit, B., Roncero, O.: $Ar \cdots I_2$: a model system for complex dynamics. *Int. Rev. Phys. Chem.* **22**, 153–202 (2003)

8. Ray, S.A., McCoy, A.B., Glennon, J.J., Darr, J.P., Fesser, E.J., Lancaster, J.R., Loomis, R.A.: Experimental and theoretical investigation of the $\text{He}^{\cdots}\text{I}_2$ rovibronic spectra in the $\text{I}_2\text{B-X}$, 20—0 region. *J. Chem. Phys.* **125**, 164314–164319 (2006)
9. Pakhira, S., Das, A.K.: Spectroscopy and dissociation of $\text{I}_2\text{-Rg}$ (Rg = Kr and Xe) van der Waals complexes. *Theor. Chem. Accounts.* **130**, 95–101 (2011)
10. Wey, J., Makarem, C., Reinitz, A.L., Darr, J.P., Loomis, R.A.: Accurate measurement of the T-shaped and linear $\text{Ar}^{\cdots}\text{I}_2(\text{X}, \nu'=0)$ binding energies using vibronic-specific $\text{I}_2(\text{B}, \nu)$ fragment velocity-map imaging. *Chem. Phys.* **399**, 172–179 (2012)
11. Darr, J.P., Loomis, R.A.: Dissociation dynamics of higher-order $\text{He}_2^{\cdots}\text{I}^{35}\text{Cl}(\text{B}, \nu' = 3)$ complexes. *Chem. Phys. Lett.* **586**, 34–39 (2013)
12. Makarem, C., Loomis, R.A.: Spectroscopic identification of the $\text{Ar}^{\cdots}\text{I}_2(\text{B}, \nu')$ potential. *Chem. Phys. Lett.* **651**, 119–123 (2016)
13. Akopyan, M.E., Novikova, I.Y., Poretsky, S.A., Pravilov, A.M.: Rare gas-iodine complexes in the ion-pair states. *Chem. Phys.* **310**, 287–295 (2005)
14. Akopyan, M.E., Buchachenko, A.A., Lukashov, S.S., Novikova, I.Y., Poretsky, S.A., Pravilov, A.M.: Resonant optical excitation of the I_2 ion-pair states through the RgI_2 complexes in the valence states correlating to the $^2\text{P}_{1/2} + ^2\text{P}_{1/2}$ limit. *Chem. Phys. Lett.* **427**, 259–264 (2006)
15. Akopyan, M.E., Lukashov, S.S., Novikova, I.Y., Poretsky, S.A., Pravilov, A.M., Torgashkova, A.S.: Optical population of free iodine molecule ion-pair states and their $\text{RgI}_2(\text{IP})$ complexes via RgI_2 vdW complexes of valence states correlating with the third dissociation limit. *Chem. Phys.* **336**, 109–120 (2007)
16. Akopyan, M.E., Lukashov, S.S., Poretsky, S.A., Pravilov, A.M., Torgashkova, A.S.: On mechanism of population of the $\text{I}_2(\beta)$ state under photolysis of the $\text{I}_2 + \text{SF}_6$ mixture. *Chem. Phys. Lett.* **470**, 191–195 (2009)
17. Akopyan, M.E., Lukashov, S.S., Maslennikova, Y.D., Poretsky, S.A., Pravilov, A.M.: Time-resolved studies of decay of the $\text{XeI}_2(\text{IP})$ complexes. *Chem. Phys.* **362**, 27–33 (2009)
18. Lukashov, S.S., Poretsky, S.A., Pravilov, A.M.: Optical population of gerade and ungerade iodine ion-pair states via MI_2 vdW complexes of valence states correlating with the third dissociation limit, $\text{M} = \text{I}_2, \text{Xe}$. *Chem. Phys.* **399**, 122–129 (2012)
19. Goldstein, N., Brack, T.L., Atkinson, G.H.: Quantitative absorption spectroscopy and dissociation dynamics of I_2 van der Waals complexes with He, Ar, Kr, Xe. *J. Chem. Phys.* **85**, 2684–2691 (1986)
20. Burke, M.L., Klemperer, W.: Efficiency and mechanism of electronic predissociation of the B state Ar-I_2 . *J. Chem. Phys.* **98**, 6642–6650 (1993)
21. Stevens Miller, A.E., Chuang, C.-C., Fu, H.C., Higgins, K.J., Klemperer, W.: Dynamics of linear and T-shaped Ar-I_2 dissociation upon B-X optical excitation: a dispersed fluorescence study of the linear isomer. *J. Chem. Phys.* **111**, 7844–7856 (1999)
22. van de Burgt, L.J., Nicolai, J.-P., Heaven, M.C.: Laser induced fluorescence study of the HeBr_2 van der Waals complex. *J. Chem. Phys.* **81**, 5514–5520 (1984)
23. Brinza, W., Western, C.M., Evard, D.D., Thommen, F., Swartz, B.A., Janda, K.C.: Molecular beam-laser spectroscopy of Ne-Cl_2 : observation of a metastable vibrationally excited van der Waals molecule. *J. Phys. Chem.* **88**, 2004–2009 (1984)
24. Philippoz, J.M., van den Bergh, H., Monot, R.: Product vibrational state distributions in the photodissociation of iodine-rare gas clatters. *J. Phys. Chem.* **91**, 2545–2250 (1987)
25. Drobitz, J.C., Lester, M.I.: Optical-optical double resonance of the ICl-Ne complex: binding energies in the $\text{E}(0^+)$, $\text{A}(^3\Pi_1)$ and $\text{X}(^1\Sigma^+)$ states. *J. Chem. Phys.* **88**, 1662–1669 (1987)
26. Cline, J.I., Sivakumar, N., Evard, D.D., Bieler, C.R., Reid, B.P., Halberstadt, N., Hair, S.R., Janda, K.C.: Product state distribution for the vibrational predissociation of NeCl_2 . *J. Chem. Phys.* **90**, 2605–2016 (1989)
27. Breen, J.J., Willberg, D.M., Gutmann, M., Zewail, A.H.: Direct observation of the picosecond dynamics of $\text{I}_2\text{-Ar}$ fragmentation. *J. Chem. Phys.* **93**, 9180–9184 (1990)
28. Burroughs, A., Kerenskaya, G., Heaven, M.C.: Spectroscopy and dynamics of $\text{I}_2(\text{B})\text{-Ne}$. *J. Chem. Phys.* **115**, 784–791 (2001)

29. Darr, J.P., Loomis, R.A.: Experimental interrogation of the multidimensional He+ICl(E, v^{\dagger}) and He+ICl(β, v^{\dagger}) intermolecular potential energy surfaces. *J. Chem. Phys.* **129**, 144306–144311 (2008)
30. Zhang, Y., Vidma, K., Parker, D.H., Loomis, R.A.: Photodissociation of the linear Ar-I₂ van der Waals complex: velocity-map imaging of the I₂ fragment. *J. Chem. Phys.* **130**, 104302 (2009)
31. Baturó, V.V., Lukashov, S.S., Poretsky, S.A., Pravilov, A.M., Zhironkin, A.I.: The ArI₂(ion-pair states) van der Waals complexes. *Chem. Phys. Lett.* **647**, 161–164 (2016)
32. Baturó, V.V., Cherepanov, I.N., Lukashov, S.S., Poretsky, S.A., Pravilov, A.M.: The HeI₂(ion-pair states) van der Waals complexes. *Chem. Phys. Lett.* **662**, 250–256 (2016)
33. Kantrowitz, A., Grey, J.: A high intensity source for the molecular beam. Part I. *Theor. Rev. Sci. Instr.* **22**, 328–332 (1951)
34. Fenn, J.B., Deckers, J.: Molecular beam from nozzle sources. In: Laurmann, J.A. (ed.) *Rarefied Gas Dynamics*, vol. V.I, pp. 497–515. Academic, New York (1963)
35. Reis, V.H., Fenn, J.B.: Separation of gas mixture in supersonic jet. *J. Chem. Phys.* **39**, 3240–3250 (1963)
36. Anderson, J.B., Fenn, J.B.: Velocity distribution in molecular beam from nozzle sources. *Phys. Fluids*, **8**, 780–787 (1965)
37. Anderson, J.B., Andres, R.P., Fenn, J.B.: Supersonic Nozzle Beams. *Adv. Chem. Phys.* In: Ross J (ed.) *Molecular Beam*, vol. 10, pp. 275–317. Intersci. Publ., New York/Sidney (1969) (published Online: 14 MAR 2007)
38. Saenger, K.L.: Pulsed molecular beams: a lower limit on pulse duration for fully developed supersonic expansions. *J. Chem. Phys.* **75**, 2467–2469 (1981)
39. DePaul, S., Pullman, D., Friedrich, B.: A pocket model of seeded supersonic beams. *J. Phys. Chem.* **97**, 2167–2171 (1993)
40. Morse, M.D.: Supersonic beam sources. *Exp. Methods Phys. Sci.* **29B**, 21–47 (1996)
41. Pravilov, A.M.: *Radiometry in Modern Scientific Experiments*. Springer, Wien/New York (2011)
42. Okabe, H.: *Photochemistry of Small Molecules*. A Willey Intersci. Publ, New York/Brisbane/Toronto (1978)
43. Naumkin, F.Y., Knowles, P.J.: On the adequacy of pairwise additive potentials for rare gas-halogen systems: the effect of anisotropy of interactions between atoms. *J. Chem. Phys.* **103**, 3392–3399 (1995)
44. Buchachenko, A.A., Stepanov, N.F.: Ar-I₂ interactions: the models based on the diatomics-in-molecule approach. *J. Chem. Phys.* **104**, 9913–9925 (1996)
45. Roos B.O. (Ed.): *Lecture Notes in Chemistry 58, Lecture Notes in Quantum Chemistry*. Springer-Verlag, Berlin (1992)
46. Roos B.O. (Ed.): *Lecture Notes in Chemistry 64, Lecture Notes in Quantum Chemistry II*. Springer-Verlag, Berlin (1994)
47. Prosmiiti, R., Valdés, Á., Villarreal, P., Delgado-Barrio, G.: Three dimensional ab initio potential and ground state dynamics of the HeI₂ complex. *J. Phys. Chem. A* **108**, 6065–6071 (2004)
48. Valdés, Á., Prosmiiti, R., Villarreal, P., Delgado-Barrio, G., Werner, H.-J.: Ab initio potential energy surface and spectrum of the B(³Π) state of the HeI₂ complex. *J. Chem. Phys.* **126**, 204301–204309 (2007)
49. Rohrbacher, A., Williams, J., Janda, K.C.: Rare gas-dihalogen potential energy surfaces. *Phys. Chem. Chem. Phys.* **1**, 5263–5276 (1999)
50. García-Gutierrez, L., Delgado-Tellez, L., Valdés, Á., Prosmiiti, R., Villarreal, P., Delgado-Barrio, G.: Intermolecular ab initio potential and spectroscopy of the ground state of HeI₂ complex revisited. *J. Phys. Chem. A* **113**, 5754–5762 (2009)
51. Delgado-Tellez, L., Valdés, Á., Prosmiiti, R., Villarreal, P., Delgado-Barrio, G.: HeI₂ interaction potential based on an interpolation scheme. *Int. J. Quantum Chem.* **112**, 2971–2975 (2012)

52. Kalemoss, A., Valdés, Á., Prosmitti, R.: Theoretical investigation of the He-I₂(E³Π_g) ion-pair state: Ab initio intermolecular potential and vibrational levels. *J. Chem. Phys.* **137**, 034303–034308 (2012)
53. Lukashov, S.S., Privilov, A.M., Zhironkin A.I.: The free-rotor HeI₂ (ion-pair) complexes. *Chem. Phys. Letts.* (will be submitted)
54. Delgado-Tellez, L., Valdés, Á., Prosmitti, R., Villarreal, P., Delgado-Barrio, G.: *Ab initio* characterization of the Ne-I₂ van der Waals complex: intermolecular potentials and vibrational bound states. *J. Chem. Phys.* **134**, 214304–214309 (2011)
55. Blazy, J.A., DeKoven, B.M., Russell, T.D., Levy, D.H.: The binding energy of iodine–rare gas van der Waals molecules. *J. Chem. Phys.* **72**, 2439–2444 (1980)
56. Baturo, V.V., Lukashov, S.S., Poretsky, S.A., Privilov, A.M.: Luminescence of the NeI₂ van der Waals complexes. *Chem. Phys. Lett.* (submitted)
57. Prosmitti, R., Villarreal, P., Delgado-Barrio, G.: An ab initio CCSD(T) potential energy surface for the Ar-I₂(X) complex. *Chem. Phys. Lett.* **359**, 473–479 (2002)
58. Baturo, V.V., Kevorkyanz, R., Lukashov, S.S., Poretsky, S.A., Privilov, A.M., Zhironkin, A.I.: The KrI₂(ion-pair states) van der Waals complexes. *Chem. Phys. Lett.* **684**, 357–362 (2017)
59. Johnson, K.E., Wharton, L., Levy, D.H.: The photodissociation lifetime of the van der Waals molecule I₂He. *J. Chem. Phys.* **69**, 2719–2724 (1978)
60. Sharfin, W., Johnson, K.E., Wharton, L., Levy, D.H.: Energy distribution in the photodissociation products of van der Waals molecules: iodine–helium complexes. *J. Chem. Phys.* **71**, 1282–1299 (1992)
61. Gutmann, M., Willberg, D.M., Zewail, A.H.: Real-time dynamics of clusters. II. I₂X_n (n = 1: X = He, Ne and H₂) picosecond fragmentation. *J. Chem. Phys.* **97**, 8037–8047 (1992)
62. Valdés, Á., Prosmitti, R., Villarreal, P., Delgado-Barrio, G.: Ab initio vibrational predissociation dynamics of He-I₂(B) complex. *J. Chem. Phys.* **126**, 244314–244317 (2007)
63. García-Vela, A.: Effect of intermolecular excitation in the vibrational predissociation dynamics of van der Waals complexes and the implication for control. *J. Phys. Chem. A.* **118**, 6395–6406 (2014)
64. Herzberg, G.: *Molecular Spectra and Molecular Structure. III. Electronic Spectra and Electronic Structure of Polyatomic Molecules.* Van Nostrand Reinhold Company, Toronto/New York/London (1966)
65. Heaven, M.C., Buchachenko, A.A.: Oriented dynamics in van der Waals complexes. *J. Mol. Spectrosc.* **222**, 31–45 (2003)
66. Kenny, J.E., Johnson, K.E., Shafrin, W., Levy, D.H.: The photodissociation of van der Waals molecules: complexes of iodine, neon, and helium. *J. Chem. Phys.* **72**, 1109–1119 (1980)
67. Pakhira, S., Mondal, B., Das, A.K.: Spectroscopic properties of I₂-Rg (Rg = He, Ne, Ar) van der Waals complexes. *Chem. Phys. Lett.* **505**, 81–86 (2011)
68. Darr, J.P., Glennon, J.J., Loomis, R.A.: Observation of bound-free transitions of the linear ArI₂(X, v = 0) complex in and above the I₂B-X spectral region. *J. Chem. Phys.* **122**, 13101–13104 (2005)
69. Roncero, O., Buchachenko, A.A., Lepetit, B.: Competition between adiabatic and nonadiabatic fragmentation pathways in the unimolecular decay of the ArI₂(B) van der Waals complex. *J. Chem. Phys.* **122**, 034303–034312 (2005)
70. Steinfeld, J.I.: Rate data for inelastic collision processes in the diatomic halogen molecules. *J. Phys. Chem. Ref. Data.* **13**, 445–553 (1984)
71. Kubiak, G., Fitch, P.S.H., Wharton, L., Levy, D.H.: The fluorescence excitation spectrum of the ArI₂ van der Waals complex. *J. Chem. Phys.* **68**, 4477–4480 (1978)
72. Tellinghuisen, J.: Potentials for weakly bound states in I₂ from diffuse spectra and predissociation data. *J. Chem. Phys.* **82**, 4012–4016 (1985)
73. Lepetit, B., Buchachenko, A.A., Halberstadt, N.: Electronic and vibrational predissociation in ArI₂ photodissociation dynamics. *J. Chem. Phys.* **116**, 8367–8375 (2002)

74. Roncero, O., Caloto, D., Janda, K.J., Halberstadt, N.: From the sparse to the statistical limit of intramolecular vibrational redistribution in vibrational predissociation: ArCl_2 as an example. *J. Chem. Phys.* **107**, 1406–1418 (1997)
75. Saenger, K.L., McClelland, G.M., Herschbach, D.R.: Blue shift of iodine in solvent complexes formed in supersonic molecular beams. *J. Phys. Chem.* **85**, 3333–3337 (1981)
76. Valentini, J.J., Cross, J.B.: The photodissociation cage effect in van der Waals complexes: fluorescence spectra of $\text{I}_2 \text{ B}(3\Pi_{0+u})$ from the hindered photodissociation of I_2Ar at 488 nm. *J. Chem. Phys.* **77**, 572–573 (1982)
77. Baturo, V.V., Lukashov, S.S., Poretsky, S.A., Privilov, A.M.: The RgI_2 (ion-pair states) van der Waals complexes. *Eur. J. Phys. D.* **71**(9), 1–12 (2017)
78. Cockett, M.C.R.: The spectroscopy of the Rydberg and ionic states of the $\text{I}_2\text{-Ar}$ van der Waals complex. *J. Electron Spectrosc. Relat. Phenom.* **97**, 171–190 (1998)
79. Wensink, W.A., van Voorst, J.D.W.: Noble-gas broadening of an optical transitions of I_2 measured of coherent transience. IV. Three-dimensional calculations of quantum mechanical elastic collision rates for small velocity changes of I_2 molecules (in a coherent superposition of two electronic states) interacting with noble gases (He, Ne, Ar, Kr, Xe). *Chem. Phys.* **99**, 155–175 (1985)
80. Beswick, J.A., Halberstadt, N., Janda, K.C.: Structure and dynamics of noble gas-halogen and noble gas ionic clusters: when theory meets experiment. *Chem. Phys.* **399**, 4–16 (2012)
81. Taylor M.A., Pio J.M., van der Veer W.E., Janda K.C.: Competition between electronic and vibrational predissociation dynamics of the HeBr_2 and NeBr_2 van der Waals molecules. *J. Chem. Phys.* **132**, 104309–104307 (2010)
82. Beattie, D.A., Cockett, M.C.R., Lawley, K.P., Donovan, R.J.: $(2 + 1)$ REMPI spectra of the $\text{I}_2\text{-Kr}$ and $\text{I}_2\text{-N}_2$ van der Waals complexes and the $(2 + 1')$ ZEKE-PFI photoelectron spectrum of $\text{I}_2^+\text{-Kr}$. *J. Chem. Soc. Faraday Trans.* **933**, 4245–4251 (1997)

Conclusions

A variety of up-to-date methods, such as (1+1) two step, (1 + 2)-photon optical-optical double resonance technique, three-step three-color and perturbation facilitated excitation schemes as well as resonance enhanced multiphoton ionization (REMPI) with velocity map imaging (VMI) have been used for study of spectroscopic parameters of the valence, IP and Rydberg states of an iodine molecule. Spectroscopic characteristics of the majority of these states are described well at this point, and these techniques can be utilized for further investigation of the intra- and intermolecular perturbations in the molecule states.

For the precise *ab-initio* calculation of heavy I₂ molecule, both correlation and relativistic effects should be taken into account. High-precision correlation calculations by coupled-cluster and multireference configuration interaction methods within both full electron four-component and relativistic two-component effective core potential frameworks are available for valence states of the I₂. Non-adiabatic perturbations in the *B* state, which manifest in the coupling between the *B* and (*ab*) valence states or the *B* state predissociation are studied in details. The work of Pique *et al.* on the mixing of (*ab*) states is still one of the most cited works on the theory of the hyperfine interaction perturbations in the I₂.

The IP states are well studied experimentally, but high-precision theoretical studies are still required. The *ab-initio* calculations of IP states carried out at the present are fragmental and do not give sufficient accuracy. The molecular orbital or “atom-in-molecule” approaches provide good qualitative and sometimes quantitative description of the optical IP-V transitions. Perturbations caused by *HFI* are still described unsatisfactory.

The experimental and theoretical studies identify two mechanisms for CINAT between the IP states of iodine molecule – “*approach-induced*” for collisions with molecular partners possessing large electric permanent dipole and quadrupole moments, transition dipole moment, and more common “*collision-induced*” one for collisions with rare gas atoms. The approach-induced mechanism manifests itself only in $E0_g^+ \xleftrightarrow{M} D0_u^+$ non-adiabatic transitions and gives large transition cross

sections, including the giant ones, up to $\sim 10^3 \text{ \AA}^2$ that exceed the gas-kinetic cross up to ~ 30 times. This process is highly selective: almost 90% of the products are formed in a single v_D vibrational level with a $\Delta J = \pm 1$ change in the angular momentum. The necessary conditions for this mechanism to occur are the existence of a final v_D level in a quasi-resonance with initially excited v_E level (*ca.* $|\Delta E| \leq 25 \text{ cm}^{-1}$, $M = \text{I}_2(X)$, or larger if transitions are resonant due to rotational transitions in M molecules, $M = \text{H}_2\text{O}$). The features of the approach-induced mechanism can be qualitatively interpreted in the framework of an electrostatic model and the semiclassical Born approximation.

Collisions with rare gas atoms represent a second mechanism for CINAT. For $E \xleftrightarrow{\text{Rg}} D$ energy transfer, much smaller rate constants and significantly broader product state distributions (vibrational and rotational) are observed, especially for $\text{Rg} = \text{Ar} - \text{Xe}$. Strict selection rules for electronic transitions lack for these CINATs, and other IP states of the tier are also populated. The rotational product state distributions obey the high- ΔJ propensity rule, thus being much broader than those observed for approach-induced transitions. Rotational energy transfer can play a significant role as compensating process for the energy difference between the initial and final vibrational energy levels. This fact provides a rationale for why CINAT with rare gas collisions results in broad vibrational product state distributions.

Studies of non-adiabatic transitions between IP states in van der Waals complexes provide more detailed and direct information on the non-adiabatic dynamics than CINAT studies due to much more rigid constraints on available energy, angular momentum, and average orientation of the interacting particles. They facilitate the analysis of the symmetry selection and propensity rules for electronic and vibrational predissociations of complexes and provide spectroscopic data to test directly the theoretical *PESs*.

Another very interesting and challenging problem is studies of molecular structures in which interaction of the electrophilic region of a halogen atom (acceptor of electrons) and a nucleophilic region of the other or the same molecular structure (donor of electrons) occurs. This specific interaction specializes as halogen bond (XB). XBs are mostly due to electrostatic interaction, but polarizing, exchange and dispersion ones are of great importance, also. XB is considered as a specific subset of intermolecular interactions according to IUPAC recommendation since 2013 (earlier it has been regarded as a special case of donor-acceptor, exchange or van der Waals (vdW) interaction). Halogen bonds manifest themselves in weakly-bound complexes with molecular partners, mainly. A large number of complexes of dihalogens, and interhalogens, XY , with two- and triatomic molecules and organic species *in the ground states* has been studied using spectroscopy and supersonic molecular beam technique. The excited electronic states of these complexes are promising objects for studies providing abundant information on spectroscopic parameters as well as mechanism of population and decay of these complexes.

Appendix

Table A1 The electronic energy (T_e), vibrational constant (ω_e), unharmonicity ($\omega_e x_e$), rotational constant for the $v = 0$ vibrational level (B_e), equilibrium internuclear distance (R_e), dissociation limit, dissociation energy for the $v = 0$ vibrational level, and radiative lifetime of the valence and ion-pair states of the iodine molecules

State	T_e , cm ⁻¹	ω_e , cm ⁻¹	$\omega_e x_e$, cm ⁻¹	B_e , 10 ⁻² cm ⁻¹	R_e , Å	Diss. limit	D_0 , cm ⁻¹	τ_{rad} , ns	Transitions observed	Refs.
X_0^+	0	214.520797	0.6079224	3.736794	2.666	<i>aa</i>	12440.23		$F_0^+, D_0^+, B_0^+ \leftrightarrow X; F_0^+ \rightarrow X$	[1, 2]
A_2_u	10042.0(2)	108.28(8)	1.15(2)	2.813(1)	3.0730 (8)	<i>aa</i>	9984.7	$\sim 6 \cdot 10^6$	$D_2^g \leftrightarrow A'$	[3]
$A1_u$	10907.416(9)	92.95(2)	1.56(1)	2.7398318(2)	3.114	<i>aa</i>	1641.3	$\sim 450 \cdot 10^3$	$A \leftarrow X_0^+, c'1_g, c'1_g \rightarrow A; \beta 1_g \rightarrow A;$ $G1_u \rightarrow A$	[4]
$B'0_u^-$	12190	20.5	0.29			<i>aa</i>	350		$g_0^+ \rightarrow B'$	[5, 6]
$a1_g$	12141.177(4)	23.623(6)	0.483(3)	1.43(1)	4.311	<i>aa</i>	394.35		$B_0^+ \rightarrow a1_g$	[7]
$C1_u$	19916.3 ^b	20.8 ^b	0.51 ^b	1.342	4.45	<i>aa</i>	224		$C \leftarrow X_0^+$	[8]
$a'0_g^+$	123303.402(1)	17.68(2)	0.4285(9)	1.233(6)	4.642(2)	<i>aa</i>	235.09		$B_0^+ \rightarrow a'0_g^+$	[7]
(1)2 _g	12309(2)	20(1)	0.5(1)	1.42(8)	4.34(1)	<i>aa</i>	238 (2)		$\delta 2_u \rightarrow (1)2_{e-g}$	[9]
B_0^+	15769.0485	125.6724	0.752677	2.903876	3.024800	<i>ab</i>	4318.853	see Fig.3.4	$B \leftrightarrow X_0^+, f_0^+, E_0^+ \rightarrow B$	[10]
(2)0 _g ⁺	19286.4(5)	64.4(2)	1.23(1)		3.645	<i>ab</i>	832.0(2)		$F'0_u^+ \rightarrow (2)0_g^+$	[11]
$c1_g$	19685(2)	29.5(4)	0.51(4)	1.62(2)	4.05(2)	<i>ab</i>	450(2)		$H1_u, \gamma 1_u \rightarrow c$	[12]
(2)2 _u	19827(2)	25.6(4)	0.611(2)	1.47(4)	4.25	<i>ab</i>	297			[13, 14]
$c'1_g$	19880.5(2)	24.4(1)		1.427(5)	4.315(5)	<i>ab</i>	258(2)		$\gamma 1_u \rightarrow c'$	[15, 16]
0 _g ⁻ (<i>ab</i>)	19744.5(2)	29.5(4)	0.51(4)	1.62(2)	4.052(2)	<i>ab</i>	391.3(3)		$h_0^+ \rightarrow 0_g^-(ab)$	[17]
(3)1 _u	19913(1)	22.29(2)	0.611(2)	1.401(1)	4.355(3)	<i>ab</i>	237(2)		$\beta 1_g, G1_g \rightarrow 3(1_u)$	[14]
(4)1 _u	20030.51	14.948	0.4662	1.234	4.64	<i>ab</i>	112		$\beta 1_g, G1_g \rightarrow 4(1_u)$	[14]
0 _u ⁻ (<i>ab</i>)	19967(2)	18.2(9)	0.42(9)	1.335(8)	4.46(1)	<i>ab</i>	184(2)		$g_0^+ \rightarrow 0_u^-(ab)$	[14]
0 _u ⁻ (<i>bb</i>)	27277.6	35.13(3)	0.707(2)	1.738(6)	3.910(7)	<i>bb</i>	458.2		$g_0^+ \rightarrow 0_u^-(bb)$	[18]
0 _g ⁺ (<i>bb</i>)	27305.98(1)	33.340(5)	0.7340(6)	1.702(1)	3.9509	<i>bb</i>	430.67		$0_g^+(bb) \leftarrow B_0^+$; $B_0^+ \leftarrow 0_g^+(bb)$	[19]

$1_u(bb)$	27373.88(4)	29.24(1)	0.635(2)	1.631(2)	4.036(5)	bb	364.82	$\beta 1_g \leftarrow 1_u(bb)$	[20]
$D^+ 2_g$	40388.2(1)	103.960(9)	0.2080(3)	2.056(2)	3.594(2)	$^3P_2 + ^1S_0$	31719.1	$D \leftrightarrow A$	[3]
$\beta 1_g$	40821.04(2)	105.023(4)	0.2258(3)	2.0420(2)	3.607	$^3P_2 + ^1S_0$	31259.8	$\beta \leftarrow A 1_u; \beta \leftarrow 1_u(bb)$	[21]
$D0_u^+$	41026.307	95.0784	0.10838	2.06785	3.584	$^3P_2 + ^1S_0$	31095.5	$D \leftrightarrow X; D \rightarrow a 1_g^+$	[22]
$E0_g^+$	41411.8	101.3628	0.197930	1.99692	3.647	$^3P_2 + ^1S_0$	30706.8	$D \rightarrow (2)0_g^+$	
$\gamma 1_u$	41621.444(6)	94.739(4)	0.1709(7)	1.9586(1)	3.68305	$^3P_2 + ^1S_0$	30510.5	$E \leftrightarrow B0_u^+; E \rightarrow A 1_u C 1_u$	[23]
$\delta 2_u$	41787.780(8)	100.644(3)	0.2102(3)	1.8586(2)	3.78744 (5)	$^3P_2 + ^1S_0$	30331.2	$\gamma \leftarrow X0_g^+;$ $\gamma \rightarrow a 1_{g^+} c 1_{g^+} c 1_g$	[24]
$f0_g^+$	47026.2	104.1447	0.211335	2.0803	3.5737	$^3P_0 + ^1S_0$	31538.9	$\delta \rightarrow (1)2_g$	[25]
$g0_g^-$	47085.777(7)	104.065(2)	0.1936(9)	2.0822(6)	3.572	$^3P_1 + ^1S_0$	31479.4	$f \leftrightarrow B0_u^+; f \rightarrow A 1_u C 1_u$	[23]
$F0_u^+$	47217.35	96.31275	0.4125426	2.05413	3.5963	$^3P_0 + ^1S_0$	31351.6	$g \leftarrow B0_u^+ \sim 0_u^-(ab)$	[26]
$G1_g$	47558.645(4)	106.656(2)	0.2233(3)	2.10892(8)	3.5493	$^3P_1 + ^1S_0$	31005.3	$F0_u^+ \leftrightarrow X0_g^+$	[27, 28]
$H1_u$	48280.337(3)	107.960(1)	0.2647(1)	1.99046(7)	3.6534	$^3P_1 + ^1S_0$	36282.8	$G \leftrightarrow (3)1_u(4)1_u B0_u^+, A 1_u$	[29]
$h0_u^-$	48646.548(6)	102.344(2)	0.2186(3)	1.859(6)	3.7804	$^3P_1 + ^1S_0$	29917.5	$H \leftarrow B0_u^+ \sim c 1_g$	[17]
$F^+0_u^+$	51706.237(2)	131.00(1)	0.5162(1)	2.19489(5)	3.4791	$^1D_2 + ^1S_0$	30.486	$h \leftarrow B0_u^+ \sim 0_u^-(ab)$	[17]
$f^+0_u^-$	55409.9	96.98	0.1865	1.8156	3.8250	$^1D_2 + ^1S_0$	26.800	$F^+ \rightarrow X0_g^+$	[30]
$1_g^+(D_2)$	53216.288(7)	106.932(3)	0.2077(3)	2.1420(5)	3.5218	$^1D_2 + ^1S_0$	29.988	$f^+ \leftrightarrow B0_u^+$	[23, 31]

Transitions observed are also presented (see Chap. 3 for details)

^aRadiative lifetime for the $v = 0$ vibronic level [33]

^b*ab-initio* calculation [34]

References

1. Gerstenkom, S., Luc, P.: Description of the absorption spectrum of iodine recorded by means of Fourier Transform Spectroscopy : the (B-X) system. *J. Phys.* **46**, 867–881 (1985). <https://doi.org/10.1051/jphys:01985004606086700>
2. Martin, F., Bacis, R., Churassy, S., Vergès, J.: Laser-induced-fluorescence Fourier transform spectrometry of the $X0_g^+$ state of I_2 : Extensive analysis of the $B0_u^+ \rightarrow X0_g^+$ fluorescence spectrum of $^{127}I_2$. *J. Mol. Spectrosc.* **116**, 71–100 (1986). [https://doi.org/10.1016/0022-2852\(86\)90254-7](https://doi.org/10.1016/0022-2852(86)90254-7)
3. Zheng, X., Fei, S., Heaven, M.C., Tellinghuisen, J.: Spectroscopy of metastable species in a free-jet expansion: The $D' \leftarrow A'$ transition of I_2 . *J. Chem. Phys.* **96**, 4877–4883 (1992). <https://doi.org/10.1063/1.462895>
4. Appadoo, D.R.T., Le Roy, R.J., Bernath, P.F., Gerstenkorn, S., Luc, P., Vergès, J., Sinzelle, J., Chevillard, J., D'Aignaux, Y.: Comprehensive analysis of the A–X spectrum of I_2 : An application of near-dissociation theory. *J. Chem. Phys.* **104**, 903–913 (1996)
5. Viswanathan, K.S., Tellinghuisen, J.: The 2880-Å Emission Spectrum of I_2 : Ion-Pair States near $47\,000\text{ cm}^{-1}$. *J. Mol. Spectrosc.* **101**, 285–299 (1983)
6. Motohiro, S., Nakajima, S., Aoyama, K., Kagi, E., Fujiwara, H., Fukushima, M., Ishiwata, T.: Analysis of the $0_g^- (^3P_1) - B ^3\Pi(0_u^-)$ system of I_2 by perturbation-facilitated optical-optical double resonance. *J. Chem. Phys.* **117**, 9777–9784 (2002)
7. Churassy, S., Martin, F., Bacis, R., Vergès, J., Field, R.W.: Rotation–vibration analysis of the $B0_u^+ - a1_g$ and $B0_u^+ - a'0_g^+$ electronic systems of I_2 by laser-induced fluorescence Fourier-transform spectroscopy. *J. Chem. Phys.* **75**, 4863–4868 (1981)
8. Inard, D., Cerny, D., Nota, M., Bacis, R., Churassy, S., Skorokhodov, V.: $E0_g^+ \rightarrow A1_u$ and $E0_g^+ \rightarrow B''1_u$ laser-induced fluorescence in molecular iodine recorded by Fourier-transform spectroscopy. *Chem. Phys.* **243**, 305–321 (1999). [https://doi.org/10.1016/S0301-0104\(99\)00077-4](https://doi.org/10.1016/S0301-0104(99)00077-4)
9. Bature, V.V., Cherepanov, I.N., Lukashov, S.S., Poretsky, S.A., Pravilov, A.M.: Molecular parameters for weakly bound $2_g(aa, ab)$ and $0_u^-(ab)$ states of molecular iodine and dipole moment functions of transitions to these states. *J. Phys. B At. Mol. Opt. Phys.* **49**, 125101. (8pp) (2016)
10. Barrow, R.F., Yee, K.K. $B0_u^+ - X0_g^+$ system of $^{127}I_2$: rotational analysis and long-range potential in the $B0_u^+$ state. *J. Chem. Soc., Faraday Trans. 2.* **69**, 684–700 (1973). <https://doi.org/10.1039/F29736900684>
11. Ishiwata, T., Ohtoshi, H., Sakaki, M., Tanaka, I.: Spectroscopic study on the iodine molecule by a sequential three-photon excitation. *J. Chem. Phys.* **80**, 1411–1416 (1984)
12. Jewsbury, P.J., Ridley, T., Lawley, K.P., Donovan, R.J.: Parity mixing in the valence states of I_2 probed by optical-optical double-resonance excitation of ion-pair. *J. Mol. Spectrosc.* **157**, 33–49 (1993). <https://doi.org/10.1006/jmsp.1993.1003>
13. Tellinghuisen, J.: $D' \rightarrow 2_u(^3\Delta)$ transition in I_2 . Analysis by classical and quantum spectral simulations. *J. Phys. Chem.* **87**, 5136–5140 (1983)
14. Bature, V.V., Cherepanov, I.N., Lukashov, S.S., Poretsky, S.A., Pravilov, A.M.: Spectroscopic constants and potential energy curves of some iodine valence ungerade weakly bound states. *J. Phys. B At. Mol. Opt. Phys.* **48**, 055101. (8pp) (2015). <https://doi.org/10.1088/0953-4075/48/5/055101>
15. Ridley, T., Lawley, K.P., Donovan, R.J.: Observation of weakly bound valence states of I_2 . *J. Chem. Phys.* **127**, 154306–154312 (2007)
16. Akopyan, M.E., Lukashov, S.S., Maslennikova, Y.D., Poretsky, S.A., Pravilov, A.M.: Hyperfine coupling of the iodine $E0_g^+, v_E = 19$ and $\gamma1_u, v_\gamma = 18$ ion-pair states. *J. Phys. B At. Mol. Opt. Phys.* **40**, 1173–1181 (2007). <https://doi.org/10.1088/0953-4075/40/6/008>
17. Motohiro, S., Nakajima, S., Ishiwata, T.: Perturbation-facilitated optical-optical double resonance spectroscopy of the $h0_u^+ (^3P_1)$ and $H1(^3P_1)$ ion-pair states of I_2 . *J. Chem. Phys.* **117**, 187–196 (2002)

18. Baturo, V.V., Cherepanov, I.N., Lukashov, S.S., Poretsky, S.A., Pravilov, A.M., Zhironkin, A. I.: Heterogeneous and hyperfine interactions between valence states of molecular iodine correlating with the $I(^2P_{1/2}) + I(^2P_{1/2})$ dissociation limit. *J. Chem. Phys.* **144**, 184309–184308 (2016). <https://doi.org/10.1063/1.4948630>
19. Akopyan, M.E., Baturo, V.V., Lukashov, S.S., Poretsky, S.A., Pravilov, A.M.: Spectroscopic constants and the potential energy curve of the iodine weakly bound 0_g^+ state correlating with the $I(^2P_{1/2}) + I(^2P_{1/2})$ dissociation limit. *J. Phys. B At. Mol. Opt. Phys.* **46**, 055101. (9pp) (2013). <https://doi.org/10.1088/0953-4075/46/5/055101>
20. Akopyan, M.E., Baturo, V.V., Lukashov, S.S., Poretsky, S.A., Pravilov, A.M.: Spectroscopic constants and the potential energy curve of the iodine weakly-bound 1_u state correlating with the $I(^2P_{1/2}) + I(^2P_{1/2})$ dissociation limit. *J. Phys. B, At. Mol. Opt. Phys.* **025101**(7pp), 48 (2014)
21. Perrot, J.P., Broyer, M., Chevaleyre, J., Femelat, B.: Extensive study of the $1_g(^3P_2)$ ion pair state of I_2 . *J. Molec. Spectr.* **98**, 161–167 (1983)
22. Tellinghuisen, J.: The D state of I_2 : A case study of statistical error propagation in the computation of RKR potential curves, spectroscopic constants, and Frank-Condon factors. *J. Mol. Spectrosc.* **217**, 212–221 (2003). [https://doi.org/10.1016/S0022-2852\(02\)00055-3](https://doi.org/10.1016/S0022-2852(02)00055-3)
23. Wilson, P.J., Ridley, T., Lawley, K.P., Donovan, R.J.: Double resonance ionisation nozzle cooled spectroscopy (DRINCS) of the $E(^3P_2)$, $f(^3P_0)$ and $f'(^1D_2)$ 0_g^+ ion-pair states of I_2 . *Chem. Phys.* **182**, 325–339 (1994). [https://doi.org/10.1016/0301-0104\(94\)00047-6](https://doi.org/10.1016/0301-0104(94)00047-6)
24. Ishiwata, T., Motohiro, S., Kagi, E., Fujiwara, H., Fukushima, M.: Optical-optical double-resonance spectroscopy of the $1_u(^3P_2)$ and $2_u(^3P_2)$ states of I_2 through the $A^3\Pi(1_u)$ state. *Bull. Chem. Soc. Jpn.* **73**, 2255–2261 (2000). <https://doi.org/10.1246/bcsj.73.2255>
25. Ishiwata, T., Yotsumoto, T., Motohiro, S.: Optical–optical double resonance spectroscopy of I_2 through the parity mixed valence states. *Bull. Chem. Soc. Jpn.* **74**, 1605–1610 (2001). <https://doi.org/10.1246/bcsj.74.1605>
26. Motohiro, S., Nakajima, S., Aoyama, K., Kagi, E., Fujiwara, H., Fukushima, M., Ishiwata, T.: Analysis of the $0_g^-(^3P_1) - B'^3\Pi(0_u^-)$ system of I_2 by perturbation-facilitated optical–optical double resonance. *J. Chem. Phys.* **117**, 9777–9784 (2002). <https://doi.org/10.1063/1.1516790>
27. Hoy, A.R., Brand, J.C.D.: The $F0_u^+$ state of diatomic iodine: Effects of configuration interaction. *Chem. Phys.* **109**, 109–115 (1986). [https://doi.org/10.1016/0301-0104\(86\)80189-6](https://doi.org/10.1016/0301-0104(86)80189-6)
28. Ishiwata, T., Kusayanagi, T., Hara, T., Tanaka, I.: An analysis of the $F(0_u^+)$ ion-pair state of I_2 by optical-optical double resonance. *J. Mol. Spectrosc.* **119**, 337–351 (1986). [https://doi.org/10.1016/0022-2852\(86\)90029-9](https://doi.org/10.1016/0022-2852(86)90029-9)
29. Kagi, E., Yamamoto, N., Fujiwara, H., Fukushima, M., Ishiwata, T.: Optical–Optical Double Resonance Spectroscopy of the $1_g(^3P_1) - A^3\Pi(1_u) - X^1\Sigma_g^+$ Transition of I_2 . *J. Mol. Spectrosc.* **216**, 48–51 (2002). <https://doi.org/10.1006/jmsp.2002.8676>
30. Ishiwata, T., Tokunaga, A., Shinzawa, T., Tanaka, I.: An analysis of the $F'0_u^+$ ion-pair state of I_2 by optical-optical double resonance. *J. Mol. Spectrosc.* **117**, 89–101 (1986). [https://doi.org/10.1016/0022-2852\(86\)90094-9](https://doi.org/10.1016/0022-2852(86)90094-9)
31. Ishiwata, T., Yamada, J., Obi, K.: Optical-optical double-resonance spectroscopy of the $I_2 0_g^+(^1D)$ ion-pair state. *J. Mol. Spectrosc.* **158**, 237–245 (1993). <https://doi.org/10.1006/jmsp.1993.1068>
32. Ishiwata, T., Takekawa, H., Obi, K.: Optical-optical double-resonance spectroscopy of the $I_2 1_g(^1D)$ ion-pair state. *J. Mol. Spectrosc.* **159**, 443–457 (1993). <https://doi.org/10.1006/jmsp.1993.1141>
33. Lawley, K.P., Jewsbury, P., Ridley, T., Langridge-Smith, P., Donovan, R.: Einstein A-coefficients and transition dipole moments for some ion-pair to valence transitions in I_2 . *Molec. Phys.* **75**, 811–828 (1992)
34. de Jong, W.A., Visscher, L., Nieuwpoort, W.C.: Relativistic and correlated calculations on the ground, excited, and ionized states of iodine. *J. Chem. Phys.* **107**, 9046–9058 (1997). <https://doi.org/10.1063/1.475194>

Index

A

Absorption cross-section, 27
Action spectra, 14, 141, 179
Angular momentum of the nuclei rotation, 99
Approach-induced, 181
Asymptotic model, 24, 32, 37, 73, 77
Autoionization, 49

B

Beer law, 8
Bent, 155, 156
Binding energies, 141, 154, 155, 158, 163, 165, 168, 170, 177, 182
Branching ratios, 119, 163, 165, 170, 178, 180, 182

C

CC method, 150, 151
CCSD method, 150
CCSD model, 150, 151
CCSDT model, 150
CCSD(T), 151, 152, 157, 178, 181
CINAT, 93, 94, 96–98, 111–122, 124–126, 128–134, 162, 181, 182
CINAT cross-sections, 111, 132
Clebsch-Gordan coefficients, 108, 124, 125
Collision-induced, 181
Collision-induced non-adiabatic transitions, 14, 93
Collision-induced predissociation, 91, 93
Collision-induced processes, 32, 125
Cordes band, 33
Coulomb potential, 30, 83

Coupled-cluster method, 150
Cross-sections, 7–9

D

Diatomics-in-molecule, 24
Dipole electric allowed transition, 7
Doppler contour, 10

E

Electronic angular momentum, 99
Electronic configuration, 21, 25, 32, 37, 86
Electronic deactivation, 91, 92
Electronic Hamiltonian, 99, 100, 105
Electronic predissociation, 139–141, 162, 173, 181
Electronic wavefunction, 100
Electrostatic model, 121, 124–126, 129
Equilibrium distance, 24, 33, 44, 50, 73, 154–156, 158, 170, 171
EVCC-IOS approximation, 103
EVCC-IOS (6×6) method, 111, 112, 114–116
Excitation spectra, 27, 33–35, 45, 47, 68, 69, 74, 157, 160, 161, 164, 166, 169, 177, 180
Excitation spectrum, 8

F

Fourier-transform spectroscopy method, 7
Franck-Condon densities (FCDs), 95, 174
Franck-Condon factor, 13
Free-rotor, 140, 153, 154, 156, 157, 159, 160, 163–165

G

Gerade, 9, 10, 15, 16

H

Heavy Rydberg, 36, 83

Heterogeneous interaction, 61

HFI electronic matrix element, 14

Homogeneous interaction, 84

Homonuclear halogens, 140

Hyperfine interaction, 13, 59

Hyperfine structure, 10

I

I₂(IP → V) luminescence, 8

IDIM PT1 model, 105, 106, 110, 111

Interhalogens, 140, 141

Internuclear distance, 99

Intracavity absorption spectroscopy, 178

Ion-pair (IP) state, 7

IOS approximation, 103, 104

IP state, 9–11, 13–15

Isolated diatomic molecule wavefunction, 99

J

jj coupling, 39

L

Laser-induced luminescence spectroscopy techniques, 141

Lifetime, 62, 82

Linear, 140, 149–151, 153–159, 163–165, 167, 168, 170, 171, 173–176, 178, 181

Luminescence depletion techniques, 141

Luminescence spectra, 30, 141, 162, 165, 166, 172, 176, 178

Luminescence spectrum, 8

M

Mach number, 143, 164

Massey parameter, 93, 98, 124

Molecular orbital theory, 22, 37

MR-CISD method, 150

Multi-reference configuration interaction (MR-CI) method, 149, 150, 152, 154, 158

N

Nd:YAG laser harmonic, 12

Non-adiabatic, 93, 94, 98, 99, 111

Non-adiabatic transition, 93, 98, 162, 182

O

One-atom cage effect, 176

P

Permanent electric dipole, 98, 126, 134

Permanent electric dipole moment, 126

Permanent electric quadrupole moments, 118, 133

Permanent quadrupole moments, 118

Perturbation-facilitated, 35, 93

three-step excitation scheme, 14

two-step excitation scheme, 13–14

Perturbation-facilitated optical-optical double resonance (PFOODR), 69, 74, 78

Perturbation-irrelevant, 94

Photoionization, 66

(1 + 2)-Photon, 10, 11

Photon flux Φ , 9

Photon irradiance, 9, 10

Polarizability, 117, 119, 133, 139, 181–183

Polarization, 44

Predissociation, 10, 16, 91–93, 95, 113, 141, 157, 173, 175, 181

gyroscopic, 63

hyperfine, 63, 64

spontaneous, 63, 65

Probability, 93, 95, 111, 113, 124–126, 129, 134

Propensity rules, 94, 118, 120, 125, 132, 133

Pump-probe method, 141

Pump-probe technique, 66

Q

Quantum defect, 24, 42, 48, 83, 85

R

Rate constants, 92, 94–98, 104, 105, 111–123, 126, 128–130, 132–134

RCCSD(T), 151, 154, 164, 170

REMPI, 34, 35, 43, 44, 47–49, 65, 84, 177, 180

Resonance enhanced multiphoton ionization,

15

Rotational, 91, 94, 99, 100, 103, 111, 112, 114, 116, 122, 124–126, 128, 134
R-T processes., 94
Rydberg, 23–25, 30, 35, 36, 42–50, 177, 178, 180
Rydberg state, 15, 16

S

Saturation, 9, 10, 13, 62
Scattering equations, 100
Selection rules, 33, 35, 42–45, 60, 61, 63, 64, 76
Spectator, 140, 161, 176, 182
Spectroscopic characteristics, 140, 141, 153, 159, 163, 168, 178
Spin-orbit interaction, 22, 23, 31
 splitting, 22
Spontaneous predissociation, 93, 95

T

Three-step three-color, 11, 13
Transition dipole moment, 28, 37
Transition dipole moment function, 28
Transition electric dipole moments, 98, 129, 132, 134
T-shaped, 140, 153–164, 167–176, 178, 179, 181, 183
Two-photon absorption, 10
Two-state model, 61, 68, 71, 78, 82

U

UCCSD(T), 151, 154, 155
Ungerade, 9–11, 13

V

vdW complexes, 139, 140, 148, 151–183
vdW levels, 153–156, 158, 159, 163, 170, 171, 173, 175
Velocity-map imaging, 16, 141
Vibrational distributions, 94, 97, 114, 116, 117, 120, 121, 126, 131, 132, 141, 167, 176
Vibrational modes, 122, 128, 129
Vibrational populations, 129, 133, 180, 182
Vibrational predissociation, 140, 141, 167, 173
Vibrational progression, 36, 44, 49, 168, 171, 177
Vibrational quantum numbers, 92, 99, 100, 171
Vibrational relaxation, 91
Vibrational temperature, 145
Vibrational wave function, 99, 100
V-T + R-T processes, 94, 95
V-T processes, 95

X

x/D value, 144

Ω

Ω-Splitting, 71, 73, 74